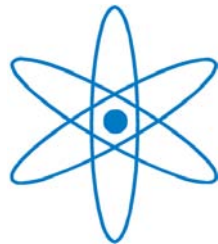# PHYSIK DEPARTMENT

Complex Microfluidics

Dissertation
von

Bernhard Wunderlich

TECHNISCHE UNIVERSITÄT MÜNCHEN

TECHNISCHE UNIVERSITÄT MÜNCHEN

Lehrstuhl für Biophysik E27

Complex Microfluidics

Bernhard K. Wunderlich

Vollständiger Abdruck der von der Fakultät für Physik der Technischen Universität München zur Erlangung des akademischen Grades eines

Doktors der Naturwissenschaften

genehmigten Dissertation.

Vorsitzender: Univ.-Prof. Dr. M. Zacharias

Prüfer der Dissertation:

1. Univ.-Prof. Dr. A. Bausch

2. Univ.-Prof. Dr. E. Frey,

Ludwig-Maximilians-Universität München

Die Dissertation wurde am 14.11.2012 bei der Technischen Universität München eingereicht und durch die Fakultät für Physik am 08.01.2013 angenommen.

Für Jenny, Emmi und Lisa.

SUMMARY

The behaviour of complex fluids with macromolecular constituents plays an important role in countless industrial applications, biological processes and in our daily life. When put under flow, such fluids exhibit a variety of non-Newtonian properties, which are usually related to an out-of-equilibrium conformation of the macromolecules in the fluid. Despite decades of intensive research on polymer solutions with significant progress, the sophisticated interplay between the microscopic dynamics of the polymers and the macroscopic properties of the solution is not yet fully resolved.

In this work we demonstrate, how properly designed microfluidic devices can be used to both monitor macromolecular dynamics and measure bulk fluid properties. To this purpose, steady and oscillatory flows of model polymer fluids were established in microfluidic channels. We surveyed single polymers in flow, developed new methods to determine macroscopic response functions and investigated fluid-structure interactions. The demonstrated versatility turns microfluidic lab-on-a-chip devices into ideal platforms for studying the physics of complex fluids and mimicking biological systems in vitro.

In the first part of this thesis, individual fluorescently labelled actin filaments were followed with a moveable microscope stage while flowing down a microchannel. The full conformational dynamics of the tumbling filaments in shear could be resolved and evaluated. Based on the experimental findings, a telescopic rod model describing the tumbling of semiflexible polymers was proposed. A force balance between the frictional drag and the restoring bending forces in the filament allowed for the calculation of the filament's typical bending radius R_U and the average tumbling time τ_T. In first approximation, the orientational dynamics of semiflexible tumbling filaments were found to be equivalent to those of stiff Brownian rods in shear. The experimentally determined values of τ_T and R_U for stiff and semiflexible filaments are in good agreement with the theoretical predictions. Motivated by the success of the rather simple U-turn model, an extension describing the tumbling dynamics in the entire regime of rigidities has been developed. Literature data for flexible DNA in shear flow was shown to be in accordance with the proposed model.

Apart from the tumbling dynamics, microfluidic devices also enable the analysis of higher order effects in flow. As an example, lift forces induced by a hydrodynamic interaction of shear-aligned polymers with the channel walls were studied by monitoring the evolution of a depletion layer in a solution of fluorescent λ-DNA in shear flow. Hereby, a sufficiently long residence time of the fluid in the channel was achieved by using low-frequency, high amplitude oscillatory

shear.

In the second part of the work, novel differential microfluidic viscometers for measuring the rate dependence of the shear and extensional viscosities $\eta(\dot{\gamma})$ and $\Lambda(\dot{\epsilon})$ in non-Newtonian fluids were proposed and tested with polymer- and worm-like-micellar solutions. Experiments with prototypes of the proposed shear viscometer showed, that the device is well suited for measurements of the local power-law exponent n of $\eta(\dot{\gamma})$, which expresses the fluid's shear-thinning properties. An apparent transient extensional viscosity of dilute polymer solutions could successfully be determined in realisations of the extensional differential rheometer. As no purely extensional, steady homogeneous flowfield is established in the extensional rheometer device, the determined transient viscosity can serve as an estimate for the true extensional viscosity $\Lambda(\dot{\epsilon})$.

The last part of the thesis focusses on the coupling of oscillatory flows to channel deformations induced by the driving pressure of the flow. We demonstrate, how the viscoelastic response of PDMS channel walls to forces can be utilized as a microfluidic pressure sensor. The propagation of periodically applied pressure pulses and the corresponding flow rates have been measured along a microchannel. The experimental results could be described with a one-dimensional equivalent circuit model of the channel. Pressure and flow are governed by a diffusion equation, and the observed dispersion and damping of pressure and flow rate step pulses could be quantitatively explained.

The results shown in this thesis demonstrate, that microfluidic devices offer a multisided approach for studying complex fluid dynamics. Especially the possibility to bundle different analytical and functional tools in a single lab-on-a chip implementation opens promising perspectives for prolific microfluidic applications beyond the examples presented here.

.

CONTENTS

1. INTRODUCTION

Many liquids in our everyday life are complex fluids, including industrial fluids such as paints or paper pulp as well as foods like mayonnaise or biofluids like blood, spittle or mucus. In general, complex fluids are viscoelastic, which means that their response to an external force is inbetween that of a purely viscous liquid and an elastic solid. According to the specific flow conditions applied, the same fluid can behave very differently. The observed non-Newtonian rheological properties like shear-thinning, rod-climbing or drag reduction in turbulent flows can be traced back to the complex dynamical behaviour of the fluids building blocks. Thus, identifying the dynamics of macromolecules like polymers in flow is of fundamental importance for understanding the non-linear rheology of fluids. As the size of the constituents of complex fluids is typically on the scale of several nanometers to hundreds of microns, microfluidic devices offering channel widths in a range of $10\,\mu$m to $1\,$mm provide an ideal platform to study the microscopic mechanisms of complex fluids in flow.

Besides this well-founded interest in revealing the fluid dynamics on the molecular level, there is a growing need for small-sized analytical instruments, which are capable of measuring bulk fluid properties and open for incorporation into numerous emerging lab-on-a-chip applications. Driven by the trend of miniaturization in biotechnology, manufacturing and chemical processing industries, a range of microfluidic devices to measure bulk rheological properties like the shear and extensional viscosity has been developed [82]. The high surface-to-volume ratio, the absence of inertial effects up to high deformation rates and the small amount of required sample volumes allow microrheometers to explore a regime unavailable to conventional viscometers. Especially measurements of the extensional viscosity are still challenging, and simple and robust methods would be desirable. The extensional viscosity of dilute polymer solutions with near-Newtonian shear viscosity can exceed the shear viscosity by up to 3 orders of magnitude, which is utilized in oil recovery to increase the flow resistance of liquids in porous media [79, 43]. Extensional viscosity is also important in polymer-induced drag reduction in turbulent pipe flows [72]. Moreover, it governs the stringiness of physiological fluids like saliva, cervical mucus, synovial fluid and sputum, which can be used as a diagnostic tool [43].

The proper operation of increasingly complex microfluidic devices requires an efficient control of spatiotemporally changing pressure and flow rates, which is still posing a major challenge for the broad applicability of microfluidic devices. The majority of microfluidic devices consists of channels imprinted into a block of the elastomeric material PDMS which is bonded to a glass substrate [75].

The cheap and easy lithographic production, the optical transparency, the good thermal stability, the high biocompatibility of the surface and the high gas permeability, which enables oxygen supply for living cells, makes PDMS particularly suited for life-science applications. While in simple steady-state flows with moderate operating pressures the effects of the deformation of the material under pressure are negligible, fluid-structure-interactions due to the elastic response of the channel material can significantly alter the flow conditions in transient flows. A long standing interest in pulsatile flows of complex fluids in soft environment comes from medical applications — understanding vessel diseases needs a quantitative understanding of cardiovascular flow behavior in elastic channels. As with standard microfluidic technology almost any complex 2D geometry is readily available and the viscoelastic properties of the PDMS walls can be tuned by varying the amount of crosslinkers, microfluidics present an ideal system for studying fluid-structure interactions in elastic fluidic networks. Increasingly more complex model systems of the capillary system may be built and examined. This sets the stage for an experimental link between the macro- and microcirculatory regime [4, 85, 114, 83, 30, 98, 3], as well as for testing simulations in well defined circumstances.

In this thesis, we investigate the dynamics of complex fluids in microchannels in a multi-lateral approach: After a short introduction on basic fluid dynamics in microchannels, we study the dynamics of individual polymers in simple shear flow in the first part of the work. As model polymers we chose semiflexible, fluorescently labelled actin filaments, whose conformations in flow can be fully resolved using a motorized microscope stage. The direct observation of the entire conformational dynamics allows for the formulation of a simple theoretical description of the filament dynamics on the basis of a balance of thermal fluctuations, frictional drag and elastic bending forces. The discussion of the proposed U-turn model for the tumbling dynamics of the semiflexible polymer reveals some generic bulk features of polymer solutions in the non-Newtonian flow regime.

In the second part, we target the bulk properties of complex fluids by proposing and testing novel differential viscometers for measuring shear- and extensional viscosity in microchannels. To this purpose, an equal pressure drop is applied to a reference and an analyzer channel and the ratio of flow rates between the channels is detected. By an appropriate design of reference and analyzer channel, the local power-law exponents of shear and extensional viscosity can be determined from the measured flow rate ratio. This enables the calculation of relative values for $\eta(\dot{\gamma})$ and $\Lambda(\dot{\epsilon})$.

Finally, we probe the response of a Newtonian fluid in a viscoelastic microchannel to transient periodic pressure pulses in order to study the occuring fluid-structure interactions. We describe the modulation of the flow due to the channel deformations with a one-dimensional equivalent circuit model, which yields a diffusive pressure propagation along the channel. For all applications, a simple physical basis for the frequency response of the transport properties of microfluidic devices is provided, enabling a quantitative design approach for more complex devices.

2. MATERIALS AND METHODS

2.1 Microfluidic Channels and Measurement Setup

Microfluidic channels with rectangular cross sections were fabricated following the standard protocol [75]. Unless inidcated differently, PDMS and cross-linker (SYLGARD 184 Silicone Elastomer Kit) were mixed in a ratio of 10:1 and cured for 2 hours at 70 °C. For studying the fluid-structure interactions in chapt. 6, PDMS and cross linker were mixed in a ratio of 20:1 to yield soft channels with well defined viscoelasticities with a length of $l = 20\,\text{mm}$, width $w = 60\,\mu\text{m}$ and height $h = 80\,\mu\text{m}$. For the study of the tumbling dynamics in chapter 4, channels with a higher aspect ratio $w = 30\,\mu\text{m}$ and $h = 60\,\mu\text{m}$ were used, so that in the vicinity of the observation plane at $z = h/2$ the velocity gradient was predominantly aligned with the xy-plane. High aspect ratio channels of width $w = 45\,\mu\text{m}$ and height $h = 150\,\mu\text{m}$ were used for the oscillatory measurements of the λ-DNA solution in section 4.5 to minimize wall effects from the channel top and bottom. The hyperbolic constrictions with circular cross section
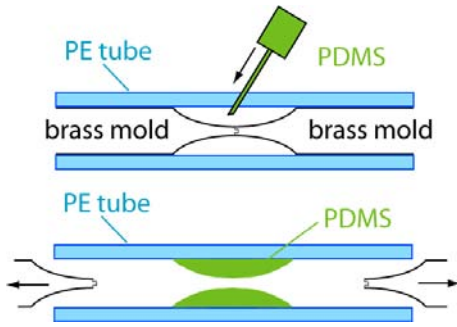
Figure 2.1: Channels with cylindrical semihyperbolical constrictions were produced by filling Polyethylen tubes with PDMS. Removable brass molds were used to obtain the hyperbolic shape of the constrictions.

used in the differential extensional viscometer (sect. 5.4.4) were fabricated from polyethylen tubings with an inner diameter of 6.5 mm. The tubings were stuffed with two opposing brass molds giving the semihyperbolic shape (see fig. 2.1). PDMS mixed with cross linker was injected with a syringe to fill the constriction. After curing, the brass molds were removed resulting in a constriction with the desired shape. To prevent a slipping of the PDMS constriction at higher operating pressures, additional syringe needles were pinched through the tube in the convergion region before PDMS curing. After curing, the needles fixed the PDMS constriction within the tube (see fig. 5.16).

The measurement setup consisted of a Zeiss Axiovert 200 microscope with
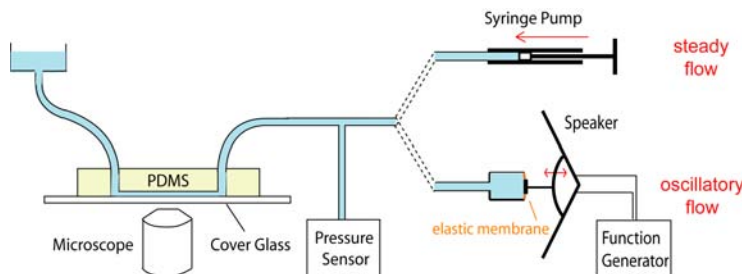
Figure 2.2: Schematics of measurement setup: The microfluidic device is placed on a motorized microscope stage. For steady flow generation, a syringe pump is connected to the device. For oscillatory flows, a fluid reservoir with a membrane which is coupled to a speaker can be connected.

a motorized microscopy stage (Thorlabs Max 203) on which the microchannels were mounted. Videos wer captured in the midplane of the channel at $z = 0.5h$ using a Hamamatsu orca camera with OpenBox [91] software for recording, except as noted otherwise. For the study of the fluid-structure-interactions in chapter 6, videos were recorded with a high-speed camera (Phantom V5.1, Vision Research) at 500 fps. For experiments in oscillatory flow, a speaker was coupled to the membrane of a fluid reservoir which in turn was connected with the microfluidic channels via $d = 0.5\,\text{mm}$ metal and polymeric tubings. Rectangular and sinusoidal voltage signals of different frequencies and amplitudes were applied to the speaker to generate periodic pressure pulses at the channel entrance $(x = 0)$, while the other end of the channel $(x = 20\,\text{mm})$ was connected to a small reservoir exposed to ambient pressure. For experiments with steady flow, a motorized syringe pump (WPI SP 200) was connected to the channel inlet. Fig. 2.2 shows the schematics of the measurement setup, fig. 2.3 shows a picture of the oscillatory flow setup. In some experiments, a pressure sensor (WPI, BLPR2) was connected via a T-crossing before the inlet of the microfluidic device, so that the applied pressure could be monitored.

Rheological properties of the solutions in shear were determined by measurements with a conventional cone-plate rheometer (AR-G2, TA-Instruments). CaBER measurements were performed in a self-made capillary breakup extensional rheometer [84].

2.2 Materials

Actin filaments were prepared following standard protocols [92]. Polymerized F-Actin was suspended in F-Buffer containing 45.5% (w/v) sucrose at a final concentration of 0.5 nM. The concentration of the sucrose was chosen to adjust the refractive index of the actin solution to the refractive index of the PDMS for minimizing refraction effects at the channel walls. In order to decrease photodamage effects ascorbic acid was added to an amount of 1 mM.
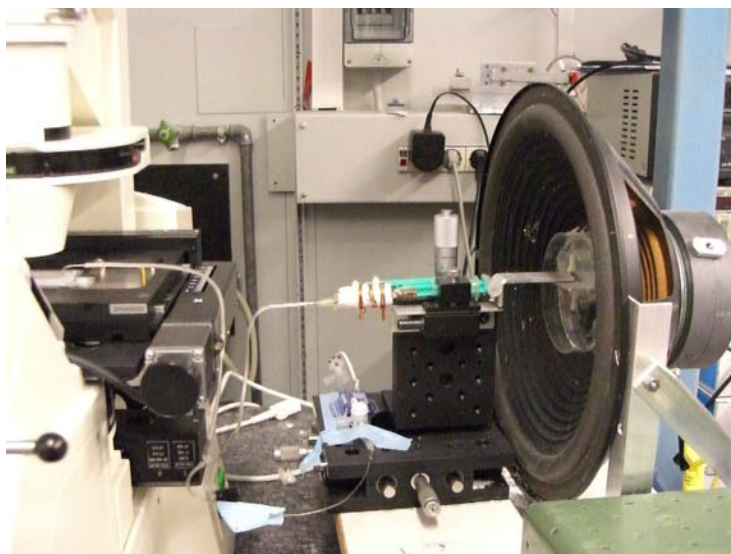
Figure 2.3: Picture of the setup in the oscillatory mode showing the microscope stage with microfluidic device (left) and the speaker (right), which is connected to the membrane of the fluid reservoir. The membrane is stretched onto the front half of a dissected 5 ml syringe tube and sealed by twirled copper wire (middle). An additional pressure sensor is connected for measuring the generated pressure (middle, located beneath the fluid reservoir on the (x, y)-stage). The fluid reservoir which is coupled to a speaker is placed on a (x, y, z)-stage. By adjusting the relative position of the reservoir with respect to the speaker, a net drift can be induced or suppressed in the oscillatory flow.

λ-DNA was purchased from New England BioLabs GmbH and labelled with YOYO-1 iodide (invitrogen). A 10 pM solution of the labelled λ-DNA was prepared in 40 mM EDTA, 50 mM NaCl, 50% (w/w) Glycerol, 15% (wt/wt) Glucose buffer with 10 mg/ml BSA and each 2.5% (v/v) glucose oxidase and catalase for the experiments in section 4.5.

Model polymer fluids used in chapter 5 were prepared as aqueous solutions in deionized water with Polyacrylamide (PAA, 5-6 MDa, Sigma Aldrich) in different concentrations. For a variation of the solvent viscosity, PAA solutions in various mixtures of glycerol (Sigma Aldrich) were used. Water-glycerol solutions were also used as Newtonian reference fluids. A commercially available shower gel (Lavera, basis sensitiv Duschbad) was used as worm-like-micellar solution.

For the experiments in chapter 5 and 6, fluorescently labelled melamin resin beads of 1 μm diameter (microparticles GmbH, Berlin; Rhodamin B MF-Polymerpartikel) were used to determine the flowrate ratio and track the motion of the fluids and the channel walls. They were suspended in the working fluid and in the crosslinker solution prior mixing with PDMS at concentrations below 0.5% (v/v). Fig. 2.2a shows a bright field image of the fluid filled channel
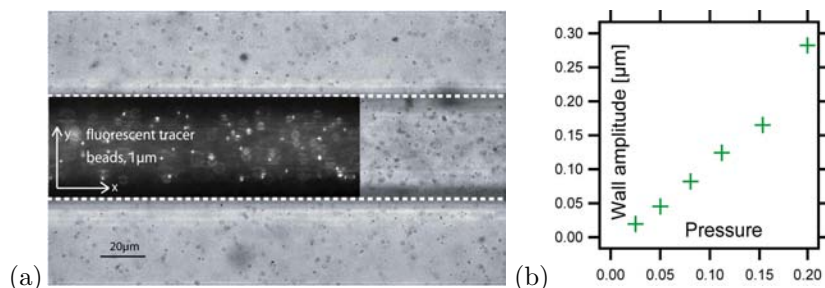
Figure 2.4: (a) Bright-field-videoframe of the fluid filled channel with stracer beads in the fluid and in the PDMS matrix; the dotted lines indicate the position of the channel walls, the scalebar represents $20\,\mu$m. The inset shows a fluorescence microscopy image of tracer beads in the fluid in the same channel. (b) For low and moderate pressures, the amplitude of the measured wall displacement in a $f = 0.5\,$Hz sinusoidal flow depends linearly on the pressure.

with melamin beads in both fluid and the walls. The inset shows a fluorescence microscopy picture of the tracer fluid in the channel.

2.3   Determination of Polymer Dynamics and Velocity Fields

Polymer dynamics and velocity fields were determined by image-analysis of the recorded videos. The conformation of the actin filaments was traced semi-automatically by applying self-written path finding algorithms in Matlab. L_c is determined as the average length traced for each filament, so that the measured values for the contour length slightly exceed L_{c} in some frames due to the tracing error. The position of the channel walls was easily recognized by a quantitative analysis of the jump in intensity which occurs at the boundary solution-PDMS. The shear-rate was determined by assuming a parabolic flow profile with known positions of the channel walls and the filament.

For the purpose of comparison between experiment and theory we performed a limited number of Brownian dynamics simulation runs of a single semiflexible multibead-chain subjected to shear flow at constant shear rate, in the presence of implicit solvent and isotropic friction, and taking into account metric forces, following standard recipes [77]. For the reported results the chain is composed of 30 beads interacting via (i) a finitely extendable nonlinear elastic (FENE) spring as in [62], (ii) purely repulsive Lennard–Jones potential, and (iii) bending Hamiltonian $H^{\mathrm{bend}} \propto \sum_{i=1}^{N-2} \mathbf{t}_i \cdot \mathbf{t}_{i+1}$, where $\mathbf{t}_i$ denotes the unit vector connecting adjacent beads i and $i+1$.

Additional simulations for the dynamics of Brownian rods in shear were done with a self-written MATLAB script.

The velocity field of solutions with tracer particles in straight channels in steady and oscillatory shear was determined by evaluating recorded videos with self-written Matlab scripts [57]. The channel wall mations were analyzed by

using particle tracking algorithms implemented in OpenBox [91].

All FEM-simulations were done with COMSOL Multiphysics.

2.4 Local Pressure Sensing with Channel Wall Deflection

The viscoelastic response of the PDMS material to changes in pressure allows for the use of the channel itself as a local pressure sensor. To this end, the displacement $Y(x,t)$ of the channel wall caused by transient pressures has to be measured with sufficient accuracy, which was achieved by tracking visible particles embedded in the PDMS (see fig. 2.2a). The tracking algorithm applies bidirectional Gaussian fits over the intensity profiles of the beads, giving a spatial resolution beyond the optical diffraction limit. By averaging traces from a high number of tracked beads, a very high resolution of the wall motion on the order of several nm can be achieved. If periodic pressure changes with frequency ω_0 are applied, the according wall movement $Y(x,t)$ will have the same periodicity and it is conveniently expressed by its Fourier components

$$Y(x,t) = \sum_{n=0}^{N} Y_n(x,t) \exp(i\omega_0 n t + \phi_n) \tag{2.1}$$

where the highest mode number $N = \omega_0/\omega_s$ is determined by the data sampling frequency ω_s of the wall motion measurement. In the linear regime, the strain ϵ of the PDMS deformation is related to the wall displacement $Y(x,t)$ and channel width w via a geometrical factor f_{geom}

$$\epsilon = f_{\mathrm{geom}} Y/w, \tag{2.2}$$

which depends on the channel and measurement geometry and can be determined from finite elemente method simulations (see section 6.2.1). The deformation of viscoelastic solids can be calculated with a complex, frequency dependent Young modulus $E^\star = E' + iE''$ relating stress σ and strain ϵ of a periodic deformation $\epsilon(t) = \epsilon_0 e^{i\omega t}$:

$$\sigma(t) = E^\star(\omega)\epsilon(t) \tag{2.3}$$

The pressure for each Fourier component ϵ_n of the strain can thus be calculated as

$$p_n = |E^\star(\omega_n)|\epsilon_n \exp[i(\omega_n t + \phi_n - \delta(\omega_n))] \tag{2.4}$$

where $\tan \delta(\omega) = E''(\omega)/E'(\omega)$ and $\omega_n = n\omega_0$. The Young modulus $E^\star$ of an isotropic material is related to the complex shear modulus $G^\star$ via the Poisson ratio ν:

$$E^\star = 2G^\star(1 + \nu) \tag{2.5}$$

The shear modulus $G^\star(\omega)$ can be measured in a conventional rotational rheometer. Altogether, the pressure can be determined from the measurable wall displacement $Y(x,t)$ as:

$$p(x,t) = \sum_{n=0}^{N} 2(1+\nu)|G^\star(\omega_n)|\frac{f_{\mathrm{geom}}}{w} Y_n(x,t) e^{i(\omega_n t + \phi_n - \delta(\omega_n))}. \tag{2.6}$$

This calculation only holds in the linear regime, where the amplitude of the wall deflection is proportional to the pressure amplitude. Figure 2.2b shows the wall deflection amplitude measured with sinusoidal pressure of different ampitudes applied to a $60 \times 80\,\mu$m cross sectional PDSM channel. The measurement shows a linear deformation up to wall displacements of ~ 150nm.

2.5   Determination of Flowrate Ratio in Differential Viscometer

For the differential microfluidic viscometer introduced in chapter 5, the flowrate ratio $X = Q_a/Q_r$ of the fluid streams Q_a, Q_r flowing through a reference and an analyzer channel has to be measured. In the rectangular microfluidic devices, this has been done optically with a microscope by unifying both streams in a detection channel K_d with small aspect ratio $h/w \ll 1$ resulting in Hele-Shaw flow, where h and w are height and width of the channel K_d. In the region of fully developed flow all streamlines are parallel to the channel walls and the lateral velocity profile across the channel is flat except for a small region of width on the order of h next to the channel walls. Thus, the relative width of the fluid streams d_r, d_a is approximately proportional to the flowrates Q_r, Q_a as long as $d_r, d_a \gg h$. Hence, the flowrate ratio X can be determined as

$$X = \frac{Q_a}{Q_r} = \frac{d_a}{d_r} \tag{2.7}$$

by measuring d_r, d_a, which was done in two ways:

Optical Determination of d_r, d_a with Marker Fluid

The widths d_r, d_a of the fluidstreams can be determined by visually seperating Q_r and Q_a with a stream of marker fluid Q_m introduced into the detection channel inbetween analyzer and reference channel (see fig. 2.5). The marker fluid was produced by mixing a small amount of colored tracer particles into the analyte fluid, which ensures equal viscosity properties and avoids surface tension effects between analyte and marker fluid. The flowrate Q_m of the marker fluid is set an order of magnitude lower than the feeding channel flowrate Q resulting in a thin stream of marker fluid Q_m between Q_a and Q_r.

Determination with Depletion Layer

Alternatively, the marker fluid channel was omitted and marker particles were directly suspended in the analyzing fluid stream Q. As the center of the spherical marker particles cannot get nearer to the wall than the particle radius r_p, restricted volume effects create a depletion zone seperating the unifiying streams of Q_r and Q_a in the detection zone (see fig. 2.6a). The depletion zone can be observed in the microscope image and has a width of at least $2r_p w_d/(w_a + w_r)$, where $w_d, w_a w_r$ are the widths of detection, analyzer and reference channel. Fig. 2.6b 1-3 shows a 1% (w/w) PAA solution with fluorescently labeled melamin resin beads with $r_p \approx 0.5\,\mu$m radius as tracer particles at different positions
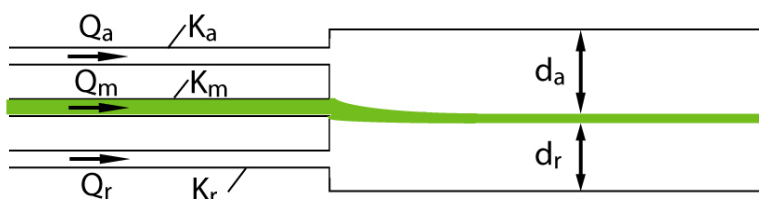
Figure 2.5: To determine the flowrate ratio Q_a/Q_r an additional channel K_m with marker fluid flowing into the detection zone between analyzer and reference channel is inroduced. If the aspect ratio of the detection zone is small $h/w \ll 1$, the flowrate ratio is given by the ratio of the width of the reference and analyzer channel streams d_a/d_r in the region of fully developed flow.

while flowing along a channel of width $300\,\mu$m and length $l = 4\,$cm, where the arrows indicate the position of the channel walls. The resulting depletion zone between two unifying fluid streams is marked by the arrow in fig. 2.6b 4. Clearly, a depletion layer much wider than r_p evolves along the channel. This could be caused by a lift force, which is known to act on spherical particles in shear near walls with no slip boundary condition [59]. Although the lift force is an inertial effect, it occurs even at low Reynolds numbers in creeping flow conditions, and its magnitude decreases with increasing distance to the wall. Moreover, any local enhancement of the streaming velocity near the wall will be accompanied by a locally reduced distance of the streamlines to the wall. Thus, the roughness of the channel walls as well as flows around corners will cause the particles to bump with the wall resulting in a widening of the restricted layer. Both optical
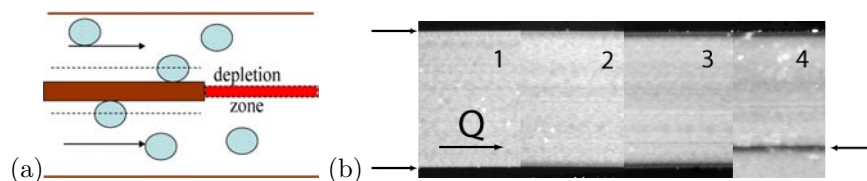
Figure 2.6: (a) Due to the finite size of the fluid markers a restricted area for the center of mass of the tracer particles develops in the detection zone, which can be optically detected to evaluate the flowrate ratio $X = Q_a/Q_r$. (b) 1 % wt. PAA solution wuth fluorescently labeled markers of $1\,\mu$m diameter flowing in a straight channel with $300 \times 60\,\mu$m cross section, arrows on the left indicate the position of the channel walls. Pict. 1-3: While flowing along the channel a depletion zone wider than the particle radius develops at the walls. After unification of two streams with depletion layers at the wall, a visible depletion zone seperates the fluid streams (pict. 4, see arrow.)

detection methods require that the markers have a sufficiently low diffusion constant to prevent a vanishing of the seperation line due to diffusion of the tracer particles before the region of fully developed flow is reached. This condition

sets a lower limit for the flowrate Q at which the differential viscometer can be operated with the optical detection method for X.

Determination with Balance

In the devices where channels with circular cross sections were used, reference and analyzer channels where open to atmospheric pressure at the ends (see fig. 5.10). The flowrate ratio has been determined by weighing the amounts of liquids m_a, m_r flowing through K_r and K_a in equal time intervals, which gives $X = m_a/m_r$.

3. BASIC FLUID DYNAMICS IN MICROFLUIDIC CHANNELS

3.1   Flow Classification

Any velocity field $\mathbf{u}(\mathbf{x}, t)$ of a flow can be decomposed into the sum of a uniform flow, a rotational flow and an extensional flow. Therefore, the transformation that a fluid element represented by a small distance vector $\mathbf{h}$ connecting two nearby points $\mathbf{x}$ and $\mathbf{y}$ undergoes in a small time step $\mathrm{d}t$ consists of a *rigid translation*, a *rigid rotation* and a *deformation* [20]:

$$\mathbf{u}(\mathbf{y}) = \mathbf{u}(\mathbf{x}) + \nabla\mathbf{u}(\mathbf{x}) \cdot \mathbf{h} + O(h^2) \tag{3.1}$$

$$= \underbrace{\mathbf{u}(\mathbf{x})}_{\text{translation}} + \underbrace{\mathbf{D} \cdot \mathbf{h}}_{\text{deformation}} + \underbrace{\mathbf{S} \cdot \mathbf{h}}_{\text{rotation}} + O(h^2). \tag{3.2}$$

Herein, the velocity gradient tensor $\mathbf{A} = (\nabla\mathbf{u})$ has been split into its deformational and rotational components $\mathbf{A} = \mathbf{D} + \mathbf{S}$ given by the deformation and vorticity tensors [20]

$$\mathbf{D} = \frac{1}{2}[\nabla\mathbf{u} + (\nabla\mathbf{u})^T] = \dot{\boldsymbol{\gamma}} \quad \text{and} \quad \mathbf{S} = \frac{1}{2}[\nabla\mathbf{u} - (\nabla\mathbf{u})^T]. \tag{3.3}$$

Depending on the time evolution of the seperation of two nearby fluid elements, it is common to classify flows as *strong, marginally weak* and *strictly weak* [34, 11, 103]:

- In *strong flows*, two material points seperate exponentially.

- In *marginally weak flows*, two material points seperate linear or quadratically.

- In *strictly weak flows*, the distance between two material points varies sinusoidally and material lines get shrinked and expanded periodically.

A more detailed discussion is given in section A.1 in the apppendix.

3.1.1   Planar Flows

A very descriptive explanation for the classification of flows into strong, marginally weak and strictly weak flows can be given for planar flows, where the velocity-component in one direction is zero, e.g. $\mathbf{u}(\mathbf{x}) = (u_x(x, y,), u_y(x, y), 0)$. Then, it

(a) coordinate system

(b) $\rho = 0$

(c) $\rho^2 < 1$

(d) $\rho^2 = 1$

(e) $\rho^2 > 1$

(f) $\rho^2 = \infty$
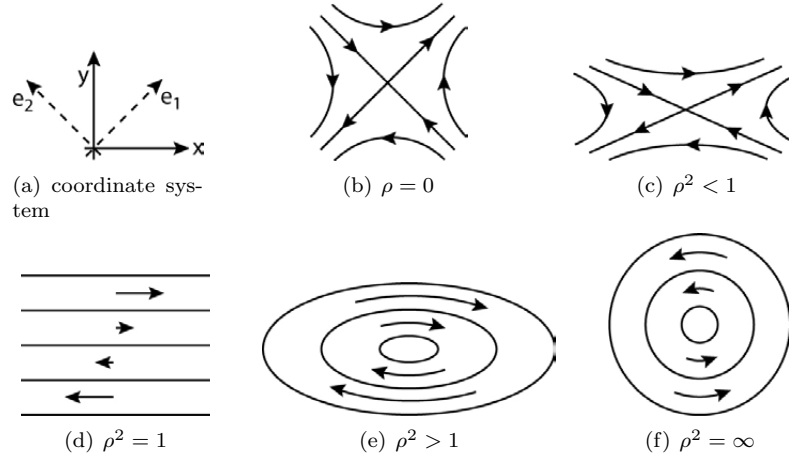
Figure 3.1: The ratio of the rotational to the deformational component changes the type of flow from strong (b,c) to marginally weak (d) to strictly weak (e,f).

is sufficient to discuss the flow field in 2D, and the velocity gradient tensor can be written in the principal coordinate system of $\mathbf{D}$ as [35]:

$$\mathbf{A} = \begin{pmatrix} \dot{\epsilon} & \omega \\ -\omega & -\dot{\epsilon} \end{pmatrix} \tag{3.4}$$

The fluid elements in planar flows are rotated with rotation rate ω around an axis perpendicular to the flow plane xy. Simultaneously, they get deformed in the flow plane, namely getting stretched along $\mathbf{e}_1$ and shrinked along $\mathbf{e}_2$ (see fig 3.1a) with rate $\dot{\epsilon}$. Depending on the ratio of rotation and deformation rate $\rho = \omega/\dot{\epsilon}$, the flow is strong ($\rho^2 < 1$) or strictly weak ($\rho^2 > 1$). For $\rho = 0$ and $\rho = \infty$ the flow is planar extensional, resp. purely rotational. The special case of equal rotation and deformation rate ($\rho^2 = 1$) represents the velocity field of *simple shear* with parallel streamlines. Fig. 3.1 b–f schematically shows the appending velocity fields in the different regimes.

3.1.2 Simple Shear Flow

The velocity field of simple shear flow can be generated by two parallel plates sliding past each other (see fig. 3.2): In an affine deformation, the displacement of the upper plate by a distance a in the x-direction induces a strain in the fluid of $\gamma = a/d$, where d is the plate separation in the y-direction. Moving the upper plate with a constant velocity $v = \dot{\gamma}d$ by applying a constant stress σ to the fluid (where σ is the dragging force per unit area) creates a uniform velocity field $\mathbf{u} = (\dot{\gamma}y, 0, 0)$ with straight, parallel streamlines. The corresponding velocity
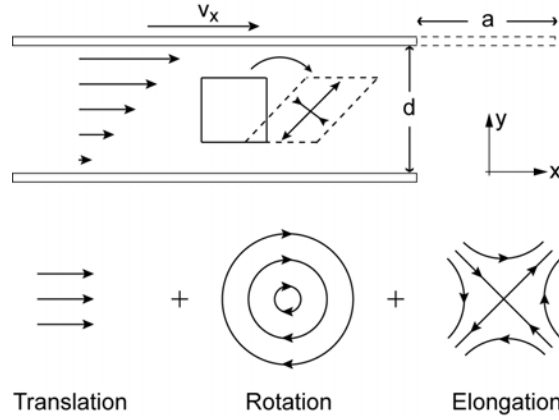
Figure 3.2: A uniform planar shear flow can be generated by two parallel plates sliding past each other.

gradient tensor is given by

$$(\nabla \mathbf{u}) = \begin{pmatrix} 0 & \dot{\gamma} & 0 \\ 0 & 0 & 0 \\ 0 & 0 & 0 \end{pmatrix} = \underbrace{\frac{1}{2}\begin{pmatrix} 0 & \dot{\gamma} & 0 \\ -\dot{\gamma} & 0 & 0 \\ 0 & 0 & 0 \end{pmatrix}}_{\mathbf{S}} + \underbrace{\frac{1}{2}\begin{pmatrix} 0 & \dot{\gamma} & 0 \\ \dot{\gamma} & 0 & 0 \\ 0 & 0 & 0 \end{pmatrix}}_{\mathbf{D}}. \quad (3.5)$$

In cylindrical coordinates, the velocity field $\mathbf{u} = (\dot{\gamma}y, 0, 0)$ of simple shear reads:

$$\mathbf{u} = \begin{pmatrix} \dot{r} \\ \dot{\phi} \\ \dot{z} \end{pmatrix} = \begin{pmatrix} \dot{\gamma}r\sin\phi\cos\phi \\ -\dot{\gamma}\sin^2\phi \\ 0 \end{pmatrix}. \quad (3.6)$$

3.1.3 Extensional Flow

Generally, extensional flow is a rotation free, purely deformational flow (i.e. $\mathbf{S} = 0$) with a homogeneous flow field. The velocity field of a rotation free flow is given by [10]

$$\begin{pmatrix} u_x \\ u_y \\ u_z \end{pmatrix} = \frac{1}{2}\begin{pmatrix} -\dot{\epsilon}(1+b)x \\ -\dot{\epsilon}(1-b)x \\ 2\dot{\epsilon}z \end{pmatrix}, \quad (3.7)$$

where $0 \le b \le 1$ and $\dot{\epsilon}$ is the *elongation rate*. Several special extensional flows are obtained for particular choices of the parameter b [10]:

Uniaxial elongational (extensional) flow:	$(b = 0, \dot{\epsilon} > 0)$	(3.8)
Biaxial stretching flow:	$(b = 0, \dot{\epsilon} < 0)$	(3.9)
Planar elongational flow:	$(b = 1)$	(3.10)

Fig. 3.3 shows a cylindrical filament in uniaxial extensional flow with the corre-
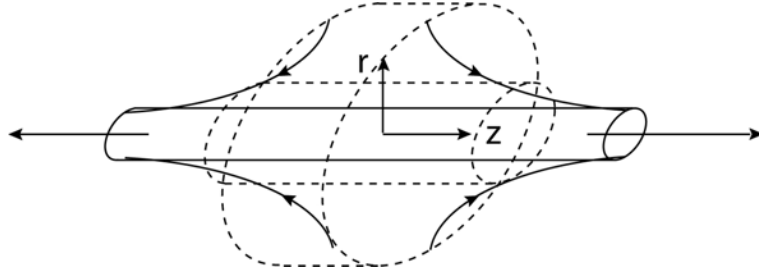
Figure 3.3: Hyperbolic radial streamlines created by stretching of a cylindrical filament in uniaxial extensional flow.

sponding hyperbolic radial streamlines. The flow field in cylindrical coordinates is given as

$$\mathbf{u}(\mathbf{x}) = \begin{pmatrix} u_r \\ u_\phi \\ u_z \end{pmatrix} = \begin{pmatrix} -\frac{1}{2}\dot{\epsilon}r \\ 0 \\ \dot{\epsilon}z \end{pmatrix}. \tag{3.11}$$

Biaxial extensional flow is equivalent to uniaxial extensional flow with reversed flow-direction.

The velocity field of planar extensional flow ($b = 1$) is shown in fig. 3.1b and given in cartesian and cylindrical coordinates as

$$\begin{pmatrix} u_x \\ u_y \\ u_z \end{pmatrix} = \begin{pmatrix} -\dot{\epsilon}x \\ \dot{\epsilon}y \\ 0 \end{pmatrix}, \quad \text{and} \quad \begin{pmatrix} u_r \\ u_\phi \\ u_z \end{pmatrix} = \begin{pmatrix} r\dot{\epsilon}(\cos\phi - \sin\phi) \\ \dot{\epsilon}\sin(2\phi) \\ 0 \end{pmatrix}. \tag{3.12}$$

3.2 Channel Flows in Low Reynolds Regime

3.2.1 Navier Stokes Equations

The motion of the fluid with velocity field $\mathbf{u}(\mathbf{x}, t)$ and mass density $\rho(\mathbf{x}, t)$ is described by the equations of conservation of mass, momentum and energy [10]: For incompressible fluids, the conservation of mass equation $\frac{\partial \rho}{\partial t} + (\nabla \cdot \rho\mathbf{u}) = 0$ reduces to the continuity equation:

$$(\nabla \cdot \mathbf{u}) = 0. \tag{3.13}$$

The conservation of momentum yields the equation of motion:

$$\rho\frac{\partial \mathbf{u}}{\partial t} + \rho(\mathbf{u} \cdot \nabla)\mathbf{u} = -[\nabla \cdot \boldsymbol{\pi}] + \mathbf{f}, \tag{3.14}$$

where $\boldsymbol{\pi}$ is the total stress tensor and $\mathbf{f}$ are body forces acting on the fluid. The total stress tensor of incompressible fluids $\boldsymbol{\pi} = p\boldsymbol{\delta} + \boldsymbol{\sigma}$ contains the hydrostatic pressure p and the stresses due to velocity gradients in the fluid. These stresses occur during deformation of a fluid element in flow and are expressed in the stress tensor $\boldsymbol{\sigma}$[10]. In a Newtonian fluid, $\boldsymbol{\sigma}$ is related to the deformation rate

tensor $\mathbf{D}$ by the steady-state viscosity η, which is a material function of the fluid (see sec. 3.3.1):

$$\boldsymbol{\sigma} = -2\eta\mathbf{D} \tag{3.15}$$

With this constitutive equation the total stress tensor becomes $\boldsymbol{\pi} = p\boldsymbol{\delta} - 2\eta\mathbf{D}$ Together with eq. (3.14) we obtain the Navier-Stokes equations for an incompressible Newtonian fluid:

$$\rho(\frac{\partial\mathbf{u}}{\partial t} + (\mathbf{u}\cdot\nabla)\mathbf{u}) = -\nabla p + \eta\Delta\mathbf{u} + \mathbf{f}. \tag{3.16}$$

With given flow geometry and boundary conditions, the flow of a Newtonian fluid is uniquely defined by eq. 3.16 and can be solved numerically or in simple cases analytically.

3.2.2   Reynolds Number in Microfluidic Flows

By introduction of a characteristic length L_0 and a characteristic velocity u_0 the Navier-Stokes equation (3.16) can be made dimensionless [12]:

$$\text{Re}\left(\frac{\partial\tilde{\mathbf{u}}}{\partial\tilde{t}} + (\tilde{\mathbf{u}}\cdot\tilde{\nabla})\tilde{\mathbf{u}}\right) = -\tilde{\nabla}\tilde{p} + \tilde{\nabla}^2\tilde{\mathbf{u}}, \quad \text{with} \quad \text{Re} \equiv \frac{\rho u_0 L_0}{\eta}. \tag{3.17}$$

Re is the dimensionless *Reynolds number* and $\tilde{\mathbf{r}} = \mathbf{r}/L_0$, $\tilde{\mathbf{u}} = \mathbf{u}/u_0$, $\tilde{t} = tu_0/L_0$, $\tilde{p} = pL_0/(\eta u_0)$ are the dimensionless coordinates, velocity, time and pressure, and $\tilde{\nabla} = L_0\nabla$ is the dimensionless Nabla-operator. The Reynolds number is a measure for the ratio between the inertial and the viscous forces in the flow. For Reynolds numbers up to $Re \approx 2000$ the flow in straight channels is generally laminar, for $Re > 2000$ the flow becomes turbulent [102]. For small Reynolds numbers, the flow is viscosity dominated and the left hand side of eq. (3.16) can be neglected, yielding *Stokes flow* described by the linear *Stokes equation* [12]:

$$0 = -\nabla p + \eta\Delta\mathbf{u}. \tag{3.18}$$

Due to the small characteristic length L_0 on the order of typically 10-1000 μm, the Reynolds number in microfluidic flows is usually $Re < 2000$, so that laminar flow is guaranteed. However, $Re \ll 1$ is often not fulfilled, so that inertial effects may not be generally neglected, especially in oscillatory flows.

3.2.3   Laminar Channel Flow

In laminar flow conditions, analytical solutions can be obtained for the pressure-driven, steady-state flow of Newtonian and power-law fluids in straight, rigid channels with constant cross section and no-slip boundary condition at the channel walls in some geometries. For the simple case of a Newtonian fluid in a circular channel, the dependence of the flowrate on the pressure drop along the channel is given by the Hagen-Poiseuille equation $Q = \frac{\pi R^4 \Delta p}{8\eta L}$. The corresponding parabolic flow profile and the Newtonian wall shearrate $\dot{\gamma}_w$ are given

by:

$$u_z(r) = \frac{\Delta p R^2}{4 \eta L} \left[1 - \left(\frac{r}{R} \right)^2 \right], \qquad \dot{\gamma}_w = \frac{4Q}{\pi R^3}. \tag{3.19}$$

While for circular channels an analytical solution can be given for power-law fluids[1] as well, no analytic solution is available in general. Some special cases with analytical solutions are given in section A.3. Moreover, in non-circular ducts, the shear rate is not constant along the wall. Nevertheless, semi-analytical solutions for $Q(p)$ using average wall shearrates can be given with the help of numerically determined shape factors. Generally, the averaged wall shearrate of a power-law fluid flowing through a channel with an arbitrary constant cross section of area D can be given in the form

$$\dot{\gamma}_w = \frac{Q}{\tilde{h}^3} \cdot F_{\dot{\gamma}}(n), \tag{3.20}$$

where $\tilde{h} = \sqrt{D}$ is the average diameter of the channel and $F_{\dot{\gamma}}(n)$ is a shape factor depending on the cross sectional geometry of the channel and the power-law index n of the fluid (comp. eqs. A.78, A.83, A.85). The shearrate dependent viscosity $\eta(\dot{\gamma}_w)$ of the fluid can be determined by measuring the pressure drop Δp along a channel section of length L in fully developed flow as

$$\eta(\dot{\gamma}_w) = \frac{D^2 \Delta p}{QL} F^{\star}(n), \tag{3.21}$$

where $F^{\star}(n)$ is a function of the cross sectional geometry and the power-law index n of the fluid (see eq. A.79, A.86). Thus, the hydrodynamic resistance of a channel with constant cross section and length L is given by

$$R = \frac{\Delta p}{Q} = \frac{\eta(\dot{\gamma}_w) L}{D^2 F^{\star}(n)} \tag{3.22}$$

for power-law fluids.

3.2.4 Numerical Determination of Shape Factors $F_{\dot{\gamma}}$ and $F^{\star}$

For the flow of non-Newtonian fluids in channels with rectangular cross section the hydrodynamic resistance $R = \Delta p/Q$ and the dependence of the wall shear rate on flowrate Q and powerlaw index n have to be determined numerically. For a power-law fluid, channel resistance and shearrate can be expressed by eqs. 3.22 and 3.20 with the numerical factors $F^{\star}(h/w, n)$ and $F_{\dot{\gamma}}(h/w, n)$ which depend on the channel aspect ratio h/w and the exponent n of the shear viscosity. For the evaluation of experiments with channels of different aspect ratios, the flowrate and the averaged wall shear rate of a powerlaw fluid with exponents $n \in [0.2; 1]$ have been determined by FEM-simulations in rectangular channels

---

[1] the viscosity of a power-law fluid depends on the shear rate as $\eta(\dot{\gamma}) = A\dot{\gamma}^{n-1}$, see section 3.3.1

with aspect ratios from $h/w = 0.4$ to 1. Fig. 3.5 shows contour plots of the evaluated shape factors $F^\star(h/w, n)$ and $F_{\dot\gamma}(h/w, n)$. Comparison of the numerical results for the Newtonian fluid ($n = 1$) with the analytical expressions given in section 3.2.3 showed a numerical error smaller than 10% for all geometries under investigation. The velocity profiles $u(x)$ across the midplane of the channel at $z = h/2$ show that a decreasing power-law index n corresponds with an increase of the exponent in the curve describing the shape of the flow profile. Fig. 3.4 exemplarily shows the numerically determined flow profiles in a channel with $h/w = 0.8$ for a Newtonian fluid ($n = 1$, blue curve) and a strongly shear thinning fluid ($n = 0.35$, red curve). The flow profiles can be fitted with the shape obtained in cylindrical and slit flow geometry ($h/w = 0$, see eq. A.77):

$$u(x) = u_{\max}\left[1 - \left(\frac{x}{w/2}\right)^m\right]. \tag{3.23}$$

The fits are shown by the dashed black curves in fig. 3.4. The comparison to curves fitted with the analytically predicted exponents for cylindrical channels $m = 1/n+1$ (dotted lines) shows, that the flow profiles in rectangular and cylindrical geometry are similar, yet the fits for cylindrical geometry yield slightly higher exponents m_{fit}.
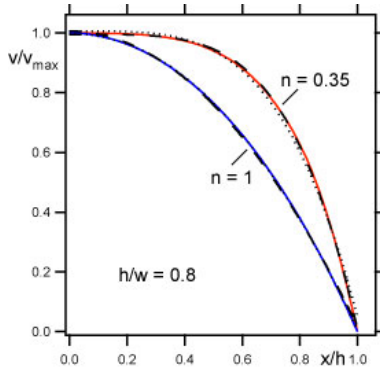
Figure 3.4: Flow profiles in a rectangular channel with aspect ratio $h/w = 0.8$ determined by FEM-simulation at $z = h/2$. Blue curve: Flow profile of Newtonian fluid $n = 1$, dashed curve: fit according to eq. 3.23 yielding an exponent $m_{\text{fit}} = 2.1$, which is slightly above the theoretical value $m_{\text{th}} = m = 1/n + 1 = 2$ of a parabolic flow profile in a circular channel shown by the dotted curve. Red curve: Flow profile of shear-thinning fluid with $n = 0.35$; dashed curve: fit according to eq. 3.23, exponent $m_{\text{fit}} = 4.3$, dotted curve : theoretical flow profile for circular channel with $m = 1/n + 1 = 3.9$.

3.3   Viscosity of Complex Fluids

Generally, the viscosity of a fluid is a material function relating the stresses caused by friction in a fluid under flow to the underlying velocity gradient in a constitutive equation. Especially in complex fluids, the stress tensor $\boldsymbol{\sigma}$ is not only depending on the geometry of the deformation but also on the deformation history of the fluid. According to the deformation properties, different constitutive equations can thus be formulated, which define different viscosity functions for the same fluid.
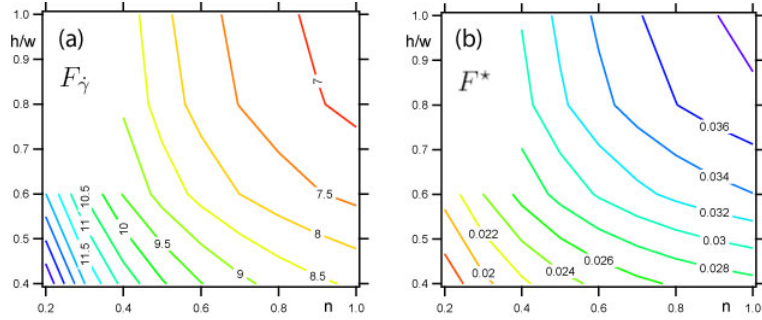
Figure 3.5: Shape factors $F_{\dot{\gamma}}(h/w, n)$ and $F^\star(h/w, n)$ in dependence of shear viscosity exponent n and channel aspect ratio h/w. $F_{\dot{\gamma}}(h/w, n)$ and $F^\star(h/w, n)$ have been evaluated for $n = 0.2, 0.3, ..., 1$ and $h/w = 0.4, 0.6, 0.8, 1$ from FEM simulations. For $n < 0.4$ and $h/w > 0.6$ the simulation did not converge.

3.3.1   Steady State Viscosity

In many flows the fluid is deformed on a time scale much longer than the fluid's relaxation time. It is therefore useful to analyze fluids in flows with constant stretch history, where the velocity gradient along the streamlines is constant, so that for long times the stress tensor $\boldsymbol{\sigma}$ is solely depending on the velocity gradient tensor $\mathbf{A}$. This relationship defines the *steady state viscosity* of the fluid. For Newtonian fluids the steady-state viscosity is a constant which is independent of the form of the velocity gradient tensor and the flowrates. Furthermore, the stress is not altered by the rotational component of the flow, so that the stress in a Newtonian fluid depends only on the deformation rate tensor and is given by the constitutive equation (3.15) introduced in section 3.2.1:

$$\boldsymbol{\sigma} = -2\eta \mathbf{D} \qquad (3.24)$$

In contrast, the stress occuring in non-Newtonian fluids generally changes with the flow rate and can be substantially different when the deformation is accompanied by a simultaneous rotation. Thus the relation between $\boldsymbol{\sigma}$ and $\mathbf{A}$ depends on both the flow rates and the exact form of $\mathbf{A}$ which makes it very difficult to find a constitutive equation defining the general steady-state viscosity of a complex fluid. The fluid properties are therefore usually described by defining material functions for special flow fields, namely the *shear viscosity* in viscometric flows and the *extensional* or *elongational viscosity* in extensional flows [10]. Consequently, in the literature on the rheology of complex fluids it is common to classify steady flows according to these two basic flow types into shear flows, extensional flows and mixed flows (i.e. a superposition of shear and extensional flow) rather than into strong, marginally weak and strictly weak flows (see. section A.1), although a mixed flow in this sense can either be strong or strictly weak with completely different behaviour of the fluid [65].

Steady-State Shear Viscosity

The steady state shear viscosity $\eta(\dot{\gamma})$ is defined in simple shear flow with $\mathbf{u} = (\dot{\gamma}y, 0, 0)$ as the proportionality factor between $A_{xy} = \dot{\gamma}$ and the corresponding element of the stress tensor which is the shear stress σ_{xy}[10]:

$$\sigma_{xy} = \eta(\dot{\gamma})A_{xy} = \eta(\dot{\gamma})\dot{\gamma}. \tag{3.25}$$

Generally $\eta(\dot{\gamma})$ is a function of the shear rate $\dot{\gamma}$. The viscosity of Newtonian fluids is frequently named μ, the *kinematic viscosity* ν is defined as $\nu = \mu/\rho$. Note that although A_{xy} is the only nonzero element of $\mathbf{A}$, the other elements of $\boldsymbol{\sigma}$ do not necessarily all vanish in non-Newtonian fluids. These normal forces manifest in many non-Newtonian phenomena like the *rod climbing* observed in stirred polymer solutions. To characterize the normal stresses in shear, two more material functions Ψ_1, Ψ_2 similar to the steady-state shear viscosity are defined, which are called the *first normal stress difference* and the *second normal stress difference*. A detailed explanation is given in reference [10].

There are many well-established devices to measure shear viscosity in different flow geometries including capillary rheometers, rotational cylinders and plate-plate rotational rheometers. To determine the shear viscosity curves $\eta(\dot{\gamma})$ for the complex fluids used in the experiments in this work, a cone-plate rheometer was used, where the viscosity is determined by measuring the torque needed to shear the fluid in the gap between the bottom plate and the rotating cone.

Steady-State Extensional Viscosity

The velocity field of rotation free flows is described by eq. 3.7 and the according stress tensor in its most general form reads [10]:

$$\boldsymbol{\pi} = p\boldsymbol{\delta} + \boldsymbol{\sigma} = \begin{pmatrix} p + \sigma_{xx} & 0 & 0 \\ 0 & p + \sigma_{yy} & 0 \\ 0 & 0 & p + \sigma_{zz} \end{pmatrix} \tag{3.26}$$

For incompressible fluids there are only two normal stress differences of experimental interest [10] and corresponding material functions Λ_1, Λ_2 are defined:

$$\text{first normal stress difference:} \quad \sigma_{zz} - \sigma_{xx} = -\Lambda_1(\dot{\epsilon}, b)\dot{\epsilon} \tag{3.27}$$
$$\text{second normal stress difference:} \quad \sigma_{yy} - \sigma_{xx} = -\Lambda_2(\dot{\epsilon}, b)\dot{\epsilon}. \tag{3.28}$$

As in the steady state the stress in the fluid depends only on the velocity gradient $\mathbf{A}$, the two viscosity functions depend only on the elongation rate $\dot{\epsilon}$ and the flow type parameter b [10]. The *extensional viscosity* $\Lambda(\dot{\epsilon})$ (or *elongational viscosity*) is defined as the viscosity function for the special rotation free flow with $b = 0$ (uniaxial extensional flow) where due to the cylindrical symmetry the second normal stress difference vanishes $\sigma_{yy} - \sigma_{xx} = 0$ [10]:

$$\Lambda(\dot{\epsilon}) = \Lambda_1(\dot{\epsilon}, 0) \tag{3.29}$$

Similarly, we can define an extensional viscosity $\Lambda_p(\dot{\epsilon})$ for planar extensional flow $(b = 1)$:

$$\Lambda_p(\dot{\epsilon}) = \Lambda_1(\dot{\epsilon}, 1). \tag{3.30}$$

With $\sigma = -2\eta\mathbf{D}$ the first normal stress difference for a Newtonian fluid in rotation free flow gives

$$\sigma_{zz} - \sigma_{xx} = -(3 + b)\eta\dot{\epsilon} \tag{3.31}$$

which yields an extensional viscosity of $\Lambda = 3\eta$. The ratio between extensional and shear viscosity is called *Trouton ratio Tr* and is thus $Tr = 3$ for a Newtonian fluid in uniaxial extensional flow. For non-Newtonian fluids with rate dependent viscosities, the Trouton ratio is defined as $Tr = \Lambda(\dot{\epsilon})/\eta(\dot{\gamma})$ with $\dot{\epsilon} = \dot{\gamma}$ and can reach values on the order of $Tr = 10^3 \ldots 10^4$.

Constitutive Equations in Steady State Flows

A constitutive equation frequently used to describe rate dependent viscosities is the power-law equation. A *power-law fluid* is defined as a fluid, where the shear or extensional viscosity follows the deformation rate with

$$\eta(\dot{\gamma}) = A\dot{\gamma}^{n-1} \quad \Lambda(\dot{\epsilon}) = B\dot{\epsilon}^{k-1}, \tag{3.32}$$

where $n, k > 0$ are the power-law exponents of shear and extensional viscosity. For $n = k = 1$ the fluid is Newtonian, for $0 < n < 1$ the viscosity drops with the shear rate and the fluid is called shear-thinning, for $n > 1$ the fluid is shear-thickening. For most complex fluids the viscosity is well described by eq. 3.32 only in a certain range of flow rates, so we can rewrite eq. 3.32 locally around $\dot{\gamma}_0, \dot{\epsilon}_0$:

$$\eta(\dot{\gamma}) = \eta_0 \cdot \left(\frac{\dot{\gamma}}{\dot{\gamma}_0}\right)^{n-1}, \quad \Lambda(\dot{\epsilon}) = \Lambda_0 \cdot \left(\frac{\dot{\epsilon}}{\dot{\epsilon}_0}\right)^{k-1} \tag{3.33}$$

Many non-Newtonian fluids, especially polymer solutions, behave like a Newtonian fluid at low flow rates, obey a shear-thinning powerlaw at intermediate flow rates until the viscosity drops down to the solvent viscosity in the high shear rate regime. A suitable constitutive equation describing this behaviour is the *Carreau-Yasuda model* [10]:

$$\frac{\eta(\dot{\gamma}) - \eta_\infty}{\eta_0 - \eta_\infty} = (1 + (\lambda\dot{\gamma})^a)^{(n-1)/a} \tag{3.34}$$

Here, η_0 is the viscosity at zero shear rate, η_∞ is the solvent viscosity, λ is a time constant, n corresponds to the powerlaw exponent n in the powerlaw regime and a is a dimensionless parameter describing the transition between the Newtonian and the shear-thinning regime.

4. POLYMER DYNAMICS IN SHEAR FLOW

Due to the inherently large number of degrees of freedom involved, deciphering the configurational dynamics of individual macromolecules in flow remains a challenging task even in the relatively simple case of linear polymers in dilute solution without intermolecular hydrodynamic interactions. Intensive research has been performed studying the complex behaviour of single flexible polymers, which has been first observed experimentally and described by Chu, Shaqfeh et al. [100, 93]. The polymer's response to flow was found to be determined by its entropic elasticity and it was possible to model its behavior via simulations or dumbbell models [18, 15, 31] and to study ensemble properties rather than the dynamics of individual flexible molecules[41, 48]. Results based on a normal mode analysis of a perturbation extension of stiff filaments are available for the description of semiflexible filaments [78]. For flexible filaments, three modes of shear-induced stretching transitions have been discussed [107]: recoil, restretch, and tumble. Cross-correlations between thickness and extension fluctuations revealed a causal chain relationship leading to four phases of motion: thickening, stretching, thinning, and crumpling recoiling. In the limit of thermal [26] and non-thermal [50] rodlike filaments their conformation is set by the bending energy. With increasing flexibility of the filaments the coupling of the flow to their conformational dynamics and the effect of persistence length needs yet to be explored. A transition from enthalpic to entropic response of polymers in shear flow has been proposed based on a Gaussian semiflexible polymer model and solved analytically for the two limiting cases of stiff rods and fully flexible polymers [115, 116]. An experimental confirmation as well as the continuous description, which captures all the regimes from stiff to flexible is still lacking. To this end the origin and effect of the force balances acting on single polymers need to be identified. Yet, the experimental observations are limited by the optical resolution, which does not allow the resolution of the local configurational dynamics of flexible polymers. Due to the optical accessibility, semiflexible actin filaments can thus be used as an ideal model system to study the coupling of the flow to the conformational dynamics. Microfluidic channels combined with fluorescence microscopy provide a defined flow field in which both the spatial conformation of the polymer and its temporal evolution can be captured and studied.

In this chapter, we show how a microfluidic device combined with a semiautomated moving microscope stage enables us to directly observe the full conformational dynamics of actin filaments in simple shear flow. After a brief discussion of conformations and thermal motion of polymers in equilibrium, the coupling

of the diffusive motion to the deterministic drift due to shear-induced friction forces is addressed. Based on the experimental findings, an analytical model describing the balance of frictional drag, bending and elastic forces is derived for the dynamics of filaments in the stiff and semiflexible regime. Comparison with experimental data for flexible polymers of other groups as well as additional Brownian dynamics simulations shows, that a straightforward extension of the model to the flexible regime, which is most important in practical applications, can be done. Subsequently, we discuss how the observed dynamics of individual polymers is linked to the non-Newtonian bulk properties of polymer solutions.

4.1 Equilibrium Properties of Polymers in Dilute Solution

To understand and quantify the experimentally observed dynamics of polymers in shear, we make use of some well established concepts for the description of equilibrium polymers in dilute solution. Generally, there are several coarse-grained models to represent the conformation and dynamics of flexible linear polymer chains in solution. These include discrete models like the *bead-stick model*, the *bead-spring model* and the *pearl-necklace model* [108], where the polymer is modeled by a large number of pearls or beads representing a monomer subunit, which are connected either by rigid rods or springs. Alternatively, for a description of the polymer in the flexible as well as in the semiflexible and stiff regime, continuos models like the *worm-like-chain model* (WLC-model) are used [47]. In the discrete description, the polymer conformation is given by the n position vectors of the monomers $\mathbf{R}_i$. For the continuous description we parametrize the polymers conformation by the arc length $\sigma \in [0; L_c]$, so that the local position of a polymer segment is given by $\mathbf{r}(\sigma)$.

We will neglect excluded volume effects and intermolecular hydrodynamic interactions. In this case, the equilibrium conformation of a linear flexible polymer in dilute solution can be described as a 3-D random walk of n steps. A chain with such a random walk conformation is called *ideal chain* and a solvent in which a polymer adopts this conformation is called *theta solvent*.

4.1.1 Persistence Length L_p and Kuhn length b_k

The mechanical stiffness of a polymer filament in the continuous ideal chain model is determined by the flexural rigidity EI, where E is the filaments elastic Young modulus and I is the geometrical moment of inertia, which depends on the filaments cross section. In solution, the chain undergoes thermal fluctuations. The average cosine of the difference in the local orientational angle $\Delta\theta(\sigma) = \theta(\sigma) - \theta(0)$ between two points of the chain seperated by a distance σ along the chain is found to decay exponentially with the distance σ in 3D as [47]

$$\langle \cos[\Delta\theta_{3D}(\sigma)] \rangle = \exp\left(-\frac{\sigma}{L_p}\right), \quad \text{where } L_p = \frac{EI}{k_B T} \tag{4.1}$$

is the characteristic decay length of the orientational correlation of the chain called the *persistence length*. With $\sigma = L_c$ it follows from eq. 4.1 that in the

flexible limit $L_c/L_p \gg 1$ the average orientational angle between the polymer ends is expected to be $\Delta\theta = \pi/2$. This indicates a completely random orientation of the polymer ends: The probability density for the angle α between two randomly orientated vectors in 3D is $p(\alpha) = \frac{\sin \alpha}{2}$, so that the average angle between them follows as

$$\langle \alpha \rangle = \int_0^\pi \alpha p(\alpha) \mathrm{d}\alpha = \frac{1}{2} \int_0^\pi \alpha \sin \alpha = \frac{1}{2} [\sin \alpha - \alpha \cos \alpha]_0^\pi = \frac{\pi}{2} \qquad (4.2)$$

In the flexible limit, the worm-like-chain model is thus equivalent with the discrete model of a freely jointed chain, where the polymer is represented by $N_k = L_c/b_k$ freely rotating chain segments of length b performing a random walk (FJC-model). The segment length b_k is given by the persistence length and is called the Kuhn length $b_k = 2L_p$, and N_k gives the number of Kuhn steps of the random walk [47]. With a persistence length of $L_p = 16\,\mu$m, the actin filaments with lengths of $3 - 40\,\mu$m used in the experiments fall in the regime of stiff ($L_c \ll L_p$) and semiflexible ($L_c \approx L_p$) polymers.

4.1.2 End-to-End Vector Length R_{ee}

The worm-like-chain model gives an analytical formula for the mean squared length of the end-to-end vector $\mathbf{R}_{\mathrm{ee}}$ as a function of contour and persistence length L_c, L_p [47]:

$$\langle R_{\mathrm{ee}}^2 \rangle = 2L_p^2 \left[\exp\left(-\frac{L_c}{L_p} \right) - 1 + \frac{L_c}{L_p} \right] \qquad (4.3)$$

In the stiff limit, the polymer can be approximated with a rod conformation, consequently eq. 4.3 reveals an end-to-end length equal to the contour length L_c. In the flexible limit we get $\langle R_{\mathrm{ee}}^2 \rangle = 2L_pL_c$, which corresponds to the random walk result of the discrete FJC-model: The i-th step with length b_k of the random walk is always independent of the $(i-1)$ steps taken before. With an average perpendicular orientation of two random vectors, the mean-squared end-to-end length $\mathbf{R}_i^{\mathrm{ee}2}$ of a random walk with i steps can thus be calculated as

$$\langle R_i^{\mathrm{ee}2} \rangle = \langle R_{i-1}^{\mathrm{ee}}{}^2 \rangle + b_k^2, \quad \text{so that } \langle R_n^{\mathrm{ee}2} \rangle = n b_k^2 = \frac{L_c}{2L_p}(2L_p)^2 = 2L_pL_c \quad (4.4)$$

follows from iteration from $i = 2...n$.

The mean squared end-to-end distance can be used for extending the definition of the Kuhn-length b_k and number of Kuhn steps N_k to the semiflexible regime by setting

$$b_k \equiv \frac{\langle R_{\mathrm{ee}}^2 \rangle}{L_c} \quad \text{and} \quad N_k = L_c^2 / \langle R_{\mathrm{ee}}^2 \rangle. \qquad (4.5)$$

Radius of Gyration R_g

Another important quantity characterizing the polymers equilibrium conformation is the *radius of gyration* R_g. In the discrete description of the polymer as a

chain of n connected monomers with position vectors $\mathbf{R}_i$, the radius of gyration is defined as [88]

$$R_g^2 \equiv \frac{1}{n} \sum_{i=1}^{n} (\mathbf{R}_i - \mathbf{R}_{\text{com}})^2 \quad \text{with } \mathbf{R}_{\text{com}} \equiv \frac{1}{n} \sum_{i=1}^{n} \mathbf{R}_i, \tag{4.6}$$

where $\mathbf{R}_{\text{com}}$ is the position of the center of mass of the polymer. Adopting eq. 4.6 to the continuous description, the radius of gyration is given as

$$R_g^2 = \frac{1}{L_c} \int_0^{L_c} (\mathbf{r}(\sigma) - \mathbf{r}_{\text{com}})^2 \mathrm{d}\sigma, \quad \text{with } \mathbf{r}_{\text{com}} = \frac{1}{L_c} \int_0^{L_c} \mathbf{r}(\sigma) \mathrm{d}\sigma. \tag{4.7}$$

For the worm-like-chain model, the mean-square of the radius of gyration can be calculated as [116]

$$\langle R_g^2 \rangle = \frac{1}{3} L_p L_c \left\{ 1 - \frac{3L_p}{L_c} + \frac{6L_p^2}{L_c^2} \left[1 - \frac{L_p}{L_c}(1 - \exp(-L_c/L_p)) \right] \right\}, \tag{4.8}$$

which gives a radius of gyration of $R_g^2 = L_c^2/12$ for the rod in the stiff limit and $R_g^2 = L_p L_c/3 = R_{\text{ee}}^2/6$ in the flexible limit. The same result for the flexible limit can be derived in the discrete description for a random walk conformation of the polymer [88]:

$$\langle R_g^2 \rangle = \frac{b^2 N}{6} = \frac{\langle R_{\text{ee}}^2 \rangle}{6} \tag{4.9}$$

4.1.3 Diffusion of Linear Polymers

Lateral Diffusion

The three dimensional mean-square displacement for the lateral diffusive motion of a colloidal particle during the time t is given as [88]:

$$\langle [\mathbf{r}(t) - \mathbf{r}(0)]^2 \rangle = 2NDt \overset{N=3}{=} 6Dt \tag{4.10}$$

where N is the number of spatial dimensions for the diffusion. According to the Einstein relation, the diffusion coefficient D is given by the ratio of thermal energy and friction coefficient ζ of the particle [88]: $D = k_B T/\zeta$. Assuming an isotropic friction coefficient ζ_b per monomer and neglecting hydrodynamic interactions between polymer subunits, the diffusion coefficient for the center of mass motion of the polymer is independent of the internal conformation and given as

$$D = \frac{k_B T}{n \zeta_b} = \frac{k_B T}{c_L L_c} \tag{4.11}$$

where the second expression represents the continuous description with the isotropic friction coefficient c_L per unit length. When an anisotropic friction coefficient is used (see section 4.2.1), the lateral diffusion becomes conformation dependent. For a straight rod conformation with drag coefficients $\zeta_\perp = 2\zeta_\parallel \approx n\zeta_b$, resp. $c_\perp = 2c_\parallel \approx c_L L_c$ the diffusion parallel to the rod is enhanced, because hydrodynamic interaction reduces the friction tangential to the rod: $D_\parallel = 2D_\perp = 2D$.

Rotational Diffusion of Stiff, Semiflexible and Flexible Polymers

Apart from the lateral displacement of the center of mass, thermal motion also randomly changes the polymer orientation. If internal rearranging motions of the polymer are neglected, for short times the diffusion of the orientational vector $\mathbf{u}(t) \equiv \mathbf{R}_{\mathrm{ee}}/\sqrt{R_{\mathrm{ee}}^2}$ can be described as a 2D random walk with an angular mean-square displacement of

$$\langle \alpha(t)^2 \rangle = 4D_r t \tag{4.12}$$

where $\alpha(t)$ is the angle between $\mathbf{u}(t)$ and $\mathbf{u}(0)$, and D_r is the rotational diffusion coefficient. As the available angular space is finite, for long times the angular mean-square displacement saturates at the value corresponding to the value expected for two uncorrelated vectors, which can be calculated with the probability density $p(\alpha)\mathrm{d}\alpha = \sin\alpha\mathrm{d}\alpha$ as $\langle \alpha^2(t \to \infty) \rangle = (\pi^2 - 4)/2$. Thus, the angular mean-squared-displacement of a polymer saturates at $\pi^2/2 - 2$. It is more convenient to discuss the rotational diffusion in terms of the difference of the orientation vectors $(\mathbf{u}(t) - \mathbf{u}(0))$ instead of the angular difference $\alpha(t)$. For small angular differences $\alpha \ll 1$, both descriptions are equivalent $\alpha(t) \approx \mathbf{u}(t) - \mathbf{u}(0)$. The mean-square-displacement $MSD_r(t)$ of the orientational vector can be calculated from the correlation function of the orientation vectors [27]:

$$MSD_r(t) \equiv \langle (\mathbf{u}(t) - \mathbf{u}(0))^2 \rangle = 2(1 - \langle \mathbf{u}(t)\mathbf{u}(0) \rangle). \tag{4.13}$$

The average correlation function decays exponentially with the orientational relaxation time τ_r[27]:

$$\langle \mathbf{u}(t)\mathbf{u}(0) \rangle = \exp(-t/\tau_r) = \exp(-2D_r t), \tag{4.14}$$

where $\tau_r = 1/(2D_r)$ is given by the rotational diffusion coefficient D_r. Thus, the orientational diffusion of a polymer without internal rearrangements is given as [27]

$$MSD_r(t) = 2(1 - \exp(-2D_r t)), \tag{4.15}$$

which reproduces the linear mean-square displacement $MSD_r(t) = 4D_r t$ of a 2D random walk for short times. For long times $t \to \infty$, the orientational vectors are uncorrelated and thus on average perpendicular to each other, so that their average distance is $\sqrt{2}$ and the mean-square displacement saturates at $MSD_r(t \to \infty) = 2$.

As there is no analytical expression available in the literature describing D_r in the entire regime of rigidities, the rotational diffusion coefficient D_r has been derived for the average equilibrium conformation of the polymer in the appendix B.3 yielding

$$D_r = \frac{k_B T}{\gamma} = \frac{12 k_B T}{c_\perp L_c R^2} = D_{\mathrm{rod}} \frac{L_c^2}{R^2}, \tag{4.16}$$

where we introduced the rotational diffusion coefficient of the stiff rod

$$D_{\text{rod}} = \frac{12k_BT}{c_\perp L_c^3} = \frac{24k_BTL_p}{\zeta_b L_c^3} \qquad (4.17)$$

and an effective polymer extension

$$\langle R^2 \rangle \equiv \frac{1}{2}\left(\langle R_{\text{ee}}^2 \rangle + 12\langle R_g^2 \rangle\right) \qquad (4.18)$$

calculated from the equilibrium end-to-end vector length $\langle R_{\text{ee}}^2 \rangle$ and the radius of gyration $\langle R_g^2 \rangle$. In the stiff limit, R^2 approaches $R_{\text{ee}}^2 = L_c^2$ and eq. 4.16 reproduces the diffusion coefficient of the rod $D_{\text{rod}} = 1/(2\tau_r)$. In the flexibe limit, the effective extension approaches $R^2 \rightarrow \frac{3}{2}R_{\text{ee}}^2 = 3L_pL_c$ giving $D_r = 1/(3\tau_R)$, where

$$\tau_R = \sum_{i,\text{odd}}^{\infty} \tau_i = \frac{\pi^2}{8}\tau_1 = \frac{c_\perp L_p L_c^2}{12k_BT} \qquad (4.19)$$

is the Rouse relaxation time of the polymer with [27]

$$\tau_i = \frac{\zeta_b n^2 b_k^2}{3\pi^2 k_BT i^2} = \frac{2}{3\pi^2}\frac{c_\perp L_p L_c^2}{k_BT i^2}. \qquad (4.20)$$

Herein, we used an isotropic friction coefficient $c_L = c_\perp = \zeta_b/b_k$, $n = L_c/b_k$ and $b_k = 2L_p$ to yield the continuos description. To crosscheck with existing theories, eq. 4.16 was compared with the rotational diffusion constant obtained from the numerical results for the characteristic times τ_i of semiflexible and flexible polymers given in Winkler et al [41], where

$$D_r = \frac{1}{2\tau_r}, \qquad \tau_r = \frac{3}{2}\sum_{i,\text{odd}}^{\infty} \tau_i \qquad (4.21)$$

was used. Remarkably, an excellent agreement with a deviation below 3% was discovered, which confirms the use of eq. 4.16 for the calculation of the rotational diffusion coefficient.

Eq. 4.15 only holds for polymers without any internal motion, meaning that they are "frozen" in an averaged conformation. Thus, eq. 4.15 can be understood as describing the average orientation of the polymer on a longer timescale, where fast internal conformational changes are averaged out. On the short timescale, the internal rearranging motions of the polymer additionally contribute to the mean-square displacement of the end-to-end vector orientation. Thus, $MSD_r(t)$ becomes nonlinear in time with increasing flexibility of the polymer. In the flexible limit, $MSD_r(t)$ is subdiffusive with $MSD_r(t) \sim t^{0.5}$. An approximate expression for the nonlinear mean-square displacement of semiflexible and flexible polymers is derived in the appendix in section B.1 yielding

$$MSD_r(t) = 2\sum_{i,\text{odd}}^{\infty} \frac{D_1}{D_i}a_i\left(1 - \exp(-2D_i t)\right) \qquad (4.22)$$

where $a_1 = 1$ and $a_i = \frac{2}{3}$ for $i > 1$ and $D_i = 1/(3\tau_i)$ given by the relaxation times τ_i as defined in [41]. Note that this is only a first order approximation, namely the resulting saturation value of $MSD_r(t = \infty) = \pi^2/4$ is too high by a factor of $\pi^2/8$.

The above results have been determined by assuming an isotropic friction coefficient $c_L = c_\perp$. We can approximately include the reduction of the friction tangential to the filament by hydrodynamic interactions by using $c_\parallel = \frac{1}{2}c_\perp$ for the tangential friction. In the stiff rod limit, all friction occuring upon a rotation of the polymers end-to-end vector is perpendicular to the rod. Thus, introducing $c_\parallel$ leaves the obtained result for D_r unchanged in the stiff limit. With increasing flexibility, the monomeric segments of the polymer are increasingly randomly orientated with respect to the frictional drag. Splitting the drag into the parallel and perpendicular components and averaging over all possible orientation angles yields an effective friction coefficient of $c_{\text{eff}} = c_\perp/\sqrt{2}$ for the completely random orientation in the flexible limit. On the other hand, the calculated diffusion coefficient $D_r = D_{\text{rod}}L_c^2/R^2$ decreases from $D_r = D_{\text{rod}}L_c^2/R_{\text{ee}}^2$ in the stiff limit by a factor of $2/3$ to $D_r = \frac{2}{3}D_{\text{rod}}L_c^2/R_{\text{ee}}^2$ during the transition from stiff to flexible. With $\sqrt{2} \times \frac{2}{3} \approx 1$ this suggests, that

$$D_r = D_{\text{rod}}\frac{L_c^2}{R_{\text{ee}}^2} \tag{4.23}$$

can be taken as a fairly good approximation for the diffusion coefficient in the entire regime of rigidities under the assumption of an anisotropic friction coefficient $c_\perp = 2c_\parallel$.

4.2 Tumbling Dynamics of Single Polymers in Shear Flow: Theoretical Framework

Since the behaviour of single DNA filaments in extensional flow was first observed [100, 93], a lot of progress has been made in describing the dynamics of flexible polymers with simulations or dumbbell models [18, 15, 31, 96, 24]. From theoretical analysis [41, 48] and experimental observations, three modes of shear-induced stretching transitions had been discussed for the entropy dominated flexible polymers [107]: recoil, restretch and tumble. In contrast, the polymer conformation in the stiff and semiflexible regime is rather dominated by the bending energies in the filament. While the transition between enthalpic and entropic response of the filament to the shear forces has been proposed and analytically solved for the limiting cases of stiff and fully flexible polymers [115, 116], a continuos description applying to the entire regime of rigidities including the semiflexible regime is still lacking.

In this section we will derive a theoretical framework describing the dynamics of linear polymers in shear. The model is based on the experimental findings with semiflexible actin filaments, which will be shown and discussed in the subsequent section.
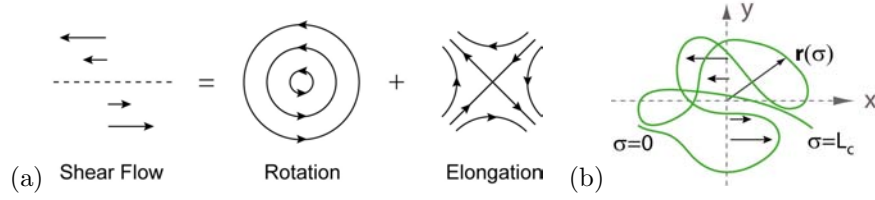
Figure 4.1: (a) The rotational and elongational flow components of simple shear lead to a rotation and simultaneous deformation of a molecule subjected to shear. (b) Center of mass coordinate system with shear gradient into the negative y-direction and conformation coordinate $\sigma \in [0; L_c]$.

4.2.1 Dynamics of Center of Mass

The flow-gradient plane shall be aligned with the x, y plane of the coordinate system with the gradient of the shear flow $\dot{\gamma}$ pointing into the negative direction of the y-axis (see fig. 4.1b). With an isotropic friction coefficient per unit length c_L, the local frictional force exerted on a polymer segment of length $d\sigma$ is directly proportional to the relative velocity between the rod segment $\dot{\mathbf{r}}(\sigma) \equiv \mathbf{v}(\sigma)$ and the surrounding fluid $\mathbf{u}(\mathbf{r}(\sigma))$:

$$d\mathbf{F}^{\text{frict}}(\sigma) = c_L \mathbf{v}_{\text{rel}} d\sigma = c_L \cdot (\mathbf{u}(\mathbf{r}(\sigma)) - \mathbf{v}(\sigma)) \, d\sigma. \tag{4.24}$$

As all the intermolecular forces mutually exerted by parts of the polymer have to vanish in total, the polymers center of mass motion $\dot{\mathbf{R}}_{\text{com}}$ is determined by the sum over the frictional forces on the local segments

$$\mathbf{F}^{\text{frict}}_{\text{com}} = \int_0^{L_c} d\mathbf{F}^{\text{frict}}(\sigma) = \int_0^{L_c} c_L \cdot (\mathbf{u}(\mathbf{r}(\sigma)) - \mathbf{v}(\sigma)) \, d\sigma. \tag{4.25}$$

Let $\mathbf{u}_{\text{com}}$ be the fluid velocity at the center of mass, and $y(\sigma)$ be the y-distance of a polymer segment with respect to the center of mass. Then, the fluid velocity $\mathbf{u}(\mathbf{r}(\sigma))$ is given by $\mathbf{u}(\mathbf{r}(\sigma)) = \mathbf{u}_{\text{com}} - y(\sigma)\dot{\gamma}\mathbf{e}_x$ and we can rewrite eq. 4.25 as:

$$\mathbf{F}^{\text{frict}}_{\text{com}} = \int_0^{L_c} c_L \cdot (\mathbf{u}_{\text{com}} - y(\sigma)\dot{\gamma}\mathbf{e}_x - \mathbf{v}(\sigma)) \, d\sigma = c_L L_c(\mathbf{u}_{\text{com}} - \dot{\mathbf{R}}_{\text{com}}), \tag{4.26}$$

where we used $\int y(\sigma)d\sigma = 0$ from eq. 4.7 and $\dot{\mathbf{R}}_{\text{com}} = \frac{1}{L_c}\int_0^{L_c} \mathbf{v}(\sigma)d\sigma$ from differentiation of eq. 4.7. As long as the thermal motion is negligible with respect to the frictional forces, friction dominates the polymer dynamics and we get the equation of motion for the center of mass as

$$m\ddot{\mathbf{R}}_{\text{com}} = c_L L_c(\mathbf{u}_{\text{com}} - \dot{\mathbf{R}}_{\text{com}}) = c_L L_c \mathbf{v}^{\text{com}}_{\text{rel}}. \tag{4.27}$$

Hence, the polymer gets accelerated into the direction of the relative velocity between the polymer and the fluid at the center of mass $\mathbf{v}^{\text{com}}_{\text{rel}}$ until the polymer's center of mass velocity equals the fluid's velocity. In an overdamped system

where the frictional forces dominate over the inertial forces we can therefore assume, that the polymer's center of mass follows the fluid streamlines and $\mathbf{v}_{\text{rel}}^{\text{com}} = 0$.

The above considerations neglect any hydrodynamic interaction between the local polymer segments. However, the friction coefficient c_L is anisotropic for non-spherical objects. For a long rod with length L and diameter d and $L \gg d$, end effects can be neglected and the frictional force for dragging the rod with velocity $\mathbf{v}_{\text{rel}}$ through the water is given as [47]:

$$\mathbf{F}^{\text{frict}} = \zeta_{\perp} \mathbf{u}_{\perp} + \zeta_{\parallel} \mathbf{u}_{\parallel}, \quad \text{with}\, \zeta_{\perp} = 2\zeta_{\parallel} \quad \text{and}\, \zeta_{\parallel} = \frac{2\pi\eta L}{\ln(L/d)}. \tag{4.28}$$

Hereby, $\zeta_{\perp}, \zeta_{\parallel}$ are the anisotropic drag coefficients of the rod. In a WLC representation of the polymer as a "snake" with cylindrical cross section of diameter d it is therefore reasonable to introduce an anisotropic friction coefficient per unit length with

$$c_{\perp} = \frac{4\pi\eta}{\ln(L/d)} \quad \text{and} \quad c_{\parallel} = \frac{2\pi\eta}{\ln(L/d)}, \tag{4.29}$$

which accounts for hydrodynamic interactions between neighbouring, aligned monomers reducing the friction tangential to the polymer segment. It is obvious that the local lengthscale L over which the polymer friction is approximated by the rod expression in eq. 4.29 should be in the range of the persistence length L_p. Due to the anisotropy in the friction coefficient, an asymmetric conformation of the polymer may lead to rheophoretic forces [61, 60] inducing a small drift of the center of mass which will be neglected here. It is therefore convenient to discuss the dynamics in the center of mass system of the polymer where only rotational motions and conformational changes occur.

The local fluid velocity at the center of mass $\mathbf{R}_{\text{com}}$ can thus be determined from the measured filament trajectory. From the known flowprofile of the Newtonian dilute actin solution and the optically detected lateral position of the filament in the channel, the local shearrate $\dot{\gamma}$ in the vicinity of $\mathbf{R}_{\text{com}}$ was evaluated for the tumbling filaments.

Weissenberg number

The dimensionless *Weissenberg number* Wi characterising the flow strength experienced by the polymers is given as the product of the flow rate and the characteristic relaxation time τ_{rel} of the polymer. For polymers tumbling in shear, the characteristic timescale is given by the rotational relaxation time $\tau_r = 1/(2D_r)$, which is determined by the rotational diffusion coefficient D_r. Together with the shear rate $\dot{\gamma}$, the flow strength is characterized by

$$\text{Wi} = \dot{\gamma}\tau_r = \frac{\dot{\gamma}}{2D_r}. \tag{4.30}$$

4.2.2   Tumbling Time τ_T

As we do not distinguish between the polymer ends, we define the characteristic timescale of the rotational motion in shear as the tumbling time τ_T in which the orientation of the polymer is reversed. The tumbling time τ_T is hence given by the time interval, in which the end-to-end vector of the polymer is rotated by an angle π in the direction of the rotational component of the flow. In the experiments, τ_T was determined as the average time interval between consecutive end-to-end vector orientations in the direction of the shear gradient ($\phi = \pi/2 + n\pi$, with ϕ denoting the angle between the end-to-end vector $\mathbf{R}_{\mathrm{ee}}$ and the flow direction).

The shear flow is a mixture of a rotational flow with $\omega = \dot\gamma/2$ and an elongational flow with $\dot\epsilon = \dot\gamma/2$ (see section A.2). For spherical, rigid objects like hard spheres, the friction forces originating from the pointsymmetric elongational flow field cancel out. Thus, the rotational component of the flow will cause a rigid sphere in shear to rotate with an angular velocity of $\dot\phi = \dot\gamma/2$. As the thermal motion of the sphere is undirected, this is valid for both non-thermal and Brownian spheres. Thus, the tumbling time of a sphere in shear is given as

$$\tau_T = \frac{\pi}{\dot\phi} = \frac{2\pi}{\dot\gamma}, \tag{4.31}$$

so that the tumbling frequency $f_T = 2\pi/\tau_T = \dot\gamma$ is equal to the shear rate.

In general, linear polymers like the used actin filaments are non-spherical and deformable in substantially strong flows. Thus, the tumbling dynamics are more complicated and will be discussed for stiff, semiflexible and flexible polymers in detail in the following.

4.2.3   Stiff Polymers: Brownian Rod Dynamics

If the persistence length L_p is much higher than the contour length L_c, the shear forces cannot effectively bend the polymer and the polymer conformation can be approximated by a stiff rod with length L_c. Since then the conformation is fixed, the dynamics is reduced to rotational motion around the center of mass located at $\sigma = L_c/2$. We first restrict the discussion to thin rods lying aligned in the shear plane xy, so that the position of the rod is solely determined by the orientational angle ϕ (see fig. 4.2). The frictional force on a segment $\mathrm{d}\sigma$ of the rod is given by eqs. 4.24, 4.28 as:

$$\begin{aligned}
\mathrm{d}\mathbf{F}^{\mathrm{frict}}(\sigma) &= \mathbf{f}^{\mathrm{frict}}(\sigma)\mathrm{d}\sigma = \left(c_\perp(\mathbf{u}_\perp(\sigma) - \mathbf{v}_\perp(\sigma)) + c_\|(\mathbf{u}_\|(\sigma) - \mathbf{v}_\|(\sigma))\right)\mathrm{d}\sigma \\
&= \left(c_\perp \mathbf{v}_\perp^{\mathrm{rel}} + c_\| \mathbf{v}_\|^{\mathrm{rel}}\right)\mathrm{d}\sigma
\end{aligned} \tag{4.32}$$

With cylindrical coordinates in the center of mass frame we get $r(\sigma) = \sigma - L_c/2$, and the tangential and perpendicular velocity components point into the direction of the coordinates r and ϕ. With $\mathbf{u}$ known from eq. 3.6 we can calulate the frictional force as

$$\mathrm{d}\mathbf{F}^{\mathrm{frict}}(r) = \begin{pmatrix} \mathrm{d}\mathbf{F}_r^{\mathrm{frict}} \\ \mathrm{d}\mathbf{F}_\phi^{\mathrm{frict}} \end{pmatrix} = \begin{pmatrix} -c_\| \dot\gamma \sin\phi \cos\phi \\ c_\perp(\dot\gamma \sin^2\phi - \dot\phi) \end{pmatrix} r\,\mathrm{d}r \tag{4.33}$$
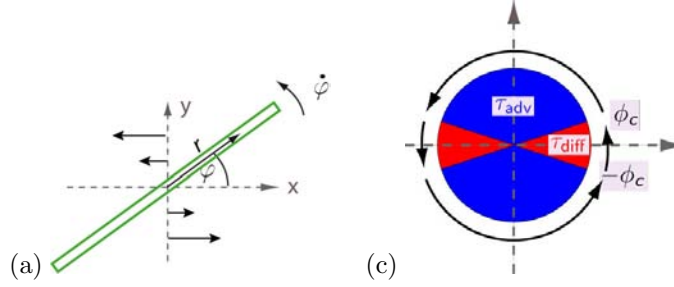
Figure 4.2: (a) Schematics of stiff rod in shear flow. For simplification, the rod is assumed to be aligned to the shear plane xy. (b) The tumbling of thermal rods in shear can be divided into a deterministic, advective phase (blue) and a stochastic diffusive phase (red) located symmetrically around the flow aligned conformation at $\phi = 0$. The seperating angle is denoted as critical angle ϕ_c.

with $r \in [-L_c/2; L_c/2]$. As the rod is symmetric about the center of mass at $r = 0$, the frictional forces in the radial direction cancel each other in total, giving $\dot{\mathbf{R}}_{\mathrm{com}} = 0$. The frictional forces into the angular direction give rise to a torque of

$$M = \int_{-L_c/2}^{L_c/2} r \mathrm{d}\mathbf{F}_\phi^{\mathrm{frict}} = \frac{c_\perp L_c^3}{12}(\dot{\gamma}\sin^2\phi - \dot{\phi}), \tag{4.34}$$

which will accelerate the rod and make it rotate.

Non-Thermal Rod Dynamics

Without thermal motions, the rod rotation is set by a vanishing frictional force in the angular direction in the overdamped case, so that the rod will rotate in shear flow with an angular velocity of

$$\dot{\phi} = \dot{\gamma}\sin^2\phi. \tag{4.35}$$

In the above derivation we only considered drag forces arising from a relative velocity difference which was equal on the length scale of the rod diameter. However, in the case of full flow alignment at $\phi = 0$ where eq. 4.35 predicts a metastable fixpoint of the dynamics, there is a non-negligible flow gradient across the width of the rod, which causes a remaining torque on the rod at $\phi = 0$. Thus, eq. 4.35 is only strictly valid in the case of thin rods with negligible aspect ratio $d/L \approx 0$. The angular dynamics of a non-thermal cylinder with finite aspect ratio in shear is described by Jeffery's equation [26]:

$$\dot{\phi} = \dot{\gamma}(\sin^2\phi + \kappa^2\cos^2\phi), \tag{4.36}$$

with $\kappa^2 = \frac{3}{2}(d/L)^2\ln(L/d)$ for long cylinders with negligible end-effects. Eq. 4.36 can be integrated. With $\phi(t=0) = 0$ it gives

$$\tan[\phi(t)] = -\kappa\tan(\dot{\gamma}\kappa t), \quad \text{and} \quad \tau_T = \pi/(\dot{\gamma}\kappa) \tag{4.37}$$

for the dynamics and the tumbling time of the non-thermal rod[26].

Brownian Rod Dynamics

For an infinitely thin rod, the advective motion is described by eq. 4.35 with a stationary point in the fully aligned conformation at $\phi = 0$ and $\phi = \pi$. As the rod approaches $\phi = 0$, the diffusive motion becomes non-negligible and eventually helps the rod to overcome the stationary point. Thus, we can divide the tumbling motion into two distinct phases: A deterministic *advective phase* with insignificant thermal motion, in which the dynamics is set by eq. 4.35, and a stochastic *diffusive phase* governed by the rotational diffusion of the rod. Due to the symmetry of the advective contribution in the Jeffery equation, we suppose that the angular interval of the diffusive phase is symmetrical about the aligned state $[-\phi_c; \phi_c]$, where ϕ_c is the critical angle seperating advective and diffusive phase (see fig. 4.2b). The contribution of each phase to the total tumbling time can now be calculated seperately:

$$\tau_T = \tau_{\text{adv}} + \tau_{\text{diff}} \tag{4.38}$$

The critical angle ϕ_c of tumbling thermal rods has been shown [58] to satisfy $\langle (d/dt)(\phi^2/2) \rangle = D_{\text{rod}}$ or equivalently $\phi\dot{\phi} = D_{\text{rod}} = \phi\dot{\gamma}\sin^2\phi \approx \dot{\gamma}\phi^3$, yielding the critical angle ϕ_c as:

$$\phi_c = \left(\frac{D_{\text{rod}}}{\dot{\gamma}} \right)^{1/3}. \tag{4.39}$$

A more demonstrative qualitative derivation of ϕ_c can be given as follows: To determine the angular interval dominated by diffusion $[-\phi_c; \phi_c]$, we approximate the advective drift strength in the interval by $\langle \dot{\phi} \rangle \approx \dot{\phi}(\phi_c) = \dot{\gamma}\sin^2\phi_c \approx \dot{\gamma}\phi_c^2$ for small critical angles $\phi_c \ll 1$. Diffusion and drift are equally strong at $\phi = \phi_c$, meaning that the time $\tau_{\text{diff}}^{-\phi_c \to \phi_c} = (\Delta\phi)^2/(2D_{\text{rod}}) = 2\phi_c^2/D_{\text{rod}}$ needed to pass the interval of length $\Delta\phi = 2\phi_c$ by diffusion is equal to the time $\tau_{\text{adv}}^{-\phi_c \to \phi_c} = \Delta\phi/\langle \dot{\phi} \rangle = 2/\dot{\gamma}\phi_c$ needed for an advective drift with velocity $\langle \dot{\phi} \rangle$. This directly gives the above result $\phi_c = (D_{\text{rod}}/\dot{\gamma})^{1/3}$. With eqs. 4.39 and 4.30 we can express ϕ_c in terms of the Weissenberg number as $\phi_c = (2\text{Wi})^{-1/3}$ showing that the condition $\phi_c \ll 1$ is fulfilled in strong shear flows where $Wi \gg 1$.

The deterministic time τ_{adv} can be calculated by integrating the inverse of eq. 4.35 over the angular interval of advection:

$$\begin{aligned} \tau_{\text{adv}} &= \int_{\phi_c}^{\pi-\phi_c} \frac{\text{d}\phi}{\dot{\phi}(\phi)} = \frac{1}{\dot{\gamma}} \int_{\phi_c}^{\pi-\phi_c} \frac{\text{d}\phi}{\sin^2\phi} = -\frac{1}{\dot{\gamma}} \left[\frac{1}{\tan\phi} \right]_{\phi_c}^{\pi-\phi_c} \\ &= \frac{2}{\dot{\gamma}\tan\phi_c} \overset{\phi_c \ll 1}{\approx} \frac{2}{\dot{\gamma}\phi_c} = 2D_{\text{rod}}^{-1/3}\dot{\gamma}^{-2/3} \end{aligned} \tag{4.40}$$

In the diffusive phase, for $\phi_c \ll 1$ a mean first passage time $\langle \tau_{\text{diff}} \rangle$ can be calculated analytically using standard methods starting out from the Langevin equation corresponding to eq. 4.35:

$$\dot{\phi} = \dot{\gamma}\sin^2\phi + \sqrt{2D_{\text{rot}}}\,\eta, \qquad \langle \eta(t) \rangle = 0, \quad \langle \eta(t)\eta(t') \rangle = \delta(t-t'). \tag{4.41}$$

where η is the stochastic term describing the thermal motion. It is convenient to introduce a potential $U(\phi) = -\dot{\gamma}\phi^3/3$ so that the deterministic term $\dot{\gamma}\sin^2\phi \approx \dot{\gamma}\phi^2 = -U'(\phi)$ can be regarded as the corresponding force. For $\phi > \phi_c$, the advective drift force prevents the filament from diffusing back towards $\phi < \phi_c$. At the other edge of the diffusive interval at $\phi = -\phi_c$, the positive drift force pushes filaments with $\phi < -\phi_c$ back towards $\phi > -\phi_c$. We thus consider an angle ϕ sitting in potential $U(\phi)$, leaving the valley at barrier located at $\phi = \phi_c$ (adsorbing boundary), and assuming a reflecting boundary at $-\phi_c$ (assuming positive rate $\dot{\gamma}$), using the methods described in ref. [46]. The result is

$$\langle \tau_{\text{diff}} \rangle \approx (5/3)\phi_c^2/D_{\text{rod}} = (5/3)D_{\text{rod}}^{-1/3}\dot{\gamma}^{-2/3}, \tag{4.42}$$

a detailed derivation is given in sec. B.4. Then, with $\phi_c = (D/\dot{\gamma})^{1/3}$ the total average tumbling time can be calculated from eq. 4.38 as

$$\tau_T = \tau_{\text{adv}} + \langle \tau_{\text{diff}} \rangle = 2D_{\text{rod}}^{-1/3}\dot{\gamma}^{-2/3} + \frac{5}{3}D_{\text{rod}}^{-1/3}\dot{\gamma}^{-2/3} = \frac{11}{3}D_{\text{rod}}^{-1/3}\dot{\gamma}^{-2/3}. \tag{4.43}$$

With $D_{\text{rod}} \sim L_c^{-3}$, the tumbling time of the rod is thus directly proportional to the rod length L_c. We can rewrite eq. 4.43 in terms of the Weissenberg number as

$$\frac{\tau_T}{\tau_r} = \frac{11 \times 2^{1/3}}{3}\text{Wi}^{-2/3} \tag{4.44}$$

Orientational Distribution Function

The stationary probability density function $p_{\text{stat}}(\phi)$ for the orientation of Brownian rods in shear can be calculated from the Fokker-Planck equation for the orientational distribution function $p(\phi, t)$, see appendix B.5:

$$\frac{\partial p(\phi)}{\partial t} = \frac{\partial(\dot{\phi}(\phi)p(\phi))}{\partial \phi} + D_{\text{rod}}\frac{\partial^2 p(\phi)}{\partial \phi^2}, \tag{4.45}$$

with $\dot{\phi}(\phi) = \dot{\gamma}\sin^2\phi$ from Jeffery's equation. According to [58], the center of the peak in the stationary probability density function is in a good approximation with the critical angle $-\phi_c$, so that the most probable angle for the rod is slightly before reaching the fully aligned state. If the rod located at $\phi = -\phi_c$ diffuses into the negative angular direction away from the aligned state, the advective forces will drive it back to $-\phi_c$, making $-\phi_c$ a reflective boundary for the diffusion. If the diffusing rod reaches ϕ_c, it escapes the diffusive interval $[-\phi_c; \phi_c]$ and the advection induces another tumbling flip of the rod. Thus, the maximum of $p_{\text{stat}}(\phi)$ is located at the backward boundary between dominating advective forces and diffusion at $-\phi_c$.

Out-of-Shear Plane Fluctuations of Brownian Rods

So far we assumed a perfect alignment of the Brownian rod within the shear plane (xy-plane) for the calculation of the rod dynamics. In reality, the Brownian rod may diffuse out of the shear plane resulting in a non-zero azimuthal

angle $\theta \neq 0$ betwen the rod and the xy-plane. The velocity field of simple shear with shear rate $\dot{\gamma}$ in spherical coordinates is given as

$$\mathbf{u} = \begin{pmatrix} \dot{r} \\ \dot{\phi} \\ \dot{\theta} \end{pmatrix} = \dot{\gamma} \begin{pmatrix} -r \sin^2 \theta \sin \phi \cos \phi \\ \sin^2 \phi \\ \sin \theta \cos \theta \sin \phi \cos \phi \end{pmatrix}. \tag{4.46}$$

In the advective phase, an infinitely thin rod in overdamped conditions with $\theta \neq 0$ will thus perform a kayaking motion with [26]:

$$\dot{\theta} = \dot{\gamma} \sin \theta \cos \theta \sin \phi \cos \phi, \quad \dot{\phi} = \dot{\gamma} \sin^2 \phi. \tag{4.47}$$

Hence, the advective dynamics in the rotational direction of the shear ϕ are not affected by $\theta \neq 0$. If $\theta \ll 1$ is small during the diffusive phase, the diffusive motion into the ϕ direction is also not altered by a small azimuthal angle. Then, the angular dynamics along the ϕ-axis are correctly described within the $\theta \approx 0$ approximation used above.

The magnitude of the azimuthal angle in the diffusive phase can be estimated as follows: As the above discussion for the orientational distribution revealed, within the diffusive phase the rod spends most of the time near $-\phi_c$. In the interval $\phi \in [-\pi/2; 0]$, a rod with $\theta \neq 0$ experiences an advective drag of $\dot{\theta} = \dot{\gamma} \sin \theta \cos \theta \sin \phi \cos \phi$ driving it towards the shear plane with $\theta = 0$. This induced drift makes $\theta = 0$ a stable stationary point with $\dot{\theta} = 0$ for the θ-advection. Contrary, $\theta = \pm \pi/2$ is an unstable fixpoint, so that thermal fluctuations will drive rods away from a perpendicular alignment to the shear plane. Thus, thermal rods do not stay aligned with the z-axis, although the conformation perpendicular to the shear plane would be the optimal conformation to reduce the frictional dissipation.

Within $\phi \in [-\phi_c; 0]$ the rod thus azimuthally diffuses in a potential well, which limits the maximum angle that the rod can reach to a critical azimuthal angle $|\theta| \leq \theta_c$. The frictional torque T acting on a rod with $\dot{\theta} = 0$ in the azimuthal direction can be calculated from the velocity component $v_\theta = r \sin \theta \cos \theta \sin \phi \cos \phi$ of the shear as

$$T(\theta, \phi) = 2 \int_0^{L_c/2} r f^{\mathrm{frict}}(r) \mathrm{d}r = 2 \int_0^{L_c/2} r c_\perp v_\theta \mathrm{d}r$$
$$= \int_0^{L_c/2} r^2 \dot{\gamma} c_\perp \sin \theta \cos \theta \sin 2\phi \mathrm{d}r = \tfrac{1}{24} c_\perp \dot{\gamma} L_c^3 \sin \theta \cos \theta \sin 2\phi. \tag{4.48}$$

By integration we get the azimuthal potential $U(\theta, \phi) = -\int_0^\theta T(\theta') \mathrm{d}\theta'$ for the diffusing rod:

$$U_\theta(\theta, \phi) = -\frac{1}{48} c_\perp L_c^3 \dot{\gamma} \sin 2\phi \sin^2 \theta \tag{4.49}$$

If the time t_{ϕ_c} the rod spends in the vicinity of $-\phi_c$ in the diffusive phase is long enough to explore the potential, the rods averaged absolute value for the azimuthal angle at $-\phi_c$ can be calculated by equating the potential and thermal energy $U_\theta(\theta_c, -\phi_c) = \frac{1}{2} k_B T$, which yields

$$\theta_c^2 = \frac{24 k_B T}{c_\perp L_c^3 \dot{\gamma}} \frac{1}{\sin(2\phi_c)} = \frac{D_{\mathrm{rod}}}{\dot{\gamma}} \cdot \frac{2}{\sin(2\phi_c)} = \frac{2\phi_c^3}{\sin(2\phi_c)} \approx \phi_c^2 \tag{4.50}$$

Therefore, the typical azimuthal rod orientation at $-\phi_c$ should be given as $\langle|\theta_c|\rangle = \phi_c$. The timescale t_{U_θ} to explore the potential is then $t_{U_\theta} \approx \theta_c^2/2D_{\text{rod}} = \frac{3}{10}\tau_{\text{diff}}$ well below the time spent in the diffusive phase. While the rod diffuses from ϕ_c to $\phi = 0$, it experiences a positive drift in the ϕ-direction and a focussing drift towards $\theta = 0$, which vanishes as the rod approaches $\phi = 0$. Thus, the mean squared azimuthal angle is expected to be slightly higher at $\phi = 0$ than at $\phi = \phi_c$. Due to the focussing drift, the additional mean squared displacement away from the flow aligned state $\theta = 0$ should be less than ϕ_c^2, and as a lower limit we will assume $\langle\theta^2\rangle(\phi = 0) \approx \phi_c^2$. During $[0; \phi_c]$ the rod experiences a small drift in θ directed away from $\theta = 0$ of strength $\dot\gamma \sin\phi \cos\phi$ and a positive drift in ϕ of $\dot\gamma \sin^2\phi$. In the region where the drift is non negligible ($\phi \lesssim \phi_c$) the drift in θ and ϕ is of comparable strength. Therefore we can assume the mean squared angle θ^2 to increase by the same amount as ϕ^2 during the passage from $\phi = 0$ to $\phi = \phi_c$, resulting in a lower estimate for $\theta(\phi_c)$:

$$\langle\theta^2(\phi_c)\rangle \geq \theta_c^2 + \phi_c^2 = 2\phi_c^2. \tag{4.51}$$

In the range of sufficiently strong flow (Wi $\gg 1$), the assumption, that the rods are approximately aligned in the shear plane within $[-\phi_c; \phi_c]$ should therefore be justified in the calculation of the angular ϕ-dynamics. As the diffusive forces dominate over the aligning advective forces once the rod passes $-\phi_c$, we can expect the minimum for the mean square azimuthal angle to occur at $-\phi_c$, which means that it coincides with the maximum of the probability density function $p(\phi)$.

In the advective regime, the azimuthal trajectory of the rod can be determined: Division of the two equations of motion in the advection regime for θ and ϕ eq. 4.47,4.36, seperation of the variables and integration yields for infinitely thin rods [26]:

$$\tan[\theta(t)]^{-1} = \tan[\theta(t = 0)]^{-1}\sqrt{\frac{1 - \cos^2[\phi(t = 0)]}{1 - \cos^2[\phi(t)]}} = \tan[\theta(t = 0)]^{-1}\frac{\sin[\phi(t = 0)]}{\sin[\phi(t)]}. \tag{4.52}$$

4.2.4 *Semiflexible Polymers: "U-turn" Tumbling*

Buckling Length L_b

A polymer in a straight rodlike conformation rotating in shear following Jeffery's equation only experiences frictional forces in the tangential direction. The local magnitude of the friction force is given by eq. 4.33. In the advective phase above ϕ_c, these radial forces may overcome the critical buckling force of the filament, which can be calculated from the Euler force

$$F_c = \pi^2\frac{EI}{L^2}, \tag{4.53}$$

which gives the critical force for a beam of length L to collapse under compression [47]. For a given flow rate $\dot\gamma$ we can deduce the critical length L_b at

which we can expect buckling to occure during the tumbling motion as (see appendix B.6, eq. B.114):

$$L_b = 2\pi^{3/4} R_{\mathrm{U}} \quad \text{with} \quad R_{\mathrm{U}} = \left(\frac{4}{\pi} \frac{k_B T L_p}{c_\| \dot\gamma} \right)^{1/4} . \tag{4.54}$$

Thus, for polymers with length $L_c < L_b$, the rodlike description is a good approximation, whereas for longer contour lengths $L_c > L_b$ the polymer buckles and its conformation strongly deviates from the rodlike shape during the tumbling. For non-thermal rods, the critical buckling angle α_b at which a polymer rotating away from the aligned state starts to buckle can be estimated as $\alpha_{\mathrm{b}} = \frac{1}{2}(L_b/L_c)^4$ (see appendix B.6). Thus, in the angular interval between $[\alpha_{\mathrm{b}}; \pi - \alpha_{\mathrm{b}}]$ we cannot expect polymers with $L_c > L_p$ to follow the Brownian rod dynamics.

Force Balance between Frictional and Bending Forces

To describe the polymer filaments in a strongly bent conformation, the frictional forces have to be balanced with the elastic bending forces occuring along the filament for non-zero curvature. With $\alpha(\sigma)$ being the local angle between the filament and the flow direction, the curvature κ and the local bending radius R_{bend} are given by the first derivative of the local angle $R_{\mathrm{bend}}^{-1} = \kappa = \mathrm{d}\alpha/\mathrm{d}\sigma$. The local curvature is related to the local bending moment $M_b(\sigma)$ by the beam equation [47]:

$$\kappa(\sigma) = \frac{M_b(\sigma)}{EI} = \frac{1}{k_B T L_p} \int_0^\sigma \mathrm{d}\mathbf{F}^{\mathrm{frict}}(\sigma') \times (\mathbf{R}(\sigma') - \mathbf{R}(\sigma))\mathrm{d}\sigma' \tag{4.55}$$

where M_b is given by integrating the vector product of the local frictional force $\mathrm{d}\mathbf{F}^{\mathrm{frict}}(\sigma')$ and the acting leverarm $(\mathbf{R}(\sigma') - \mathbf{R}(\sigma))$. The frictional forces are depending on the local velocity difference $\mathbf{v}_{\mathrm{rel}}$ between fluid and filament, which in turn is dependent on the conformational vector $\mathbf{R}$, its derivative $\mathbf{R}'$ and its dynamics $\dot{\mathbf{R}}$ (see eq. 4.32). The curvature κ depends on the second derivative of the conformation vector with respect to the arc length $\mathbf{R}'' = \mathrm{d}^2\mathbf{R}/\mathrm{d}\sigma^2$. Differentiation of eq. 4.55 with respect to σ yields the differential equation for the semiflexible filaments conformation, which is of the type

$$F(\mathbf{R}(\sigma), \mathbf{R}'(\sigma), \mathbf{R}'''(\sigma), \dot{\mathbf{R}}(\sigma)) = 0 \tag{4.56}$$

and generally cannot be solved analytically. However, an analytical solution for the dynamics can be calculated if the complexity of the conformational space is reduced by approximating the motion of the filament with a basic conformational cycle.

U-turn Model

Motivated by the characteristic tumbling conformations observed in the experiments shown in section 4.3, we assume that the conformational space is

restricted to a stadium shaped track during an interval $\phi \in [\phi_{\min}; \phi_{\max}] = [\phi_{\min}; \pi - \phi_{\min}]$ with

$$\phi_{\min} = \arctan\left(2R_{\mathrm{U}}/(L_c - \pi R_{\mathrm{U}})\right). \qquad (4.57)$$

where R_{U} is the stadium radius. A detailed discussion of the resulting force balance calculations is given in the appendix (B.6) and will be sketched in the following.

In this "U-turn"-model, the filament is supposed to run on a stadium track with constant radius R_{U} and track velocity $v(\sigma)$. This assumption is a priori postulated by the experimental observation and will be legitimated by the results posterior. Depending on an asymmetry due to initial thermal fluctuations, a polymer starting from the flow aligned conformation can begin a U-turn run either on the left or on the right half-circle of the stadium. After completing the run towards full alignment, another tumbling cycle can be started. As we do not distinguish between the polymer ends, we only discuss an angular interval of $\phi \in [0; \pi]$ for the orientation of the end-to-end vector to capture the entire tumbling dynamics. Fig. 4.3a shows a filament performing a counterclockwise U-turn run on the right halfcircle of the stadium. It is convenient for the calculations
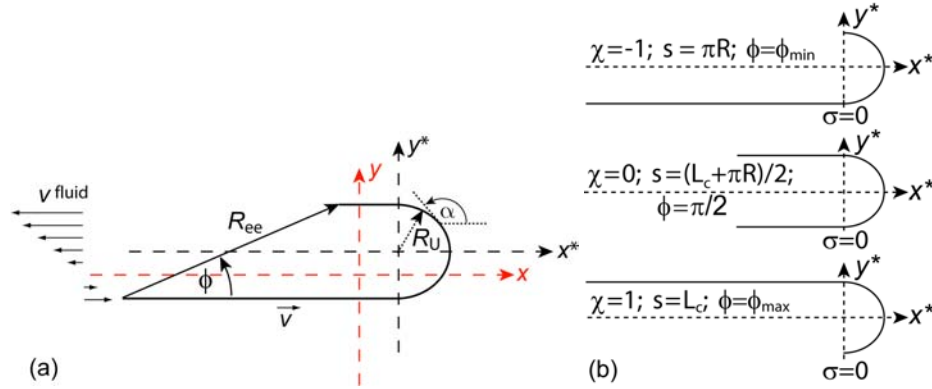
Figure 4.3: (a) Schematics and coordinate systems of the U-turn/stadium model: The semiflexible filament in the strongly bent state is supposed to run on a U-turn track with fixed radius R_{U}. The coordinate system of the U–turn frame (x^*, y^*) is shown in black, the center of mass frame (x, y) is shown in red. (b) Extremal filament conformations with corresponding interrelated coordinates χ, s, and ϕ (Eqs. B.117 and B.148).

to introduce a conformation coordinate $\chi(\sigma)$ running from $\chi \in [-1; 1]$ which defines the conformation of the filament during the U-turn. Fig. 4.3b shows the filament conformations for the three extremal conformations corresponding to $\chi = -1, 0, 1$ representing a letter l, U and J conformation.

Force Balance in U-turn model

The track velocity $v(\chi, R_U)$ can be calculated by assuming that the tangential frictional forces along the filament vanish:

$$\int_0^{L_c} c_\parallel \mathbf{v}_\parallel^{\mathrm{rel}} d\sigma = 0. \tag{4.58}$$

This should be approximately fulfilled in overdamped conditions, where the accelerative forces along the U-turn track are negligible compared to the frictional forces. The local tangential relative velocity $\mathbf{v}_\parallel^{\mathrm{rel}}$ is given as the difference of the fluid velocity and the filament velocity, which can be calculated from the track velocity $v(\chi)$ and the local conformation set by R_U and χ (see schematics in fig 4.4a). Thus, the track velocity $v(R_U, \chi)$ for a conformation specified by χ is given in terms of the yet unknown U-turn radius R_U. If the filament is long
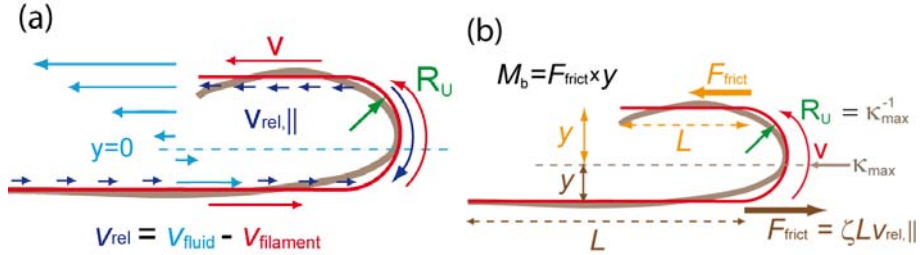
Figure 4.4: (a) The friction acting on the filament is determined by the relative velocity between fluid and filament. From the track velocity v and the conformation given by (R_U, χ) the local filament velocity can be calculated in the U-turn model. The local fluid velocity is set by the shearrate and the distance to the center of mass streamline $y = 0$. In overdamped conditions, the integral over the relative velocity tangential to the filament vanishes, which sets $v(R_U)$. (b) At the point of maximum curvature $\kappa_{\mathrm{max}}(\sigma_b)$, the filament bending can be treated analogous to a rod fixed in a wall. There, the bending moments M_b exerted by the flow aligned parts of the filament are equal, which yields a condition determining the leverarms y. Then, the inverse of κ_{max} is taken as a measure for the U-turn radius $R_U(v)$.

with respect to the U-turn half-circle $L_c \gg \pi R$, the calculation shows that the track velocity depends only weakly on the conformation coordinate χ. In 0-th order in terms of $\pi R/L_c$, the track velocity is obtained from eq. B.130 as

$$v(R_U) = \dot{\gamma} R_U + O(\pi R/L_c). \tag{4.59}$$

The equation for the bending forces eq. 4.55 is evaluated at the point of maximum curvature $\kappa(\sigma_b) = \kappa_{\mathrm{max}}$ by only considering the frictional forces arising from the flow aligned parts of the filament. At σ_b the bending moments M_b exerted from both flow aligned parts are equal and the inverse of the maximum

curvature is taken as an approximation for the U-turn radius $R_{\mathrm{U}} \approx \kappa_{\max}^{-1}$ (see fig 4.4b). Thus, eq. 4.55 gives the U-turn radius in dependence of the track velocity and the conformation coordinate $R_{\mathrm{U}}(v, \chi)$. Together with $v(R_{\mathrm{U}}, \chi)$ from eq 4.59, the track velocity and the U-turn radius can be determined in the limit of long filaments $L_c \gg \pi R_{\mathrm{U}}$. The result for R_{U} shows only a slight dependence on χ, which supports the assumption of a constant U-turn radius, and R_{U} can be determined as

$$R_{\mathrm{U}} = \left(\frac{4}{\pi} \frac{k_B T L_p}{c_{\|} \dot{\gamma}} \right)^{\frac{1}{4}} . \tag{4.60}$$

A detailed calculation of R_{U} and v is given in the appendix B.6.

Angular Dynamics and Tumbling Time

The result for the track velocity v implies, that within the interval $[\phi_{\min}; \phi_{\max}]$ the velocity of the filaments ends is approximately given by the velocity of the surrounding fluid. Consequently, the angular dynamics of the semiflexible filament in this interval is equivalent to the stiff rod dynamics with $\dot{\phi} = \dot{\gamma} \sin^2 \phi$. For filaments with $L_b < L_c \leq L_p$ to which the semiflexible description applies, it
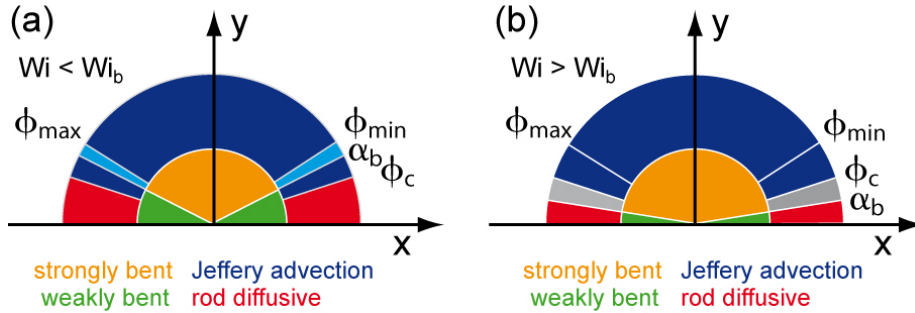
Figure 4.5: Schematics for the angular dynamics of semiflexible filaments tumbling in shear showing the critical angle ϕ_c, the buckling angle α_b and the U-turn region $[\phi_{\min}; \phi_{\max}]$. (a) For Weissenberg numbers $\mathrm{Wi} < \mathrm{Wi}_b$ the dynamics is rodlike. (b) For very high Weissenberg numbers $\mathrm{Wi} > \mathrm{Wi}_b$ the filament is strongly bent within the diffusive phase (gray region) and the dynamics resemble those of flexible polymers.

can be shown that the buckling angle α_b describing the onset of strong bending is always smaller than the minimum U-turn angle $\phi_{\min}$ (see B.6). This supports the use of the U-turn model in the angular interval $[\phi_{\min}; \phi_{\max}]$.

According to the relation between the buckling angle and the critical angle, two different regimes can be distinguished for the dynamics of the semiflexible filament (see fig. 4.5). The regimes are seperated by the Weissenberg number Wi_b at which the buckling angle equals the critical angle ϕ_c seperating advective

and diffusive phase of the Brownian rod. Wi_b is obtained as (see B.6):

$$\text{Wi}_b = 540 \left(\frac{L_p}{L_c} \right)^{3/2} . \tag{4.61}$$

A Weissenberg number $\text{Wi} < \text{Wi}_b$ implies $\phi_c < \alpha_\text{b}$, so that the interval, where the filament is only weakly bent, includes the entire diffusive phase (see fig. 4.5a). We assume that the angular dynamics in the small remaining advective intervals $[\alpha_\text{b}; \phi_\text{min}]$ and $[\phi_\text{max}; \pi - \alpha_\text{b}]$ shown in light blue can also be approximated by the stiff rod advection dynamics of Jeffery's equation. Then we can conlude, that the entire dynamics of the semiflexible polymers is equivalent to the dynamics of the Brownian rod. Consequently the average tumbling time for the semiflexible filament with $L_b < L_c < L_p$ is given by eqs. 4.43, 4.44 as

$$\tau_T = \frac{11}{3} D_\text{rod}^{-1/3} \dot{\gamma}^{-2/3}, \quad \frac{\tau_T}{\tau_r} = \frac{11 \times 2^{1/3}}{3} \text{Wi}^{-2/3} \left(\frac{D_r}{D_\text{rod}} \right)^{\frac{1}{3}}, \tag{4.62}$$

where $D_r/D_\text{rod} \approx 1$ for filaments shorter than L_p.

If the flow strength gets very high with $\text{Wi} > \text{Wi}_b$, the buckling angle becomes smaller than the critical angle. This means, that the shear forces are able to strongly bend the nearly flow aligned filament even within the diffusive phase determined for the rod (grey interval). Then, we cannot use the diffusion coefficient of the stiff rod D_rod to describe the motion in the diffusive phase. Instead, an effective diffusion coefficient depending on the average conformation of the polymer in the diffusive phase has to be used. Such a correctional term is introduced in paragraph 4.2.5 for the description of flexible polymers. Therefore, under very strong flow conditions, the semiflexible polymers can be rather described analogous to flexible polymers. Effectively, the strong shear forces reduce the lengthscale on which segments of the polymer can move independently of each other, which is usually given by the Kuhn length b_k, resp. by the persistence length L_p. In very strong flow, the shear forces thus induce $b_k^\text{eff} < b_k$. This may result in $N_k^\text{eff} > 1$ even for polymers with $L_c < L_p$, making the polymer appear more flexible.

4.2.5 *Flexible Polymers: Generalized Model Description*

For polymers with longer contour lengths $L_c > L_p$ the tumbling motion gets more complicated. Due to compressive forces and thermal fluctuations, segments of the chain can start tumbling motions independently, so that "multiple tumblings" are induced by the shear forces, which means that several U-turn runs can be performed simultaneously before a reorientation of $\mathbf{R}_\text{ee}$ is reached. Therefore, the conformations during the tumbling get more and more stochastic with increasing flexibility of the filament. This is accompanied by a growing importance of entropic effects. For flexible polymers in shear with $L_c \gg L_p$, the U-turn radius R_U typically becomes larger than the persistence length L_p indicating that mechanical bending energies are negligible with respect to the thermal energy. In the flexible limit, entropic forces dominate over the mechanic

bending forces described in the U-turn model and determine the filaments response to the flow field. The semiflexible polymers with an equilibrium end-to-end length $R_{\mathrm{ee}}^{\mathrm{eq}}$ near L_c get compressed by the shear flow, and the mechanical spring of the bent filament acts against the compression. In contrast, the random coil of a flexible filament with an end-to-end length $R_{\mathrm{ee}}^{\mathrm{eq}} \approx \sqrt{2L_p L_c}$ gets stretched by the shear forces, which act against the contractile entropic spring of the polymer.

We can extend the model description of the stiff and semiflexible regime to the flexible regime by using ensemble averaged values for the angular velocity $\dot{\phi}(\phi)$ and the length of the end-to-end vector $\mathbf{R}_{\mathrm{ee}}(\phi)$.

Advective Phase

If the flow strength is sufficiently high, there will be an advective dominated phase during the rotation of $\mathbf{R}_{\mathrm{ee}}(\phi)$. Assuming that in this advective phase the average entropic spring force acting on the ends of the polymer points into the direction of the center of mass, we can conclude that the polymer's angular and radial dynamics are decoupled in the advective phase. Thus, the end-to-end vector $\mathbf{R}_{\mathrm{ee}}$ is expected to rotate with an angular velocity given by Jeffery's equation $\dot{\phi} = \sin^2 \phi$ during the advective phase. This can be exemplified with the two limiting cases for the spring stiffness: If the deformation of the polymer is small with respect to the equilibrium conformation, the entropic spring force can be neglected. Then, the polymer ends in first order simply follow the surrounding fluid, so that $\dot{\phi}$ equals the rotational component of the shear flow. Thus, the end-to-end vector $\mathbf{R}_{\mathrm{ee}}(\phi)$ shrinks in the first quadrant $\phi \in [0; \pi/2]$ and is stretched in the second quadrant $\phi \in [\pi/2; \pi]$ of the coordinate system, while simultaneously being rotated with $\dot{\phi} = \sin^2 \phi$ (comp. with the velocity field of simple shear illustrated in fig. 4.1a). Once the entropic spring force accompanied by the extension is strong enough to stop the extension, the shear forces further align the stretched polymer in the same way as they align a stiff rod. This is accompanied by a drag of the polymer parts towards the center of mass streamline in the y-direction, which is absent during the shrinking/extension phase. However, the angular velocity is still given by Jeffery's equation, which illustrates that the advective rotational motion does not depend on the spring force.

Diffusive Phase

With increasing alignment of the polymer, the average advective forces acting on the polymer decrease. Thus we can expect the occurence of a diffusive phase around the aligned state at $\phi = 0$, where the rotational diffusion governs the dynamics of $\mathbf{R}_{\mathrm{ee}}(\phi)$. As the shear forces decrease, the entropic forces tend to recoil the polymer. Thus, a stretched polymer in the nearly flow aligned state can take several tumbling pathways:

- *recoil*: If the time spend in the diffusive phase is much longer than the polymer relaxation time $\tau_{\mathrm{diff}} \gg \tau_{\mathrm{rel}}$, the polymer completely recoils in the

diffusive phase.

- *flipping*: For $\tau_{\mathrm{diff}} \ll \tau_{\mathrm{rel}}$ the polymer will pass the diffusive phase in a stretched configuration. After passing ϕ_c, the shear forces will induce a tumbling of the stretched polymer.

- *restretch*: If $\tau_{\mathrm{diff}} \approx \tau_{\mathrm{rel}}$ are on the same order of magnitude, a partly recoiled polymer at $\phi > \pi - \phi_c$ can diffusive backwards towards $\pi - \phi_c$ into a region with higher shear forces causing a restretching of the polymer.

Due to the stochastic nature of the diffusive process, a polymer can randomly take all three pathways during the tumbling. For $\tau_{\mathrm{diff}} \ll \tau_{\mathrm{rel}}$ we assume that the diffusive process can be described by an effective average diffusion coefficient D_{diff} in the diffusive phase, which is approximately constant throughout the diffusive phase. Thus, D_{diff} neglects internal conformational changes during the diffusive phase, where the polymer has a mean-square extension $L_{\mathrm{diff}}^2 = \langle R_{\mathrm{ee}}^2(\phi = 0) \rangle$. Then, we can extend the description of the tumbling dynamics of the stiff and semiflexible regime with a symmetrical diffusive phase $[-\phi_c; \phi_c]$ to the flexible regime simply by replacing D_{rod} with $D_{\mathrm{diff}}(L_{\mathrm{diff}})$. Then, eqs. 4.39 and 4.43 give a generalized critical angle and a generalized tumbling time of

$$\phi_c = \left(\frac{D_{\mathrm{diff}}}{\dot{\gamma}} \right)^{1/3}, \qquad \tau_T = \frac{11}{3} D_{\mathrm{diff}}^{-1/3} \dot{\gamma}^{-2/3}. \tag{4.63}$$

We assume that the conformation of the stretched polymer in the diffusive phase with averaged end-to-end length L_{diff} can be approximated by the conformation of an equivalent equilibrium polymer of higher persistence length $\tilde{L}_p$ and equal contour length resulting in an equal end-to-end length $L_{\mathrm{diff}} = R_{\mathrm{ee}}(L_c, \tilde{L}_p)$. Then, we can use the approximate expression for the diffusion coefficient of polymers of all rigidities (eq. 4.23) to get:

$$D_r = D_{\mathrm{rod}} \frac{L_c^2}{L_{\mathrm{diff}}^2} \tag{4.64}$$

Thus, the generalized expression for the tumbling time of stiff, semiflexible and flexible polymers in shear flow is given as:

$$\tau_T = \frac{11}{3} D_{\mathrm{rod}}^{-1/3} \dot{\gamma}^{-2/3} \left(\frac{L_{\mathrm{diff}}}{L_c} \right)^{2/3}, \qquad \frac{\tau_T}{\tau_r} = \frac{11 \times 2^{\frac{1}{3}}}{3} \left(\frac{L_{\mathrm{diff}}}{R_{\mathrm{ee}}^{\mathrm{eq}}} \right)^{2/3} \mathrm{Wi}^{-2/3}. \tag{4.65}$$

In the latter form, our result extends the considerations in Ref. [31] for dumbbells to semiflexible chains, recovers the limits of stiff chains and the one for flexible chains under strong flows for $L_{\mathrm{diff}} = L_c$ [115], while providing in addition a novel prefactor. While L_{diff} is accessible in experiments, it is usually not reported, and could be estimated numerically based on a model such as the one for semiflexible chains [115] or via simulation.

4.3 Tumbling Dynamics of Polymers in Shear Flow: Results & Discussion

To test the theoretical considerations of the previous section, actin filaments with varying contour lengths ranging from $L_c = 3 - 40$ μm were subjected to shear flow with flowrates $\dot{\gamma} = 4 - 20\text{s}^{-1}$ in a microfluidic channel. To this purpose, a flowrate of $2\,\mu$l/h was applied to a channel with a cross section of $30\,\mu$m $\times$ $60\,\mu$m using the steady flow setup shown in fig. 2.2. A semi-automated moveable microscope stage was used to follow the fluorescently labelled filaments in the shear plane and record movies of up to 40 tumbling events for an individual filament. As the actin filaments have a persistence length of about $L_p = 16$ μm, experimental data for the tumbling dynamics and conformations in the range of rodlike ($L_c \ll L_p$) and semiflexible filaments ($L_c \approx L_p$) could be evaluated. To further test the predictions of the theoretical models in section 4.2 over the entire range of stiff to flexible polymers, additional non-equilibrium Brownian dynamics simulations (NEBD) of polymers with varying rigidity have been performed and evaluated. Furthermore, results from experiments with flexible DNA molecules in shear performed by other authors were compared to the proposed theory. The experiments with the actin filaments were performed by Markus Harasim[1], NEBD-simulations were done by Martin Kröger[2].

4.3.1 Regime I: Rodlike Polymers in Shear Flow

Fig. 4.6a shows snaphots of a short, rather stiff filament of length $L_c = 4$ μm tumbling in shear flow with $\dot{\gamma} = 5\text{s}^{-1}$ while the camera follows the filament's center of mass. The conformation of the filaments has been tracked to evaluate the time course of the angular motion $\phi(t)$ and the temporal evolution of the end-to-end vector length R_{ee} shown in Fig. 4.6 b,c for a $3\,\mu$m filament in a shear flow with $\dot{\gamma} = 7\,\text{s}^{-1}$. The filament shows no significant bending during the tumbling. This is in accordance with the theoretical prediction of eq. 4.54, which yields a buckling length of about $L_b \approx 5\,\mu$m for the actin filaments at the given experimental flow strength.

Timecourse of orientational angle $\phi(t)$

The timecourse of the end-to-end vector angle $\phi(t)$ of the tumbling $3\,\mu$m filament in fig. 4.6b shows a characteristic stairstep shape reflecting the angular dynamics of a Brownian rod in shear. Each step corresponds to a flip of the filament by π in the direction of the rotational component of the flow and thus represents one tumbling event. Starting from a flow aligned conformation in the diffusive phase, the filament performs a random walk in the orientational angle ϕ. If the random walk leads the filament into the negative ϕ direction ($\phi \in [-\phi_c; 0]$), the filament feels an increasing forward drift due to the advective drag given by Jeffery's equation 4.35. Thus, motion against the rotational component of the

---
[1] Lehrstuhl für Biophysik, Technische Universität München
[2] Dept. of Materials, Polymer Physics, ETH Zürich
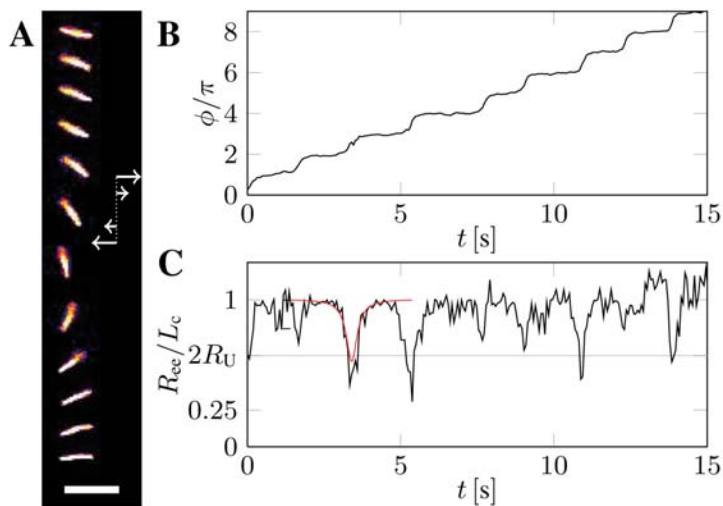
Figure 4.6: A: Snapshots of short rodlike filament of length $L_c = 4\,\mu$m tumbling in shearflow with $\dot{\gamma} = 5\mathrm{s}^{-1}$, timeline from top to bottom. B: Timecourse of the orientational angle ϕ of the end-to-end vector of a $L_c = 3\,\mu$m filament in flow with $\dot{\gamma} = 7\mathrm{s}^{-1}$. C: Timecourse of the measured end-to-end vector length $\mathbf{R}_{\mathrm{ee}}(t)$ corresponding to the filament in B. The red line shows the dip in $\mathbf{R}_{\mathrm{ee}}$ presumably caused by a azimuthal out of shear-plane motion simultaneous with the flip in ϕ-direction as predicted theoretically by eq. 4.67.

flow is hindered, and the advective forward drag acts as a reflective boundary for the diffusion at $\phi = -\phi_c$. On the other hand, a random walk leading to the positive end of the angular interval of the diffusive phase is enhanced by the advective drift. Once the filament passes the point of no return at ϕ_c, the advective drift dominates and makes it impossible for the filament to diffuse backward again, and a deterministic forward flip of the filaments orientation is initiated. Thus, the advective drift rectifies the diffusive motion of the filament leading to the overall monotonic increase of $\phi(t)$, where each of the regular shaped, steep steps corresponds to a flip with the high rotational speed of the advective phase around $\phi = \pi/2$. The flat plateaus located at multiples of π between tumblings correspond to the diffusive phase around the flow aligned state at $\phi = n\pi$, where the dynamics of the filament is governed by the rotational diffusion of the filament. The stochastic nature of the diffusive passage from $-\phi_c$ to ϕ_c is reflected in the varying length of the plateaus.

Angular Velocity $\dot{\phi}$

The recorded movies allow for a determination of the angular velocity $\dot{\phi}(\phi)$ of the tumbling filaments. The diamonds in fig. 4.7a show the resulting angular velocity of an actin filament with $L_c = 4\,\mu$m, where $\dot{\phi}(\phi)$ has been averaged over many tumbling cycles. The angular velocity predicted by Jeffery's equation 4.35

is shown as the black line for comparison. The excellent agreement between theory and experiment shows, that actin filaments with $L_c \ll L_p$ follow the dynamics of Brownian rods within the advection phase.

The relatively high number of observed tumbling events of up to 40 tumblings per filament allows to determine experimental values for the average tumbling time $\langle \tau_T \rangle$ by dividing the observed time by the number of tumbling events detected. The results for two filaments evaluated in the rodlike regime ($L_c = 3 \,\&\, 4\,\mu$m) are shown in fig. 4.8, where the normalized tumbling time is shown in dependence of the Weissenberg number Wi. The rodlike filaments are represented by the two blue diamonds with Wi $< 10^2$. In the stiff regime, the correction factor $D_r/D_{\rm rod} = (R_{\rm ee}^{\rm eq}/L_{\rm diff})^2 = 1$. The experimental values are in good agreement with the theoretical prediction from eq. 4.44 which is shown by the black line.
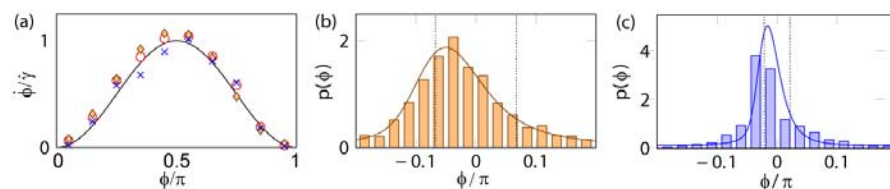
Figure 4.7: (a) Angular velocity $\dot\phi$ normalized by shearrate $\dot\gamma$ vs. orientation angle ϕ of actin filaments with lengths of $3\,\mu$m($\diamond$), $8\,\mu$m($\times$) and $16\,\mu$m($\circ$). All filaments follow the dynamics predicted by Jeffery's equation for thin rods (solid black line). (b) and (c): Probability distributions of the orientational angle ϕ in the vicinity of flow alignment at $\phi = 0$ for a $4\,\mu$m (b) and a $16\,\mu$m filament (c) at shearrate $\dot\gamma \approx 4\,$s^{-1}. The critical angles $\pm\phi_c$ and the probability distribution predicted by the theory for a stiff polymer are indicated by the dashed and solid lines.

Orientational Distribution Function

The stationary probability density function $p_{\rm stat}(\phi)$ has been evaluated experimentally and compared with the theoretical prediction derived from the Fokker-Planck equation (see. section 4.2.3). Fig. 4.7b shows the experimental orientational distribution of a tumbling filament with length $L_c = 4\,\mu$m (histogram) and the theoretical function for $p_{\rm stat}(\phi)$ (solid line) around the flow aligned state. The diffusive angular interval $[-\phi_c; \phi_c]$ as calculated by eq. 4.39 is indicated by the dashed vertical lines confirming that the center of the orientational distribution function lies approximately at $-\phi_c$. The sharp peak of the probability density function at ϕ_c in the vicinity of $\phi = 0$ shows that the filaments are strongly aligned by the shear flow. The high degree of alignment corresponds to the plateaus of $\phi(t)$ in fig. 4.6. The filament spends most of its time in the shear flow near $\phi = 0$.
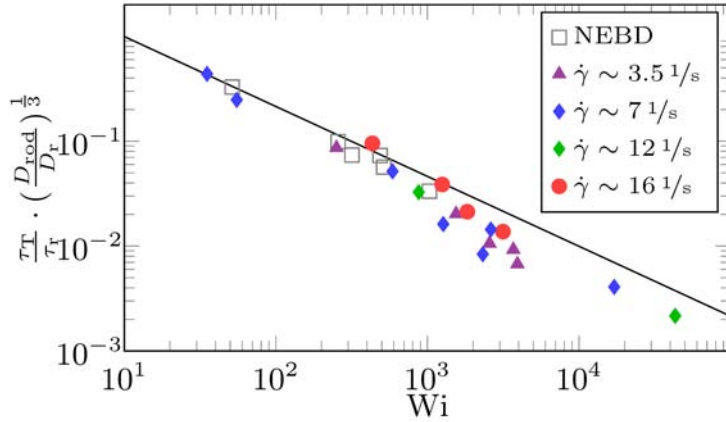
Figure 4.8: Normalized tumbling times of actin filaments in shear in dependence of the Weissenberg number Wi. Data spans actin with contour lengths $L_c = 3 - 40\,\mu$m, different shear rates are indicated by color. For comparison, non-equilibrium Brownian Dynamics simulations for filaments with different rigidities have been performed (squares). Measured tumbling times are in good agreement with the theoretical prediction of the model (solid line).

Azimuthal Motion

Although the snapshots of the polymer conformations in fig. 4.6a do not show a pronounced bending of the filament during the tumbling, the evaluation of the end-to-end vector length in Fig. 4.6c shows some significant dips in the normalized end-to-end length R_{ee}/L_c occuring simultaneously with the flipping of the end-to-end vector. Rather than indicating a bending of the filament, these dips can be attributed to a non-negligible azimuthal angle of the filament occuring around $\phi = \pi/2$. Due to the short length of the filament, a filament with an azimuthal angle $\theta \neq 0$ appears as projected onto the focal plane of the microscope, which is the shear plane xy. As described in section 4.2.3, a Brownian rod which is not perfectly aligned with the shear plane performs a kayaking-like motion, where the trajectory of the azimuthal angle θ is given by eq. 4.52. Taking the starting point of the advective motion at the critical angle $\theta(t = t_0) = \theta(\phi_c)$ we can use the derived value for the mean-square azimuthal angle $\langle \theta^2(\phi_c) \rangle = 2\phi_c^2$ to calculate the expected mean-square value for the azimuthal angle at $\phi = \pi/2$ and get:

$$\tan[\theta(\phi = \pi/2)] = \tan[\sqrt{2}\phi_c]\frac{1}{\sin\phi_c} \tag{4.66}$$

With $\phi_c \ll 1$ we can use $\tan[\sqrt{2}\phi_c] \approx \sqrt{2}\phi_c$ and $\sin\phi_c \approx \phi_c$. Simple geometrical considerations lead to the result that the timecourse of the projected, normalized

length $\langle L_c^{xy} \rangle / L_c = \cos[\theta(t)]$ should follow

$$\frac{L_c^{xy}(t)}{L_c} = \sqrt{\frac{1 + (\dot{\gamma}t)^2}{3 + (\dot{\gamma}t)^2}}, \tag{4.67}$$

where $t = 0$ corresponds to the conformation with $\phi = \pi/2$. Thus, the minimum length at the flip is predicted as

$$L_c^{xy}(t = 0)/L_c = \sqrt{1/3} \approx 0.58. \tag{4.68}$$

The red line in fig. 4.6c shows the timecourse $L_c^{xy}(t)$ during a flip predicted from eq 4.67 for $\dot{\gamma} = 7\,\text{s}^{-1}$ in good agreement with the observed dips in the measured values for $\mathbf{R}_{ee}$. To further test the theoretical predictions for the azimuthal
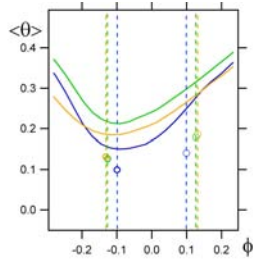
Figure 4.9: Solid lines: NEBD-simulation data showing the averaged azimuthal angle $\sqrt{\langle \theta^2(\phi) \rangle}$ for filaments with rigidities of $L_c/L_p \sim 0.3$, Wi ~ 440 (blue), $L_c/L_p \sim 2.3$, Wi ~ 250 (green) and $L_c/L_p \sim 28$, Wi ~ 42 (yellow) in shear flow. Theoretical predictions from eq. 4.51 are shown by the open circles.

motion, data for the azimuthal angle θ of nonequilibrium Brownian dynamics (NEBD) simulations of filaments with varying rigidities has been evaluated. Fig. 4.9 shows $\sqrt{\langle \theta^2(\phi) \rangle}$ in the vicinity of $-\phi_c$, where the theory predicts a minimum for the average azimuthal angle. The comparison of the NEBD simulations with the predicted values of $\sqrt{\langle \theta^2(-\phi_c) \rangle} = \phi_c$ and $\sqrt{\langle \theta^2(\phi_c) \rangle} = \sqrt{2}\phi_c$ shown by the open circles confirms the location of the predicted minimal azimuthal angle at $-\phi_c$ for the studied filaments ranging from stiff ($L_c/L_p \sim 0.1$, blue line), to semiflexible ($L_c/L_p \sim 1$, green) and rather flexible filaments ($L_c/L_p \sim 10$, yellow). Both the minimum value at $\phi = -\phi_c$ and the estimated value at $\phi = \phi_c$ are higher than predicted. For $\phi = \phi_c$ this could be caused by the neglected positive drift for θ^2 in the interval $[0; \phi_c]$. Obviously, further work is necessary to quantitatively understand the azimuthal dynamics in the diffusive phase.

4.3.2   Regime II: Semiflexible Polymers in Shear Flow

Conformation and Dynamics

Fig. 4.10a shows the timecourse of the conformations during a tumbling event for two actin filaments of $L_c = 8\,\mu\text{m}$ and $L_c = L_p = 16\,\mu\text{m}$ length. Both filaments exhibit the typical U-turn motion of the tumbling during the advective phase. For $\phi \in [-\pi/2; 0]$, the filament gets stretched by the frictional forces, so that bending fluctuations get damped. In contrast, for $\phi \in [0; \phi_c]$, the filament gets compressed, and bending fluctuations in a filament with near straight conformation are enhanced. Once the end-to-end vector of the filament passes
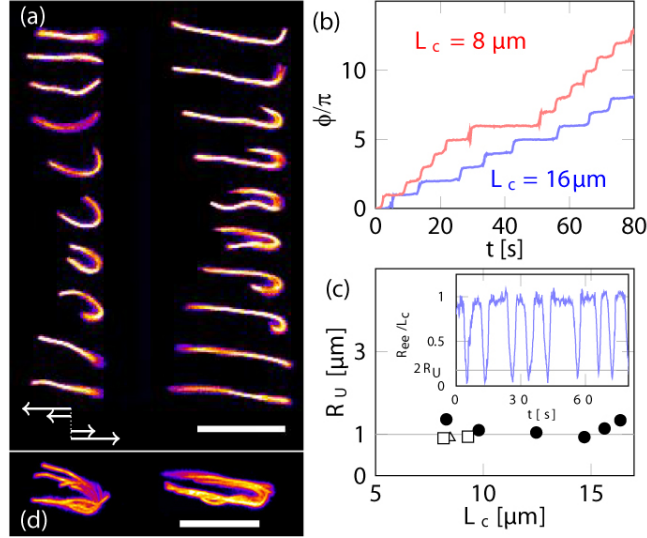
Figure 4.10: (a) Successive images of two fluorescently labelled actin filaments of length $L_c = 8\,\mu$m and $16\,\mu$m in a shear flow with $\dot{\gamma} = 6\mathrm{s}^{-1}$. The direction of the shear is indicated by the arrows, the scale bar is $10\,\mu$m. (b) Timecourse of the normalized orientational angle $\phi(t)/\pi$ of the end-to-end vector $\mathbf{R}_{\mathrm{ee}}(t)$. (c) Mean curvature radius R_{U} of the filament's U-turn conformation vs. contour length L_c for shear rates of 6 (filled circles), 12 (squares) and $19\,\mathrm{s}^{-1}$ (triangles). Inset: Timetrace of normalized end-to-end vector length R_{ee}/L_c corresponding to the $\phi(t)$ trace of the $L_c = 16\,\mu$m filament shown in (b). (d) Overlay of the conformations in (a) illustrating the filament motion on a U-turn track with approximately constant radius during the tumbling.

the point of no return at ϕ_c, a tumbling motion is induced. Depending on the initial asymmetry of the associated bending fluctuation, either the front or the back end of the filament becomes the leading end in the tumbling. In the center of mass system, the filament performing a flip of π in the end-to-end vector angle resembles a train running on a U-turn track. The timecourse $\phi(t)$ (fig. 4.10b) shows the same characteristic stairsteps with stochastic plateaus around multiples of π as discussed for regime I. The corresponding timetrace of the end-to-end vector length shown in the inset of fig. 4.10c exhibits sharp dips associated with the strongly bent U-turn conformation in the advective phase.

Advective Phase: U-turn model

The overlay of the conformations in the different stages of the tumbling in fig. 4.10d shows, that the radius of the U-turn R_{U} is approximately constant throughout the U-turn. This motivates the approximation of the filament's con-

formations in the strongly bent state with the U-turn model described in section 4.2.4, which enables an analytical solution of the dynamics via a forcebalance between the frictional forces and the elastic bending forces in the filament. The theoretical conclusions can now be compared with the experimental observations. Note that the experimental stadium tracks are slightly tilted, which is neglected in the theoretical framework.

The model predicts R_{U} to be independent of the filament length and only weakly dependent on the shear rate $R_{\mathrm{U}} \sim \dot{\gamma}^{-1/4}$ with $R_{\mathrm{U}} \approx 1.1\mu$m for actin filaments exposed to the experimental shearrates. As the stadium width of the model is determined by $\Delta y = 2R_{\mathrm{U}}$, the experimental U-turn radius has been evaluated as half of the average maximum y-extension of the filament during the tumbling. Fig. 4.10c shows that the experimental values of R_{U} for various contour lengths L_c are in good agreement with the theoretical prediction confirming the independence of R_{U} on the contour length. Note that the theoretical value $R_{\mathrm{U}} \approx 1.1\mu$m does not contain any fitting parameter and is solely based on the known diameter of the actin filaments, the experimentally determined shear rate and the buffer viscosity.

The constant track velocity v derived in the force-balance calculation predicts an end-to-end vector angular dynamics following Jeffery's equation 4.35 for thin rods. The averaged angular velocity $\dot{\phi}(\phi)$ for two filaments of 8μm and 16μm is shown in fig. 4.7a in excellent agreement with the theory. The U-turn model also gives an analytical solution for the dynamics of the end-to-end vector length $R_{\mathrm{ee}}(t)$ (see appendix, B.6). In the interval $[\phi_{\min}; \phi_{\max}]$ the track velocity v predicts the timecourse of the end-to-end vector length to follow (eq. B.152)

$$R_{\mathrm{ee}}(t) = 2R_U \sqrt{1 + (\dot{\gamma}t)^2}, \tag{4.69}$$

where $\phi(t = 0) = \pi/2$ has been chosen. Fig. 4.11 shows the experimental $R_{\mathrm{ee}}(t)$ timetraces of filaments with different contour lengths in good agreement with the model predictions. Together with the angular dynamics, the U-turn model thus describes the full dynamics of the end-to-end vector of semiflexible polymers in shear flow by a telescopic Brownian rod model.

Diffusive Phase and Tumbling Time

The presented experimental data shows, that the advective dynamics of the semiflexible filaments are described by Jeffery's equation derived for the advection of stiff rods. As the conformation of the semiflexible filaments is nearly rodlike within the diffusive phase, also the dynamics in the diffusive phase should be comparable to those in the stiff regime. Thus, the entire angular dynamics of tumbling semiflexible filaments should be equivalent to those of stiff rods with the same contour lengths, so that eq. 4.43 should be valid in both regimes. The experimentally determined tumbling times are shown in fig 4.8. For equal shear rates, longer filaments correspond to higher Weissenberg numbers Wi. Comparison with the theoretical prediction (dashed line) shows a fairly well agreement between the experimental data and the model.
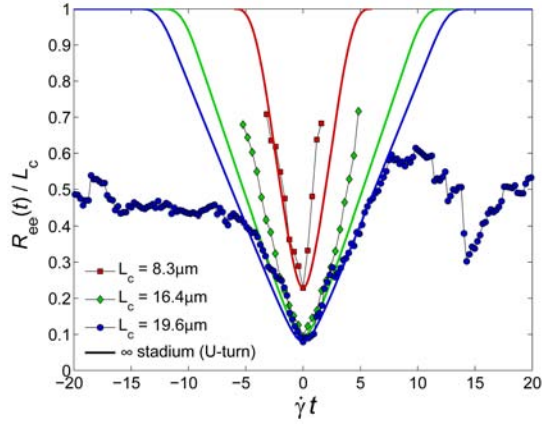
Figure 4.11: Experimental data for the reduced end-to-end distance $R_{\text{ee}}(t)/L_c$ vs. reduced time $\dot{\gamma}t$. The solid lines show the theoretical prediction following from the telescopic Brownian rod model.

Orientational Distribution Function
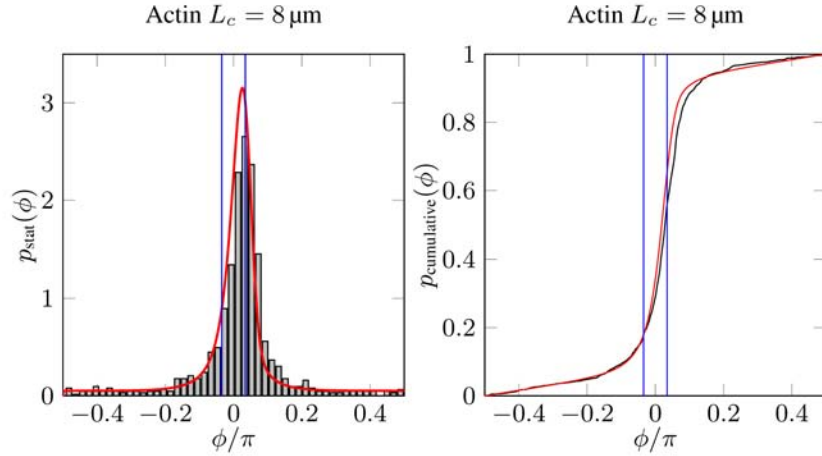
Figure 4.12: (a) Measured stationary orientational distribution function $p_{\text{stat}}(\phi)$ is shown for a semiflexible actin filament with $L_c = 8\,\mu\text{m}$ in shear. Good agreement with the theoretical curve calculated for a stiff Brownian rod (solid line) is observed. The theoretical critical angle $\pm\phi_c$ is indicated by the vertical lines. (b) Cumulative plot of the data in (a).

The experimentally determined orientational distribution function for a semi-flexible filament with length $L_c = 8\mu\text{m}$ is shown in fig. 4.12a. As suggested by the equivalence in the angular dynamics, the stationary probability density function is in accordance with the Brownian rod model curve shown in red. The maximum of p_{stat} is in good agrement with the predicted position at ϕ_c (the direction of shear was reversed in this experiment). The diffusive interval $[-\phi_c;\phi_c]$ is indicated by the vertical blue lines. The cumulative plot in fig. 4.12b shows

that the experimental distribution is in accordance with the theoretical calculation in the entire angular interval $[-\pi/2; \pi/2]$. For long semiflexible filaments, the measured distribution starts to deviate from the theoretical curves, as can be seen in the data for a $16\,\mu$m filament shown in fig. 4.7c.

Multiple U-turns for $L_c > L_p$

For long filaments with $L_c > L_p$, the measured tumbling times in fig 4.8 tend to be a bit shorter than theoretically predicted. These filaments belong to a regime, where several U-turn motions can occur simultaneously during the tumbling. With increasing contour length L_c, thermal fluctuations may disalign the flow aligned sections of the filament during the U-turn motion. Compressive forces occuring in the rear part of the filament (see eq. B.135) can further reinforce fluctuations. Such independent fluctuations of parts of the filament may induce more than one U-turn runs to be started simultaneously, where the turns can propagate separately through the filament. Such multiple tumblings can be induced at the ends of the filament as well as in the middle, so that even loop formations may occure. Fig. 4.13 exemplarily shows one of the many conformational pathways the filament can take for a complete reversal of the end-to-end vector. Despite this complex behaviour, the averaged dynamics in the advective phase still follows Jeffery's equation and the overall tumbling time is in reasonable agreement with eq. 4.43. A change in the scaling from
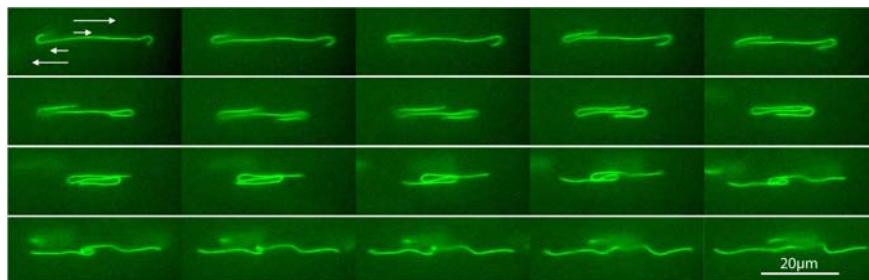
Figure 4.13: Snapshots of tumbling $L_c = 40\,\mu$m actin filament showing multiple simultaneous U-turn motions characteristic for the $L_c > L_p$ regime. The velocity gradient direction is indicated by the arrows. With increasing length, the number of possible pathways for an end-to-end reversal drastically increases.

$\tau_T \sim \mathrm{Wi}^{-2/3}$ to $\tau_T \sim \mathrm{Wi}^{-0.8}$ has been found in simulations of flexible polymers for the regime of high Peclet-numbers, where Kuhn segments start to tumble individually [24]. This suggests, that the observed shorter tumbling times at $\mathrm{Wi} \gg 1$ where the multiple tumbling sets in, could correspond to a similar scaling change. Clearly, further investigations are necessary to gain a deeper insight into the mechanisms governing the polymer dynamics in the transition regime from semiflexible to truly flexible filaments.

4.3.3 Regime III: Flexible Regime, $L_c \gg L_p$

In the truly flexible regime, the contour length is much higher than the persistence length and the polymers are dominated by entropy rather than by mechanical elastic bending energy. Consequently, for typical shearrates reached in experiments, the calculated bending radius is bigger than the filaments persistence length indicating the negligibility of the bending energies (e.g. for DNA with $L_c = 80\,\mu$m and $L_p = 50$ nm in the experiments in [106], $R_{\mathrm{U}} \sim 150$ nm).

However, the theoretical treatment for the stiff and semiflexible regime can be extended to the flexible regime by assuming an effective diffusion coefficient D_{diff} in the diffusive phase, based on the asumption that the polymer relaxation time is larger than the time spent in the diffusive phase (see section 4.2.5). Then, a unified description for the entire regime of rigidity from stiff to fully flexible can be given by equation 4.65:

$$\frac{\tau_T}{\tau_r} = \frac{11 \times 2^{\frac{1}{3}}}{3} \left(\frac{L_{\mathrm{diff}}}{R_{\mathrm{ee}}^{\mathrm{eq}}}\right)^{2/3} \mathrm{Wi}^{-2/3}$$

This general formula for the tumbling time was tested with simulated data of nonequilibrium Brownian dynamics simulations with rigidities ranging from $L_c/L_p \approx 0.1 - 60$. The resulting tumbling times are shown by the open squares in fig. 4.14 and are in good agreement with the theoretical prediction (dashed line). The diffusive length was evaluated as $L_{\mathrm{diff}}^2 = \langle R_{\mathrm{ee}}^2(\phi = 0)\rangle$. Additionally, experimental data for flexible polymers from Gerashchenko et al.[31] (blue squares) and Teixeira et al. [106] (DNA, green triangles: 22 μm, red triangles: 80 μm) is shown, demonstrating the excellent agreement with eq. 4.65. The experimental data from the actin filaments is shown by the gray circles for comparison.

The extension of the tumbling time formula to the flexible regime was based on the assumption that $\tau_{\mathrm{diff}} < \tau_{\mathrm{rel}}$. The relaxation time of the polymer is on the order of the rotational relaxation time τ_r, so that with $\tau_{\mathrm{diff}} = 5/11\tau_T$ we can estimate the assumption to be fulfilled for $\tau_T/\tau_r < 2$. Due to the absence of data for L_{diff} for the DNA data, the correctional factor $(R_{\mathrm{ee}}^{\mathrm{eq}}/L_{\mathrm{diff}})^{2/3}$ was calculated by assuming an average stretch of $L_{\mathrm{diff}} = 0.75L_c$ in the diffusive phase, which yields a correctional factor of about 0.16 and 0.1 for the 22 μm and the 80 μm DNA. Thus, $\tau_{\mathrm{diff}} < \tau_{\mathrm{rel}}$ should be fulfilled for data points with values below 0.32 resp. 0.2 for the 22 μm and the 80 μm DNA (green and red triangles). This implies that more than half of the DNA data points do not fulfill $\tau_{\mathrm{diff}} < \tau_{\mathrm{rel}}$ while still obeying eq. 4.65 surprisingly well. For data points with Wi < 10, the assumed extension in the diffusive phase $L_{\mathrm{diff}} = 0.75$ is certainly too high. With $L_{\mathrm{diff}} \to R_{\mathrm{ee}}^{\mathrm{eq}}$ for Wi $\to 1$, the data points are expected to be shifted increasingly upwards with decreasing Wi if the real (unfortunately unavailable) values for L_{diff} had been used. These higher values reflect the transition to the $\tau_T \sim \mathrm{Wi}^{-1}$ scaling expected from eq. 4.31 for undeformed polymers at low Wi. However it should be noted, that for Wi < 1 the rectifying nature of the shear flow for the rotational diffusion as well as the alignment of the end-to-end vector with the shear plane is lost, so that in the 3-dimensional case the tumbling time is

no longer reasonably defined. Nonetheless, the agreement between data with $\mathrm{Wi} \gg 1$ and the theory supports the validity of the model, yet more detailed analysis of experimental and simulated polymers in shear needs to be done particularly in the flexible regime to fully unravel the dynamic behaviour.
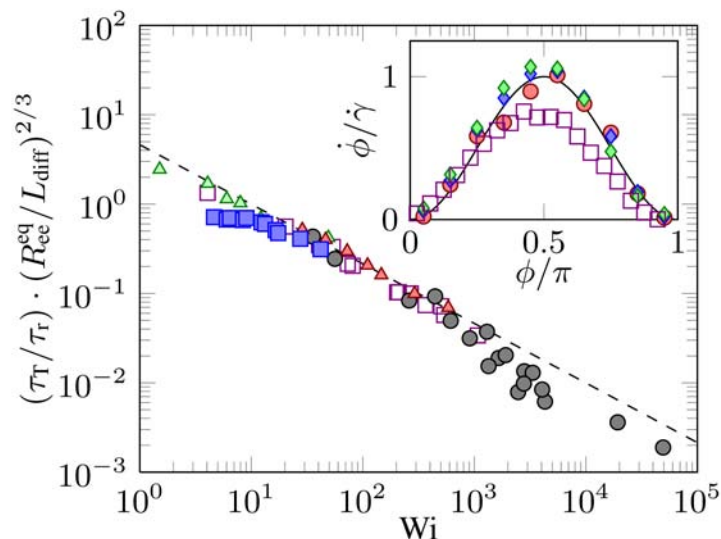
Figure 4.14: Dimensionless tumbling times τ_T/τ_r multiplied by $(R_{ee}^{eq}/L_{diff})^{2/3}$ for flexible DNA molecules. Blue squares denote experimental data extracted from Gerashchenko *et al.* [31], and green and red triangles denote experimental DNA data for a $22\,\mu$m and $80\,\mu$m DNA extracted from Teixeira *et al* [106]. For the extracted data the diffusive length L_{diff} is assumed to be $0.75L_c$. Experimental data of fig. 4.8 for stiff and semiflexible actin is shown by the grey circles. Open squares denote simulated data points of nonequilibrium Brownian dynamics simulations where $L_{diff}^2 = \langle R_{ee}^2(\phi = 0)\rangle$ was used for the simulation data with different flexibilities and shearrates. The tumbling times for the different shear rates fall onto a master curve (dashed line), following the theoretical prediction, eq. 4.65. **Inset**: Angular velocity $\dot{\phi}$ vs. orientation angle ϕ of simulated flexible filament data (violet open squares). The actin data of fig. 4.7a is shown for comparison ($3\,\mu$m: green diamonds, $8\,\mu$m: blue diamonds, $16\,\mu$m: red circles). There is a first order agreement with the Jefferey dynamics (solid line) for the simulated flexible filament, but the deviation from theory is higher than for the experimental data.

4.4 Microscopic Origin of Non-Newtonian Properties

The findings about the dynamics and conformations of polymers in shear flow now enable us to give qualitative explanations for bulk phenomena such as

shear thinning, drag reduction and viscoelastic effects observed in dilute poly-
mers solutions. To understand how these macroscopical properties are linked to
the microscopical dynamics of the individual polymers, we start discussing the
simple case of thermal Brownian rods. A one-dimensional Brownian dynamics
simulations based on the Langevin equation 4.41 was performed to study the
dynamics over a wider range of flow strengths Wi as possible in the experiments
with actin filaments. The $\phi(t)$ trajectories of the simulations with Weissenberg
numbers Wi $\gg 1$ exhibit the same characteristic stairstep shape with stepheight
π and stochastically varying plateau lengths as observed for the rodlike actin
filaments. Fig. 4.15a-e shows the obtained orientational distribution functions
of the simulated rods in a range of Wi $= 0.1 - 1000$ (blue lines). While in weak
flow the distribution function is near constant indicating an almost completely
random orientation of the rods, a peak in $p_{\mathrm{stat}}(\phi)$ emerges for Wi > 1. For
higher flow strengths, the peak gets sharper and its center approaches $\phi = 0$.
The critical angle is written in terms of Wi as $\phi_c = 2^{-1/3}\mathrm{Wi}^{-1/3}$ (see eq. 4.39)
and is indicated by the vertical red lines in fig. 4.15. The peak center position
can be identified with $-\phi_c$ for suffiently strong flows with Wi $\gg 1$.
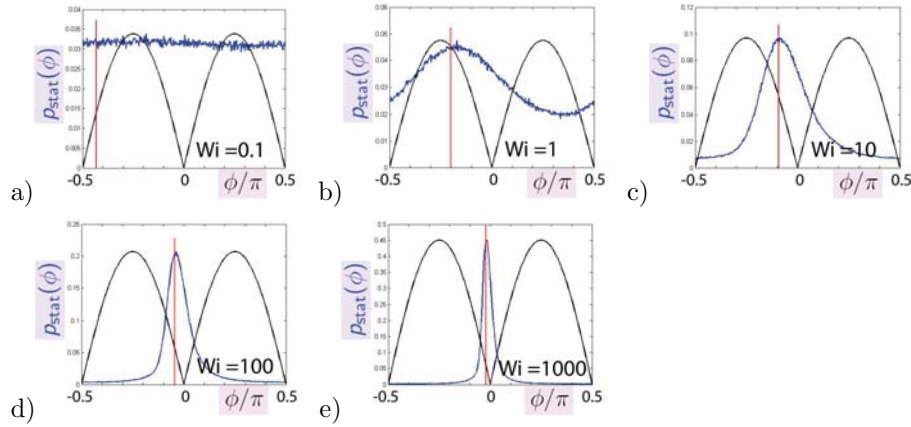
Figure 4.15: Stationary orientational distribution of a stiff Brownian rod in a
1-D simulation for different Weissenberg numbers Wi $= 0.1 - 1000$ (blue). The
vertical red line indicates $-\phi_c$ as calculated by eq. 4.39. The black line shows
the functional form of $\sin\phi\cos\phi$, which is proportional to the friction at the
rod. With increasing Wi, the increasing alignment towards $\phi_c \ll 1$, the rod
predominantly spends its time in a region of low frictional dissipation, which
can explain shear-thinning observed in solutions with rods.

Shear-Thinning in Dilute Polymer Solutions: Stiff Regime

The energy dissipation rate p_V of the amount of energy per time and unit volume dissipated in a viscous, simple shear flow can be calculated by

$$p_V = \sigma \dot{\gamma}, \tag{4.71}$$

where σ is the shear stress in the fluid. With $\sigma = \eta \dot{\gamma}$, we can relate the shear viscosity with the energy dissipation rate as

$$\eta = \frac{p_V}{\dot{\gamma}^2} \tag{4.72}$$

The steady state shear viscosity of dilute polymer solutions is determined by the solvent viscosity η_s and the viscosity contribution η_{pol} linked to the dissipation caused by friction between the polymer and the surrounding fluid. With C denoting the concentration of polymers in a dilute solution, where we neglect intermolecular hydrodynamic interactions between the individual polymers, we can thus calculate the polymer contribution to the viscosity from the energy dissipated per time P at a single polymer :

$$\eta_{\mathrm{pol}} = \frac{C \langle P \rangle}{\dot{\gamma}^2}. \tag{4.73}$$

Here, $\langle P \rangle$ is the ensemble average over all polymers in the solution, resp. the time average of a single polymer. As the thermal motion of the polymer does not contribute to the dissipation, η_{pol} is related to the occuring friction due to the advective part of the polymer motion. We can thus relate the local microscopic advective friction forces $F_{\mathrm{frict}}(\phi)$ and the orientational distribution function p_{stat} to the bulk shear viscosity. The energy dissipation rate $\mathrm{d}P$ of a polymer section of length $\mathrm{d}\sigma$ is given as

$$\mathrm{d}P(\phi) = f_{\mathrm{frict}}(\phi, \sigma) \mathrm{d}\sigma v_{\mathrm{rel}}(\phi, \sigma) = c_L v_{\mathrm{rel}}^2 \mathrm{d}\sigma \tag{4.74}$$

so that the molecular energy dissipation rate is obtained as

$$P(\phi) = \int_0^{L_c} \mathrm{d}P = \int_0^{L_c} c_L v_{\mathrm{rel}}^2(\phi, \sigma) \mathrm{d}\sigma. \tag{4.75}$$

to finally yield

$$\langle P \rangle = \int_0^\pi p_{\mathrm{stat}}(\phi) P(\phi) \mathrm{d}\phi. \tag{4.76}$$

In the case of stiff rods in shear, the frictional forces occur only tangential to the rod and are given by eq. 4.33, so that the friction at the rod is strongly depending on its orientation:

$$f_{\mathrm{frict}}(r, \phi) = c_\parallel v_{\mathrm{rel}} = c_\parallel r \dot{\gamma} \sin \phi \cos \phi \tag{4.77}$$

where $r = \sigma - L_c/2$ is the local distance to the center of mass of the rod with $\sigma \in [0; L_c]$. This orientational dependance of the friction is shown by the black

lines in fig. 4.15. It is immediately evident that with the flow strength getting bigger, the increasing alignment concentrates the rods more and more in a region of less frictional dissipation. Consequently, the steady state shear viscosity $\eta(\dot{\gamma})$ of dilute stiff rod solutions is expected to drop with increasing flowrate. Indeed, dilute solutions of rigid rod-like molecules like the tabac mosaic virus exhibit a shear-thinning of the steady state viscosity[112].

The energy dissipation rate at the rod is obtained as

$$P(\phi) = 2 \int_0^{L_c/2} (\dot{\gamma} r c_\| \sin\phi\cos\phi)^2 \mathrm{d}r = \frac{1}{6} c_\| \dot{\gamma}^2 L_c^3 \sin^2\phi\cos^2\phi. \qquad (4.78)$$

For weak flows $\mathrm{Wi} \ll 1$, the rods are equally distributed in their orientation (see fig. 4.15), making $p_\mathrm{stat}(\phi) = \mathrm{const}$. Thus, we can conclude, that the zeroshear viscosity contribution of the rods $\eta(\dot{\gamma} = 0) = \eta_0$ should rise with increasing length of the rods as $\eta_\mathrm{polym} \sim L_c^3$. For solutions with equal weight per volume (w/v) concentrations of polymers, this indicates a quadratic increase of η_0 with polymer length.

Eq. 4.78 allows for an estimation of the polymer contribution to the overall friction in dilute solution. We assume that hydrodynamic interactions are negligible if the concentration of the stiff polymers does not exceed one stiff polymer of length L_c in a volume of L_c^3. The dissipation of the background solvent is given by eq. 4.72 as $P_\mathrm{solv} = \eta \dot{\gamma}^2 L_c^3$. With the friction coefficient from eq. 4.29 we can thus calculate the ratio of dissipated energy at the rod in comparison to the energy dissipated in the sheared solvent as

$$\frac{P_\mathrm{rod}}{P_\mathrm{solv}} = \frac{c_\| \sin^2\phi\cos^2\phi}{6\eta} \approx \frac{\sin^2\phi\cos^2\phi}{\ln(L_c/d)} \ll 1 \qquad (4.79)$$

As the rod spends about half of the tumbling time in the diffusive phase nearly flow aligned, the viscosity contribution of thin rods in dilute solution will be small compared to the solvent viscosity and we cannot expect to measure large non-Newtonian effects. Nevertheless its worthwhile discussing the basic effects of flow alignment and deformation in the simple case without hydrodynamic interactions, although a direct experimental quantification is difficult in the dilute regime.

For $\dot{\gamma} > 0$, the alignment increases with increasing filament length, because the critical angle scales as $\phi_c \sim L_c^{-1}$. The ratio of time spent in the diffusive and advective phase $\tau_\mathrm{diff}/\tau_\mathrm{adv} = 5/6$ is independent of L_c, so that the stationary probability density function p^adv in the advective phase can be approximated by $\frac{3}{11}\frac{\phi_c}{\sin^2\phi}$. [3] Thus, the higher friction $P(\phi)$ for longer rods is partly compensated by the higher alignment, predicting $\eta_\mathrm{pol} \sim \dot{\gamma}^{-1/3} L_c$ for solutions of equal (w/v) concentrations.

---

[3] The probability density in the advective phase is approximatly proportional to the inverse of $\dot{\phi}(\phi)$: $p^\mathrm{adv} \sim \sin^{-2}\phi$[115]. With $\int_{\phi_c}^{\pi-\phi_c} p_\mathrm{stat}^\mathrm{adv} = 6/11$ we get $p_\mathrm{stat}^\mathrm{adv} \approx \frac{3}{11}\frac{\phi_c}{\sin^2\phi}$.

Shear-Thinning in Dilute Polymer Solutions: Semiflexible Regime

If the frictional forces are strong enough to bend the rods onto the U-turn track of the tumbling semiflexible filament, the dissipation is reduced. The force-balance model derived in section B.6 yields a relative velocity between the dominating straight parts of the filament and the fluid of $v_{\mathrm{rel}} \sim \dot{\gamma} R_{\mathrm{U}}^2 / L_c$ (see eq. B.131) which is approximately constant throughout the U-turn and along the filament. This corresponds to a dissipation of

$$P = c_{\|} L_c v_{\mathrm{rel}}^2 \sim c_{\|} \dot{\gamma}^2 R_{\mathrm{U}}^4 / L_c \sim \dot{\gamma} k_B T \frac{L_p}{L_c} \qquad (4.80)$$

during the U-turn motion $\phi \in [\phi_{\min}; \phi_{\max}]$. Thus, by bending the rod into a stripe of width $2R_{\mathrm{U}}$, the frictional dissipation is reduced from a term of the order $c_{\|} \dot{\gamma}^2 L_c^3$ for the straight rod to a term on the order of $c_{\|} \dot{\gamma}^2 R_{\mathrm{U}}^4 / L_c$ for the bent rod. Due to this additional reduction of the dissipation, the shear-thinning caused by the alignment effects discussed for the stiff rods is further increased. Therefore, dilute solutions of semiflexible polymers with contour length L_c should exhibit a more pronounced shear thinning than solutions with an equal concentration of stiffer polymers of the same length. Indeed, a reduced viscosity for semiflexible filaments in shear compared to stiff filaments of the same length is found in simulations of non-thermal dilute suspensions of rods [118].

The result for the energy dissipation rate in eq. 4.80 is somewhat puzzling. It implies the rather counterintuitive finding, that during the U-turn phase a longer filament dissipates less frictional energy than a shorter one. This is reflected in the independence of the U-turn radius on the filament length L_c, which has been directly observed in the experiments in fig. 4.10c: A bending radius independent of the filament length suggests that the bending forces exerted by the flow-aligned straight parts of the filament are independent of L_c, meaning that for $L_c \gg \pi R_{\mathrm{U}}$ the frictional force per unit length f along the flow aligned parts of the filament scales with $f \sim 1/L_c$. The frictional force is proportional to the relative velocity of the surrounding fluid v_{rel}, whereas the energy dissipation rate P in turn scales with $L_c v_{\mathrm{rel}}^2$ resulting in the observed $P \sim 1/L_c$ proportionality. This is in strong contrast to the rising dissipation for tumbling stiff rods $P \sim L_c^3$. Obviously, the U-turn motion helps to keep large parts of the filament aligned with the fluid, which reduces the friction. The higher the fraction of aligned parts of the filament is, the less energy is being dissipated. However, this unusual implication is restricted to the small regime of $L_b < L_c < L_p$. For longer contour lengths $L_c > L_p$, the filament segments tumble independently. As the obserevd U-turn radius for multiple tumblings is comparable to R_{U} in single tumbling, this means that the dissipated energy on average rises linearly with the number of involved U-turns and thus with contour length L_c.

The unusual prediction for the length dependence of the dissipation implies that the U-turn model might be oversimplified for quantifying the shear viscosity correctly. All the more, these considerations show the importance of microscopic models to unravel the macroscopic bulk features of complex solutions and the need for further investigations.

Shear-Thinning in Dilute Polymer Solutions: Flexible Regime
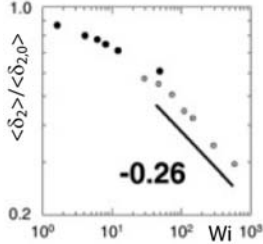
Figure 4.16: Mean polymer thickness $\langle \delta_2 \rangle$ in velocity gradient direction of DNA in shear normalized by equilibrium thickness $\langle \delta_{2,0} \rangle$ in dependence of the Weissenberg number. The contour length of the DNA is $22\,\mu$m (black circles) and $80\,\mu$m (open circles), graph taken from [106]. In strong flow, the thickness scales as $\mathrm{Wi}^{-1/4}$.

For flexible polymers in shear, a confinement into a small strip in the y - direction of the shear gradient similar to the U-turn track of semiflexible filaments is observed. The average extension δ_2 in the gradient direction of $80\,\mu$m DNA in shear was found to scale with $\delta_2 \sim \mathrm{Wi}^{-0.26}$ for higher shear rates (see fig. 4.16). Thus, a shear thinning comparable to that of semiflexible polymers is expected for dilute solutions of flexible polymers as well. Note that the experimentally observed exponent for δ_2 of -0.26 coincides with the exponent of the U-turn radius $R_\mathrm{U} \sim \mathrm{Wi}^{-1/4}$, which gives the scaling of the shear gradient extension in the U-turn model for the semiflexible filament. This scaling can be theoretically rationalized by a simple model: We assume that the shear deformed polymer conformation can be decomposed into several undisturbed random walks on a small lengthscale, analogous to a Pincus-blob representation of the polymer [22]. The maximum length l of the undisturbed chain in random walk conformation is assumed to match the length of a Rouse chain with a relaxation time matching the inverse of the shear rate:

$$\tau_\mathrm{rel}^l = \frac{c_\perp L_p l^2}{12 k_B T} = \dot{\gamma}^{-1} \tag{4.81}$$

where we used the Rouse relaxation time τ_rel^l given by eq. 4.19. Thus, the length of the undisturbed chain portion for a polymer in flow is given as

$$l = \sqrt{\frac{12 k_B T}{c_\perp L_p \dot{\gamma}}} = \sqrt{\frac{2 D_\mathrm{rod}}{\dot{\gamma}} \frac{L_c^2}{R_\mathrm{ee}^2}} L_c = L_c \mathrm{Wi}^{-1/2} \tag{4.82}$$

where eq. 4.23 was used for the last step to yield the dependence of the length of the random walk section of the polymer on the Weissenberg number. The dimension of the polymer in shear gradient direction can then be estimated by the radius of gyration of the random walk section of length l as

$$\delta_2 \sim \sqrt{\frac{2 L_p l}{6}} = R_g^\mathrm{eq} \mathrm{Wi}^{-1/4}. \tag{4.83}$$

Thus, both the theory for semiflexible and flexible filaments predicts a $\mathrm{Wi}^{-1/4}$ dependence of the lateral polymer extension, which implies comparable shear thinning properties for the bulk steady state viscosity in dilute solutions.

In summary, the properties of the shear flow allow the shear forces to align the polymers with the flow and elastically deform them. Both effects lead to a decrease of the average extension of the polymers in the flow gradient direction, which reduces the frictional forces. Therefore, dilute solutions of linear polymers are generally shear-thinning for Wi > 1 in laminar flow conditions.

Viscoelasticity of Dilute Polymer Solutions

An elastic deformation of the polymers in shear, which reduces the friction between the polymer and the fluid, is automatically accompanied by an elastic component of the fluid. A deformation in the flow only occurs if the time that the polymer needs to relax to the equilibrium conformation is longer than the timescale of the flow $\tau_{\mathrm{rel}} > 1/\dot{\gamma}$. Consequently, the relaxation motion taking place after a sudden stop of the flow or at a flow reversal in oscillatory flow drags the fluid into the opposite direction of the initial deformation. Thus, the fluid appears as viscoelastic.

By taking a closer look at the stationary probability function of the orientational angle ϕ in fig. 4.15, it becomes clear, that even solutions with stiff rods which cannot be deformed by the flow are expected to exhibit some elasticity: The maximum in p_{stat} located around $-\phi_c$ is slightly asymmetric with a higher slope on the left side of the peak. If the flow is suddenly stopped, diffusion will drive the flow aligned rods back towards an equal angular distribution. With the gradient of p_{stat} being higher on the left side, the flux of diffusing rods against the rotational direction of the shear flow will be higher than the flux of diffusing rods into the flow direction. Thus, the majority of the rods diffuses backward. On average, the diffusing rods will therefore drag the fluid along in the backward direction and cause an elastic retraction motion of the fluid after a sudden stop of the applied shear stress. Therefore, the asymmetric alignment of the rods in the flow is accompanied by an entropic elasticity of the fluid.

Normal Forces

The asymmetric orientational distribution function p_{stat} leads to an asymmetry in the occuring frictional forces. Due to these asymmetries, the frictional forces exerted onto the fluid by the tumbling polymers do not cancel out. On average, this leads to non-vanishing normal forces in the directions perpendicular to the flow, which give rise to many prominent features of non-Newtonian flows such as the rod-climbing *Weissenberg effect*.

Drag Reduction in Turbulent Flows

With the microscopical insight gained by the shear flow experiments, phenomena in more complex flows can be addressed, for which the experimental approach with fluorescently labelled actin filaments could be equally well suited as in the case of simple shear. One example are mixed flows from purely rotational to purely elongational flows. Amongst others, such flows are of special interest

when laminar flows cross over into turbulent flows at high Reynolds numbers. Then, the homogeneous 1:1 mixture of rotational and elongational flow is heterogenously split into dynamically changing areas with locally predominantly rotational flows and predominantly elongational flows, giving rise to the typical vortex structures in turbulent flows. The addition of a small amount of polymers with high molecular weight has been found to decrease the flow resistance of fluids in the high Reynolds number regime, despite an enhancement of the zero-shear viscosity η_0 by the polymers. Although this effect of drag reduction is known for a long time[110], its microscopical mechanisms are not yet fully resolved.

However, analogously to the shear-thinning discussion above, a qualitative explanation for one of the mechanisms involved can be given by considering the dynamics of the individual polymers. In the absence of rotational flow components, polymers in elongational flows will be aligned in the flow gradient direction. In contrast to the shear flow, where alignment occurs perpendicular to the shear gradient direction, this increases the local frictional forces at the polymers. As a consequence, flexible polymers being deformed in elongational flows exhibit even stronger frictional forces leading to a stronger deformation. This causes a deformation feedback mechanism leading to a steep increase of the elongational viscosity once the threshold of deformation is overcome. Therefore, both stiff and flexible long polymers, will significantly damp occuring elongational flow fields. On the other hand, due to the shear thinning effects discussed above, the shear viscosity is only moderately increased by the polymers in shear flows with Wi $\gg$ 1. Thus, the added polymers can efficiently damp the turbulences in the high Reynolds regime Re $\gg$ 1 explaining the observed drag reduction.

4.5   Surface Effects: Cross Stream Migration

If the size of the fluid constituents reaches the same order of magnitude as the distance to the channel walls, surface effects can occur in complex fluids under flow. Due to the high surface to volume ratio, boundary layer effects are particularly important in microfluidic devices and offer potential applications for particle segregation and manipulation. Accordingly, microfluidics feature excellent conditions to study interactions of particles or molecules with the channel walls. With contour lengths of tens of microns, the size of many polymers is within the range of typical microfluidic channel dimensions, so that confinement effects can possibly influence the flow conditions in the entire channel. In this section, the flow behaviour of flexible polymers in high aspect ratio channels with $w = 45\,\mu$m, $h = 150\,\mu$m was studied to test for an influence of theoretically predicted lift-forces near the channel walls. As currently a lot of effort is put into developing lab-on-a-chip devices for high throughput analysis of DNA, the behaviour of DNA molecules in microfluidic flows is of special interest. Therefore fluorescently labelled λ-DNA with a contour length of $21\,\mu$m was chosen as model polymer for the experiments. Instead of directly looking at the dy-

namics of individual polymers as done with the actin filaments, local changes in the bulk concentration of the polymers under flow were observed by averaging and comparing long time exposure pictures of DNA solution in equilibrium and under flow. To this end, movies were recorded in fluorescence microscopy in the channel midplane at $z = h/2$. Due to the high aspect ratio of the channel, the lateral fluorescence intensity profiles should be essentially unaffected by interactions with the channel's bottom and top walls.

4.5.1 Lift Forces: Theory

Spherical particles in shear near no slip boundaries are known to migrate cross-streamline due to inertia effects at non-zero Reynolds number [52, 59], which could give rise to the depletion layer observed in microfluidic channels with particle laden fluids (see section 2.5). For non-spherical particles, a shear-induced repulsion caused by hydrodynamic interactions with the channel wall has been described by Sendner et al.[95]. Provided that the flow is strong enough to stretch the flexible polymers, both stiff, semiflexible and flexible polymers experience a flow alignment with a peak around $-\phi_c$ in an unbounded shear flow (see discussion in the previous sections). As long as the tumbling filaments are not sterically hindered by the walls, the dynamics remain essentially unchanged in the presence of the wall. Due to the non-vanishing average orientational angle between filament and wall, the hydrodynamic interaction with the wall generates a net lift force driving the polymer away from the wall.

The magnitude of the lift force acting on an individual polymer in steady shear has been simulated for dumbbells as well as rods [95]. Due to the induced drift on individual polymers directed away from the walls, a depletion layer develops. Its thickness L_d is set by a balance of the flux induced by the lift force and the diffusive flux due to the developing concentration gradient. Consequently, it takes at minimum a time on the order of $t = L_d^2/2D$ to reach a steady state density profile in the channel. For DNA molecules it is therefore difficult to reach the required residence times in the channel for the concentration profile to fully develop, especially at higher shearrates. To circumvent this problem, the use of oscillatory flow with large strain amplitudes has been proposed to keep the molecules in the channel flow for unlimited durations [16, 51], and both simulations and experiments have been performed to determine the evolution of the steady state concentration profile.

4.5.2 Experimental Results & Discussion

A $10\,\mathrm{pM}$ solution of YOYO-labelled λ-DNA was prepared and put under oscillatory shear by applying sinusoidal pressure pulses with a frequency of $f = 0.5\,\mathrm{Hz}$ to the microfluidic channel. This resulted in an effective oscillatory strain of the solution with an amplitude of about $\gamma = 50 \pm 10$, which was estimated by dividing the amplitude of the fluid displacement in the channel center by half of the channel width. This corresponds to an effective shearrate with a maximum of $\dot{\gamma} = 2\pi f \approx 150\mathrm{s}^{-1}$. Fig. 4.17 shows the development of a depletion layer of
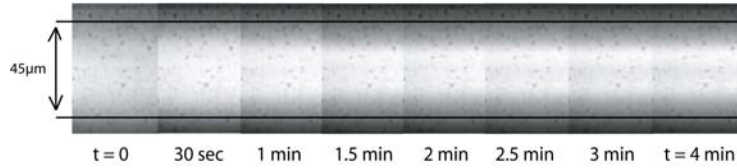
Figure 4.17: A 10 pM solution of fluorescently labelled Λ-DNA is put under oscillatory shear with $f = 0.5\,\text{Hz}$ and $\gamma = 50$ in a microchannel of $45\,\mu\text{m}$ width. The picture shows a time series of 30 second averages of the recorded fluorescence intensity under shear. The picture at $t = 0$ was recorded with a very small drift velocity in the channel in near equilibrium.

$L_d \approx 10\,\mu\text{m}$. The evolution of the appendant cross-sectional fluorescence intensity profile is shown in fig. 4.18a. The intensity profiles have been normalized to an equal amount of integrated intensity to account for a loss of intensity during the measurement due to partial bleaching of the dye. Note that the equilibrium profile recorded at $t = 0$ is not flat. This might be attributed to background fluorescence of blurred out of focus DNA-molecules from throughout the channel. Therefore, a determination of the DNA concentration profile from the intensity profile is tedious. As a rough estimate, the intensity profiles have been divided by the equilibrium profile resulting in the concentration profiles in fig. 4.18b. While the concentration of the DNA has to be zero outside of the channel in the PDMS walls, the recorded fluorescence intensity is not (the channel walls are indicated by the vertical dashed lines in fig. 4.18a). This might be attributed to light from out of focus planes, and the estimated concentration profiles have been normalized to zero at the channel walls at $x = 0\,\mu\text{m}$, $x = 45\,\mu\text{m}$ in fig. 4.18b. The comparison with the concentration profiles determined in simulations taken from [16] shown in fig. 4.18c shows a qualitative agreement. The width of the zone filled with DNA has been evaluated by determining the full width at half maximum of the concentration profiles. The timecourse of the resulting depletion layer thickness L_d is shown in fig. 4.18d and shows an exponential development of the depletion layer. With a timeconstant of $\tau = 34\,\text{s}$ the steady state depletion layer of $L_d \approx 10\,\mu\text{m}$ is reached after about 1.5 min. of oscillatory shearing. The concentration profile takes about 3 minutes to reach its steady state with a pronounced dip in the middle of the channel. The diffusion constant D of the DNA-molecules has been experimentally determined by tracking single molecules in equilibrium in the channel before the oscillatory shear. Evaluation of the mean-square displacement yields $D \approx 0.3\,\mu\text{m}^2/\text{s}$. Both the depletion layer thickness and the width of the dip are on the order of 10 μm, which predicts a timescale of $t_{\text{equ}} \approx (10\,\mu\text{m})^2/2D \approx 170\text{s}$ for the system to equilibrate. This is within the range of the observed equilibration times, supporting the idea of a diffusion influenced shape of the concentration profile.

Both the timescale of the profile developement and the width of the observed depletion layer are consistent with the simulation and the experiments in [51], where the dip has been attributed to a competition of lift force induced DNA

migration away from the walls and migration away from the center due to a gradient in chain mobility[51]. The difference in chain mobility may be explained by the anisotropic friction coefficient of the DNA, which causes a smaller diffusion coefficient for extended chains for motion perpendicular to the extension compared to coiled molecules in equilibrium. While the dip has been reported to repeatedly diminish and reappear in the experiments in reference [51], the dip in the experiment evaluated in this work was permanent once the steady state profile had developed.
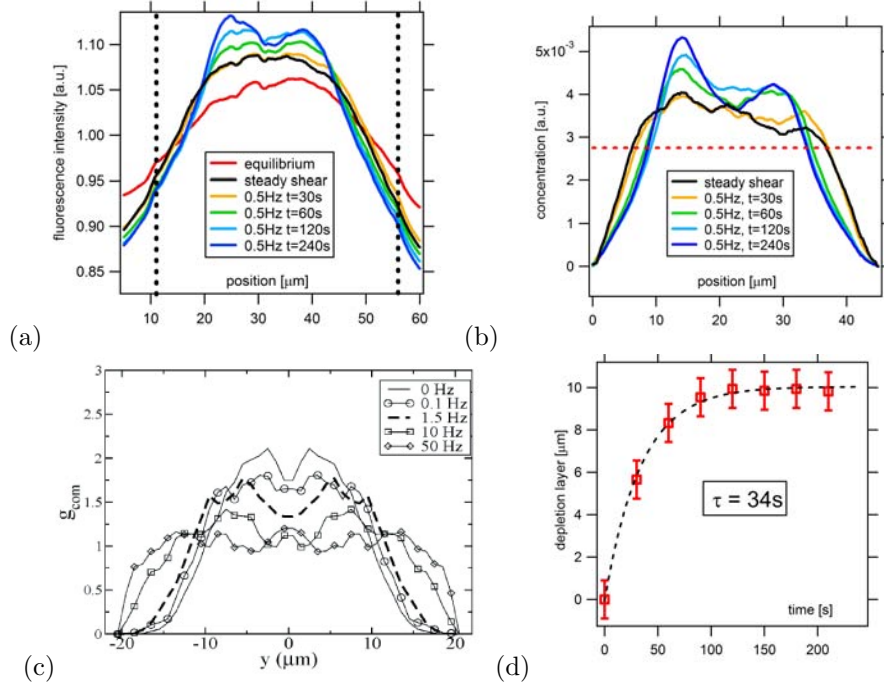
Figure 4.18: (a): Time evolution of the fluorescence intensity profile of labelled λ-DNA solution in the channel under oscillatory shear with $f = 0.5\,\text{Hz}$ and $\gamma = 50$. The equilibrium (red line) and steady shear (black line) profiles are shown for comparison. To account for bleaching effects, the intensity in each profile was adjusted to get equal amounts of total fluorescence intensity. (b): Intensity profiles were normalized by the equilibrium profile. Afterwards, the intensity at the channel walls was set to zero by substracting a linear profile given by the normalized intensities at the walls. The resulting profiles were adjusted to matching total intensities again. (c) Simulation data showing the distribution of the center of mass of a polymer solution in oscillatory channel flow for parameters describing λ-DNA (graph taken from[16]). Frequencies $f = 0, 0.1, 1.5, 10, 50\,\text{Hz}$ correspond to strains of $\gamma = \infty, 2300, 150, 23, 4.6$, so that our experiment with $f = 0.5\,\text{Hz}, \gamma = 50$ lies inbetween the $f = 0.1\,\text{Hz}$ and $f = 1.5\,\text{Hz}$ curves. Qualitatively, our results for the concentration profile in steady state is in good agreement with the theoretical prediction. (d) Temporal evolution of the depletion layer thickness L_d, which was measured via the full width at half maximum ($FWHM$) of the concentration profiles in (b) as $L_d = (FWHM - w)/2$, where $w = 45\,\mu\text{m}$ is the channel width. The dashed line shows an exponential fit to the measured values of L_d.

5. DIFFERENTIAL MICROFLUIDIC VISCOMETER

In the previous chapter we showed, that microfluidics open the way to observe and characterize the dynamics of individual polymers in flow. With typical widths on the order of $100\,\mu$m, microfluidic channels are still much bigger than the lateral dimensions of the polymers in the flowfield. Thus, microfluidic devices are equally suited for directly measuring bulk viscosity properties like the shear viscosity η and the extensional viscosity Λ. The opportunity to combine bulk property measurements with simultaneous observation of individual macromolecular dynamics provides an excellent field for studying complex fluids in flow.

Apart from offering these exciting possibilities, microfluidic viscometers may feature several other advantages compared with macroscopic rheometers. While classical shear rheometers such as capillary and rotational rheometers typically require sample fluids on the order of 1 ml, viscometers on the $100\,\mu$m lengthscale can be operated with liquid amounts in the μl range. Moreover, microfluidic rheometers may offer advantages in the high shear rate regime, where macroscopic flows are affected by inertial effects and viscous heating. With its closed geometry, measurements in a microfluidic viscometer do not suffer from artefacts due to protein films adsorbed at the air-water interface which occur in cone-plate rheometers [97]. With the intensive efforts that have been made in developing numerous lab-on-a-chip applications for the manipulation and analysis of complex fluids in microfluidic devices in recent years, a growing interest in microfluidic rheometric techniques has emerged to open the way for new microfluidic tools and lines of application. A good overview over existing techniques and devices for measuring shear viscosities and extensional viscosities in microfluidics is given in [82].

In this chapter we will introduce a novel differential technique to measure the non-Newtonian properties of the shear viscosity $\eta(\dot{\gamma})$ and extensional viscosity $\Lambda(\dot{\epsilon})$. As the proposed differential viscometer does not require a pressure sensor, the technique is both simple and robust. Rather than absolute values of the viscosity, the device determines the powerlaw exponents n, k of the viscosities, which give the slope of the flowrate dependence of $\ln(\eta(\dot{\gamma}))$ and $\ln(\Lambda(\dot{\epsilon}))$ (see eq. 3.32). Thus, the technique is especially suited for characterizing non-Newtonian fluids. The method is open to miniaturization and parallelization, so that the device could be used for online monitoring of fluid properties in a production line as well as being incorporated into existing lab-on-a-chip applications.

We will start by briefly rationalizing the different response of polymer so-

lutions to shear and extensional flow. Then we will explain the working principle of the proposed differential viscometer, show some possible microfluidic realisations and discuss the possibilities and limitations of the approach with experimental results obtained from measurements in both shear and extensional differential viscometers.

5.1 Shear and Extensional Viscosity of Polymer Solutions

While the velocity field of simple shear flow is a 1:1 mixture of rotational and elongational flow, purely extensional flow fields do not contain any rotational component (see section 3.1.3). As a consequence, the properties of polymer solution are fundamentally different in shear and extensional flows, although flexible polymers get aligned and stretched in both cases. In shear flow (see fig. 5.1 left), stretching and alignment occurs in the direction of flow (see chapter 4), which is perpendicular to the velocity gradient. Thus, the frictional dissipation is reduced by the alignment leading to the typical decrease in the viscosity $\eta(\dot{\gamma})$ with increasing shear rate $\dot{\gamma}$, which sets in once the flow is sufficiently strong to deform the equilibrium conformation of the polymer. The typical rate dependence of the shear viscosity is shown by the red curve in the graph in fig. 5.1 right. Simultaneously, the rotational component of the flow induces tumbling of the polymer, so that the polymer never reaches a stationary state. In contrast, in extensional flow the stretching and aligning occurs in the direction of the velocity gradient (see fig. 5.1 middle). Thus, a deformation in extensional flow increases the frictional forces acting on the polymer. Hence, a deformation of the polymer induces a feedback mechanism, so that the polymer undergoes a coil-stretch transition. The polymer in purely extensional flow is thus either essentially undeformed or almost completely stretched. Consequently, the extensional viscosity $\Lambda(\dot{\epsilon})$ shows a threshold behaviour with a steep increase once a critical deformation rate $\dot{\epsilon}$ is overcome (blue curve in fig. 5.1 right).

5.2 Capillary Rheometer

The microfluidic differential viscometer is an extension of the capillary rheometer, which can be used to extract the shear viscosity of a fluid: A pressure driven flow with flowrate Q is established through a circular capillary with a radius R by applying a pressure difference Δp between a fluid reservoir connected to one capillary die end and the open other end of the capillary die (see fig. 5.2). The shear viscosity $\eta(\dot{\gamma})$ can be determined from the pressure drop along the capillary p_c and the flow rate Q with eq. A.79. Eq. 3.21 can be used in the general case of a capillary with arbitrary constant cross-section. To calculate the viscosity $\eta(\dot{\gamma}_w)$, the power-law index n of the fluid must be known. In case of unknown n, several measurements at different pressure drops and flowrates $\Delta p, Q$ have to be performed and the power law index can be identified as [74]:

$$\frac{1}{n} = \frac{\mathrm{d}\ln Q}{\mathrm{d}\ln p_c}.$$

(5.1)
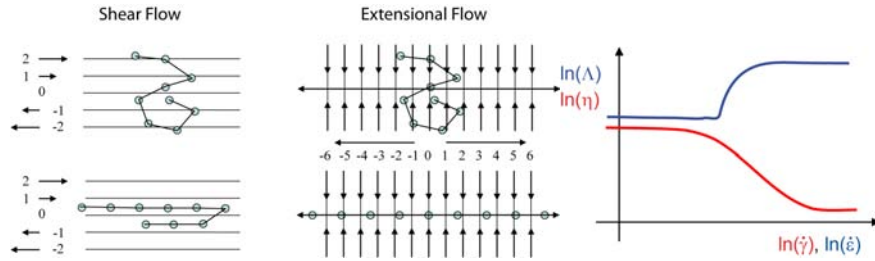
Figure 5.1: The difference in the rate dependency of the viscosity in shear and elongational flow can be traced back to the individual polymer dynamics: Equilibrium conformation (Wi $<$ 1, up) vs. stretched conformation (Wi $\gg$ 1, down) of flexible polymers in shear and extensional flow. In shear flow (left), stretching and alignment leads to a reduction of the frictional forces acting on the polymer. In extensional flow (middle), the polymer deformation and alignment increases the frictional forces. Right: Consequently, the shear visosity drops with the shear rate (red curve), while the extensional velocity rises once a threshold elongational rate is overcome (blue curve).
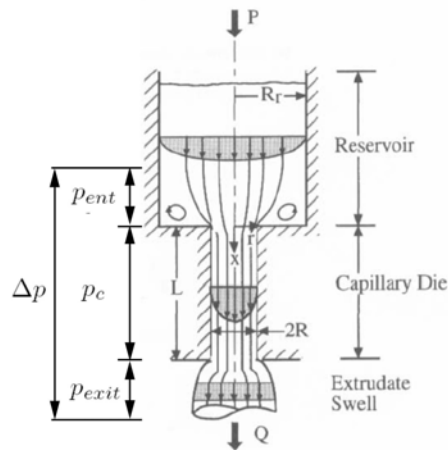
Figure 5.2: Schematics of a capillary rheometer, taken from [74]. The pressure difference Δp needed to drive a flow with flowrate Q through a capillary of known diameter is measured to determine the shear viscosity $\eta(\dot\gamma)$ of the fluid (see text).

There are different contributions to the measured total pressure drop Δp besides the capillary pressure drop p_c. Hereby, the entrance pressure drop p_{ent} and the exit pressure drop p_{exit} are the most important ones. While the exit pressure drop arising from elastic effects of the fluid is usually small and can often be neglected [33], the entrance pressure drop can be very large for polymer solutions with high extensional viscosities. A way to extract the capillary pressure p_c is to measure the total pressure drop Δp for a fixed flowrate Q with capillaries of different lengths L. By plotting Δp over L and extrapolating to $L = 0$, the entrance pressure p_{ent} can be determined, so that p_c can be extracted (see. fig 5.3). This procedure is known as *Bagley correction*. Some capillary rheometers work

with two capillaries of different length (double barrel rheometers), so that by simultaneously pushing the fluid with the same flowrate through both capillaries and measuring the corresponding pressure drops the capillary pressure p_c can be extracted assuming a linear Bagley plot. The entrance pressure is often
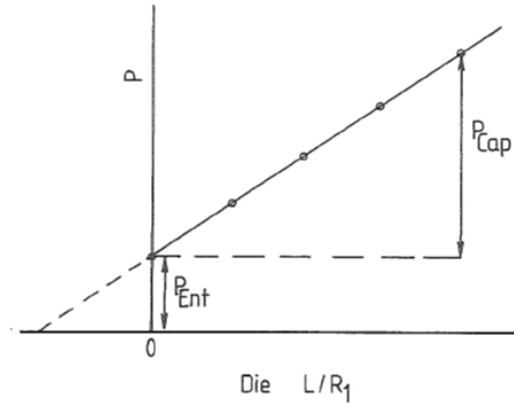
Figure 5.3: The entrance pressure p_{ent} and the pressure drop over the capillary p_c can be determined by measuring the total pressure drop Δp for capillaries with various lengths and extrapolating to $L = 0$ (here, the capillary length L is given in terms of L/R_1 where R_1 is the radius of the capillary). Fig. taken from [33].

neglected for very long capillaries with a length to radius ratio $L/R > 60$ [74].

5.3 Differential Shear Rheometer

5.3.1 Existing Microfluid Differential Rheometers
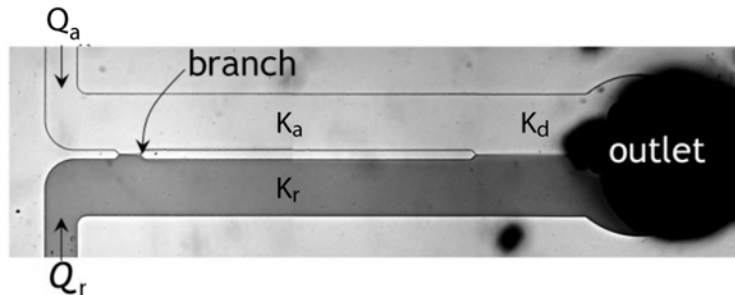
Figure 5.4: Comparative microfluidic rheometer [19]: The fluid to be analyzed flows in a channel K_a parallel to a Newtonian reference fluid in a reference channel K_r with a known flowrate Q_r. The flowrate of the analyte fluid Q_x is adjusted to equalize the pressure drop across reference and analyzer channel. Assuming a Newtonian flow profile in the analyzer channel the viscosity of the analyte fluid can be determined (see text, fig. taken from [19]).

While in the standard double barrel capillary rheometer, the principle of measuring viscosity by comparing two parallel flows is used to eliminate the

entrance and exit pressures, a microfluidic rheometer using two identical channels but different fluids has been introduced in [19] and is shown in fig 5.4. A reference channel K_r and an analyzing channel K_a of same length and cross section are connected with a branch and end in a common channel K_d. The reference channel is fed with a Newtonian reference fluid of known viscosity η_r and flowrate Q_r which is marked with a dye. The analyzing channel is fed with the fluid of unknown viscosity η_x, and the flowrate Q_x in the analyzing channel is adjusted in such a way, that no fluid passes through the branch (see fig 5.4). Then, the pressure drop Δp along K_r and K_a from the branch to the common end is equal for both channels. From the electronic-hydraulic analogy (see section 6.1.1), the steady state laminar, incompressible flow inside the channel is described by [19]:

$$Q = \frac{\Delta p}{R} \tag{5.2}$$

where R is the hydraulic resistance of the channel, which is given for a rectangular channel and a Newtonian fluid by eq. A.82. As the geometries of comparator channels K_r and K_a are equal, the unknown viscosity can be determined by equating eq. 5.2 for both channels [19]:

$$\eta_x = \eta_r \frac{Q_r}{Q_x}. \tag{5.3}$$

The big advantage in this measurement is that no external pressure transducers are needed. However, there are some drawbacks remaining:

- Due to the long equilibration times in microfluidic systems, the adjustment of the flowrates until no fluid flows through the branch can be tedious and time-consuming.

- As the reference fluid and the fluid to be analyzed stream into the same channel where they start to mix, the measurement cannot be performed in series for further analyzation of the fluid.

- Eq. (5.3) is only valid if the fluid of unknown viscosity η_x behaves Newtonian.

5.3.2   Working Principle of Differential Viscometer

To overcome these drawbacks, a differential shear rheometer is proposed here and its working principle is shown in fig. 5.5: A common feeding channel K_f fed with a known flow rate Q of the fluid to be analyzed splits into two comparator channels: a reference channel K_r and an analyzer channel K_a which have the same cross section but different lengths L_r and L_a. Analyzer and reference channels reunify in a common detection channel K_d, where the ratio Q_a/Q_r of fluid passing the two comparator channels is determined. If the difference in the entrance pressure drops can be neglected, the pressure drop across both channels
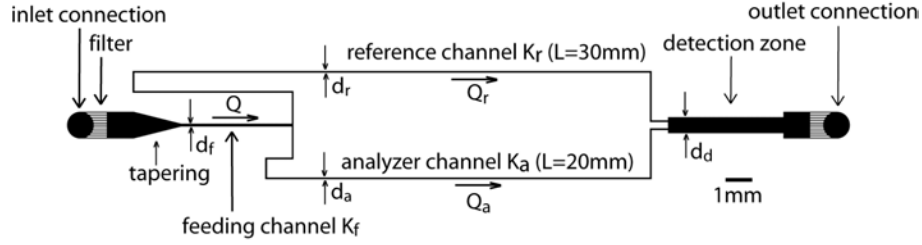
Figure 5.5: Lithography mask for the production of a microfluidic differential viscometer showing the channel geometry. A common feeding channel splits into a reference and an analyzer channel of same width and height but different lengths. The channels lead into a wide detection zone, where the flowrate ratio of analyzer and reference flow $X = Q_a/Q_r$ is optically detected. The shear viscosity exponent n can be calculated from $X(Q)$ (see text).

is equal. The hydrodynamic resistances of analyzer and reference channel are given by eq. 3.22, and the wall shear rates $\dot{\gamma}_{a,r}$ are obtained from eq. 3.20:

$$R_{a,r} = \eta(\dot{\gamma}_{a,r}) \frac{L_{a,r}}{F^\star(n)}, \quad \text{with } \dot{\gamma}_{a,r} = Q_{a,r} \cdot F_{\dot{\gamma}}(n) \tag{5.4}$$

The measured flowrate ratio X is given by the inverse of the ratio of the hydrodynamic resistances of the comparator channels:

$$X = \frac{Q_a}{Q_r} = \frac{R_r}{R_a} = \frac{\eta(\dot{\gamma}_r)}{\eta(\dot{\gamma}_a)} \cdot \frac{L_r}{L_a} \tag{5.5}$$

The flowrates in analyzer and reference channel can be calculated from the known flowrate $Q = Q_a + Q_r$ as

$$Q_a = \frac{X}{X+1}Q, \qquad Q_r = \frac{1}{X+1}Q. \tag{5.6}$$

Assuming a power law for the viscosity $\eta(\dot{\gamma}) = A\dot{\gamma}^{n-1}$ we get

$$X = \left(\frac{\dot{\gamma}_r}{\dot{\gamma}_a}\right)^{n-1} \cdot \frac{L_r}{L_a} = \left(\frac{Q_r}{Q_a}\right)^{n-1} \cdot \frac{L_r}{L_a} = \left(\frac{1}{X}\right)^{n-1} \cdot \frac{L_r}{L_a} \tag{5.7}$$

Thus, the power law exponent n can be determined from the known ratio of the lengths of analyzer and reference channel and the measured flow rate ratio X:

$$n = \frac{\ln(L_r/L_a)}{\ln X} = \frac{\ln(X_N)}{\ln X}, \tag{5.8}$$

where $X_N \equiv L_r/L_a$ is the flowrate ratio expected for a Newtonian fluid. In the experiments, the measured Newtonian flowrate X_N can slightly deviate from the value predicted by the device geometry. To account for such deviations

we calibrate the measurement geometry with a Newtonian fluid and use the experimentally determined value of X_N for the data evaluation.

In a conventional rheometer the absolute value $\eta(\dot\gamma)$ of the viscosity at a given shearrate is determined, which is illustrated schematically by the red curve in the log-log plot in fig. 5.6 on the left. In contrast, the differential measurement directly identifies the local power law index n, which is reflected in the slope of the viscosity curve $\eta(\dot\gamma)$ in a log-log plot shown by the green curve in fig. (5.6) right:

$$\frac{\mathrm{d}(\ln\eta)}{\mathrm{d}(\ln\dot\gamma)} = n - 1 \tag{5.9}$$

As the measurement thus yields the differential $n-1$ of the viscosity, the method
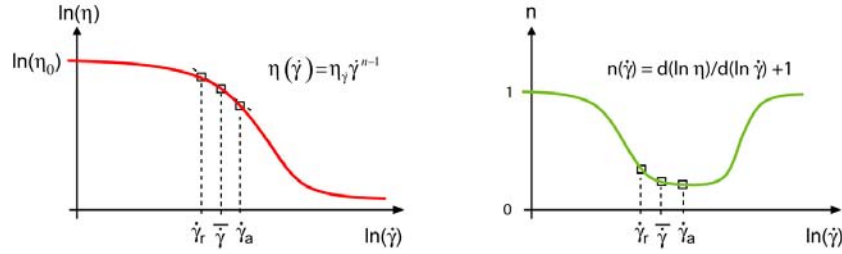
Figure 5.6: Schematics of the shear viscosity measurement in the differential viscometer. From the measured flowrate ratio X, the ratio of the apparent shear viscosities in analyzer and reference channel $\eta(\dot\gamma_a)/\eta(\dot\gamma_r)$ and the ratio of the shear rates in the channels $\dot\gamma_a/\dot\gamma_r$ can be determined (left). Thus, X determines the slope of the logarithm of $\eta(\dot\gamma)$, which gives the power-law index $n(\dot\gamma)$ of the shear viscosity at the intermediate shear rate $\bar{\dot\gamma}$ shown on the right.

is especially suited to characterize non-Newtonian fluids. While a Newtonian fluid with $n = 1$ has a constant shear viscosity, $n < 1$ and $n > 1$ correspond to a shear-thinning, resp. shear-thickening fluid. Thus, the powerlaw index n specifies how "non-Newtonian" the fluid is in the vicinity of the averaged flowrate $\bar{\dot\gamma} = \sqrt{\dot\gamma_a\dot\gamma_r}$ in the channels K_a, K_r. To determine the absolut values of the viscosity with eq. (3.21), an additional measurement of the pressure drop along the channels is needed. Alternatively, the whole curve of n versus $\bar{\dot\gamma}$ can be measured and the viscosity η can be identified by integration of the curve if one basic value $\eta(\dot\gamma)$ is known.

Generally, for a complex fluid the powerlaw description will only be valid locally in a certain interval of shearrates around $\dot\gamma_0$ according to eq. (3.33). For the measurement of n it is therefore mandatory that the channel shearrates $\dot\gamma_a, \dot\gamma_r$ fall within the interval where the powerlaw description is sufficiently fulfilled. The shearrates $\dot\gamma_a, \dot\gamma_r$ are proportional to the flowrates Q_a, Q_r in analyzer and reference channel, which themselves are inversely proportional to the hydrodynamic resistance R_a, R_r of the channels. As the hydrodynamic resistances are proportional to the channel lengths, the accuracy and the sensitivity of the measurement can be tuned by the length ratio of the channels L_a/L_r. For a strongly

non-Newtonian fluid with a powerlaw index far away from $n = 1$, a length ratio L_a/L_r relatively close to unity ensures that the shearrate interval $[\dot{\gamma}_a, \dot{\gamma}_r]$ does not get too wide while still giving a good measurable signal $X = \left(\frac{L_r}{L_a}\right)^{\frac{1}{n}}$ not too close to the Newtonian value $X_N = L_a/L_r$. On the other hand, to detect only a small deviation from $n = 1$, a big ratio of L_a/L_r will result in a resolvable measurement signal $X - X_N$. For fluids with unknown properties it can be convenient to measure X in series with different length ratios L_a/L_r and pick the best fitting geometry for evaluation.

5.3.3 Design of Experimental Measurement Geometries

The principle of the differential viscometer illustrated above has been tested experimentally by performing measurements with complex fluids of different rheological properties, which have been determined with a rotational rheometer in cone-plate geometry for comparison. Measurements in various realisations of the differential shear viscometer have been performed to test for a possible influence of the measurement geometry on the results.

Basic Setup

The *basic setup* consists of one analyzer and one reference channel with the same constant, rectangular cross section and different lengths $L_a \neq L_r$. Its geometry is depicted in fig. 5.5.

"$2 \times 2L$ vs. L" - Setup
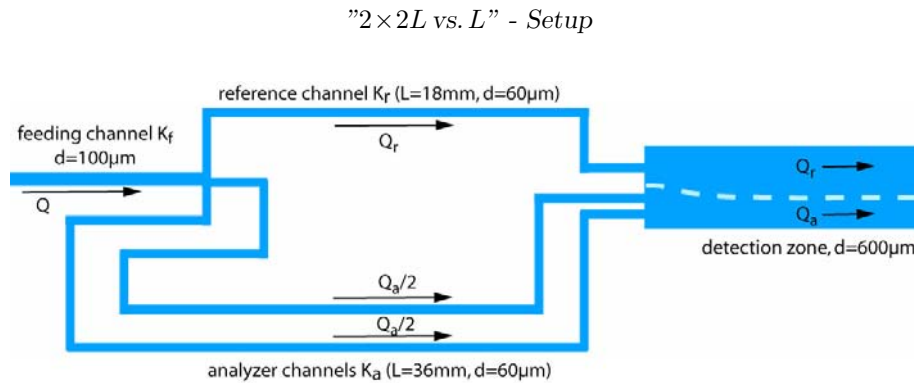
Figure 5.7: To keep the flow rate ratio close to $X = 1$, the differential shear viscometer has been tested with a reference channel of length L_r and an analyzer channel consisting of two parallel channels with twice the length $L_a = 2L_r = 36$ mm.

The "$2 \times 2L$ vs. L" - setup shown in fig. 5.7 is a modified version with 2 parallel analyzer channels of length $L_a = 2L_r$. The hydrodynamic resistance R_a of the two parallel analyzer channels can be calculated by the hydrodynamic analogy

to electric circuits (see section 6.1.1) from the resistance of the single analyzer channel R_{2L}:

$$\frac{1}{R_a} = \frac{1}{R_{2L}} + \frac{1}{R_{2L}} = \frac{2}{R_{2L}}. \tag{5.10}$$

Then, the flowrate ratio in the "$2 \times 2L$ vs. L" - device is given by (comp. eq. 5.5):

$$X = \frac{Q_a}{Q_r} = \frac{R_r}{R_a} = \frac{2\eta(\dot{\gamma}_r)}{\eta(\dot{\gamma}_a)} \cdot \frac{L_r}{L_a} = \frac{\eta(\dot{\gamma}_r)}{\eta(\dot{\gamma}_a)}. \tag{5.11}$$

Hence, the Newtonian flowrate ratio in this setup is $X_N = 1$. With the flowrate Q_a splitting equally on the two analyzer channels we get for the shearrate in the analyzer channels $\left(\frac{\dot{\gamma}_r}{\dot{\gamma}_a}\right) = \left(\frac{Q_r}{Q_a/2}\right)$ so that eq. 5.8 reads for the "$2 \times 2L$ vs. L" - device:

$$n = \frac{\ln 2}{\ln(2X_N/X)} = \frac{\ln 2}{\ln(2/X)} \tag{5.12}$$

The advantage of this setup is that the flowrate ratio X is kept close to unity, where the experimental error in determining X by measuring the width of the streams Q_a, Q_r is lowest. Fig. 5.8 shows fluorescence microscopy images of the setup on a microfluidic chip in operation. The pictured section shows the out-flux of the reference channel and the two analyzer channels into the detection channel. The analyzer fluid contains fluorescently labelled melamin resin beads with a diameter of 1 μm as marker particles. The depletion layer seperating the fluid streams Q_r and $Q_{a,1}, Q_{a,2}$ is clearly visible and indicated by the arrow (see section 2.5) . A measurement for a Newtonian fluid (50% (w/w) glycerol in water, left) is shown in comparison with a mildly and strongly shear thinning fluid (1% (w/w) PAA (middle) and 2% (w/w) PAA (right) in aqueous solution). While for the glycerol solution the depletion layer is in the channel center indicating $X \approx 1$, the flowrate ratio $X = Q_a/Q_r$ is significantly decreased for the shear thinning polymer solutions of 1% PAA and 2% PAA. This is caused by the higher shearrate in the reference channel K_r, which results in a lower viscosity of the fluid and thus a higher flowrate in K_r. At the given shearrates in the channels, the powerlaw index n of the 2% PAA soluion is apparently lower than n of the 1% PAA solution, while $n = 1$ for the glycerol solution.

Wide-Narrow Setup

Another setup (*wide-narrow setup*) to achieve the advantageous $X_N \approx 1$ Newtonian flowrate ratio uses a narrow, short analyzer channel and a wider and longer reference channel ($d_a < d_r$, $L_a < L_r$). The length of the analyzer channel is chosen in such a way, that the hydrodynamic resistance of reference and analyzer channels is approximately equal for a Newtonian fluid. Then, for equal flow rates $Q_a \approx Q_r$ the shearrate is higher in the narrow analyzer channel. Therefore, the flowrate ratio X will change for a non-Newtonian fluid with $n \neq 1$, which enables the determination of the viscosity exponent n. Fig. 5.9 shows a series of microscopy images from measurements in a wide-narrow setup with $d_a = 50\,\mu$m, $d_r = 100\,\mu$m, $L_a = 16$mm, $L_r = 52$mm and $h_a = h_r = 61\,\mu$m. The
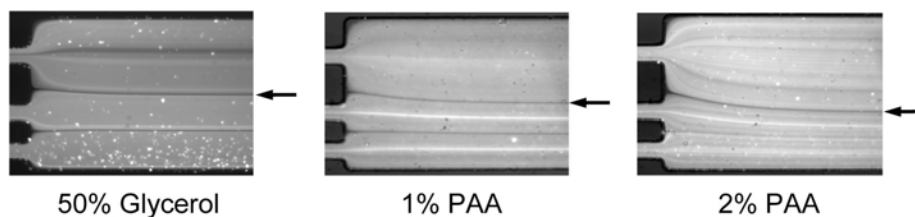
Figure 5.8: Microscopy images of the detection channel of the $2 \times 2L$ vs. L - setup with analyte fluids containing fluorescently labelled tracer particles. The flow direction is from left to right, the exit of the reference channel (up) and the two analyzer channels (down) are visible on the left edge of the images. The exposure time is set long enough to show average particle densities instead of individual tracer particles. The depletion layer seperating the fluid streams of K_a and K_r is marked with an arrow. While for the Newtonian glycerol solution (left) the depletion layer is in the channel center indicating $X \approx 1$, the flowrate ratio $X = Q_a/Q_r$ is significantly decreased for the shear thinning polymer solutions of 1% PAA (middle) and 2% PAA (right). This is caused by the higher shearrate in the reference channel K_r, which results in a lower viscosity of the fluid and a higher flowrate in K_r.

setup contains an additional channel K_m through which a stream of analyzer fluid with fluorescent markers Q_m is inserted in-between the fluid streams of analyzer and reference channel. The upper pictures in fig. 5.9 show the area at the outlet of the channels K_r, K_a and K_m into the detection channel (comp. to fig. 2.5), the lower pictures are recorded further downstream in the detection zone, where the flow profile is fully developed and the width of the streams d_r, d_a is evaluated. The measurement was taken with 2% PAA in aqueous solution as analyzer fluid.

Tube-Setup

To demonstrate the simplicity of the device, we tested a very basic *tube setup*, where the feeding channel, analyzer and reference channel are replaced by standard polypropylen tubings with a diameter of $d = 1/32$ inch connected by a T-crossing. Analyzer and reference channels had different lengths of $L_a = 15$ cm , $L_r = 30$ cm. The feeding channel was connected to a syringe pump providing known flow rates of the analyzer fluid and the flowrate ratio was determined by weighing the amounts of fluid V_a, V_r flowing out of reference and analyzer channels during an arbitrary measurement time. Fig. 5.10 shows a scheme of the tube setup.

5.3.4 Entrance and Exit Effects

The cross section of the feeding channel D_f in the microfluidic devices is bigger than the cross section of the comparator channels $D_r = D_a$, but smaller than the
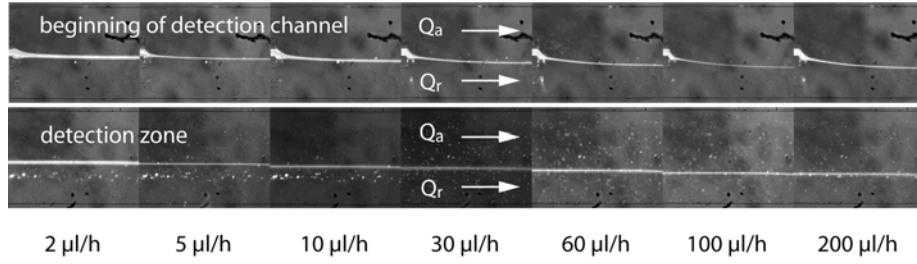
Figure 5.9: Detection zone in wide-narrow setup with additional channel K_m with marker fluid for the determination of X during a measurement with a 2% (w/w) PAA solution under different flowrates $Q = 2 - 200\mu l/h$. The upper pictures are taken right at the beginning of the detection zone, the low picture series shows a region more downstream where the flow profile is fully developed. The exit of the narrow, short analyzer channel lies above the marker channel, the wider and longer reference channel exit is beneath K_m. With increasing flowrate Q, the fraction flowing through the analyzer channel increases, which reflects the shear-thinning behaviour of the polymer solution at higher shearrates.
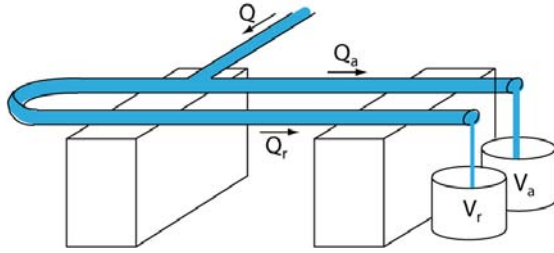
Figure 5.10: Schematics of the tube-setup: The tube with fluid coming from the syringe pump is split into analyzer and reference tube with a T-crossing. The flowrate ratio is determined by weighing the amounts of fluid V_a, V_r flowing through analyzer and reference tube in an equal time interval.

sum of the cross sectional area of both comparator channels $(D_r < D_f < 2D_r)$. Thus, the average Hencky strain of the elongation during the entrance flow from the feeding channel into the comparator channels cannot exceed the value of $\epsilon = \ln 2 \approx 0.69$. The dependence of the entrance pressure drop of polymer solutions on the Hencky strain is strongly nonlinear and the pressure drops expected for Hencky strains $\epsilon < 1$ can be expected to be small [5]. Thus, the geometry of the feeding channel ensures the limited influence of entrance flow pressure drops due to extensional viscosity effects. To satisfy the proposed constant pressure gradient $(\mathrm{d}p/\mathrm{d}z) = \Delta p/L$ for different channel lengths, which corresponds to a linear Bagley plot, the flow should be fully developed along most of the channel. This requires, that the residence time $t_r = L/\bar{v}$ of the fluid in the channel is long compared to the relaxation time of the fluid τ_0 where $\bar{v} = Q/D$ is the average fluid velocity in the channel. This corresponds to a small *Deborah number De*, which gives the ratio of fluid relaxation time and

time of observation [86]:

$$\text{De} = \tau_0/t_r = Q/(DL) \ll 1 \tag{5.13}$$

The exit pressure loss is generally smaller than the entrance pressure and can be neglected. This can be understood as follows: In a cylinder-symmetrical constriction, the Hencky strain and the elongational rates are twice as big in the direction of the flow as perpendicular. Thus, the polymers are stretched way more in the direction of flow at the channel entrance than in the perpendicular direction at the channel exit. Moreover, the shear in the channel already prestretches the polymer in the direction of flow. Hence, the stretching perpendicular to the flow at the exit coincides with the relaxation of the polymer due to the reduced shearrate. Thus, both p_{ent} and p_{exit} are neglected in the differential shear viscometer.

5.3.5 *Measurements with Semi-Dilute Polymer Solution*

Measurements in several of the aforementioned setups have been performed to determine the power-law exponent n of the shear viscosity of 1% and 2% (w/w) PAA (5-6 MDa) in aqueous solution as model polymer fluids. Fig. 5.11 shows the measurement results for the flowrate ratio $X = Q_a/Q_r$ in the "2×2L vs. L" - setup depicted in fig. 5.7 as evaluated from fluorescence microscopy images analogous to those shown in fig. 5.8. For slow flowrates, the images were obtained by averaging long-time exposure shots of the channels with the fluorescent markers. The Newtonian flowrate ratio X_N for the device calibration was obtained by averaging the measured $X(Q)$-values of a 50% (w/w) glycerol solution at different flowrates (blue squares). At low flowrates, both PAA solutions show a flowrate ratio near the Newtonian value X_N. For increasing flowrates, $X(Q)$ of the polymer solutions rises (green squares: 1% PAA, red squares: 2% PAA), indicating the shear-thinning behavior of the solutions. As expected from the cone-plate rotational rheometer measurements (see fig. C.1), the shear thinning is much more pronounced for the higher concentrated polymer solution which manifests in the higher $X(Q)$ values for the 2% PAA solution. At very high shearrates ($\dot{\gamma} > 1000s^{-1}$) a slight decrease in X indicates a viscosity function $\eta(\dot{\gamma})$ with a less steep slope. The according values for the shear viscosity exponent $n(\dot{\gamma})$ calculated from $X(Q)$ are shown in fig. 5.12. To test for a potential influence of the measurement geometry, the viscosity exponent of the 2% PAA solution has been measured in different geometries and all results are plotted together in fig. 5.12. Filled circles and upward triangles represent measurements with the basic setup with $L_a/L_r = 3/2$, filled squares represent measurements in the $2 \times 2L$ vs. L - setup and downward triangle values were obtained with the wide-narrow setup shown in fig. 5.9. Measurements for the 1% PAA solution are shown in green, measurements for the 2% PAA solution are shown in red. For comparison, the viscosity exponent obtained by differentiation of $\eta(\dot{\gamma})$-curves from rotational cone-plate rheometer measurements is displayed for both polymer solutions by the open squares. The differential viscometer re-
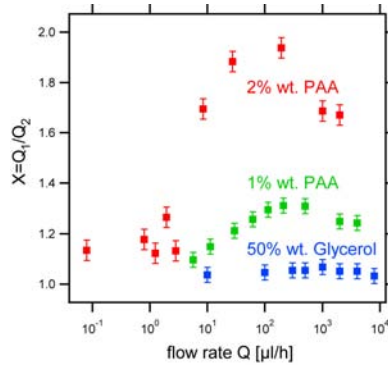
Figure 5.11: Evaluated flowrate ratios $X(Q)$ for a differential viscosity measurement in the "'2x 2L vs L"'-setup depicted in fig. 5.7 and 5.8. ■: 50% (w/w) glycerol solution; ■: 1% (w/w) PAA solution, ■: 2% (w/w) PAA solution. The higher values of X for the polymer solutions in comparison with the glycerol solutions reflect the non-Newtonian shear-thinning characteristics of these fluids.

sults are in good agreement with the rotational rheometer measurements and no dependence on the specific measurement geometry used could be observed.
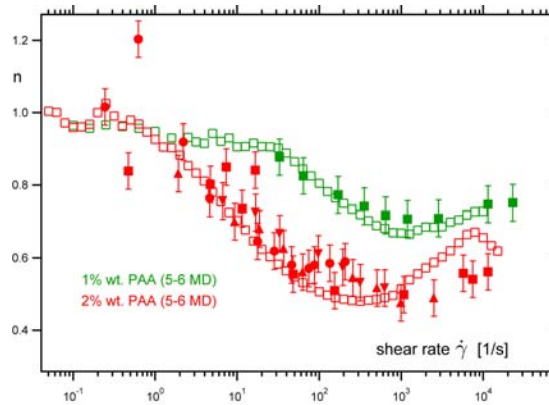
Figure 5.12: □, □: Shear viscosity exponent n determined by cone-plate rheometer measurement for 1% w/w. and 2% w/w. polyacrylamid (PAA) solutions with a molecular weight of ca. 5-6 MDa. Measurements with the differential microfluidic viscometer were performed in the basic setup (●, ▲), the $2\times 2L$ vs L-setup (■,■) and the wide-narrow geometry (▼). The results are in agreement with data extracted from measurements in cone-plate rheometry (□, □) and no sytematic dependence on the specific measurement geometry is evident.

5.3.6 *Measurements with Worm-like Micellar Solution*

As a test for the suitability of the differential viscometer for extremely shear-thinning solutions, the shear exponent of a commercially available shower gel (Lavera) has been measured. The shower gel consists predominantly of a highly concentrated lipid solution. The lipids in such solutions are known to form long worm-like micelles (WLM), which can entangle with each other. Thus, the rheological characteristics resemble much of a highly entangled polymer

(a)   (b)
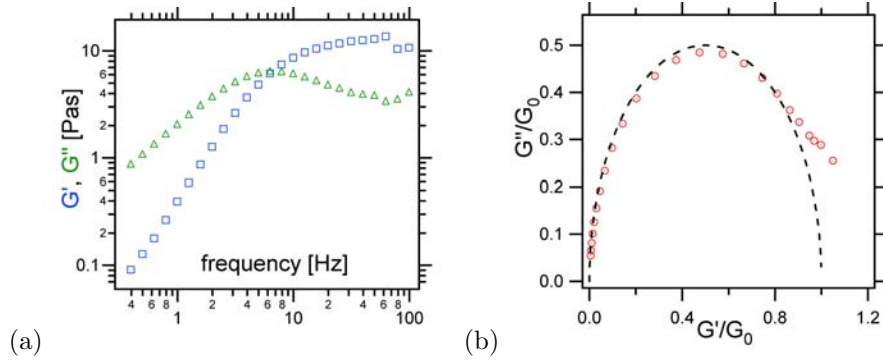
Figure 5.13: (a) Dynamic shear moduli G' ($\square$) and G'' ($\triangle$) of the shower gel. (b) Cole-Cole plot of the normalized storage and loss moduli G'/G_0, G''/G_0, where G_0 is the plateau storage modulus ($\circ$). The dashed black line shows the semicircle expected for an ideal Maxwell element.

solution with a high zero-shear viscosity and a pronounced minimum in G'' [9]. If breaking and formation of the wormlike micelles is faster than reptation of the micelles, the linear viscoelastic properties of worm-like micellar solutions are known to correspond to those of a Maxwell element with a monoexponential stress relaxation function. Then, the normalized relaxation spectrum describes a semicircle in a Cole-Cole plot, where G''/G_0 is plotted against G'/G_0 and G_0 is the storage modulus in the stress plateau region [9]. The measurement of the dynamic modulus with the rotational oscillatory rheometer shown in fig. 5.13a and the appendant Cole-Cole plot in fig. 5.13b show, that the shower gel indeed exhibits the expected properties of a WLM-solution. In steady shear, the shear forces can rupture the wormlike micelles so that entanglement points are released if the shear forces exceed a certain threshold. This leads to an extreme shear thinning in such solutions with a shear viscosity exponent near zero ($n \approx 0$). A viscosity exponent $n < 0$ has been proposed for WLM-solutions, which leads to shear-banding [29]. As the worm-like micelles can be newly formed again, the high zero shear viscosity η_0 is quickly recovered when the shear rate is reduced. The steady-state shear viscosity measured with the conventional cone-plate rheometer shows the expected strong shear-thinning behaviour with a powerlaw exponent $n \approx 0$ (green squares in fig. 5.14 c,d).

The measurements with the WLM-solution have been performed in the simple tube setup with tubes of $d = 1/32$ inch diameter and a length of $L_a = 15$ cm and $L_r = 30$ cm. For each measurement point, a fixed amount of 0.5-12 ml WLM-solution was pumped through the T-crossing with a syringe pump, and the amount of fluid flowing through the reference and the analyzer tube was measured by weighing the collected fluid. Measurements with a 50% w/w. glycerol solution were performed to determine the Newtonian flowrate ratio X_N in good agreement with the expected theoretical value of $X_N = L_r/L_a = 2$ (see fig. 5.14a, $\bullet$). Starting from $X \approx X_N$, the data for the WLM-solution show a
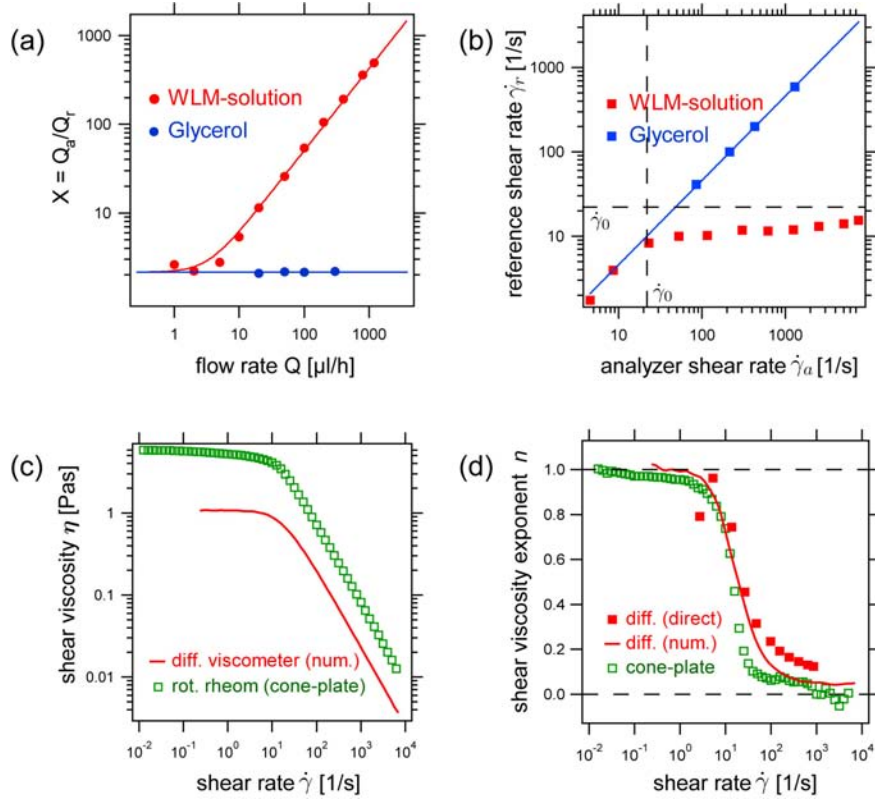
Figure 5.14: Viscosity measurements with a WLM-solution in the tube-setup: (a) Flowrate ratio for 50% (w/w) glycerol solution (•) to determine X_N and for the WLM-solution (•). (b) The shearrates according to the measurments in (a) show a stagnation of the flowrate in the reference channel once $\dot{\gamma} \approx 20\,\mathrm{s}^{-1}$ is exceeded in the analyzer channel. (c) Shear viscosity $\eta(\dot{\gamma})$ determined in the cone plate rheometer (□) and differential viscometer (red line). The differential viscometer curve contains an arbitrary offset, as the absolute value is not determined in the differential measurement. (d) Local power-law index n of the shear viscosity as determined in the cone-plate rheometer (□) and in the microfluidic viscometer (red). The directly determined values according to eq. 5.8 (■) are compared with the result of the numerical method (solid red line).

strong increase of the flowrate ratio with a more than 500-fold higher flowrate in the analyzer channel at high flowrates (fig. 5.14a, •). The comparison of the appendant shear rates (■) in fig. 5.14b shows, that once the shear rate in the analyzer channel gets higher than $20\,\mathrm{s}^{-1}$, the shearrate in the reference channel stagnates. This corresponds with the onset of the strong shear thinning in the viscosity curve at $\dot{\gamma} \approx 20\,\mathrm{s}^{-1}$ in fig. 5.14c. Obviously, with increasing Q more

and more fluid is flowing through the analyzer channel while Q_r stays approximately constant. This indicates a plateau in the $p(Q)$-curve of the analyzer channel, that corresponds to the typically observed shear stress plateau $\sigma(\dot{\gamma})$ in wormlike micellar solutions. Functionally, the parallel circuit element K_a with a lower hydrodynamic resistance operates as a flow and pressure limiter for the reference channel K_r with the WLM-solution.

From the measured flowrate ratios the values for the shear exponent n have been evaluated according to eq. 5.8 (fig. 5.14d, ■) and compared to the values determined from the cone-plate rheometer measurement (□). Due to the strong shear thinning, the flowrate interval $[\dot{\gamma}_r; \dot{\gamma}_a]$ gets very large (see fig. 5.14b). For the derivation of eq. 5.8 the shear viscosity is assumed to follow a power-law within $[\dot{\gamma}_r; \dot{\gamma}_a]$. This assumption gets increasingly poor for higher shear rates $\bar{\dot{\gamma}}$. Consequently, the sharp transition from $n \approx 1$ to $n \approx 0$ measured with the cone-plate rheometer gets smeared out in the differential measurement yielding systematically higher values $n > 0$ for high shear rates. A geometry with a smaller Newtonian flowrate ratio $X_N < 2$ would allow for a more accurate measurement of n.

Numerical evaluation of shear exponent n
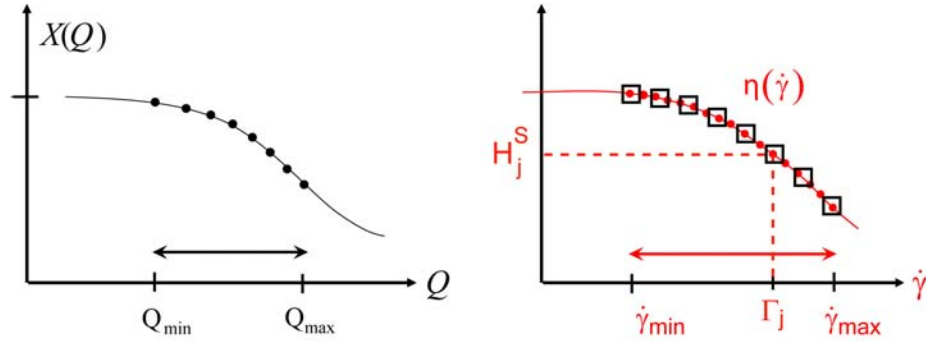
Figure 5.15: Schematics of the numerical evaluation method: The N measurement values of X on $[Q_{\min}, Q_{\max}]$ (●, left) correspond to $2N$ unknown viscosity values at $2N$ shearrates on $[\dot{\gamma}_{\min}; \dot{\gamma}_{\max}]$ (●, right). The $2N$ viscosity values are apporoximated by interpolation between N viscosity values (□), for which a linear equation system containing the N measured values for X can be solved.

To circumvent this problem without changing the setup-geometry, a numerical method to determine η and n has been developed in cooperation with Christian Cyron[1]. By simultaneously using N measured values of X on an interval $[Q_{\min}; Q_{\max}]$ it is possible to determine $j = 1 \ldots N$ interpolation values H_j^S for the shear viscosity on the interval of shear rates $[\dot{\gamma}_{\min}; \dot{\gamma}_{\max}]$ associated with $[Q_{\min}; Q_{\max}]$. Instead of assuming a powerlaw, the method is based on a

---

[1] TUM, Institute for Computational Mechanics, Chair of Prof. W.A. Wall

linear interpolation for the logarithmic values of the viscosity between the N values H_j^S. Due to the differential nature of the measurement, the resulting viscosity curve is indefinite in its absolute value, yet the shape of the viscosity curve and the corresponding values for the viscosity exponent n are fixed. As the viscosity must be monotonic on each of the interpolated intervals $[\dot{\gamma}_j, \dot{\gamma}_{j+1}]$ once the width of the shear rate intervals $(\dot{\gamma}_{\min} - \dot{\gamma}_{\max})/(N - 1)$ is sufficiently small, the method gives much more accurate values than the direct evaluation with eq. 5.8. With the $p(Q)$-curve being monotonically increasing, the roughness of $X(Q)$ is physically limited, so that strong fluctuations in X have to be attributed to experimental error (see discussion in section C.6). Therefore, with a sufficient density of measurement values on $[Q_{\min}; Q_{\max}]$, the N measurement values $X_j(Q)$ can be fitted with a smoothing function without losing information on the viscosity. A more detailed explanation of the numerical method is given in section 5.4.2. The solid red line in fig. 5.14a shows a polynomial fit of order 7 to the measured values, the resulting curves for the viscosity η and the viscosity exponent n are shown by the red lines in fig. 5.14c,d. The numerical method reproduces the low values of $n \approx 0$ observed for high shear rates with the rotational rheometer, and the shape of the viscosity curve $\eta(\gamma)$ from the differential measurement is in excellent agreement with the cone-plate rheometer values.

The powerlaw index n can thus be determined in an approach that is open to miniaturisation and parallelization, the measurement can be performed online and in series.

5.4   *Differential Extensional Rheometer*

As introduced in sec. 3.3.1 the extensional viscosity Λ is defined as the material function relating the first normal stress difference in uniaxial extensional flow with the extension rate $\dot{\epsilon}$. It is experimentally challenging to design a flow geometry creating a homogeneous uniaxial extensional flow to measure $\Lambda(\dot{\epsilon})$. Filament stretching rheometers of the Meissner or Muenstedt type [74] require a high sample viscosity and are thus only suited for polymer melts and not for (semi-)dilute polymer solutions. In a Capillary Breakup Extensional Rheometer (CaBER) the extension rate is established by the surface tension and the viscosity of the fluid itself, so that the measurement of $\Lambda(\dot{\epsilon})$ cannot be done over a range of rates $\dot{\epsilon}$. Moreover, sample necking inhibits measurements for low viscosity fluids [8]. If the fluid compartments are surface active or form a film at the air-water interface, CaBER measurements can be distorted by rheological properties of the surface films.

As an alternative, an estimate of the extensional viscosity can be evaluated by determining the hydrodynamic resistance $R_{hyd,ent}$ associated with the pressure drop P_{ent} across the converging section of a channel, especially in a flow regime where other methods do not work well [33]. A constant, tunable extension rate can be imposed on the fluid by using hyperbolic constrictions, which consist of two consecutive dies with hyperbolic shape $D(z) = \frac{a}{z}$, where D is

the cross sectional area of the die and a is a shape parameter (see fig. 5.16). By using analyzer and reference channels with such hyperbolic constrictions,
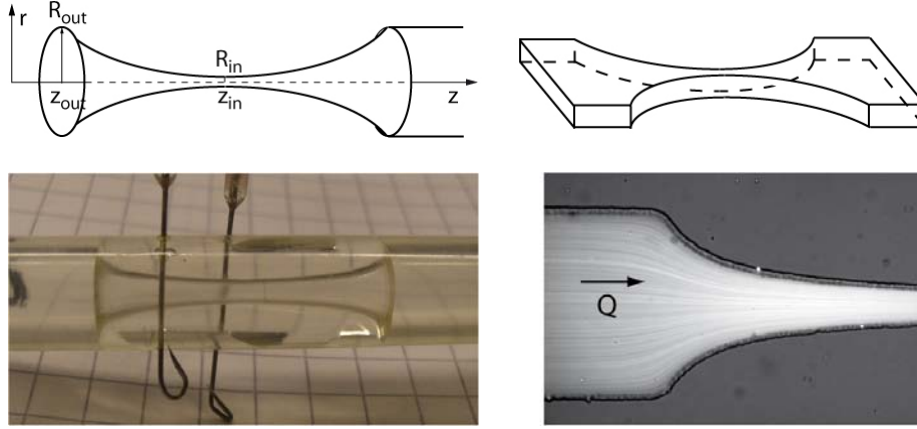
Figure 5.16: Channel constrictions with hyperbolically varying cross sections $D(z) = \frac{a}{z}$. Each constriction is made of two identical opposing dies. Left: Cylindrical constriction with semihyperbolically changing radius $R(z) \sim 1/\sqrt{z}$. The constriction shown in the photography has an outer radius $R_{out} = 3.25\,\mathrm{mm}$ and an inner radius $R_{in} = 0.73\,\mathrm{mm}$, which corresponds to a Hencky srain of $\epsilon = 3$, the shape constant is $a = 12\,\mathrm{mm}^3$. As the PDMS constriction is not covalently bound to the surrounding polyethylen tube it is fixed by syringe needles to prevent a slipping along the tube at higher operating pressures. Right: Microfluidic rectangular constriction with constant channel height h and hyperbolically varying width w. The picture shows a microscopy image of a 0.1 % (w/w) PAA solution flowing through a constriction with $h = 50\,\mu\mathrm{m}, w_{out} = 400\,\mu\mathrm{m}, w_{in} = 40\,\mu\mathrm{m}$, shape constant $a = 2.2 \cdot 10^{-3}\mathrm{mm}^3$ and Hencky strain $\epsilon = 2.3$. The streamlines of the polymer solution are visualized by fluorescent marker particles and approximately follow the shape of the channel.

the concept of the differential shear viscometer described in sec. 5.3 can be extended towards measuring $\Lambda(\dot{\epsilon})$. As a drawback of the converging die methods, the no-slip boundary condition at the channel wall will inescapably generate a region dominated by shear flow near the walls with a non-negligible component of rotational flow. Even for a hyperbolic die with complete wall slip the resulting pressure driven flow through the constriction will not be completely shear free [8]. Thus, the flow within the channel constriction is not an ideal, rotation free, uniaxial extensional flow and the contribution of the shear flow component to the pressure drop P_{ent} has to be considered.

5.4.1 Determination of Extensional Viscosity from Entrance Pressure Drops

The extensional viscosities Λ, Λ_p are defined as the first normal stress differences in uniaxial extensional and planar extensional flow (see 3.3.1). To determine the extensional viscosity from the entrance pressure drop in a converging channel, we consider cylindrical converging dies and rectangular converging dies with constant channel height h. In these constrictions, the flow is considered as a superpositon of a pure shear flow and an uniaxial extensional flow resp. a planar extensional flow. A schematic picture and an experimental realisation of a cylindrical hyperbolic channel constriction is shown in fig. 5.16.

Hencky Strain and Extension Rate in Hyperbolic Constriction

The extensional *Hencky strain* ϵ is defined by $\epsilon = \int \mathrm{d}\epsilon = \int \frac{\delta L}{L}$ where δL is the incremental length change of a fluid element of length L in the extensional direction. Thus, a total extension by a factor λ from $L \to \lambda L$ corresponds to a total extensional strain of $\epsilon = \ln \lambda$. Volume conservation requires that a fluid slice at the entrance of the hyperbolic constriction with cross-section D_{out} and length $\mathrm{d}z$ gets stretched to a length $\lambda \mathrm{d}z = (D_{\text{out}}/D_{\text{in}})\mathrm{d}z$ at the narrow end of the constriction, so that the total Hencky strain of the constriction is $\epsilon = \ln(D_{\text{out}}/D_{\text{in}})$.

The averaged local extension rate $\bar{\dot{\epsilon}}$ in the converging channel is determined by differentiating the averaged flow velocity $\bar{u} = Q/D(z)$ with respect to the flow direction z [33]. In a hyperbolic constriction with $D(z) = a/z$ the average extension rate of the fluid is thus constant along the converging region:

$$\bar{\dot{\epsilon}}(z) = \frac{\partial \bar{u}}{\partial z} = \frac{\partial}{\partial z} \frac{Q}{D} = \frac{\partial}{\partial z} \frac{Qz}{a} = \frac{Q}{a}. \qquad (5.14)$$

Contributions of Shear and Extensional Resistance to the Entrance Pressure Drop

For the determination of the extensional viscosity from the entrance pressure drop it is assumed, that mixed flow effects can be neglected, so that the shear viscosity of the fluid is unaffected by the simultaneous extensional flow and vice versa. A detailed discussion of this assumption will be given in section 5.4.6. Therefore, the pressure drop across a converging die associated with a flowrate Q can be divided into two terms

$$P^{ent} = P_S^{ent} + P_E^{ent}, \qquad (5.15)$$

which correspond to the shear resistance $R_S = P_S^{ent}/Q$ and the extensional resistance $R_E = P_E^{ent}/Q$ of the channel constriction. The contributions P_S^{ent} and P_E^{ent} have been calculated for both cylindrical and rectangular channel constrictions in section C.3 adapting the treatment of tapered channels given in [33]:

The shear and extensional resistance of a power-law fluid flowing through the constriction can be expressed as (eqs. C.28, C.29):

$$R_S^{ent} = \frac{P_S^{ent}}{Q} = \eta(\dot{\gamma}_{in}) \frac{a}{D_{in}^3 f_{hyp}(n)}; \quad R_E^{ent} = \frac{P_E^{ent}}{Q} = \frac{\Lambda(\bar{\dot{\epsilon}})}{a} \ln \frac{D_{out}}{D_{in}}, \quad (5.16)$$

where the shape factor $f_{hyp}(n)$ depends on the geometry of the cross section and the power-law index n. The associated shear- and extension rates $\dot{\gamma}, \bar{\dot{\epsilon}}$ in the die are given by (see eqs. 3.20, 5.14)

$$\dot{\gamma} = \frac{Q}{\tilde{h}_{in}^3} F_{\dot{\gamma}}^{hyp}(n), \qquad \bar{\dot{\epsilon}} = \frac{Q}{a} \quad (5.17)$$

where $F_{\dot{\gamma}}^{hyp}(n)$ depends on the die geometry and the power-law index n.

In the cylindrical constriction in fig. 5.16 left the fluid flowing through the narrowing die subsequently flows through an expanding die which is equivalent to the narrowing die with reversed flow direction. Assuming fully developed flow profiles, the shear resistance R_S of the entire constriction is thus twice the resistance of the narrowing die: $R_S = R_S^{ent} + R_S^{ex} = 2R_S^{ent}$. While the average extensional flow in the converging die corresponds to an uniaxial elongational flow with $\bar{\dot{\epsilon}}$ and strain ϵ, the flow in the expanding die corresponds to a biaxial extension with extensional rate and Hencky strain of only $\bar{\dot{\epsilon}}_{ex} = \frac{1}{2}\bar{\dot{\epsilon}}$, $\epsilon_{ex} = \frac{1}{2}\epsilon$. Hence, the pressure drop of the extensional contribution in the expanding die is expected to be much smaller than in the narrowing die and can usually be neglected [33]. The extensional resistance is thus dominated by the contribution of the entrance flow in the narrowing die: $R_E = R_E^{ent} + R_E^{ex} \approx R_E^{ent}$. Contrary, in the rectangular hyperbolic geometry (fig. 5.16 right), the fluid in the expanding die undergoes a planar extension with the same extension rate and total extensional strain as in the narrowing die. Thus, in a first approximation the pressure contribution from the expanding die can be estimated to be approximately equal to the pressure drop in the narrowing die ($R_E = R_E^{ent} + R_E^{ex} \approx 2R_E^{ent}$). As the direction of extension is now perpendicular to the channel axis instead of parallel and due to flow history effects the pressure drop in the expanding die is expected to be smaller nevertheless if mixed flow effects are non-negligible (see discussion in section 5.4.6).

Altogether, a symmetrical hyperbolic constriction composed of a narrowing and a subsequent extending die then has a shear resistance of $R_S^{hyp} = 2R_S^{ent}$ and an approximate extensional resistance of $R_E = bR_E^{ent}$ where b depends on the flow type given by the flow geometry:

$$b \approx \begin{cases} 1 & \text{for uniaxial extensional flow} \\ 2 & \text{for planar extensional flow} \end{cases} \quad (5.18)$$

With eqs. 5.16, the elongational viscosity can be calculated from the total pressure drop P^{ent} if the shear viscosity of the fluid is known. For Newtonian fluids, the calculations for constrictions with shape factors a applicable in practice show, that the contribution of the extensional resistance is negligible with

respect to the shear resistance for both cylindrical (eq C.19) and rectangular (eq C.27) constrictions. Therefore, the entrance pressure drop can only be used to measure $\Lambda(\dot{\epsilon})$ for non-Newtonian fluids in a regime where the Trouton ratio is high.

5.4.2 Working Principle of Differential Extensional Rheometer

The differential extensional rheometer expands the working principle of the differential shear rheometer towards measuring the extensional viscosity:

- In the differential shear rheometer, analyzer and reference channel have different lengths L_a, L_r, which leads to different hydrodynamic resistances $R_a \propto L_a \eta(\dot{\gamma}_a), R_r \propto L_r \eta(\dot{\gamma}_r)$ and different shear rates $\dot{\gamma}_a, \dot{\gamma}_r$ in the channels. For Newtonian fluids with constant shear viscosity $\eta(\dot{\gamma}_a) = \eta(\dot{\gamma}_r)$, the measured flowrate ratio $X_N = Q_a/Q_r = R_r/R_a = L_r/L_a$ in analyzer and reference channel is therefore different from the flowrate ratio for non-Newtonian fluids $X = (L_a \eta(\dot{\gamma}_a))/(L_r \eta(\dot{\gamma}_r))$, where the viscosity changes with the shear rate and $\eta(\dot{\gamma}_a) \neq \eta(\dot{\gamma}_r)$. Thus, the flowrate ratio X gives a measure for the local powerlaw index n of the shear viscosity expressing how non-Newtonian the shear viscosity is.

- In the differential extensional viscometer the fluid in analyzer and reference channel flows through constrictions with the same extensional strains. However, the different shape constants $a_{a,r}$ in the constriction geometries generate different extension rates $\dot{\epsilon}_{a,r}$ in analyzer and reference channels (see fig. 5.17). For a Newtonian fluid, where the extensional visosity $\Lambda(\dot{\epsilon}_a) = \Lambda(\dot{\epsilon}_r)$ is constant and independent of the extension rate, the flowrate ratio $X_N = R_r/R_a$ is therefore different from the flowrate ratio X for a non-Newtonian fluid with $\Lambda(\dot{\epsilon}_a) \neq \Lambda(\dot{\epsilon}_r)$. Thus, the measured flowrate ratio X depends on the ratio $\Lambda(\dot{\epsilon}_a)/\Lambda(\dot{\epsilon}_r)$, which can be expressed by the local power-law index k of the extensional viscosity. As not only the extension rates $\dot{\epsilon}_{a,r}$ but also the shearrates $\dot{\gamma}_{a,r}$ in reference and analyzer channels are different, the flowrate ratio X depends on both k and n and on the ratio of the viscosities $\Lambda(\Lambda(\dot{\epsilon}_{a,r})/\eta(\dot{\gamma}_{a,r}))$. Thus the analysis to extract k and Λ from a measurement of $X(Q)$ is more complicated than in the differential shear rheometer. Generaly, X gives a combined measure for the non-Newtonian characteristics of η and Λ. Analogous to the differential shear viscometer, relative values Λ/η and slopes of the $\Lambda(\dot{\epsilon})$ and $\eta(\dot{\gamma})$ curves can be directly determined from measured X-values and pressure measurements are only required to extract absolut values for Λ and η.

In the following we will discuss how the extensional viscosity Λ can be extracted from a measurement in a properly designed differential extensional viscometer, where the analyzer and reference channels contain constrictions with hyperbolically varying cross sectional area $D(z) = a/z$.

5.4.3 Design of Experimental Measurement Geometries

Differential microfluidic devices with hyperbolic constrictions were tested both in cylindrical and rectangular cross sectional geometry. The latter were fabricated with PDMS molds bonded to glass slides with the standard microfluidic lithography procedure. The cylindrical channels with constrictions were build by filling PVC tubes with PDMS using removable brass molds (see fig.2.1 in section 2). While the outer and inner cross sections D_{out}, D_{in} of all constrictions in one device were equal, the shape constants $a_a \neq a_r$ were chosen to be different in analyzer and reference channel. Analyzer and reference channel contained one or more identical constrictions in series with N_a, N_r indicating the number of constrictions. The hyperbolic sections, the feeding channel and the detection zone were connected by straight channel segments with a shared equal constant cross section D_{out}. The total length $L_{a,r}$ of these connecting channels was chosen such, that their ratio in analyzer and reference channel L_a/L_r is given by

$$\frac{L_a}{L_r} = \frac{N_a a_a}{N_r a_r}.$$ (5.19)

This ensures, that the total shear resistance in the connecting straight segments in analyzer and reference channel has the same ratio as the total shear resistance of the constriction segments (given the same power-law index n describes the viscosity at the representative wall shear rates in the straight parts and the constrictions). Especially an equal length of the connecting channels $L_a = L_r$ is of advantage in designing a microfluidic device, because then the shear resistances of reference and analyzer channel are equal ($R_{Sr} = R_{Sa}$) if the flowrates are equal ($Q_a = Q_r$). As the extensional resistance for a Newtonian fluid in the hyperbolic constrictions is negligible (see eqs. C.19, C.27), this results in an equal, constant Newtonian flowrate ratio $X_N = R_r/R_a \approx R_{Sr}/R_{Sa} = 1$. Only if the Trouton ratio increases significantly ($\Lambda(\dot{\epsilon})/\eta(\dot{\epsilon}) \gg 3$), the flowrate ratio changes ($X \neq 1$), indicating a high, non-negligible extensional viscosity.

For the experiments, three basic sets of constrictions were designed: A rectangular set with extensional strain $\epsilon = 3.0$ and two circular sets with strains $\epsilon = 3.0$ and $\epsilon = 4.2$. For each set, three types of constrictions (S, M, L) with equal cross sections D_{out}, D_{in} and different shape factors a were produced. These basic shapes S, M, L were combined in various ways for the differential devices. Fig. 5.17 exemplarily shows a differential viscometer where 4 constrictions of type S were combined in series for the analyzer channel and one constriction of type L was used for the reference channel ($N_a = 4, N_r = 1, a_r = a_L = 4a_a$, "4xS vs. L' - setup). In this design, the total length of reference and analyzer channel is equal resulting in $X_N = 1$. The geometric properties of all constrictions used are listed in table 5.1, and an overview over the different combinations of the constrictions used in the setups is given in table 5.2. The experimental setup for the determination of the flowrate ratio was equivalent to the setup used in the differential shear viscometer with rectangular channels. The setups with cylindrical cross sections were run analogously to the simple tube setup of the shear viscometer (see sec. 5.3.3).

constriction			geometrical properties			
type	shape	flow type	$a\,[\mathrm{mm}^3]$	ϵ	$D_{\mathrm{out}}\,[\mathrm{mm}^2]$	$D_{\mathrm{in}}[\mathrm{mm}^2]$
S			$4.21 \cdot 10^{-3}$			
M	rect.	planar ext.	$8.42 \cdot 10^{-3}$	3.0	$4.0 \cdot 10^{-2}$	$2.0 \cdot 10^{-3}$
L			$1.68 \cdot 10^{-2}$			
S			6.0			
M	circ. 1	uniax. ext.	12	3.0	33.2	1.66
L			24			
S			6.0			
M	circ. 2	uniax. ext.	12	4.2	33.2	1.66
L			24			

Table 5.1: Properties of the hyperbolic constrictions used in the experiments. The rectangular constrictions change from a cross section of $800\,\mu\mathrm{m} \times 50\,\mu\mathrm{m}$ to $40\,\mu\mathrm{m} \times 50\,\mu\mathrm{m}$. The circular constrictions of type 1 and 2 have outer radii of 3.25 mm and inner radii of 0.726 and 0.4 mm.

Figure 5.17: Lithography mask showing the geometry of the microfluidic rectangular "4xS vs. L" - setup. The device fulfills the condition given in eq. 5.19, which results in a Newtonian flowrate ratio $X_N = 1$. As the extensional resistance of the channels is negligible as long as the Trouton ratio is small, a deviation from X_N can be directly associated with a high non-Newtonian extensional viscosity.

FEM-simulations of the geometries were performed to determine the geometry factors $f_{\mathrm{hyp}}, F_{\mathrm{hyp}}$ of the constrictions. Fig. 5.18 shows the resulting pressure drop and fluid velocity at the channel center line for a Newtonian fluid in the planar (left) and circular (right) constriction. Inside the converging section, the velocity rises linearly along the channel, which corresponds to the desired constant extension rate of the fluid. The course of the pressure drop in the circular constriction shows, that the shear resistance in the connecting channel with constant radius r_{out} can be neglected. The ratio of shear and extensional resistance for a Newtonian fluid $(R_E/R_S)_N$ was determined with the simulations as $(R_E/R_S)_N = 5.3 \cdot 10^{-4}$ for the rectangular constrictions of shape S,

setup	N_a	N_r	a_r/a_a
4xS vs. L	4	1	4
2xM vs. L	2	1	2
M vs. 2xS	1	2	0.5
3xS vs. L	3	1	4

Table 5.2: Overview of the geometric properties of the differential viscometer setups tested in the experiments.

$(R_E/R_S)_N = 2.23 \cdot 10^{-3}$ and $2.6 \cdot 10^{-2}$ for the circular constrictions of type M with $\epsilon = 4.2$ and $\epsilon = 3.0$.
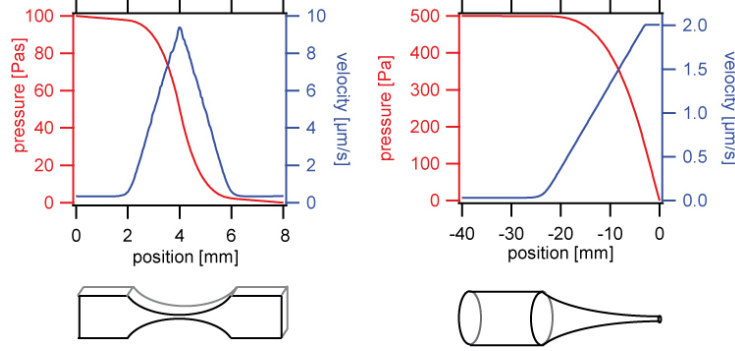
Figure 5.18: Results of a FEM-simulation for the hyperbolic rectangular constriction with $\epsilon = 3.0$ (left) and for the converging half of a circular semi-hyperbolic $\epsilon = 4.2$ constriction (right). Both constrictions shown are of type M. The graphs show the evolution of the pressure (red curves) and the fluid velocity (blue curves) along the center lines of the constrictions.

5.4.4   Data Evaluation Methods

The total resistance of analyzer and reference channel is given by the sum of the shear and extensional resistances

$$R_{a,r} = R_{Sa,r}(\eta(\dot{\gamma}_{a,r})) + R_{Ea,r}(\Lambda(\dot{\epsilon}_{a,r})). \tag{5.20}$$

The shear resistance of a constriction is dominated by the wall shear rate $\dot{\gamma}_w$ at the tightest part of the constriction. Therefore, the shear resistance of the constrictions is mainly determined by the viscosity values $\eta(\dot{\gamma}_{wr})$, $\eta(\dot{\gamma}_{wa})$, which will be referred to as $\eta(\dot{\gamma}_r)$, $\eta(\dot{\gamma}_a)$ in the following. Then, each measurement value $X(Q) = R_r(Q_r)/R_a(Q_a)$ is determined by the four unknown viscosity values $\eta(\dot{\gamma}_a), \eta(\dot{\gamma}_r), \Lambda(\dot{\epsilon}_a), \Lambda(\dot{\epsilon}_r)$:

$$X(Q) = \frac{R_r(Q_r)}{R_a(Q_a)} = \frac{R_{Sr}(\eta(\dot{\gamma}_r)) + R_{Er}(\Lambda(\dot{\epsilon}_r))}{R_{Sa}(\eta(\dot{\gamma}_a)) + R_{Ea}(\Lambda(\dot{\epsilon}_a))} \tag{5.21}$$

The shear and extension rates can be determined from $X(Q)$ with eqs. 5.6 and 5.17. As the method is differential, $X(Q)$ contains no information on the absolute viscosity values and only relative values $\Lambda(\dot{\epsilon})/\eta(\dot{\gamma})$ can be determined. Yet, even for relative values eq. 5.21 is underdetermined, so that no values for $\Lambda(\dot{\epsilon})/\eta(\dot{\gamma})$ can be extracted from a single measurement.

By assuming power-laws for the viscosities $\eta(\dot{\gamma}), \Lambda(\dot{\epsilon})$, the viscosity values $\eta(\dot{\gamma}_a), \eta(\dot{\gamma}_r)$ and $\Lambda(\dot{\epsilon}_a), \Lambda(\dot{\epsilon}_r)$ can be related by the power law exponents n, k. By connecting measurements at three different flowrates $X_1(Q_1), X_2(Q_2), X_3(Q_3)$

an analytical equation can be found for the relative viscosity $\Lambda(\dot{\epsilon})/\eta(\dot{\gamma})$. If n is known from a differential shear viscometer, two values of X are sufficient. If absolute values for $\eta(\dot{\gamma})$ have been determined with a cone-plate rheometer, two values X_1, X_2 are sufficient to calculate absolute values for $\Lambda(\dot{\epsilon})$. The analytical solution is given in the appendix C.5.

Due to the threshold-type behaviour of the extensional viscosity especially of dilute polymer solutions the power-law description of the extensional viscosity is a poor approximation in the vicinity of the onset of the rise in $\Lambda(\dot{\epsilon})$. For evaluation of the experimental data the semianalytical solution proved impractictal and repeatedly resulted in negative or imaginary viscosity values.

Numerical Method for Evaluation of $X(Q)$-Data Differential Extensional Viscometer Data

To circumvent this problem, a numerical method to evaluate $X(Q)$ analogous to the one introduced in sect. 5.3.6 for the differential shear viscometer has been developed in cooperation with Christian Cyron[2], which does not require a powerlaw description of the viscosity functions $\eta(\dot{\gamma}), \Lambda(\dot{\epsilon})$. The concept of the method is illustrated in fig. 5.19: The flow rate ratio is measured on an interval $[Q_{\min}; Q_{\max}]$ with N measurement values $X_i(Q_i)$ (left). These measurement values are associated with $4N$ unknown viscosity values. The $4N$ unknowns are reduced to N unknowns by interpolation between N basic values for the viscosity, and a linear equation system can be formulated and numerically solved. The detailed explanation of the method is discussed in the appendix (5.4.4).
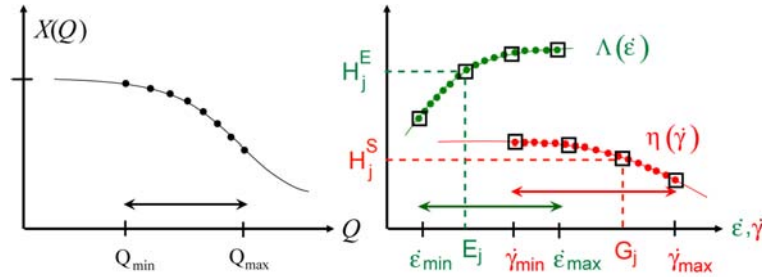
Figure 5.19: N measurement points $X_i(Q)$ (shown left) correspond to $4N$ unknown viscosity values $\Lambda(\epsilon_{a,ri}), \eta(\gamma_{a,ri})$ represented by the filled circles on the viscosity curves (right). The unknowns are reduced to N values by interpolation between the N viscosity values H_j^E, H_j^S.

As the possible values for the slope of the viscosity functions are limited, $\eta(\dot{\gamma})$ and $\Lambda(\dot{\epsilon})$ can be approximated by a sufficient number of interpolation values. Conversely, it can be shown that the slope of $X(Q)$ is limited by the condition:

$$-\frac{X(X+1)}{Q} \leq \frac{\mathrm{d}X}{\mathrm{d}Q} \leq \frac{X+1}{Q} \tag{5.22}$$

---

[2] TUM, Institute for Computational Mechanics, Chair of Prof. W.A. Wall

(see sect. C.6). Thus, high local variations in $X(Q)$ can be attributed to the measurement uncertainty, so that a smoothed function $\tilde{X}(Q)$ can be determined from $X(Q)$ and used for the data evaluation.

For the experiments, fluids with Newtonian shear viscosity have been used where R_{Sa}, R_{Sr} are independent of the shear rates $\dot{\gamma}_a, \dot{\gamma}_r$. Then, the numerical method directly yields values for $R_E(\dot{\epsilon})/R_S$ for the constrictions on the measurement interval $[\dot{\epsilon}_{\min}; \dot{\epsilon}_{\max}]$. With the Newtonian values for $(R_E/R_S)_N$ known from the FEM-simulations, the extensional visosity can be calculated from its Newtonian value $\Lambda_N = 3\eta$, resp. $\Lambda_p = 2\eta$, which has been determined in a cone-plate rheometer:

$$\Lambda(\dot{\epsilon}) = \Lambda_N \frac{R_E(\dot{\epsilon})/R_S}{(R_E/R_S)_N} = (3+b)\eta \frac{R_E(\dot{\epsilon})/R_S}{(R_E/R_S)_N} \tag{5.23}$$

where $b = 0$ for uniaxial extensional flow and $b = 1$ for planar extensional flow. However, the relative hydrodynamic resistance $R_E(\dot{\epsilon})/R_S$ is not necessarily uniquely defined by the linear equation system derived for the measured values $X_i(Q)$. This problem can be overcome if the measurement interval $[Q_{\min}; Q_{\max}]$ includes the range of low shear and extension rates where the analyte solution behaves Newtonian $\Lambda = \Lambda_N = (3+b)\eta$. Alternatively, measurements $X(Q), Y(Q)$ from two different measurement geometries can be combined to extract a unique solution for $R_E(\dot{\epsilon})/R_S$ (see discussion in C.7).

In principle, the derivation of $\Lambda(\dot{\epsilon})$ can be done analogously for fluids with non-Newtonian shear viscosity $\eta(\dot{\gamma})$. However, for an arbitrary shape of the shear viscosity function it could not be shown whether the solution $R_E(\dot{\epsilon})/R_S(\dot{\gamma})$ determind by solving the linear equation system is generally unique. Still, from the measured $X(Q)$ - curves it can be concluded if the Newtonian regime is included in the measured interval:

In the trivial case, that the contribution of the extensional viscosity to the flow resistance $R_{Ea,r}$ is negligible with respect to the shearflow resistance $(R_{E0}/R_{S0} \to 0)$, eq. (C.40) reduces to eq. (5.7): $X = \frac{L_r}{L_a} X^{1-n}$, which yields the shearflow power-law index $n = \frac{\ln(L_r/L_a)}{\ln X}$ analogous to the differential shear viscometer. For a Newtonian fluid with $n = k = 1$, eq. (C.40) gives

$$X_N = \frac{L_r}{L_a} \frac{1 + \frac{a_a}{a_r} \frac{R_{E0}}{R_{S0}}}{1 + \frac{a_r}{a_a} \frac{R_{E0}}{R_{S0}}} \tag{5.24}$$

As shown in eqs. (C.19, C.27), for constrictions with $D_{\mathrm{out}}/D_{\mathrm{in}} > 10$ and a maximum steepness of the constriction given by a wall slope of 2, the extensional resistance can usually be neglected yielding $X_N \approx \frac{L_r}{L_a}$. Thus, if the flowrate ratio $X(Q)$ equals the Newtonian value $X(Q) = X_N = \frac{L_r}{L_a}$ over a certain interval of flowrates, it can be concluded that the extensional resistance is negligible and the shear viscosity $\eta(\dot{\gamma})$ of the fluid is in the Newtonian range at the according shear rates. As both shear and extensional viscosity can be assumed to be steady functions, a unique solution for the relative values of $\Lambda(\dot{\epsilon})/\eta(\dot{\gamma})$ can then be determined from the differential measurements starting from the known Newtonian Trouton ratio.

Empirical Approximation Method

For many complex fluids, an educated guess for the overall shape of the extensional viscosity curve $\Lambda(\dot{\epsilon})$ and thus the $R_E(\dot{\epsilon})/R_S(\dot{\gamma})$ function can be made. Then, a quantification of Λ can be achieved by putting the assumed viscosity functions into the flow rate ratio equation eq. 5.21 and calculating the expected $X(Q)$-values. By comparing the obtained $X_{\text{rev}}(Q)$ values, the paramters of the input viscosity functions can be gradually adjusted until a match of the theoretical and the measured curves is achieved ($X(Q) \approx X_{\text{rev}}(Q)$). Due to the differential nature of the measurement, any multiple $(\eta', \Lambda') = c \cdot (\eta, \Lambda)$ results in the same flowrate ratios as (η, Λ), so that an absolute value for $\Lambda(\dot{\epsilon})$ can be extracted only with a known shear viscosity value $\eta(\dot{\gamma}_0)$. Still, the obtained solutions of this reverse method are not necessarily unique.

5.4.5 Experimental Results & Discussion

Dilute polymer solutions of $0.1\%\,(\text{w/w})\,\text{PAA}$ with high molecular weight (5-6 MDa) in water and in $80\%\,(\text{w/w})$ glycerol in water were chosen as analyte fluids. The shear viscosity was measured with a cone-plate rheometer and appeared as approximately Newtonian in the relevant range of shear rates with $\eta \approx 1.8\,\text{mPas}$ for the aqueous solution and $\eta \approx 0.1\,\text{Pas}$ for the solution in 80% glycerol. Measurements with the low-viscosity aqueous polymer solution were performed in the rectangular microfluidic setups, the polymeric glycerol solutions were measured in the circular constrictions.

Measurements in Planar Rectangular Hyperbolic Constrictions

Fig. 5.20a shows the measured flowrate ratios $X(Q)$ (blue squares) and $Y(Q)$ (red circles) in the microfluidic rectangular "2xM vs. L" and "4xS vs. L" - setups for a low viscosity aqueous 0.1% PAA solution. Smoothing functions $\tilde{X}(Q), \tilde{Y}(Q)$ were fitted to the data and are shown by the dashed red and blue lines. As expected, the flow rate ratios were observed to be approximately constant in a regime of low flow rates, which can be interpreted as a regime with negligible extensional resistance in the constrictions ($R_E/R_S \ll 1$). Experimental Newtonian values were determined directly as $X_N = \tilde{X}(Q), Y_N = \tilde{Y}(Q)$ in this constant flow rate regime. For flow rates corresponding to extension rates higher than $\dot{\epsilon} \approx 30\,\text{s}^{-1}$ a monotonic decrease is observed in $\tilde{X}(Q), \tilde{Y}(Q)$. This can be attributed to a rise in the extensional viscosity, which leads to a non-negligible extensional resistance in the constrictions: The extensional rate is higher in the steeper, short constrictions of the analyzer channel and the number of constrictions is higher in the analyzer channel ($N_a > N_r$). Therefore, the extensional resistance in the analyzer channel is higher than in the reference channel ($R_{Ea} > R_{Er}$). This leads to the measured monotonic decrease in $\tilde{X}(Q)$ and $\tilde{Y}(Q)$ with increasing Q. If the extensional viscosity $\Lambda_p(\dot{\epsilon})$ reaches a plateau value, the decreasing flowrate ratios $X(Q), Y(Q)$ are expected to saturate at a constant level again.
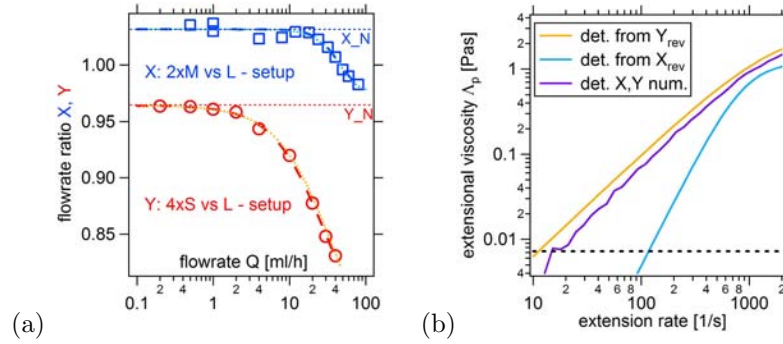
Figure 5.20: (a) Flowrate ratios $X(Q)$ (blue squares) and $Y(Q)$ (red circles) measured in a "2xM vs. L" and a "4xS vs. L" differential viscometer with rectangular planar constrictions. The analyte fluid is $0.1\%\,(\mathrm{w/w})\,\mathrm{PAA}$ in aqueous solution. Smoothing functions $\tilde{X}(Q), \tilde{Y}(Q)$ used for data evaluation are shown by the dashed blue and red curves, the dotted blue and red curves indicate the experimental Newtonian flowrate ratios X_N. The dotted light blue and orange curves indicate the flowrate ratios $X_{\mathrm{rev}}, Y_{\mathrm{rev}}$ calculated from the approximated $\Lambda(Q)$ functions shown by the light blue and orange curve in (b). (b) Apparent planar extensional viscosity determined from $\tilde{X}(Q), \tilde{Y}(Q)$. The purple line shows the numerically determined viscosity based on a combined evaluation of $\tilde{X}(Q)$ and $\tilde{Y}(Q)$. The light blue and orange curve were obtained by empirical approximation for $\tilde{X}(Q)$ and $\tilde{Y}(Q)$ seperately. The dashed black line indicates the Newtonian value of $\Lambda_p = 4\eta$.

Based on the assumption of an additivity of the extensional and the shear resistance in the channel constrictions [21], an apparent extensional viscosity can be determined from the measured curves $\tilde{X}(Q), \tilde{Y}(Q)$ following the methods described in sec. 5.4.4. To account for slight deviations between the measured and the theoretical Newtonian values for the geometry of the setups ($X_N^{\mathrm{theo}} = Y_N^{\mathrm{theo}} = 1$), a geometrical correction factor $f_c = X_N/X_N^{\mathrm{theo}}$ was introduced into the equations for the evaluation. Hereby, the factor was considered to alter solely the shear resistances $R_{Sa,r}$ without affecting the extensional resistances $R_{Ea,r}$. The extensional viscosity determined by the numerical method using $\tilde{X}(Q), \tilde{Y}(Q)$ simultaneously is shown by the purple line in fig. 5.20b. As the corresponding linear equation system has no exact solution, the curve represents a least square fit solution.

Geometry Dependence of Determined Extensional Viscosity

To check for any dependencies of the determined viscosity on the evaluation method or the setup used, an additional evaluation by empirical approximation was done for the $\tilde{X}(Q)$ and $\tilde{Y}(Q)$ curve seperately. The resulting viscosity functions are shown by the orange and light blue lines in fig. 5.20b. The dotted orange and light blue curves in fig. 5.20a show the flowrate ratios $X_{\mathrm{rev}}(Q), Y_{\mathrm{rev}}(Q)$

calculated from the approximated viscosity curves in excellent agreement with the smoothing functions $\tilde{X}(Q)$ and $\tilde{Y}(Q)$ of the experimental data.

In the Newtonian limit the extensional resistance of the constrictions is negligible with respect to the shear resistance, and R_E/R_S lies well below the measurement error of $\pm 1\%$ for the flowrate ratios $\tilde{X}(Q), \tilde{Y}(Q)$. Therefore only a significantly enhanced extensional viscosity can be detected as a deviation from X_N, Y_N, and $\Lambda_{pN} = 0$ has been assumed for the empirically approximated extensional viscosities instead of $\Lambda_{pN} = 4\eta$ for convenience. The measurement error of about 1% corresponds to a lower detection limit of $\Lambda_{\text{det}} \approx 5\Lambda_N$ for the measurements in the rectangular constrictions. Consequently, viscosity values in fig. 5.20b below 0.04 Pas can be considered artificial. The Newtonian extensional viscosity value $\Lambda_{pN} = 4\eta$ is indicated by the black dashed line.

The difference in the results for $\Lambda(\dot{\epsilon})$ obtained from the seperate evaluation of $\tilde{X}(Q)$ and $\tilde{Y}(Q)$ (light blue and orange curves in fig. 5.20b) is higher than the measurement uncertainty in X and Y suggests. Apparently, there is an inherent dependence between the measurement geometry and the obtained extensional viscosity. Most likely this is caused by the fact, that the additivity assumption of shear and extensional resistance underlying the theoretical description does not exactly hold for polymer solutions. For a more accurate data evaluation, mixed flow effects would have to be considered, which will be discussed seperately later on. Mixed flow efffects are expected to be most prominent in the planar rectangular constrictions, where the ratio of shear to extensional resistance R_S/R_E is the highest.

Measurements in Hyperbolic Constrictions with Circular Cross-section

Measurements with a 0.1% PAA in 80% glycerol solution with circular hyperbolic constrictions are shown in fig. 5.21. The measurements were performed in three different setups with a Hencky strain of $\epsilon = 4.2$ (flow rate ratios X, Y, Z shown in a) and two setups with $\epsilon = 3.0$ (X, Y shown in b). Additionally, a measurement of the overall pressure drop across the differential viscometer has been performed for the measurements in the $\epsilon = 4.2$ setups. The results are shown by the black symbols in (a), the solid black lines represent a linear pressure drop. The onset of a non-negligible extensional resistance in the constrictions should be accompanied by a nonlinear increase of the pressure curve $p(Q)$. A comparison with the flowrate ratio curves shows, that the onset of the non-Newtonian regime is much more obvious from the $X(Q), Y(Q), Z(Q)$ signals than from the $p(Q)$ curves. The expected non-linear increase in the pressure curves might be partially masked by the slight shear-thinning of the solution. As the difference in the shear rates in reference and analyzer channel is small, the shear-thinning can be neglected in the differential signal. The appendant extensional viscosities determined from the different setups and evaluation methods are shown in fig. 5.21c, the Newtonian value Λ_N is represented by the black dashed line. The uncertainty of 4% in the flowrate ratio signals yields a detection limit of $\Lambda_{\text{det}} \approx 5\Lambda_N$ and $\Lambda_{\text{det}} \approx \Lambda_N$ for the $\epsilon = 4.2$ and 3.0 setups.
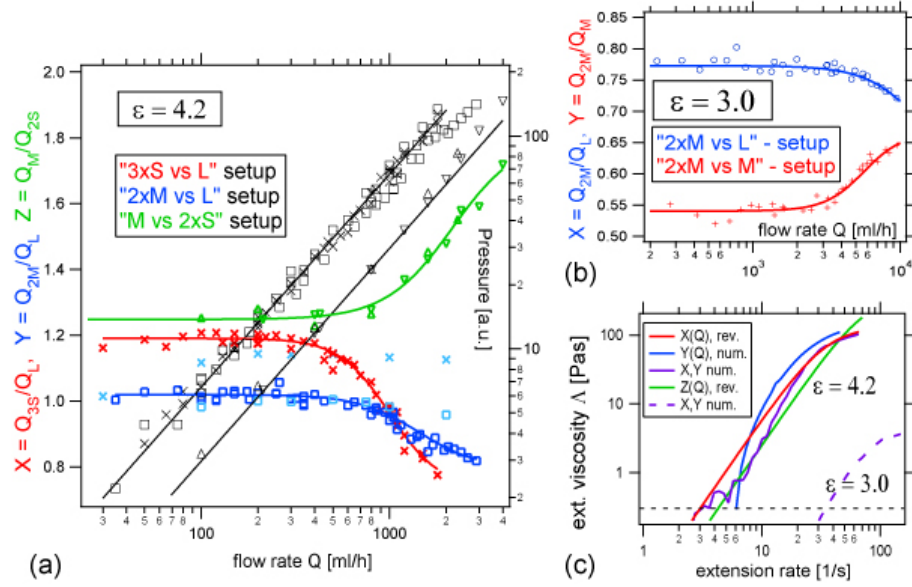
Figure 5.21: Results from measurements in circular hyperbolic constrictions. (a) Flowrate ratios from three different setups with strain $\epsilon = 4.2$ (colored symbols) and corresponding pressure drops across the device (black symbols). The light blue symbols represent measurements with a Newtonian glycerol solution. Smoothing functions are shown by the colored solid lines, the black lines show a linear fit to the pressure drops obtained in the Newtonian flowrate regime. (b) Flowrate ratios (symbols) and smoothing functions (lines) in two setups with strain $\epsilon = 3.0$. (c) Apparent extensional viscosities determined from the measurements in a and b. Results from empirical approximation of $X(Q)$ and $Z(Q)$ (red and green lines), numerical evaluation of $Y(Q)$ (blue line) and combined numerical evaluation of $X(Q)$ and $Y(Q)$ (purple solid line) are shown for the $\epsilon = 4.2$ measurements for comparison. The dashed purple line shows the result of a combined numerical evaluation from $X(Q)$ and $Y(Q)$ in the $\epsilon = 3.0$ devices.

Strain Dependence of Determined Extensional Viscosities

To check whether the determined extensional viscosities can be regarded as measures for the steady state extensional viscosity, the results from setups with matching shape factors but different Hencky strains $\epsilon = 3.0$ and $\epsilon = 4.2$ have been compared in fig. 5.21. The Newtonian ratio of extensional to shear resistance (R_E/R_S) is more than 10-fold higher in the $\epsilon = 3.0$ constrictions, which suggests that the detection limit for an enhanced extensional resistances is lower than in the $\epsilon = 4.2$ constrictions. Nevertheless, flowrates approximately an order of magnitude higher than in the $\epsilon = 4.2$ setups are required to observe a measurable deviation from the Newtonian regime in the $\epsilon = 3.0$ setups. Consequently, the evaluated extensional viscosity is about two orders of magnitude

lower for the $\epsilon = 3$ setup compared to the $\epsilon = 4.2$ setups. This suggests, that at a strain of $\epsilon = 3$ the fluid is far from having reached a steady state in the elongational flow. Systematic measurements with geometries testing further strains would be necessary to decide whether a steady state is reached in the $\epsilon = 4.2$ constrictions.

However, we can estimate a lower limit for the required strain to reach a fully stretched chain configuration in purely extensional flows of dilute polymer solutions: For the occurence of a stretching frictional force at the polymer ends, the polymer has to be extended slowlier than the surrounding fluid. Consequently, the fluids extensional strain required for a full stretching of the molecule has to be higher than the ratio of the polymers end-to-end vector in the fully stretched and in the equilibrium state: $\epsilon_{\min} = \ln(L_c/R_{\mathrm{ee}}^{\mathrm{eq}}) = 0.5 \ln N_K$. From the determined overlap concentration of about $c^\star \sim 0.4\%$ for the PAA (see fig. C.1), the number of Kuhn segments N_K can be estimated to be on the order of 10^4 (see C.1), which suggests a minimum extensional strain of $\epsilon = 4.6$ for a full stretching of the PAA chain. Indeed, a saturation of the extensional viscosity measured for 0.1% PAA and 0.2% PAA solutions in 80% glycerol with a capillary breakup extensional rheometer was observed for $\epsilon = 6$ (see fig. C.2). In mixed flows however, a possible prestretching of the molecules due to the shear flow could significantly reduce the required extensional strain for full stretching.

The observed striking difference of about two orders of magnitude for the viscosity measurements with $\epsilon = 3.0$ and $\epsilon = 4.2$ might be surprising at first sight. However, in filament stretching rheometers a rapid rise of the transient extensional viscosity with increases of several orders of magnitude within $\Delta\epsilon \sim 1$ has been both theoretically predicted and experimentally reported for model elastic fluids [5], see fig. 5.23b. Qualitatively, the sudden increase in the dissipation can be rationalized as follows: The extensional viscosity contribution of the polymers is proportional to the frictional forces stretching the polymer. In the regime where the entropic spring force is negligible compared to the frictional forces, the polymer segments follow the motion of the fluid. Thus, the polymer extension grows exponentially with ϵ at low strains, which is accompanied by an exponential growth of the entropic spring force in its linear regime. As the polymer dissipational contribution to Λ is proportional to the stretching force, this implies an exponential growth of Λ^{polym} with ϵ. For a dilute polymer solution however, the polymer contribution may still be negligible with respect to the solvent contribution of $\Lambda^{\mathrm{solv}} = 3\eta$. As the polymer reaches higher extensions, the non-linear force-extension relation of the entropic spring force causes an even over-exponential increase of the dissipation with ϵ. This causes the very rapid increase observed for Λ once the spring forces get strong enough to compete with the friction and stop the polymers further elongation.

As a conclusion for the measurements, the fluid neither experiences a purely extensional flow in the constrictions, nor can we decide whether it reaches a steady state within the experienced extensional strain. Consequently, the measured extensional viscosities have to be considered as apparent, transient extensional viscosities rather than being identified with the steady state uniaxial extensional and planar extensional viscosities Λ, Λ_p which are defined by

eqs. 3.29, 3.30.

Comparison with FSR and CaBER measurements
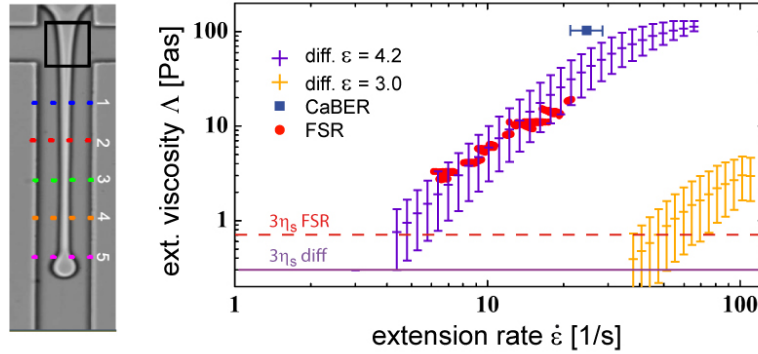
Figure 5.22: Left: Microscope image of microfluidic filament stretching rheometer (FSR) measurement taken from [6]. Right: Extensional viscosity data from the FSR measurement from [6] (red dots, 0.01% PAA (18 MDa) in 85% glycerol)) in comparison with data from the differential extensional viscometer (purple and orange $+$, 0.1% PAA (5-6 MDa) in 80% glycerol). The blue square indicates a measurement performed with the 0.1% PAA in 80% glycerol solution in a CaBER. The horizontal lines indicate the Newtonian extensional viscosity of the 0.01% PAA (dashed red) and the 0.1% PAA solution (solid purple). The 0.01% PAA solution is expected to have about 0.75% of the extensional viscosity of the 0.1% PAA solution (see explanations in the text).

The above results clearly demonstrate that an apparent extensional viscosity of the dilute polymer solutions can be determined with the proposed differential viscometer. For a quantitative rating of the results, the obtained extensional viscosities have been compared with results in established extensional viscometers. Literature values measured in a microfluidic filament stretching rheometer (FSR) are available from *Arratia et al.* [6] for a 18 MDa PAA solution of 100 ppm in an 85% (w/w) glycerol/water mixture. While in a conventional FSR a steady uniaxial extensional flow is created by seperating two cylinders with a liquid bridge inbetweeen, the fluid filament in the microfluidic FSR is stretched in a cross flow. The measurement setup and the results from [6] are shown in fig. 5.22 by the red dots; the purple and orange markers show the results of the differential viscometer measurements in the $\epsilon = 4.2$ and $\epsilon = 3.0$ circular constriction setups.

For dilute polymer solutions we can assume that the extensional viscosity is proportional to the polymer concentration and the solvent viscosity. Thus, for PAA of the same molecular weight we would expect the extensional viscosity of a 0.1% PAA in 80% glycerol solution to be about 4.3 times higher than for

a 100 ppm in 85 % glycerol solution. However, the molecular mass of the PAA used in [6] is about 3.3 times higher than the PAA used in this work. For a fully stretched chain in extensional flow, we would theoretically expect a quadratic increase of the viscous dissipation with the chain length. For solutions with equal same mass concentration, this results in a linear increase of the extensional viscosity with the molecular mass. As a rough estimate we would thus expect the extensional viscosity of the 0.01 % PAA (18 MDa) in 85 % glycerol to have about $3.3/4.3 \approx 0.75$ % of the value of the solution examined here. Indeed, the values determined in the differential viscometer with $\epsilon = 4.2$ are comparable to the values of the FSR measurement. This suggests that the values measured in the differential viscometer with $\epsilon = 4.2$ are reasonably within the range expected for a purely extensional measurement in steady-state.

To enable a more direct comparison, an additional measurement was performed with the 0.1 % PAA in 80 % glycerol solution in a capillary breakup extensional rheometer (CaBER), see fig. C.2. In a CaBER, the extensional rate is determined by the surface tension and the viscosity of the fluid. Therefore it cannot be tuned and only data for one extensional rate can be obtained, which is shown by the blue square in fig. 5.22. The extensional viscosity measured in the CaBER is slightly above the differentially measured values. This might suggest that the steady-state value is not yet reached in the differential measurement. Moreover, mixed flow effects may cause deviations between the steady-state and the apparent extensional viscosity measured in purely uniaxial extension (CaBER) and in the differential viscometer.

Operation Range of Differential Extensional Viscometer

Apart from potential mixed flow effects, the results show that the differential viscometer measurements are comparable to FSR measurements. Similarly as in the microfluidic filament stretching device, the deformation rate of the fluid in the constrictions can be set via the applied flow rate. This only works as long as the fluid streamlines follow the hyperbolic geometry of the constrictions. Once the extensional resistance becomes comparable to the shear resistance, the streamlines decouple from the geometry to decrease the extension rate in the fluid, resulting in more flat hyperbolic streamlines and occuring eddies. As the dominating shear forces keep the fluid on the track set by the channel geometry, the ratio of extensional to shear resistance in the channel both sets the sensitivity of the differential viscometer and the upper limit for the accomplishable extensional rate. The higher the Newtonian ratio $(R_E(\dot{\epsilon})/R_S(\dot{\gamma}))_N$ in a channel, the easier an increase of $\Lambda(\dot{\epsilon})$ can be measured. As soon as $(R_E(\dot{\epsilon})/R_S(\dot{\gamma}))$ approaches the order of unity we can expect the flow to decouple from the channel wall. Thus, $\text{Tr}_{\max} = (R_E/R_S)^{-1}$ sets an upper limit for the Trouton ratio measurable in the differential viscometer. With the shear forces being lowest at the wide part of the constriction, streamline decoupling is expected to start at the entrance of the constriction. Advantageously, the occurence of eddies can directly be monitored in the optical accessible microfluidic viscometer. Fig. 5.23a shows an example of extensional resistance induced eddies occuring in

a $1\,\%\,(\mathrm{w/w})$ PAA aqueous solution flowing into a rectangular step constriction.
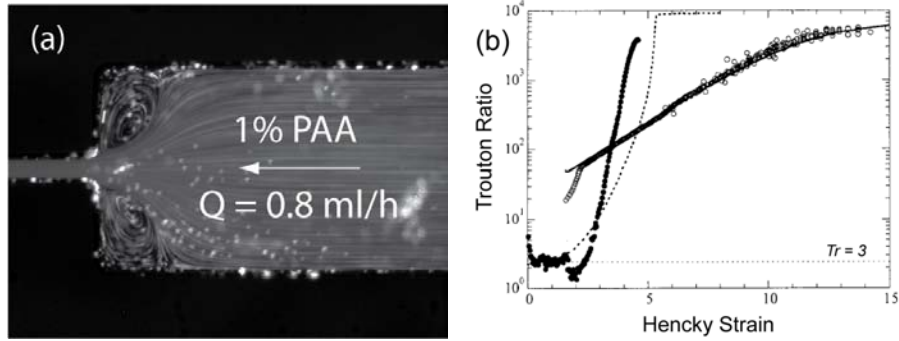
Figure 5.23: (a) Microscope image of a 1% PAA in water solution with fluorescent tracer beads flowing through a rectangular step constriction. In the entrance region, the high extensional viscosity causes the fluid streamlines to follow a hyperbolic shape, which lowers and homogenizes the extensional rate in the fluid. Eddies with circular flow occur in the corners of the constriction. (b) Measured extensional viscosities in filament stretching rheometry ($\bullet$, $De = \dot{\epsilon}\tau = 15.2$, τ: fluid relaxation) and CaBER filament thinning ($\circ$, $De \approx 0.66$) and corresponding theoretical predictions (dotted lines) showing that while for small Hencky strains $\epsilon < 1$ the extensional viscosity is small, the extensional viscosity increases drastically within $\Delta\epsilon \approx 1.5$ under filament stretching. Graph (b) taken from [5].

Advantages and Drawbacks of the Differential Extensional Viscometer

The most obvious limitation of the differential viscometer in comparison to FSR and CaBER devices is that the fluid in the differential device is elongated in a mixture of shear and extensional flow. Moreover, the higher Hencky strains reached in FSR and CaBER rheometers usually enable a steady-state evaluation of the extensional viscosity. However, the results measured in the $\epsilon = 4.2$ differential device are similar to those obtained in FSR and CaBER measurements. This shows that at least for dilute polymer solutions the differential viscometer can yield reasonable estimates for the steady-state uniaxial extensional viscosity. Furthermore, numerous practical applications as well as biological processes involve transient extensional flows as well as flows with an additional shearing component. Therefore, the microfluidic differential viscometer can serve as an ideal tool for characterizing fluids in mixed and transient extensional flows as well as for studying their physics. Also, a lubrication of the channel walls could significantly reduce the shear flow component, so that essentially uniaxial extensional flow filed can be generated in a hyperbolic die [8].

Apart from that, the differential viscometer may offer several advantages in comparison to filament stretching and capillary breakup rheometers:

- While in FSR and CaBER the dependence of Λ on the strain can be studied, the extensional rate is fixed in a CaBER. The comparison of the differential and the FSR data in fig. 5.22 shows that the range of accessible extensional rates is wider in the differential viscometer. As discussed above, the operating range can be further adjusted to the needs by choosing geometries with different Newtonian R_E/R_S ratios. The additional shear flow involved enables measurements in a range where FSR and CaBER measurements may suffer from occuring inertial or gravitational effects.

- In contrast to the CaBER and FSR technique, neither an air-water interface nor another liquid-liquid interface is involved in the differential measurement. Therefore, the differential measurement does not have to be corrected for surface tension effects. Moreover, any artifacts possibly occuring due to interfacial adsorption of molecules in the solutions can be excluded.

- The differential viscometer can be easily used with dilute, low viscosity fluids, where conventional FSR and CaBER measurements requiring the stable formation of a fluid filament may fail.

Due to the inherent oppportunities and restrictions of each of the techniques available, determining extensional viscosity functions $\Lambda(\dot{\epsilon})$ generally remains challenging. The proposed differential extensional viscometer can be a valuable tool in addition to existing devices. Its simple and robust design enables a cheap production and makes it open for parallelization and miniaturization for application in lab-on-a-chip devices. In combination with the optical accessibility and the techniques used for monitoring the single polymer dynamics in flow in chapter 4 it may serve as an ideal platform to study the connection between bulk fluid properties and the underlying macromolecular dynamics in mixed flows.

5.4.6   Mixed Flow Effects

The experimental results suggest that the additivity assumption of the hydrodynamic extensional and shear resistances R_E, R_S in the constrictions is not strictly valid. The no-slip condition at the walls inevitably evokes a shear flow component with high shear rates in the fluid near the channel walls. The resulting heterogenity in the elongational flow field could in principle be considered with an adjustment analogous to the Rabinowitsch correction (see eq. A.78), if the flow field in the constrictions can be determined. However, the combination of shear and extensional flow could significantly alter the polymer dynamics and thus query the additivity assumption for the extensional and shear resistances R_E, R_S in the constrictions. Based on the discussion of the dynamics of individual polymers in shear flow in chapter 4 we will briefly consider how an additional shear component could affect the polymer dynamics in elongational flow and discuss the resulting influence on the apparent extensional viscosity in mixed flows.

The fundamental difference in the response of polymers to shear and extensional flow has been discussed in section 5.1: Polymers in purely extensional flows reach an equilibrium state and can get fully stretched in a sharp coil-stretch transition, which occurs at $De = \dot{\epsilon}\tau > 0.5$ [100]. This explains the threshold type behaviour of the extensional viscosity, which saturates when the polymers are completely stretched. In contrast, the 1:1 mixture of extensional and rotational deformation in the shear flow induces a gradual stretching for $Wi = \tau\dot{\gamma} > 1$ [99], which is accompanied by cyclic tumblings of the polymers. Hence, the individual polymers do not reach a stationary state. An additional shear flow component with a velocity gradient perpendicular to the extensional direction could thus in principle have two effects on the apparent extensional viscosity:

- The shear flow stretches and aligns the polymers in the direction of the flow. Thus, the friction of the polymers in the extensional flow is enhanced, so that the apparent extensional viscosity begins to rise at lower extension rates and the threshold for the rise in $\Lambda(\dot{\epsilon})$ is lowered. Consequently, an additional shear flow could increase the apparent extensional viscosity in the regime below the saturation.

- The rotational component of the flow rotates the polymers away from the alignment in the extensional direction. During the induced tumbling, the extension of the polymer in the extensional flow direction is lowered due to a partial recoil, so that the additional shear flow could reduce the apparent extensional viscosity in the fully stretched regime.

The dominating of these mechanisms is determined by the ratio of shear and extensional flow and the relative orientation of the flow components.

Polymer Dynamics in Mixed Planar Flows

In the following we try to elucidate the interplay between rotational and extensional components of different strength on the polymer dynamics in more detail. Some simple considerations can be made by looking at the dynamics of non-thermal particles suspended in planar mixed flows, which has been discussed in [35]. The particle is represented by crossed dumbbells of lengths l_1, l_2 with an anisotropy coefficient $b = (l_1^2 - l_2^2)/(l_1^2 + l_2^2) \in [0; 1]$ (see fig.5.24). Then, the differential equation for the motion of the particle in its center of mass system in a velocity field with extension rate $\dot{\epsilon}$ and rotational component ω is given by [35]:

$$\dot{\phi} = b\dot{\epsilon}\cos(2\phi) + \omega \tag{5.25}$$

For shear flow ($\dot{\epsilon} = \omega = 0.5\dot{\gamma}$) eq. 5.25 reduces to

$$\dot{\phi} = \dot{\gamma}\left[\frac{l_1^2}{l_1^2 + l_2^2}\cos^2\phi + \frac{l_2^2}{l_1^2 + l_2^2}\sin^2\phi\right]. \tag{5.26}$$

Note that for a single dumbbell particle with $l_2 = 0$ eq. 5.26 reduces to $\dot{\phi} = \dot{\gamma}\cos^2\phi$, which is equivalent to Jeffery's equation 4.35 with a coordinate system

rotated by $\pi/2$. As explained in section 3.1.1 (see fig. 3.1), planar flows can be classified with a single flow parameter $\rho = \omega/\dot{\epsilon}$ to be strong (i.e extensionally dominated) for $\rho^2 < 1$, marginally weak (i.e. shear flow, $\rho^2 = 1$) or strictly weak (rotationally dominated, $\rho^2 > 1$). According to eq. 5.25, the dynamics of the suspended particle is determined by the ratio of ρ/b. Fig. 5.24 shows a plot of eq. 5.25 for various values of ρ/b. For strictly weak flow with $(\rho/b)^2 > 1$, the particle performs a continuos rotation. For $(\rho/b)^2 = 1$, the particle follows the Jeffery orbit for a rod in shear flow. In strong flow with $(\rho/b)^2 < 1$ the differential equation exhibits two stationary points. The stationary point within $[0; \pi/2]$ is stable, so that the particle gets trapped at a fixed orientation ϕ_{stat} in the flow. For $(\rho/b)^2 \ll 1$ the particle is aligned near the direction of the extensional deformation axis, reaching a perfect alignment in purely extensional flow with $\rho/b = 0$.
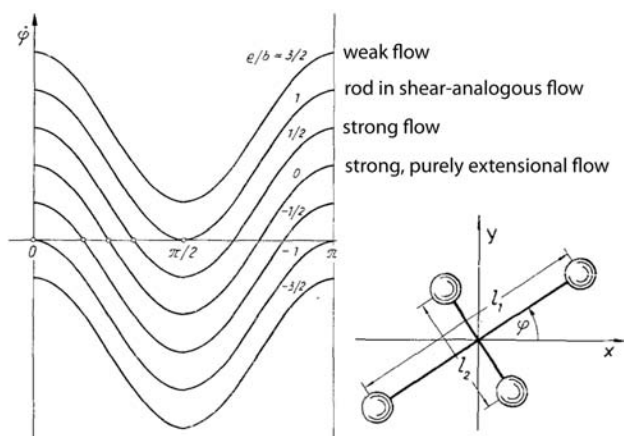
Figure 5.24: Dynamics of non-thermal particles suspended in planar mixed flow (graphs taken from [35]). The particle consists of two crossed dumbbells of length l_1, l_2 (right). The differential equation $\dot{\phi}(\phi)$ for the angular dynamics is plotted for several values of the flow parameter ρ/b (left). For $\rho/b = \pm 1$ the particle follows the Jeffery orbits of rodlike particles in simple shear flow.

In the absence of thermal rotational diffusion of the polymer we could thus expect the polymer in strong flow to be trapped at ϕ_{stat} and get permanently stretched if the frictional forces overcome the deformation threshold. In strictly weak flow, the polymer is expected to rotate continuously accompanied by a subsequent stretching and relaxing motion.

Analogously to the discussion in section 4.2.3 we can now consider the influence of the thermal rotational diffusion on the dynamics. A diffusive phase is expected to occur in angular intervals where the rotational diffusion dominates over the advective drift. This happens for $|\dot{\phi}(\phi)| \approx 0$ and has been discussed for the case of a turning point of $\dot{\phi}$ with a tangent at $\dot{\phi} = 0$ in the shear flow case $((\rho/b)^2 = 1)$. In strong flow with $(\rho/b)^2 < 1$, $|\dot{\phi}(\phi)| \approx 0$ is fulfilled in

the vicinity of the two fixpoints: While the thermal motion drives the polymer away from the unstable fixpoint, the polymer diffuses around the stable fixpoint in a potential well, which is set by the strength of the advective drift. When the intersecting interval of the $\dot{\phi}(\phi)$ curve becomes small as $(\rho/b)^2$ approaches unity, the potential barrier set by the advective drift may be overcome by the diffusive motion. Then, the particle may escape the potential well, so that the rotational diffusion makes the stable fixpoint unstable if $(\rho/b)^2 \to 1$. Consequently the polymer performs diffusion-induced tumbling motions analogous to those observed in shear flow. Similarly to the discussion for the critical angle ϕ_c seperating the diffusive and advective polymer dynamics in shear flow, we can thus define a critical value $\delta_c > 0$, which seperates the regime of "effectively strong flow" without tumblings $((\rho/b)^2 < 1 - \delta_c)$ and the regime of "shear-alike strong flow" $((\rho/b)^2 > 1 - \delta_c)$ where polymer tumbling is expected. While a stretching to $\langle R_{\mathrm{ee}} \rangle = 0.4 \ldots 0.5 L_c$ is observed in shear flow for high Wi, an almost complete stretching of the polymer is only expected in "effectively strong flow". However, the additional gradual stretching with Wi due to the shear flow is expected to smear the sharp coil-stretch transition observed in purely extensional flow.

Although the simple description with the flow parameter ρ cannot be directly applied for three dimensional flows, the qualitative behaviour of suspended particles should be conserved [35]. We can therefore calculate a lower limit for ρ in the geometries used in the experiments. This estimate of ρ then allows for a characterization of the expected polymer dynamics in the mixed flow. For simplicity, we assume a perfect alignment of the extensional flow components of the shear flow and the extension imposed by the converging die. Then, the total extension rate of the flow is calculated by adding the extension rate given by the die $\dot{\epsilon}_{\mathrm{die}} = Q/a$ with the extensional component of the shear $\dot{\epsilon}_S = \frac{1}{2}\dot{\gamma}$. Hereby, we average $\dot{\gamma}(r)$ across the circular channel cross section assuming a Newtonian flow profile,

$$\langle \dot{\gamma} \rangle = \frac{1}{Q} \int_0^R 2\pi r v(r) \dot{\gamma}(r) \mathrm{d}r = \frac{32}{15} \frac{Q}{\pi R^3} \approx \frac{2Q}{\pi R^3} = \frac{1}{2}\dot{\gamma}_w \tag{5.27}$$

where $\dot{\gamma}_w$ is the wall shear rate in the channel with radius R. Then, we can estimate the typical ratio of rotational and extensional components of the flow as:

$$\rho = \frac{\omega}{\dot{\epsilon}_{\mathrm{sum}}} = \frac{\frac{1}{2}\langle \dot{\gamma} \rangle}{\frac{1}{2}\langle \dot{\gamma} \rangle + \dot{\epsilon}_{\mathrm{die}}} = \frac{1}{1 + \pi R^3/a} \tag{5.28}$$

For a circular type M constriction, this yields a change of ρ from about 0.10 at the wide end to about 0.904 resp. 0.984 for the $\epsilon = 3.0$ and $\epsilon = 4.2$ constrictions in the narrow part. As ρ is close to unity at the tight end of the constrictions, shear induced tumblings might occur in the narrow part of the constrictions.

Influence of the Relative Orientation of Shear and Extensional Flow

The flow type resulting of the combination of the shear flow and the die extensional flow is also influenced by the orientation of the extensional flow fields of

shear and die. The velocity field of planar extensional flow can be written in polar coordinates (r, ϕ) as:

$$\begin{pmatrix} \dot{r} \\ \dot{\phi} \end{pmatrix} = \dot{\epsilon} \begin{pmatrix} r\cos(2\phi) \\ -\sin(2\phi) \end{pmatrix} \tag{5.29}$$

Unfortunately, there is no compact analytical solution for the result of the addition of two extensional flow fields of different strength $\dot{\epsilon}_S, \dot{\epsilon}_{\mathrm{die}}$ and orientation. Generally, the extension rate of two combined extensional flowfields with $\dot{\epsilon}_a, \dot{\epsilon}_b$ ranges from $|\dot{\epsilon}_a + \dot{\epsilon}_b|$ to $|\dot{\epsilon}_a - \dot{\epsilon}_b|$ depending on their relative orientation. Adding two planar extensional velocity fields with equal extension rates $\dot{\epsilon}$ with an angular difference of $\Delta\phi = \theta$ results in a velocity field of

$$\begin{pmatrix} \dot{r} \\ \dot{\phi} \end{pmatrix}_{\mathrm{sum}} = \dot{\epsilon} \begin{pmatrix} r(\cos(2\phi) + \cos(2(\phi - \theta))) \\ -(\sin(2\phi) + \sin(2(\phi - \theta))) \end{pmatrix} = \dot{\epsilon} \begin{pmatrix} r(\cos(2\phi - \theta)\cos\theta) \\ -2(\sin(2\phi - \theta)\cos\theta) \end{pmatrix} \tag{5.30}$$

The principal axes of the combined elongational flow field can be determined by calculating the angles where $\dot{\phi} = 0$ as $\phi_+ = \theta/2, \phi_- = \theta/2 + \pi/2$. The resulting extension rate is given as $\dot{\epsilon}_{\mathrm{sum}} = 2\dot{\epsilon}\cos\theta$, so that for $\theta = \frac{\pi}{2}$ the extensional flow fields cancel each other.

During the passage through the constriction, the relative orientation of the extensional components of shear and die continuously varies, and the flow changes from being extensionally dominated in the wide part of the constriction ($\dot{\epsilon}_{\mathrm{die}} \gg \dot{\epsilon}_S$) to being shear dominated in the narrow part ($\dot{\epsilon}_{\mathrm{die}} \ll \dot{\epsilon}_S$). Fig. 5.25a shows the resulting flow type according to the classification given in section 3.1 for a circular constriction of type M with $\epsilon = 4.2$. The velocity field was determined in a FEM simulation with a Newtonian fluid. The flow is found to be strong almost throughout the entire constriction. In fig. 5.25b, the varying direction of the extensional flow flield of the shear (green) and the die (red) is illustrated in the converging and diverging section of the constriction. Due to the complicated, nonuniform flowfield in the constrictions we can only make some qualitative statements on the expected polymer dynamics. Depending on the ratio of the extension rates given by the shear flow and the die $\dot{\epsilon}_S, \dot{\epsilon}_{\mathrm{die}}$ we can distinguish several regions:

- *Extension dominated region* ($\dot{\epsilon}_{\mathrm{die}} \gg \dot{\epsilon}_S$): The polymers are only slightly influenced by the shear, consequently they get aligned near the direction of the die extension, which sets the overall extension rate $\dot{\epsilon}_{\mathrm{sum}} \approx \dot{\epsilon}_{\mathrm{die}}$. The apparent extensional viscosity is presumably similar to the extensional viscosity in shear free flow ($\Lambda_{\mathrm{app}} \approx \Lambda$).

- *Extension comparable to shear* ($\dot{\epsilon}_{\mathrm{die}} \approx \dot{\epsilon}_S$): Depending on the relative direction between the extensional flow component of shear and die, the overall extension rate $\dot{\epsilon}_{\mathrm{sum}}$ can be bigger or smaller than $\dot{\epsilon}_S$, which results in strong or strictly weak flow.

- *Shear dominated region* ($\dot{\epsilon}_{\mathrm{die}} \ll \dot{\epsilon}_S$): If the shear flow dominates, the polymers get stretched and aligned near the flow direction of the streamlines, which are almost parallel to the constriction centerline.

In the converging section, the shear-stretched polymers are thus approximately aligned with the direction of the die extension (see fig. 5.25b left). The shear flow thus enhances the frictional forces occuring in the extensional flow of the die. Consequently, the shear flow lowers the threshold for the coil-stretch transition of the polymers in the extensional flow of the die, so that the sharp transition of $\Lambda(\dot{\epsilon})$ may be smeared by the shear. Below the saturation level of $\Lambda(\dot{\epsilon})$, the apparent extensional viscosity is thus expected to be higher than in purely extensional flow ($\Lambda_{\mathrm{app}}(\dot{\epsilon}) > \Lambda(\dot{\epsilon})$). The saturation level of Λ_{app} at the fully stretched state should stay essentially unchanged, unless the shear flow is strong enough to induce polymer tumblings ($\Lambda_{\mathrm{app}}(\dot{\epsilon}) \approx \Lambda(\dot{\epsilon})$). Reversely, the apparent shear viscosity should be lowered if the polymers are prevented from tumbling by the extensional flow.

The situation is different in the diverging narrow section: Here, the direction of the die extension is approximately perpendicular to the flow direction (see fig. 5.25b right). Thus, the die extension compresses the polymer along the flow direction and acts against the stretching of the shear flow. The shear strength decreases along the flow direction, so that the polymers elastic restoring force is able to recoil the polymer along the flow. Thus, the entropic elastic force induces a similar deformation onto the stretched polymer as the die extension. Consequently, we can expect the apparent extensional viscosity to be reduced. In a similar way, the entropic elasticity causes the die swell observed at the exit of capillary flows: As the no-slip condition is removed at the capillary exit, the shear component of the flow vanishes, and the shear-stretched polymers start to recoil. The polymer recoil induces a compression of the fluid in the flow direction and an extension lateral to the flow, which is observed as the characteristic swell of the exiting fluid stream. The reduction of Λ_{app} in the diverging section of the constriction thus explains, why in capillary viscometers the exit pressure drop usually can be neglected, while the entrance pressure drop has to be considered (see section 5.2).

5.4.7 Conclusion

Generally, the above discussion shows, that mixed flow effects are expected to alter both the apparent shear and extensional viscosity, because the mixed flow changes the dynamics of the polymers. A quantitative discussion is challenging, and more research has to be conducted for a better understanding of the involved mechanisms. For the experimental geometries used in the differential extensional viscometer, the shear and extensional flow components continuously alter both in their ratio and their relative direction while the fluid passes the constrictions. In combination with additional flow history effects this poses major difficulties for a quantitative analysis. To test for a possible influence of flow history effects on the results, a dependance of $X(Q)$ on the length of the connecting channel between subsequent constrictions has to be excluded to ensure

(a)

(b)
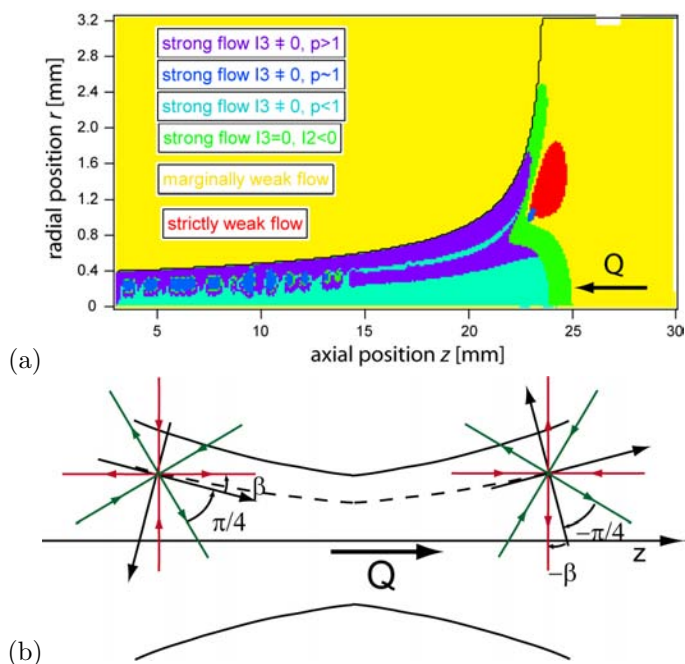
Figure 5.25: (a) Flow classification as given in section 3.1 for the flow of a Newtonian fluid in a type M circular constriction with $\epsilon = 4.2$. The underlying flowfield has been determined in a FEM simulation with a flowdirection from right to left. (b) Schematics illustrating the orientation of the extensional flowfield of the shear (green) and the die (red). The local coordinate system of the shear flow is shown by the black arrows. In the shear dominated narrow region of the constriction, the fluid streamlines are approximately aligned with the channel centerline (β small). Therefore, polymers which are stretched and aligned with the flow direction by the shear get stretched by the die extension in the converging section (left) and compressed by the die extension in the diverging section (right).

the same fluid conditions at the constriction entrances. Experimentally, systematic measurements in devices with connection channels of varying lengths could indicate a possible bias due to an insufficient fluid relaxation between the elongational flow segments. Concurrent studies of microfluidic flows after a step constriction showed, that the timescale to reach steady state conditions in microchannel flows can be significantly reduced compared to the equilibrium relaxation time of the fluid [57].

Despite these limitations, qualitative conclusions can be drawn on the basis of the discussion in section 5.4.6: In the converging sections, polymers are hindered from tumbling, and the stretching of the polymers in the flow direction is enhanced by the combination of shear and extensional flow. This should be

accompanied by a higher apparent extensional viscosity below the saturation level and a lower contribution of the polymers to the shear viscosity. In the diverging sections, the situation is reversed with counteracting stretching forces of shear and extensional flow. Thus, the apparent extensional viscosity should be lowered, while the shear viscosity should be enhanced. If the shear flow is strong enough to induce tumblings, the aforementioned effects should be weakened.

The dilute polymer solutions used in the experiments exhibit an almost Newtonian shear viscosity, which implies that the shear viscosity is dominated by the solvent contribution. Thus, the shear resistance may be considered as essentially unaffected by the die extensional flow. Then, only changes in the apparent extensional viscosity should be observed due to mixed flow effects. As discussed above, the transient values at the onset of the rise of the apparent extensional viscosity measured in mixed flow should be higher than the values measured in purely extensional flow in FSR or CaBER experiments, because the shear flow contributes to the stretching of the polymers. Contrary, the plateau value of the extensional viscosity reached at high strains and at high extension rates might be expected to be lower in mixed flows in comparison to purely extensional flow due to shear induced tumbling in the narrow section of the constrictions.

As a conclusion, the different mixture ratios of shear and extensional flow in the varying constrictions may explain the observed differences in the obtained values for the apparent extensional viscosity measured in the various setups. While the additivity assumption for the shear and extensional resistance in the constrictions is not valid generally, for the case of the investigated dilute polymer solutions with near Newtonian shear viscosity, extensional viscosities comparable to literature values measured in shear free flow are obtained with the differential viscometer. Clearly, more research has to be conducted on polymer solutions in mixed flows for a more accurate evaluation of Λ. Experiments with direct comparisons between extensional viscosities determined from hyperbolic dies and in shear free flows have shown, that reasonable values for Λ can be determined with hyperbolic die measurements [8]. However, an accurate quantitative evaluation remains challenging to date, even when a wall slip is introduced by lubrication of the walls [8].

Generally, the significance of extensional viscosity measurements suffers from the fact, that neither in most technical applications nor in many established techniques for measuring $\Lambda(\dot{\epsilon})$ a steady, spatially uniform, purely extensional flow is ever achieved. As discussed in [81], reported literature results for transient extensional viscosities measured in different devices for the same fluid vary by three orders of magnitude due to the different deformation history, so that the validity of absolute values of Λ has to be challenged. Nonetheless, the conducted experiments can serve as a successful proof of principle for the differential extensional rheometer, and both the signal generating mechanism and the evaluation yields results comparable to existing techniques. Thus, the device offers a complementary approach to existing extensional rheometers with benefits and drawbacks according to the particular needs.

6. FLUID-STRUCTURE INTERACTIONS: TRANSIENT FLOW IN VISCOELASTIC MICROFLUIDIC CHANNELS

In order to elucidate how the microscopic dynamics determine the macroscopic response of a fluid, we studied the flow of complex fluids in microchannels by observing the dynamics of the individual fluid constituents and measuring the bulk viscosity functions $\eta(\dot{\gamma})$ and $\Lambda(\dot{\epsilon})$ in the previous chapters. Aside from these inherent properties of the fluid, microfluidic flows can also be impacted by interactions with the channel walls. While a hydrodynamic interaction between individual polymers and the walls has been examined in section 4.5, the coupling of transient flows to deformations of flexible microfluidic channel walls will be investigated in this chapter.

Microfluidic channels consisting of blocks of the elastomeric material PDMS, which are bonded to a glass substrate, are widely-used, so that tethered elastic channels are of special interest. The cheap and easy lithographic production, the optical transparency, the high biocompatibility of the surface and the high gas permeability, which enables oxygen supply for living cells, makes PDMS especially suited for life-science applications. An efficient control of spatiotemporally changing pressure and flow rates is mandatory for the broad applicability of microfluidic devices. The elastic properties of PDMS have been exploited in different promising approaches for the construction of flow-regulatory devices [56, 119], valves [111, 1, 7, 55, 39, 71, 42, 37, 66] and pumps [67, 38]. An emerging concept is the exploitation of the frequency response of microfluidic devices for the fluid control comprising mixing, valves and droplet positions [68, 63]. While membrane valves are constructed by constricting the fluid channels, pumps can be constructed on the base of membrane valves rectifying a previously generated oscillatory flow [67, 68, 70]. The frequency response of devices is also important for microrheological applications, where the behavior of complex fluids is studied in such devices [16, 51]. A long standing interest in complex fluid flows in different geometries comes from medical applications — understanding vessel diseases needs a quantitative understanding of cardiovascular flow behavior in elastic channels. The transport of blood flow through elastic tubes has been modeled by the telegraphers equation and experimentally tested on the lengthscale of macrocirculation [104, 105, 117, 73, 53, 54], where inertia effects are important [13]. Microfluidic technology now enables us also to explore the regime of microcirculation, where inertia is negligible but the non-Newtonian properties of blood may dominate [13].

The aim of this chapter is to provide a simple basis for the frequency response of Newtonian fluids in microfluidic channels. To this end, the 1D-model

description of purely elastic tubes by the telegraphers equation [104] has been expanded by incorporating the viscoelastic response of the PDMS as a complex impedance. The predicted diffusive spreading of the pressure propagation and the corresponding flow profiles have been tested by applying periodic rectangular pressure pulses to a straight rectangular PDMS channel and monitoring the dynamic response of a glycerol solution in the channel. The combination of different microparticle tracking techniques allows the determination of pressure and flow profiles at any point in the channel. The experimental confirmation of the proposed model paves the way for a quantitative design approach for increasingly more complex devices.

6.1   1D - Modelling of Microfluidic Channel with Viscoelastic Walls

6.1.1   Hydrodynamic Analogy of Laminar Flows to Electric Circuits

Laminar fluid flow problems of Newtonian fluids in complex geometries can often be modelled one-dimensionally with the help of equivalent circuits analogous to electric circuits, where flow and pressure Q, p correspond to current and voltage $I^{\text{el}}, U^{\text{el}}$ [104, 12]. A three-dimensional channel is then represented by its hydrodynamic resistance

$$R = \frac{\Delta p}{Q}, \tag{6.1}$$

which is determined by the channel geometry and the viscosity η of the fluid (see section 3.2.3). For networks consisting of several connected channels, the continuity equation for incompressible fluids is reduced to the analog of Kirchhoff's junction rule, stating that the sum of all flow rates Q_n at a channel junction vanishes. The conservation of energy leads to the analog of Kirchhoff's loop rule, stating that the sum of the pressure drops p_n along a closed path of n channels in a fluidic network is zero, implying equal pressure drops over channels in parallel arrangement [12]:

$$\sum_n Q_n = 0 \qquad \sum_n p_n = 0. \tag{6.2}$$

The concept of hydrodynamic analogy can be readily extended to capacitance and inductance. From $C^{\text{el}} = Q^{\text{el}}/U^{\text{el}}$ we can deduce that a hydrodynamic capacitance C is a fluid reservoir which can uptake fluid proportional to the applied pressure. As an example, a liquid column with cross-sectional area A would have a hydrodynamic capacitance given by the amount of liquid $V = Ah$ divided by the corresponding hydrostatic pressure $p = \rho g h$, so that $C = \frac{A}{\rho g}$, where ρ is the fluid density. The fluid inertia in the 1D-model is analogous to an inductance L: The hydrodynamic inductance per unit length L_x for a channel with cross-sectional area A is given as $L_x = \rho/A$ [80]. For transient flows, complex resistances $Z = 1/(i\omega C)$ and $Z = i\omega L$ can be used to incorporate fluid capacities and inertial effects into 1-D models of fluidic networks.
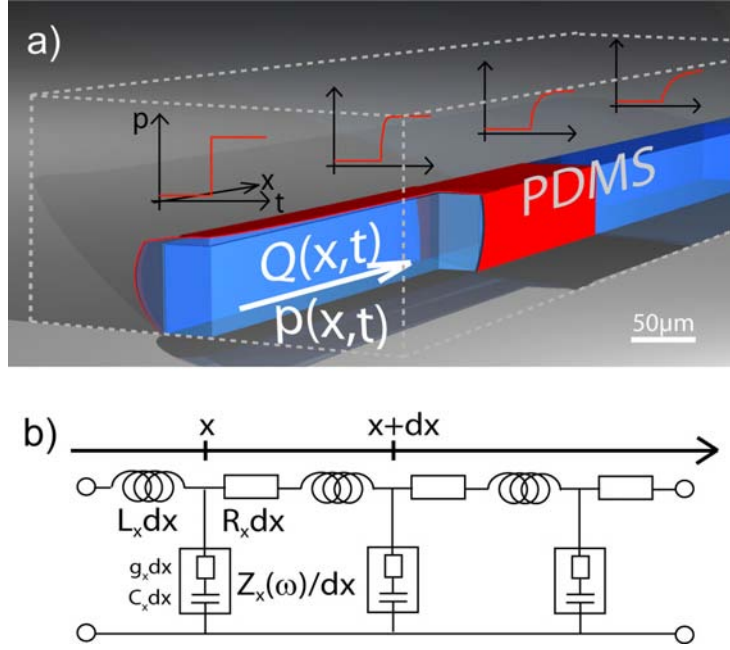
Figure 6.1: (a) Schematic representation of a deformable microfluidic PDMS channel showing the dispersion of a pressure pulse travelling along the channel. (b) Equivalent circuit with the hydrodynamic resistance $R_x \mathrm{d}x$ and hydrodynamic inductance $L_x \mathrm{d}x$ characterising the undeformed channel. The complex impedance $Z_x(\omega)/\mathrm{d}x$ describes the coupling of the viscoelastic PDMS wall deformations to the fluid flow.

6.1.2 Equivalent Circuit Model of Microfluidic Channel with Viscoelastic Walls

With these basic elements the equivalent circuit model for the fluid-structure interactions between a Newtonian fluid and a tethered channel with viscoelastic walls can be formulated. Hereby we suppose, that the cross-sectional deformation of the channel due to the transient pressure is small compared to the overall cross-section, so that the hydrodynamic resistance per unit length remains approximately unchanged ($R_x \approx \mathrm{const}$). This is a good assumption for channels with aspect ratios near unity under moderate operating pressures. Especially in shallow channels and at high operating pressures, the dependence of the hydrodynamic resistance $R_x(p(x))$ on the pressure can be quite significant and has to be considered [32, 40]. A series connection of $R_x \mathrm{d}x$ with the inertial inductance $L_x \mathrm{d}x$ then describes the 1D-model equivalent circuit element of a stiff, undeformable channel segment of length $\mathrm{d}x$.

As a widening of the channel cross section under pressure provides an extra volume to be filled by the fluid, the coupling of the wall deformation to the fluid flow can be represented by a capacitive element in the circuit. In the regime

where the generated extra volume is linear to the applied pressure, a purely elastic channel wall is simply described by a hydrodynamic capacitance per unit length C_x. Unlike in a purely elastic channel, pressure and wall deformation are out of phase in the PDMS channel. This is due to a phase shift between stress and strain, which is caused by the viscous dissipation in the deforming PDMS. To account for this phaseshift, we describe the viscoelastic PDMS walls with a complex impedance per unit length

$$Z_x(\omega) = \frac{1}{g_x(\omega)} + \frac{1}{i\omega C_x(\omega)}, \tag{6.3}$$

which consists of a resistance $1/(g_x dx)$ connected in series with a capacitance $C_x dx$. By using a frequency dependent resistance $Z_x(\omega)$ we can match the complex resistance with the actual elastic properties of the PDMS (see section 6.1.3). Due to the small amplitudes of the deformation, the inertia of the PDMS walls is negligible in the frequency range under investigation.

Note that due to the parallel arrangement of the capacities $C_x dx$ and the PDMS viscous resistances along the channel in x-direction, we express the resistance by the conductance per unit length $R_x^{\mathrm{PDMS}} = 1/(g_x)$. Thus, the fluid flow in the deformable channel can be described with the equivalent electric circuit depicted in fig. 6.1b. This equivalent circuit leads to the following differential equations for pressure $p(x,t)$ and flowrate $Q(x,t)$

$$
\begin{aligned}
-\frac{\partial p}{\partial t} &= \frac{1}{g_x} \cdot \frac{\partial^2 Q}{\partial x \partial t} + \frac{1}{C_x}\frac{\partial Q}{\partial x} \\
-\frac{\partial p}{\partial x} &= R_x Q + L_x \frac{\partial Q}{\partial t}
\end{aligned}
\tag{6.4}
$$

which are similar to the telegraphers equation. Applying a periodic pressure difference $\Delta p(t)$ with frequency ω_0 at the channel ends, where one end is held at ambient pressure, the resulting periodic pressure and flowrate pulses can be best described as the discrete sum over all frequencies

$$
\begin{aligned}
p(x,t) &= \sum_{n=0}^{\infty} p_n(x,t) \\
Q(x,t) &= \sum_{n=0}^{\infty} Q_n(x,t),
\end{aligned}
\tag{6.5}
$$

where $p_n(x,t) = \Pi_n(x)\exp(i\omega_n t)$ and $Q_n(x,t) = \Theta_n(x)\exp(i\omega_n t)$ are the Fourier components with frequencies $\omega_n = n\omega_0$ and complex amplitudes Π_n and Θ_n. With the boundary conditions $p(L,t) = 0, p(0,t) = \Delta p(t)$ the solution to eq. 6.4 can easily be obtained using the applied pressure pulse at the channel entrance $p(0,t) = \sum_{n=0}^{\infty} \Pi_{0n} \exp(i\omega_n t)$:

$$
\begin{aligned}
p_n(x,t) &= \Pi_{0n} \frac{\sinh[\lambda_n(l-x)]}{\sinh[\lambda_n l]}\exp(i\omega_n t) \\
Q_n(x,t) &= \Pi_{0n} \frac{\lambda_n}{R_x + i\omega_n L_x} \frac{\cosh[\lambda_n(l-x)]}{\sinh[\lambda_n l]}\exp(i\omega_n t)
\end{aligned}
\tag{6.6}
$$

where $\lambda_n = \sqrt{[i\omega_n R_x C_x(1 + i\omega_n L_x/R_x)]/(1 + i\tan\delta_n)}$ with $\tan\delta_n = \omega_n C_x/g_x$.

If the *Womersley parameter* $\alpha = \sqrt{wh\omega\rho/\eta}$ is small ($\alpha < 1$), the inertial terms in eq 6.6 can be neglected ($L_x \approx 0$). For water and blood in channels of microcirculatory diameter (100x100 μm^2 channel) $\alpha \leq 1$ holds up to frequencies of $\omega_{\alpha=1} \approx 100\,\mathrm{rad\,s^{-1}}$ resp. 350 $\mathrm{rad\,s^{-1}}$. Only in larger elastic channels like bigger blood vessels inertial effects must be taken into account, e.g. for blood in an aorta with $1\,\mathrm{cm^2}$ cross-section: $\omega_{\alpha=1} \approx 0.035\,\mathrm{rad s^{-1}}$. Inertial terms due to transversal acceleration of the fluid (convectional terms) will be even smaller, so that the use of the 1D model is a good approximation for flow in typical microfluidic channels. With $L_x = 0$ eq. 6.4 reduces for each Fourier component to

$$\frac{\partial p_n}{\partial t} = \frac{1 + i \tan \delta_n}{R_x C_x} \frac{\partial^2 p_n}{\partial x^2} \tag{6.7}$$

which is solved by eq. 6.6 with $L_x = 0$. Except for the small viscoelastic correction term $i \tan \delta_n$ eq. 6.7 resembles the 1D-diffusion equation with the pressure diffusion coefficient

$$D_p = \frac{1}{R_x C_x}. \tag{6.8}$$

Thus eq. 6.7 describes the pressure propagation along the channel basically as a diffusive process like the development of a chemical concentration gradient or the heat distribution over time. Together with the channel length l the diffusion coefficient D_p defines a characteristic time

$$\tau_{RC} = \frac{l^2}{D_p} = l^2 R_x C_x \tag{6.9}$$

for the transmission of pressure steps along the channel and the relaxation after a pressure step in steady state flow. For oscillatory flows, the channel acts as a low-pass filter with a cut-off frequency $\omega_{\mathrm{cutoff}} = \frac{2\pi}{\tau_{RC}}$ so that pressure and flowrate pulses disperse and get smoothed while they travel along the channel. Thus, ω_{cutoff} sets an upper limit for the frequency of switching operations in microfluidic devices. Fig. 6.1a schematically shows the dispersion of a pressure pulse propagating along the channel.

6.1.3 Complex Wall Resistance $Z_x(\omega)$ of Viscoelastic Material

The circuit representation of the viscoelastic PDMS wall (see fig.6.1b) as a conductance $g_x \mathrm{d}x$ in series with a capacitance $C_x \mathrm{d}x$ represents a Maxwell model of the PDMS (dashpot in series with a spring). To reproduce the correct frequency behaviour with this simple model, the values of g_x and C_x have to be adjusted to the viscoelastic properties of PDMS, which are given by its complex viscoelastic modulus $E^\star(\omega)$ for each frequency. The charge $Q_x^{\mathrm{el}} \mathrm{d}x$ on the capacitance corresponds to the extra volume $\mathrm{d}A\mathrm{d}x$ created by the elastic expansion of the channel. For a sinusoidal excitation with $U^{\mathrm{el}}(t) = U_0 \exp(i\omega t)$ we get with $I_C^{\mathrm{el}} \mathrm{d}x = U^{\mathrm{el}}/(Z_x^{\mathrm{el}}(\omega)\mathrm{d}x)$ being the current loading the capacitance:

$$Q_x^{\mathrm{el}} = \int I_C^{\mathrm{el}} \mathrm{d}t = \frac{1}{i\omega} I_C^{\mathrm{el}} = \frac{1}{i\omega} \frac{U^{\mathrm{el}}}{Z_x^{\mathrm{el}}} = \frac{U^{\mathrm{el}} C_x^{\mathrm{el}}}{1 + i \tan \alpha}, \tag{6.10}$$

respectively

$$U^{\text{el}} = \frac{Q_x^{\text{el}}}{C_x^{\text{el}}}(1 + i\tan\alpha), \qquad (6.11)$$

where $\tan\alpha = \omega C_x^{\text{el}}/g_x^{\text{el}}$.

For a purely elastic channel wall, the hydrodynamic capacitance per unit length C_x is given by the extra cross-sectional area per pressure $\mathrm{d}A/\mathrm{d}p$ which is created by the channel expansion. In a viscoelastic channel, there is a phase difference δ between the stress and the strain in the wall material. The stress is proportional to the local pressure, and the extra cross-sectional area $\mathrm{d}A$ is proportional to the strain ϵ, the channel cross section A and a geometrical factor k_{geom}: $\mathrm{d}A = k_{\text{geom}}A\epsilon$. In an analogous description to the electric equation 6.11, the relation between pressure and strain in the model thus reads:

$$p = \frac{k_{\text{geom}}A\epsilon}{C_x}(1 + i\tan\alpha). \qquad (6.12)$$

The phase difference of α between p and ϵ is matched to the viscoelastic properties of PDMS by setting $\delta = \alpha = \omega C_x/g_x$, where δ is the phase difference of the complex elastic modulus $E^\star$, resp. shear modulus $G^\star$ of PDMS. Comparing the absolut value of p following from eq. 6.12 with the absolut value of each Fourier component of the pressure in eq. 2.4

$$|p_n| = \frac{k_{\text{geom}}A}{C_x\cos\delta}\epsilon = |E^\star|\epsilon = 2(1+\nu)|G^\star|\epsilon \qquad (6.13)$$

reveals the correct values for $C_x(\omega)$ and $g_x(\omega)$:

$$
\begin{aligned}
C_x(\omega) &= \frac{C_{x,0}}{|G^\star(\omega)/G_{\omega_0}^\star|\cos\delta} \\
g_x(\omega) &= \frac{\omega C_{x,0}}{|G^\star(\omega)/G_{\omega_0}^\star|\sin\delta}
\end{aligned} \qquad (6.14)
$$

where $C_{x,0} = \frac{k_{\text{geom}}A}{2(1+\nu)|G_{\omega_0}^\star|}$.

6.2   Results & Discussion

To quantitatively test the implications of the 1-D diffusion equation model, a pressure step pulse was applied periodically to a microfluidic channel. The resulting local pressure and the flow rate were measured at different positions along the channel. Theoretical predictions for the dispersion of pressure and flowrate were calculated with equation 6.7 based on the experimentally determined pressure at the channel entrance at $x = 0$ and compared to the measurements.

The pressure step pulse of $f_0 = 0.5\,\text{Hz}$ was generated with the oscillatory flow setup described in sect 2.1 and applied to a straight microfluidic channel filled with an approximately $60\%\,(\text{w/w})$ glycerol solution. The channel had a rectangular cross-section of width $w = 60\,\mu\text{m}$, height $h = 80\,\mu\text{m}$ and length $l = 20\,\text{mm}$. To yield a channel slightly softer than usual, the PDMS was mixed

with crosslinker in a ratio of 20:1 instead of the standard 10:1 ratio given in [75]. The channel end at $x = l$ was exposed to ambient pressure $p(l,t) \approx 0$. The local pressure and flow conditions as a function of the position in the channel were observed at different positions along the channel at $x = 0\,$mm, $x = 7.5\,$mm, $x = 12.5\,$mm and $x = 17.5\,$mm distance to the channel entrance. To this end $1\,\mu$m beads were embedded in the PDMS as well as suspended in the fluid (Fig. 2.2) and movies with 500 frames per second were recorded in the midplane of the channel at $z = 0.5h$ to determine the motion of both the fluid and the channel walls.

6.2.1   Determination of Pressure $p(t)$ from Channel Deformations

The wall movement was determined by tracking the particles embedded in the PDMS with the custom made software OpenBox [91]. Approximately 80 beads within the first $30\,\mu$m to the wall were tracked and averaged over 3 oscillation periods on each side of the channel to obtain the lateral motion $Y_{\text{left}}, Y_{\text{right}}$ on each side of the channel. The geometrical factor f_{geom} relating the strain ϵ to the wall movement was determined in a FEM-simulation for a channel (w x h = 60 x 80 μm^2) with a 1000 x 1000 x 80 μm^3 inlet section (see fig. 6.2). To this purpose, static simulations with constant pressure were performed with a strain of 1% set by the ratio of pressure and elastic modulus $\epsilon = p/E = 1\%$. The wall displacement Y in half height of the channel $z = h/2$ was evaluated to calculate the geometrical factor according to eq. 2.2. For the experimental geometry the simulations yield a constant value of $f_{\text{geom}} \approx 0.95$ except within the first $1\,$mm next to the channel entrance and exit (see Fig. 6.2b). Thus $f_{\text{geom}} = 0.95$ was used for all evaluated channel positions except for $x = 0$, where the average wall displacement in the recording area of the video (indicated by the green box in fig. 6.2b) was used to determine $f_{\text{geom}} \approx 0.72$. The complex shear modulus $G^\star$ needed to calculate the pressure from the strain ϵ was measured in an oscillatory rheometer with a $2°$ cone-plate geometry for a constant strain $\epsilon = 0.1\%$ (see Fig. 6.3).   Using the Poisson ratio of $\nu = 0.5$ for PDMS, the pressure pulse can then be computed directly from the Fourier components of the wall movement $Y(x,t) = 0.5(Y_{\text{left}} - Y_{\text{right}})$ with eq. 2.6. The resulting experimental local pressures in the channel are shown in fig. 6.4a by the solid lines. From the obtained results a Fourier transformation is computed in order to resolve the frequency dependencies of the pressure depicted in Figs. 6.6 and 6.7a.

6.2.2   Determination of the Flowrate $Q(t)$

Videos of the channel with fluorescent beads were divided into $i = 11$ strips across the width. The fluid velocity $v_i(t)$ in each stripe was determined by cross-correlation of subsequent video frames and three oscillation periods were averaged to yield the fluid velocity during one period for each strip. For each frame, a parabolic fit in the y-direction lateral to the flow was applied to the flow profiles obtained from the 11 strips to extract the maximum fluid velocity
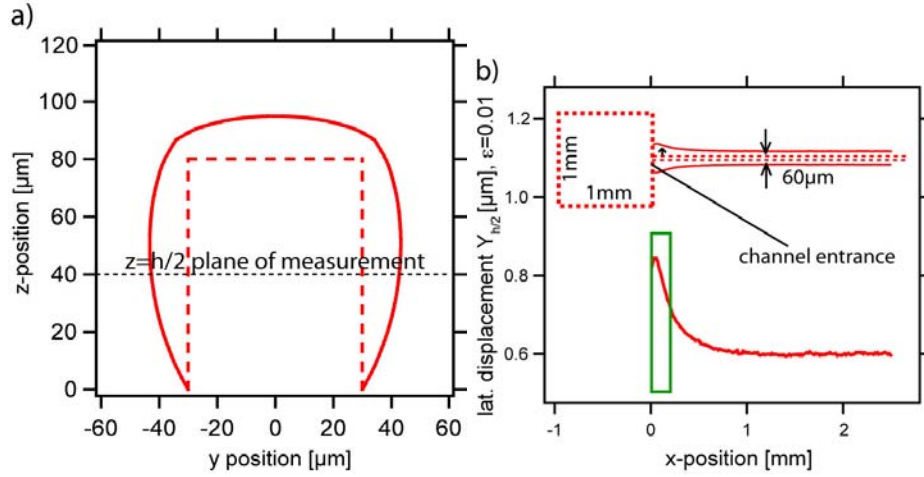
Figure 6.2: FEM-simulations to determine f_{geom} and k_{geom}. (a) Channel expansion corresponding to $\epsilon = 0.01$ in cross-section of PDMS channel. For clarity the wall displacement has been 20x enlarged. (b) Wall displacement $Y(z = h/2)$ along the channel. Near the channel entrance at $x = 0$ the expansion of the channel is higher than inside the channel. The green box shows the area recorded in the video for $Y(x = 0), Q(x = 0)$.
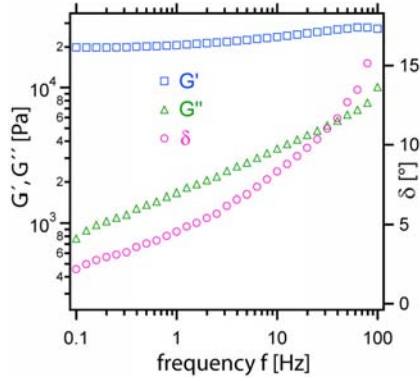
Figure 6.3: Oscillatory rheometer measurement of the complex shear modulus $G^{\star} = G' + iG''$ of PDMS with phase angle δ between stress and strain.

v_{max} for each frame. The flowrates $Q(x,t)$ were then calculated from v_{max} by using eq. A.81 and A.82 for $w < h$:

$$\frac{v_{\mathrm{max}}}{Q} = \frac{48}{\pi^3 h w} \frac{\sum_{n,\mathrm{odd}}^{\infty} \frac{(-1)^{\frac{n-1}{2}}}{n^3}\left[1 - \frac{1}{\cosh\left(n\pi\frac{h}{2w}\right)}\right]}{1 - 0.63\frac{w}{h}} \tag{6.15}$$

The flowrate curves Q differ less than $5\,\%$ from their steady state values $Q_{s.s.}$ at the end of half the period of the driving oscillation $T_0/2 = \pi/\omega_0 = 1\mathrm{s}$. The steady state flowrate has to be equal at all channel positions — yet the

Figure 6.4: Pressure p and flowrate Q pulses at $x = 0, 7.5, 12.5, 17.5$ mm in the time domain. (a) pressure pulses, (b) flowrates (solid: measured, dashed: theory); flowrates at $x = 7.5, 12.5, 17.5$ mm were offset in Q for better visibility. Inset: close up of the measured flowrates without offset showing the lag-time between flowrate pulses.
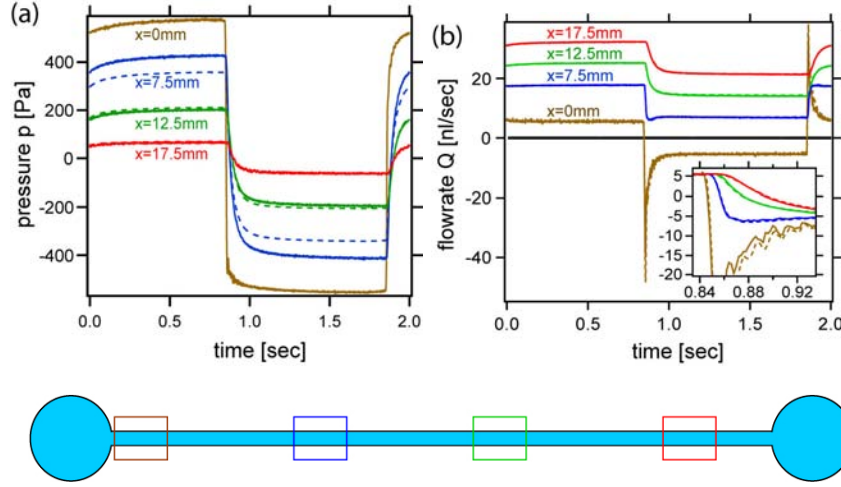
measured steady state maximum velocities vary up to 20 %, possibly due to local inhomogeneities in the channel geometry and variations in the z-position of the measurement. To account for these sources of uncertainty the absolut values of the velocity curves were scaled to yield matching steady state flowrates $Q_{s.s.}$ for the different channel positions. This does not alter the shape of the flowrate pulses and the frequency dependencies discussed. The resulting experimental flowrates are shown in fig. 6.4b. The frequency dependencies shown in Figs. 6.6a and 6.7b have been obtained by a Fourier transformation of $Q(x,t)$.

6.2.3 Calculation of Theoretical Curves

The measured pressure curve at the channel entrance was Fourier analysed to yield the N frequency components $\Pi_{0n} \exp(i\omega_n t)$ of the input pressure at $x = 0$ (N is set by the framerate f_{vid} of the recorded videos as $N = f_{\text{vid}}/2f_0$). Summing up the solution given by eq. 6.6 for each Fourier component of pressure and flowrate p_n, Q_n for $x = 7.5$, $x = 7.5$, 12.5 and 17.5 mm yields theoretical curves for p and Q along the channel $p(x,t) = \sum_{n=0}^{N} p_n(x,t), Q(x,t) = \sum_{n=0}^{N} Q_n(x,t),.$ Hereby the values for the wall resistance $Z_x(\omega)$, the channel's hydrodynamic resistance per unit length R_x and the inertial inductance L_x were determined as follows:

The complex resistance $Z_x(\omega)$ (see eq. 6.3) can be calculated from eq. 6.14 once the geometrical factor k_{geom} describing the relation between the extra cross-sectional area $\mathrm{d}A$ and expansional strain ϵ is known. The FEM-simulation

(Fig. 6.2a) suggests a geometrical factor $k_{\text{geom}} = 2.4$. The best accordance with the experimental data was achieved with $k_{\text{geom}} = 2.0$, which has been used for the theoretical calculations.

The hydrodynamic resistance per unit length R_x for a rectangular channel filled with fluid of viscosity η for $w < h$ is calculated from eq. A.82 as:

$$R_x \approx \frac{12\eta}{w^3 h}\left(1 - 0.63\frac{w}{h}\right)^{-1}.\tag{6.16}$$

As the changes of the channel cross-section due to the applied pressure in the experiment are small ($< 3\%$), the resistance can be assumed to be independent of the applied pressure $R_x = const$. A consistent value for the viscosity η can be extracted from the periodic measurement in the channel itself: Since $\omega_0 < \omega_{\text{cutoff}}$, p and Q at the end of the period of the step pulses are good estimates for the steady state values $p_{s.s.}$ and $Q_{s.s.}$ in constant flow. The overall resistance of the channel $R_x l$ has to fulfill the equation $R_x l = \frac{p_{s.s.}}{Q_{s.s.}}$ which directly sets an experimental value for the viscosity of

$$\eta = \frac{p_{s.s.}}{Q_{s.s.} l}\frac{h^3 w}{12}\left(1 - 0.63\frac{h}{w}\right)\tag{6.17}$$

The hydrodynamic inductance per unit length L_x is given by $L_x = \rho/A$, where $A = wh$ and $\rho = 1.2\,\text{gcm}^{-3}$ was used for the calculation of the theoretical curves.

The resulting theoretical curves for pressure and flowrate in the time-domain are shown by the dashed lines in fig. 6.4. An excellent agreement in the shape between experimental and theoretical curves is achieved. The pressure amplitudes show an uncertainty of at most 20% ($x = 7.5$ cm curve) between theory and experiment, which might result from uncertainties in the local structure of the PDMS channel and measuring height z. The flowrate curves, which have been calibrated by using the common steady state value, show an excellent overall agreement between experiments and theoretical predictions validating the used equivalent circuit model.

6.2.4 Discussion with Purely Elastic Channel Model

The equivalent circuit model revealed that the pressure and fluid propagation in the microfluidic channel can be described by the telegraphers equation eq. 6.6. The Fourier decomposition of the experimental pressure and flowrate pulses shows that sufficient accuracy in the data is only available up to frequencies of 25-50 Hz (see fig. 6.7). In this regime, the phase difference δ between the pressure and the wall deformation in the PDMS is relatively small with $\delta \leq 10°$ (see fig. 6.3). Moreover, the fluid inertia is negligible ($L_x \approx 0$) in the low-Reynolds regime. To understand the underlying physics and the characteristic features of the flow dynamics in PDMS channels, it is therefore instructive to discuss a purely elastic model of the channel with $\delta = 0, L_x = 0$ as an approximation. In this simple model, the channel is described by the one-dimensional diffusion

equation

$$\frac{\partial p_n}{\partial t} = D_p \frac{\partial^2 p_n}{\partial x^2} \tag{6.18}$$

where $D_p = 1/(R_x C_x)$ and $\omega_{\text{cutoff}} = 2\pi/R_x C_x l^2$ are independent of the frequency. In a classical diffusion picture, the periodic pressure pulses correspond to a varying concentration gradient, and the resulting volume flow in the channel can be identified with the diffusive flux. The implications of this simple 1-D model shall be discussed in a deeper analysis of the experimental findings in the following paragraphs.

The timescale for pressure and flow pulse propagation is given by the pressure diffusion constant D_p.

In bulk fluids and in rigid channels, pressure excitations can propagate with the speed of sound of the fluid v_c. With an elastic modulus of $G(\text{PDMS}) \sim 2 \cdot 10^4\,\text{Pa}$ for the channel and a compressive modulus of $K(\text{water}) \sim 2 \cdot 10^9\,\text{Pa}$ in the fluid, the propagation of a pressure pulse in a microfluidic device will be set by the channels mechanical and geometrical properties rather than v_c. Thus, for an oscillating pressure driving an overdamped liquid column in laminar flow, the propagation of the pressure is determined by the wall compliance and the hydrodynamic resistance of the channel, which set the diffusion constant $D_p = 1/C_x R_x$.

It can be shown (see appendix D) that the traveling time for a pressure wave to cross the entire channel length l in the low frequency limit ($\omega \ll \omega_{\text{cutoff}} = 2\pi D_p l^{-2}$) is given by $\tau(0 \to l) = \frac{l^2}{6 \cdot D_p}$. For the 20 mm long channel used here the characteristic time $\tau_{RC} = R_x C_x l^2$ is approximately 0.35 s. This gives an average low frequency phase velocity for pressure propagation across the channel of $\bar{v}_{ph} \approx 0.34\,\text{ms}^{-1}$, which is 3 orders of magnitude below v_c. The increasing lag time in the onset of the flow rate pulses (see close up in Fig. 6.4b) shows clearly the predicted time delay of the concomitant flowrate propagation at the different positions along the channel.

Pressure and flow pulses are subject to dispersion.
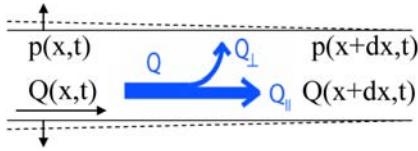
Figure 6.5: Schematics explaining the observed phase difference between pressure and flow rate and the decrease in the oscillatory flow rate amplitude along the channel. Both effects are evident by the fact, that a fraction of the flow Q fills the extra volume created by the channel expansion.

The description by a diffusion equation implies that generally the phase velocity becomes frequency dependent and higher frequency components propagate faster. Consequently, the phase velocity shows dispersion which is fre-

quency and spatially dependent. This results in a phase difference between the pressure p_n and flow Q_n along the channel, which is frequency dependent and decreases along the channel length reaching zero at the exit. The phase shift can maximally be $\Delta\phi_{p-Q} = \pi/4$ in the high frequency limit, which results directly from the solution for $\lambda_n = \sqrt{i\omega_n R_x C_x}$ for the case of an ideal elastic boundary ($\delta = 0$) (see eq.D.12). Mechanistically, one can imagine that the elastic expansion of the channel creates a local extra volume $V_{ex} \propto p_n$ in phase with the pressure. In turn, the flow into this extra volume $Q_{ex} \propto \partial V_{ex}/\partial t$ needs to be $\pi/2$ ahead of the pressure (see sketch in fig. 6.5). The phase shift of the flow into the extra volume results in a phase difference $\Delta\phi_{p-Q}$ between the total flow and the applied pressure. As the pressure drops along the channel, this extra volume decreases. Consequently, the contribution of the flow into the extra volume decreases with respect to the transported volume, so that $\Delta\phi_{p-Q}$ approaches zero. With increasing frequency, the phase shift $\Delta\phi_{p-Q}$ increases due to the simple fact, that the total volume transported per oscillation period is smaller at high frequencies, yet the extra volume is essentially independent of the frequency.

In the low and high frequency limit, analytical expressions for the phase velocity can be calculated (see appendix D). For $\omega \ll \omega_{\text{cutoff}}$ the phase velocity $v_{ph}(x) \approx 3D_p/(l-x)$ is independent of ω, and p_n and Q_n are in phase everywhere in the channel. For $\omega \gg \omega_{\text{cutoff}}$ the phase velocity becomes independent of x and grows with $\omega^{1/2}$: $v_{ph}(\omega) \approx \sqrt{2\omega D_p/(\cos\delta(1-\sin\delta))}$. Now the flowrate Q_n is generally ahead of the pressure p_n (up to $\Delta\phi_{p-Q} = \pi/4 - \delta/2$) and only at the exit (at $x \approx l$) p_n and Q_n are in phase. Fig. 6.6a shows the theoretically and experimentally determined values for the phase difference $\Delta\phi_{p-Q}$ as a function of the frequency $f = \frac{\omega}{2\pi}$, which are in excellent agreement for $f \leq 20\,\text{Hz}$.

To enable a direct comparison of the computed phase velocity $v_{ph}(x, \omega)$ with experimental results we need to define an averaged phase velocity $\bar{v}_{ph}(x_i, \omega)$. To this end the phase of a pressure pulse is determined at two points ($x = 0$ and $x = x_i$) for each frequency component and the resulting phase difference $\Delta\phi_{0-x_i}^{n,p}$ is used to obtain $\bar{v}_{ph}(\omega_n) = x_i\omega_n/\Delta\phi_{0-x_i}^{n,p}$. Fig. 6.6b shows that the frequency dependence of the measured propagation speeds is in excellent agreement with the theoretical calculations. As an important consequence from the dispersion relation, the occurrence of peaks in the flow rate is expected once a step pulse is applied. Indeed, Fig. 6.4 shows the dispersion of pressure p and flowrate Q pulses in the time-domain. For steep pressure pulses, the phaseshift of the high-frequency components generates peaks in the flow rate at the channel entrance which can significantly exceed the steady state value ($Q_{\text{peak}} \gg p_{\text{peak}}/R_x l$). This is an important consequence of the susceptibility of microfluidic devices, which needs to be accounted for if critical shear rates need to be considered. In the same way, local pressure peaks may occur if the flow is suddenly stopped by a closing valve. Especially in macrofluidic flows with inertial effects involved, very high pressure peaks associated with transient flows are observed. This phenomenon is known as *water hammer* and may cause severe damage to pipes [109].
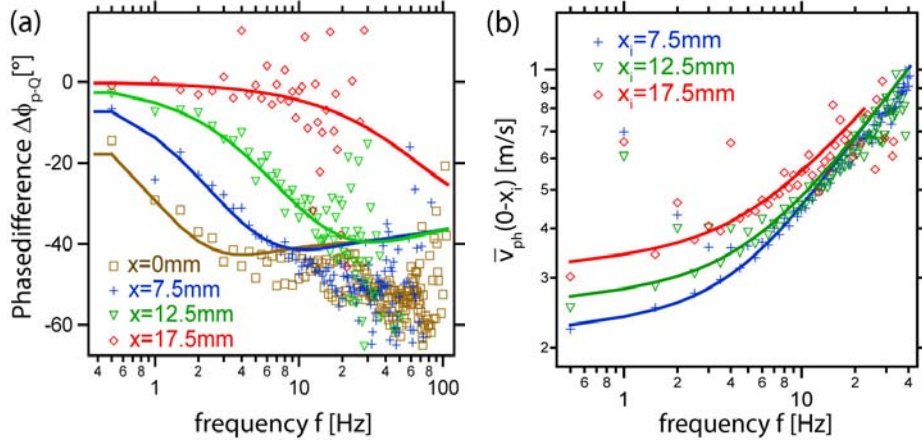
Figure 6.6: Dispersion of propagating pulses (symbols: experimental values, solid lines: theoretical values): (a) phase difference $\Delta\phi_{p-Q}$ between p_n and Q_n at $x = 0, 7.5, 12.5, 17.5$ mm. $\Delta\phi_{p-Q}$ grows with frequency and decreases towards the channel exit. (b) averaged phase velocity of pressure components p_n travelling from $x = 0$ to $x_i = 7.5, 12.5, 17.5$ mm.

The microfluidic channel is a lowpass to pressure and flow pulses.

In addition to the dispersion, high-frequency components are damped in the diffusive propagation, resulting in an effective low-pass filter property of microfluidic devices. If the frequency of a pressure signal is faster than the time it takes to propagate to a certain position in the device, it will be smeared out beyond the diffusion length of the device. Consequently, high frequency components p_n, Q_n of pressure and flowrate pulses get damped.

The characteristic time τ_{RC} sets a cutoff frequency $\omega_{\mathrm{cutoff}} = 2\pi/\tau_{RC}$ for the transmission of flow and pressure pulses for the whole device length. For $\omega_n \ll \omega_{\mathrm{cutoff}}$ eq. (6.18) becomes

$$\frac{\partial^2 p}{\partial x^2} \approx 0 \tag{6.19}$$

and the pressure drops linearly across the channel. For $\omega_n \gg \omega_{\mathrm{cutoff}}$ the damping becomes exponential and can be calculated for the pressure and flowrate:

$$|p_n(x)| \approx |\Pi_{0n} e^{-2\lambda_n x}|$$
$$|Q_n(x)| \approx |\frac{\Pi_{0n}}{R_x} \lambda_n e^{-2\lambda_n x}|. \tag{6.20}$$

Fig. 6.7 shows the lowpass characteristics of the channel for normalized pressure and flowrate pulses $|p_n(x)/p_n(0)|$, $|Q_n(x)/Q_n(0)|$. Experimental values (symbols) and theoretical curves (solid lines) are again in good agreement.
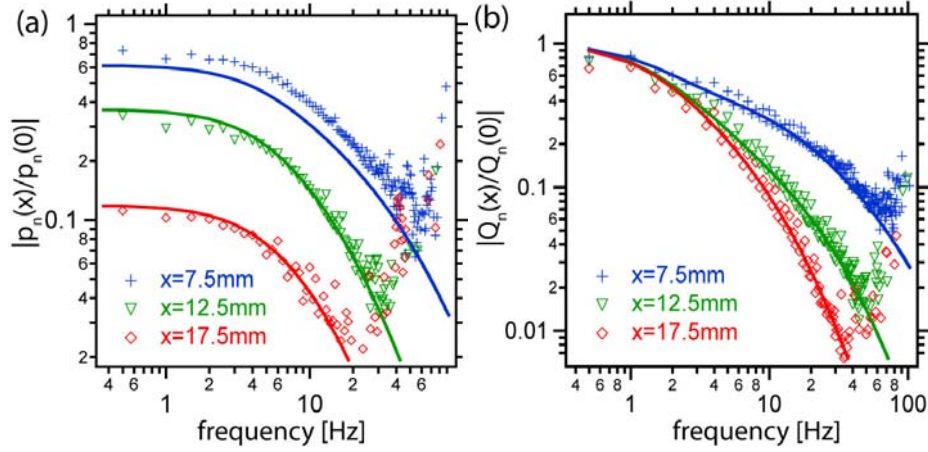
Figure 6.7: Frequency dependence of the pressure (a) and flowrate (b) transmission along the channel: Fourier components $|p_n(x)|, |Q_n(x)|$ normalized to their values $|p_n(0)|, |Q_n(0)|$ at the channel entrance. Symbols: measured values, solid lines: theoretical curves calculated from eq. (6.6).

Conclusion

The flow of Newtonian liquids in viscoelastic microfluidic channels can be described with a pressure diffusion equation. The PDMS channel acts as a low-pass filter: Fourier components with frequencies higher than ω_{cutoff} are dispersed and damped. Thus the channel effectively smoothes incoming pressure and flow pulses. To generate a uniform flow along the channel, PDMS devices should only be operated with $\omega < \omega_{\mathrm{cutoff}}$ which gives an upper limit e.g. for the operating frequency of switches and microchannel-rheometers. Sharp pressure pulses result in peaks of high flowrates in the channel entrance region and must be avoided in all applications that are sensitive to high wall shear stresses. Although these high flow rate peaks are limited to the channel entrance region, sharp changing pressure pulses that temporarily give rise to very high wall shear stresses could e.g. be used to enhance the effectivity of cleaning processes in elastic channels. The introduced method of pressure sensing by wall-motion-tracking provides a tool for further detailed investigation of transient flows in viscoelastic channels. The presented experimental approach as well as the modeling may provide a useful basis for studies of non-Newtonian-liquids in any 2-D geometry achieved with the standard PDMS soft lithography procedure. It should be well suited for simulating flows in small to intermediate blood vessels with different geometries - although in bigger vessels inertia effects need to be accounted for.

7. OUTLOOK

The present work has demonstrated that microfluidic devices are ideally suited to gain insight into the dynamics of complex fluids under flow. The discussion of the tumbling dynamics of actin filaments in chapter 4 showed, that the direct experimental observation of the conformational dynamics of polymers in flow facilitates developing theoretical models describing the underlying physical mechanisms. Due to the huge number of degrees of freedom encountered with large molecules, even in the relative simple case of linear polymers in dilute solution many non-linear effects observed in experiments or simulations are not yet fully understood. Just recently, a previously unknown regime of polymer stretching in high shear rates has been theoretically proposed and studied in simulations, yet an experimental evidence is still lacking [96, 24]. Hereby, a decrease in the average stretching length has been predicted to occur at high shear rates, where the Peclet number $Pe = \dot{\gamma}\tau_K$, given by the product of shear rate and the relaxation time of a single Kuhn segment, gets bigger than one. While for flexible polymers this regime is hardly realized without rupturing the polymers, $Pe > 1$ is easily reached in our experiments. Thus, the behaviour of long actin filaments with $L_c \geq b_K = 2L_p$ in the regime of multiple tumblings resembles the motion of segments of flexible polymer chains at $Pe > 1$. Therefore, experiments with semiflexible polymers in the $L_c \geq 2L_p$ regime shown here could help to experimentally elucidate the dynamics of flexible polymers in the proposed regime of reduced stretch.

A variety of interesting fields of research emerges from a variation of the experimental conditions used in the tumbling studies: For instance, an increase of the background viscosity could enable the direct observation of shear degredation of polymers, so that the rupture force of actin filaments could be measured. By mixing fluorescently labelled actin filaments with a high concentration of unlabelled filaments, the tumbling assay can readily be extended to the semi-dilute and entangled regime, and first experiments at high actin concentrations have already been conducted. A direct measurement of entangled semiflexible polymer dynamics in shear provides a powerful tool to further test and improve existing theories on entangled polymer solutions under flow. This is of special interest, as exisiting models of entangled solutions are based on the description of single polymer dynamics, where interactions with neighbouring polymers are considered by a confinement potential following the famous tube reptation model developed by de Gennes, Doi and Edwards [25, 27]. The confinement potential of entangled actin filaments in equilibrium has been determined experimentally and discussed theoretically recently [87, 36, 44, 45, 113].

For concentrated suspensions of rod-like polymers, excluded volume potentials induced by the neighbouring polymers can suppress the tumbling motion in flow at intermediate shear rates [64].

The experiments in chapter 5 confirmed the functionality of the proposed differential shear rheometer in a wide range of shear-viscosity exponents n. An apparent transient extensional viscosity of dilute polymer solutions has been successfully measured with the differential extensional rheometer and was found to be in accordance with values in the literature. The performance of the extensional device for use with entangled solutions, which exhibit pronounced shear thinning, has to be further inspected to establish an appropriate working range for solutions of arbitrary shear properties. While the signal generating mechanism has successfully been tested in first experiments with worm-like-micellar solutions, the determination of the extensional viscosity from the measured data gets difficult for solutions with very low shear exponents $n \approx 0$. This shows, that more research is necessary to correctly account for the combination of shear and extensional flows in the data evaluation.

The differential nature of the measurements with the proposed viscometers makes the technique especially qualified for comparative implementations, where rather a fluid characterization instead of the determination of an absolute viscosity value is required. For instance, the flowrate ratio X could be used as a regulatory parameter for process-control in industrial applications. Moreover, the flowrate ratio could be used analogously to the melt flow index MFI in polymer melts, which serves as a measure to determine the molecular weight and the polydispersity in polymer melts [89]. Hereby, the combination of the shear and the extensional viscometer could proof especially advantageous: Within a two-dimensional parameter space (X, Y) representing the fundamentally different flow properties in shear (X) and extensional flow (Y), a far more accurate characterization of the fluid could be achieved than with a single quantity like the MFI. The very simple and robust design makes the shear and extensional viscometer open for miniaturization, parallelization and cheap production, so that both devices can be readily incorporated into existing lab-on-a-chip devices. As especially in R&D applications the majority of lab-on-a-chip devices already include a microscopic survey of the externally applied sample flow, no extra external equipment is needed to run the differential viscometers.

Another exciting field for experimental studies opens up when the strategies for observation of individual polymer dynamics in chapter 4 are combined with the differential viscometers proposed in chapter 5: A non-Newtonian flowrate ratio $X \neq X_N$ indicates a different bulk rheology of the fluid in analyzer and reference channel, which is caused by the different shear and extension rates. Can we directly see a difference in the polymer dynamics related to the shear-thinning in analyzer and reference channel when we follow fluorescent polymers flowing down the channels in the shear viscometer? Can we observe the stretching of flexible labelled polymers in the constrictions of the extensional viscometer and relate the measured apparent extensional viscosity to the degree of stretching? How do the mixed flow effects in the devices influence the sharp coil-stretch transition observed in purely extensional flows? Is it possible to

watch shear-induced tumblings in shear-dominated strong flows as proposed in section 5.4.6?

Beyond the determination of the steady state viscosities η and Λ in chapter 5, the examination of the fluid-structure interactions carried out in chapter 6 opens the way for developing an oscillatory lab-on-a-chip rheometer to measure the dynamic viscosity of viscoelastic fluids: For frequencies below the cut-off frequency ω_{cutoff} of the system, the velocity field is uniform along the channel and the pressure inside the channel is in phase with the pressure at an externally connected pressure sensor (see fig 2.2). Then, the relation between stress and strain in the fluid can be determined from the measured pressure and flow velocities in the channel. Fig. 7.1a shows Lissajous-plots of the fluid velocity in the channel center vs. the applied pressure in a $f = 0.1\,\mathrm{Hz}$ large amplitude oscillatory shear measurement (LAOS) with a $2\%\,(\mathrm{w/w})\,\mathrm{PAA}$ solution. The viscoelasticity of the polymer solution causes a phase shift between stress and velocity, resulting in flat elliptical $v(p)$ curves at low pressure amplitudes. The increasing slope of the ellipses at high amplitudes clearly indicates the shear-thinning of the solution at higher oscillatory strains, which illustrates the potential for measuring non-linear rheological properties in LAOS [49]. As
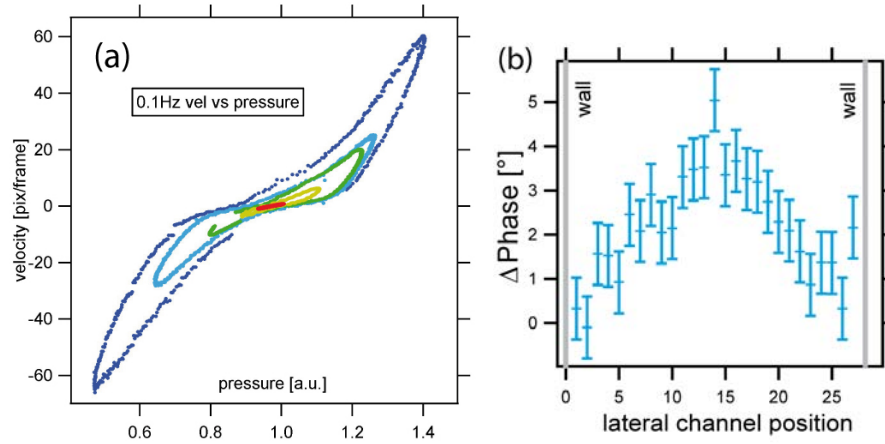
Figure 7.1: (a) Lissajous plot of a 2% (w/w) PAA solution with 5-6 MDa in large amplitude oscillatory shear ($f = 0.1$ Hz). The shape of the curves indicates shear-thinning of the fluid at higher oscillatory strains. (b) The phasedifference between external pressure sensor and fluid flow for 2% PAA solution in oscillatory shear ($f = 0.5$ Hz) depends on the lateral position in the channel (the channel width is $w = 50\,\mu\mathrm{m}$, the abscissa gives the index of the picture strip in the PIV-evaluation indicating the lateral position). Due to the fluids non-linear viscoelasticity, the fluid in the channel center is not in phase with the fluid near the channel walls.

the phase difference between stress and strain is generally strain dependent in viscoelastic fluids, a measurable phase difference occurs throughout the channel

cross section (see fig 7.1b), so that the fluid in the channel center is out-of-phase with the fluid near the channel walls. A meta-stable shear-banding state has been recently observed for well-entangled polymer solutions in large amplitude oscillatory shear [17].

For frequencies above ω_{cutoff}, fluid-structure interactions have to be considered. Transient flows of complex fluids in elastic channels are of big importance for understanding vascular deseases as well as for precise control in the operation of lab-on-a-chip devices. Thus, a lot of effort has been devoted to model oscillatory flows of non-Newtonian fluids in elastic channels, and both analytical formulations and improved numerical simulations are the subject of ongoing research [14, 28, 94]. Standard PIV techniques and the local pressure sensing method exploiting the wall deformations developed in this thesis enable the determination of local pressure and flowfield at various points in a channel network. Thus, microfluidic devices can be used as optimal test systems with model fluids as well as for mimicking microcirculation networks in vitro in arbitrary 2-dimensional geometry.

APPENDIX

A. BASIC FLUID DYNAMICS

A.1 Flow Classification

Decomposition of Flow Field: Uniform Flow + Rotational Flow + Extensional Flow

We specify the flow of a fluid by the velocity field $\mathbf{u}(\mathbf{x}, t)$ where $\mathbf{u} = (u_x, u_y, u_z)$ represents the velocity of the fluid at time t at the point $\mathbf{x} = (x, y, z)$ in space [20]: According to the types of deformation that a fluid element undergoes during flow it is common to classify different types of flows. For that purpose we will discuss the transformation that the distance vector $\mathbf{h}$ connecting two nearby points $\mathbf{x}$ and $\mathbf{y} = \mathbf{x} + \mathbf{h}$ in the fluid undergoes in a small time step $\mathrm{d}t$. The trajectory of the fluid element at the position $\mathbf{x}$ is given by the differential equation

$$\frac{\mathrm{d}\mathbf{x}}{\mathrm{d}t} = \mathbf{u}(\mathbf{x}) \tag{A.1}$$

so after a small time step $\mathrm{d}t$ the fluid element at $\mathbf{x}$ has been translated to $\mathbf{x}(t + \mathrm{d}t) = \mathbf{x}(t) + \mathbf{u}(\mathbf{x})\mathrm{d}t$. The time evolution of the distance vector $\mathbf{h}$ is governed by

$$\frac{\mathrm{d}\mathbf{h}}{\mathrm{d}t} = \frac{\mathrm{d}\mathbf{y}}{\mathrm{d}t} - \frac{\mathrm{d}\mathbf{x}}{\mathrm{d}t} = \mathbf{u}(\mathbf{y}) - \mathbf{u}(\mathbf{x}) \tag{A.2}$$

As $\mathbf{h}$ is small we can use the Taylor expansion of the velocity field for $\mathbf{u}(\mathbf{y}) = \mathbf{u}(\mathbf{x} + \mathbf{h})$ [20]:

$$\mathbf{u}(\mathbf{y}) = \mathbf{u}(\mathbf{x}) + (\nabla\mathbf{u}(\mathbf{x})) \cdot \mathbf{h} + O(h^2) \tag{A.3}$$

where

$$(\nabla\mathbf{u}(\mathbf{x})) = \begin{pmatrix} \frac{\partial u_x(\mathbf{x})}{\partial x} & \frac{\partial u_x(\mathbf{x})}{\partial y} & \frac{\partial u_x(\mathbf{x})}{\partial z} \\ \frac{\partial u_y(\mathbf{x})}{\partial x} & \frac{\partial u_y(\mathbf{x})}{\partial y} & \frac{\partial u_y(\mathbf{x})}{\partial z} \\ \frac{\partial u_z(\mathbf{x})}{\partial x} & \frac{\partial u_z(\mathbf{x})}{\partial y} & \frac{\partial u_z(\mathbf{x})}{\partial z} \end{pmatrix} \equiv \mathbf{A}(\mathbf{x}) \tag{A.4}$$

is the velocity gradient tensor of $\mathbf{u}(\mathbf{x})$ and get

$$\frac{\mathrm{d}\mathbf{h}}{\mathrm{d}t} = \mathbf{A}(\mathbf{x}) \cdot \mathbf{h} = \frac{\partial\mathbf{u}(\mathbf{x})}{\partial\mathbf{h}}. \tag{A.5}$$

Thus, $\mathbf{u}(\mathbf{x})$ induces merely a rigid translation of $\mathbf{h}$ and only $\mathbf{A} = (\nabla\mathbf{u})$ contributes to changes of the length and orientation of $\mathbf{h}$. To further examine the properties of the flow we split $\mathbf{A}$ into its symmetric and antisymmetric part[20]:

$$\mathbf{A} = \mathbf{D} + \mathbf{S} \tag{A.6}$$

with

$$\mathbf{D} = \frac{1}{2}[\nabla \mathbf{u} + (\nabla \mathbf{u})^T] = \dot{\boldsymbol{\gamma}} \tag{A.7}$$

and

$$\mathbf{S} = \frac{1}{2}[\nabla \mathbf{u} - (\nabla \mathbf{u})^T]. \tag{A.8}$$

Rate of Deformation Tensor $\mathbf{D}$

To elucidate the role of $\mathbf{D}$ and $\mathbf{S}$ we look at the differential equation (A.5) for $\mathbf{D}$ and $\mathbf{S}$ seperately following [20]:

$$\frac{d\mathbf{h}}{dt} = \mathbf{D} \cdot \mathbf{h} \tag{A.9}$$

As the matrix $\mathbf{D}$ is symmetric, there is always an orthonormal basis $\tilde{\mathbf{e}}_1, \tilde{\mathbf{e}}_2, \tilde{\mathbf{e}}_3$ in which $\mathbf{D}$ is diagonal:

$$\mathbf{D} = \begin{pmatrix} d_1 & 0 & 0 \\ 0 & d_2 & 0 \\ 0 & 0 & d_3 \end{pmatrix} \tag{A.10}$$

In this coordinate system, eq. (A.9) seperates into three linear differential equations

$$\frac{d\tilde{h}_i}{dt} = d_i \tilde{h}_i, \quad i = 1, 2, 3 \tag{A.11}$$

that are solved by

$$\tilde{h}_i(t) = \tilde{h}_{i,(t=0)} \exp(d_i t), \quad i = 1, 2, 3. \tag{A.12}$$

Hence, the vector field $\mathbf{D} \cdot \mathbf{h}$ is merely expanding or contracting along each of the axes $\tilde{\mathbf{e}}_i$ with a rate of change d_i for a unit length, and $\mathbf{D}$ is called the *rate of deformation tensor*. A flow of this type is called *purely extensional*, and the volume of a box with sides of length $\tilde{h}_1, \tilde{h}_2, \tilde{h}_3$ parallel to the $\tilde{\mathbf{e}}_1, \tilde{\mathbf{e}}_2, \tilde{\mathbf{e}}_3$ axes changes with a rate of:

$$\frac{d}{dt}(\tilde{h}_1 \tilde{h}_2 \tilde{h}_3) = (d_1 + d_2 + d_3)(\tilde{h}_1 \tilde{h}_2 \tilde{h}_3) \tag{A.13}$$

As the trace of a matrix is invariant under orthogonal transformations,

$$d_1 + d_2 + d_3 = \text{Tr}(\mathbf{D}) = \text{div}\mathbf{u}. \tag{A.14}$$

For the incompressible fluids discussed here $\text{Tr}(\mathbf{D}) = 0$.

Vorticity Tensor $\mathbf{S}$

The differential equation for the antisymmetric part of $\mathbf{A}$ reads:

$$\frac{d\mathbf{h}}{dt} = \mathbf{S} \cdot \mathbf{h} \tag{A.15}$$

Using the vorticity of the velocity field $\boldsymbol{\xi} = \nabla \times \mathbf{u}$, $\mathbf{S}$ can be expressed as

$$\mathbf{S} \cdot \mathbf{h} = \frac{1}{2} \boldsymbol{\xi} \times \mathbf{h}, \tag{A.16}$$

Hence, $\mathbf{S} \cdot \mathbf{h}$ induces a flow which is equivalent to a rotation around $\boldsymbol{\xi}(\mathbf{x})$:

$$\frac{\mathrm{d}\mathbf{h}}{\mathrm{d}t} = \frac{1}{2} \boldsymbol{\xi}(\mathbf{x}) \times \mathbf{h}. \tag{A.17}$$

This differential equation is solved by

$$\mathbf{h}(t) = \mathbf{R}(t, \boldsymbol{\xi}(\mathbf{x}))\mathbf{h}(0). \tag{A.18}$$

where $\mathbf{R}(t, \boldsymbol{\xi}(\mathbf{x}))$ is the matrix that represents a rotation through an angle t about the axis $\boldsymbol{\xi}(\mathbf{x})$. The rotation rate is related to the magnitude of $\mathbf{S}$ and $\mathbf{S}$ is called the *vorticity tensor* of $\mathbf{u}$; the flow induced by $\mathbf{S}$ is a purely rotational flow corresponding to a rigid rotation of the fluid. Writing $\mathbf{S}$ in the principal coordinate system of $\mathbf{D}$ yields [34]:

$$\mathbf{S} = \begin{pmatrix} 0 & -\omega_3 & \omega_2 \\ \omega_3 & 0 & -\omega_1 \\ -\omega_2 & \omega_1 & 0 \end{pmatrix} \tag{A.19}$$

where $\boldsymbol{\xi} = (\omega_1, \omega_2, \omega_3)$ gives the rotation rates about the axes $\tilde{\mathbf{e}}_1, \tilde{\mathbf{e}}_2, \tilde{\mathbf{e}}_3$.

Flow Decomposition

Thus, we can attribute the physical meaning to the terms in eq. (A.3):

$$\mathbf{u}(\mathbf{y}) = \mathbf{u}(\mathbf{x}) + \nabla\mathbf{u}(\mathbf{x}) \cdot \mathbf{h} + O(h^2) \tag{A.20}$$

$$= \underbrace{\mathbf{u}(\mathbf{x})}_{\text{translation}} + \underbrace{\mathbf{S} \cdot \mathbf{h}}_{\text{rotation}} + \underbrace{\mathbf{D} \cdot \mathbf{h}}_{\text{deformation}} + O(h^2) \tag{A.21}$$

Any velocity field $\mathbf{u}(\mathbf{x}, t)$ can be decomposed into the sum of a uniform flow, a rotational flow and an extensional flow, so that the transformation that a fluid element undergoes in a small time step $\mathrm{d}t$ consists of a *rigid translation*, a *rigid rotation* and a *deformation*.

Classification of Flow Fields: Strong, Marginally Weak and Strictly Weak Flows

For a classification of flows we follow [34] and [11] and look at a steady homogeneous flow field with constant stretch history and $\mathbf{u}(0) = 0$. Then eq. (A.1) reads

$$\mathbf{u}(\mathbf{x}) = \dot{\mathbf{x}} = \mathbf{x} \cdot \mathbf{A} \tag{A.22}$$

with $\mathbf{A} = (\nabla\mathbf{u})$. The solution of eq. (A.22) depends upon the three eigenvalues λ of $\mathbf{A}$ which fulfill the equation

$$\lambda^3 - I_1(\mathbf{A})\lambda^2 + I_2(\mathbf{A})\lambda - I_3(\mathbf{A}) = 0 \tag{A.23}$$

where $I_i(\mathbf{A})$, $i = 1, 2, 3$ are the principal invariants of $\mathbf{A}$ which are independent of the base of the coordinate system:

$$I_1(\mathbf{A}) \qquad = tr(\mathbf{A}) = \lambda_1 + \lambda_2 + \lambda_3 \qquad (A.24)$$

$$I_2(\mathbf{A}) \quad = \tfrac{1}{2}[I_1^2(\mathbf{A}) - tr(\mathbf{A})^2] = \lambda_1\lambda_2 + \lambda_1\lambda_3 + \lambda_2\lambda_3 \qquad (A.25)$$

$$I_3(\mathbf{A}) \qquad = \det(\mathbf{A}) = \lambda_1\lambda_2\lambda_3 \qquad (A.26)$$

For incompressible fluids $I_1 = 0$. We now use the flow decomposition into rotational and deformational components $\mathbf{A} = \mathbf{S} + \mathbf{D}$ introduced in eq. (A.6) and write $\mathbf{A}$ in the principal coordinate system of $\mathbf{D}$ in which $\mathbf{D}$ is diagonal:

$$\mathbf{A} = \begin{pmatrix} \epsilon_1 & -\omega_3 & \omega_2 \\ \omega_3 & \epsilon_2 & -\omega_1 \\ -\omega_2 & \omega_1 & \epsilon_3 \end{pmatrix} \qquad (A.27)$$

where $\epsilon_i = D_i i$ and $\omega_1 = S_{23}, \omega_2 = S_{31}, \omega_3 = S_{12}$ are the components of $\mathbf{D}$ and $\mathbf{S}$. The 3 invariants $I_i(\mathbf{A})$ can now be expressed by 5 invariants K_i depending on the components of $\mathbf{D}$ and $\mathbf{S}$:

$$K_1 \quad = I_1(\mathbf{D}) = \epsilon_1 + \epsilon_2 + \epsilon_3 = 0 \qquad (A.28)$$

$$K_2 \quad = I_2(\mathbf{D}) = \epsilon_1\epsilon_2 + \epsilon_2\epsilon_3 + \epsilon_3\epsilon_1 \qquad (A.29)$$

$$K_3 \quad = I_3(\mathbf{D}) = \epsilon_1\epsilon_2\epsilon_3 \qquad (A.30)$$

$$K_4 \quad = I_2(\mathbf{S}) = \omega_1^2 + \omega_2^2 + \omega_3^2 \qquad (A.31)$$

$$K_5 \quad = I_3(\mathbf{A}) - I_3(\mathbf{D}) = \epsilon_1\omega_1^2 + \epsilon_2\omega_2^2 + \epsilon_3\omega_3^2, \qquad (A.32)$$

so that

$$I_1(\mathbf{A}) \quad = 0 \qquad (A.33)$$

$$I_2(\mathbf{A}) \quad = K_2 + K_4 \qquad (A.34)$$

$$I_3(\mathbf{A}) \quad = K_3 + K_5. \qquad (A.35)$$

K_1 describes the compressibility of the fluid, $\sqrt{-K_2/3}$ gives the deformation rate, K_3 is related to the shape of $\mathbf{D}$, $\sqrt{K_4}$ gives the rotation rate and K_5 is related to the relative orientation of the fluid rotation and deformation.

Strong Flow

If $I_3(\mathbf{A}) \neq 0$ or $I_3(\mathbf{A}) = 0 \wedge I_2(\mathbf{A}) < 0$ the real part $\text{Re}(\lambda)$ of at least one eigenvalue λ_i is positive and the flow is classified as *strong flow* [103]. As a result of $\text{Re}(\lambda) > 0$, two material points in the fluid will seperate exponentially in time. The fluid pathways in homogeneous strong flows can have different shapes according to the value of I_3 and the parameter $p = (-I_2/3)^3/(I_3/2)^2$.

- $\underline{I_3 \neq 0 \wedge p > 1}$:
  For $I_3 \neq 0$ and $p > 1$ all three eigenvalues λ_i are real and different, and the solution of eq. (A.22) gives

$$\mathbf{x}(t) = \alpha_1\mathbf{r}_1 \exp(\lambda_1 t) + \alpha_2\mathbf{r}_2 \exp(\lambda_2 t) + \alpha_3\mathbf{r}_3 \exp(\lambda_3 t). \qquad (A.36)$$

Herein, $\mathbf{r}_1, \mathbf{r}_2, \mathbf{r}_3$ are the eigenvectors associated with the eigenvalues $\lambda_1, \lambda_2, \lambda_3$ and $\alpha_1, \alpha_2, \alpha_3$ are path parameters describing the coordinates of a point on the path at time $t = 0$. Because of the shape of the projections of the streamlines onto the planes spanned by each pair of eigenvalues this flow class is called *hyperbolic-parabolic*.

- $\underline{I_3 \neq 0 \wedge p = 1}$:

  For $I_3 \neq 0$ and $p = 1$ two eigenvalues are equal, and with $\lambda_1 = \lambda_2 = \lambda', \lambda_3 = -\lambda'$ the streamlines are given by

  $$\mathbf{x}(t) = \beta[\mathbf{r}' + \mathbf{r}''(t - t_0)] \exp(\lambda' t) + \alpha_3 \mathbf{r}_3 \exp(-2\lambda' t) \qquad (A.37)$$

  where $\mathbf{r}'', \mathbf{r}_3$ point into fixed directions, $\mathbf{r}'$ can be chosen in a fixed plane and β, α_3, t_0 are the path parameters of the fluid trajectories. In homogeneous flow fields this is the class of *hyperbolic logarithmic* flows. It includes the special case of *hyperbolic radial* flows (see sec. 3.1.3).

- $\underline{I_3 \neq 0 \wedge p < 1}$:

  For $I_3 \neq 0$ and $p < 1$ two eigenvalues of $\mathbf{A}$ are conjugate complex and with $\lambda_1 = \lambda' + i\lambda'', \lambda_2 = \lambda' - i\lambda'', \lambda_3 = -2\lambda'$ eq. (A.22) is solved by

  $$\mathbf{x}(t) = \beta[\mathbf{r}' \cos(\lambda''(t - t_0)) + \mathbf{r}'' \sin(\lambda''(t - t_0))] \exp(\lambda' t) + \alpha_3 . \mathbf{r}_3 \exp(-2\lambda' t)$$
  $$(A.38)$$

  These flows are called *elliptic spiral* flows because the projection of the fluid trajectories into the $\mathbf{r}', \mathbf{r}''$ - plane yields elliptic spirals.

- $\underline{I_3 = 0 \wedge I_2(\mathbf{A}) < 0}$:

  For $I_3 = 0$ and $I_2(\mathbf{A}) < 0$ (which corresponds to $p = \infty$) one eigenvalue of $\mathbf{A}$ is zero and the other two are real:

  $$\lambda_1 = \sqrt{-I_2}, \lambda_2 = -\sqrt{-I_2}, \lambda_3 = 0 \qquad (A.39)$$

  The fluid trajectories are hyperbolas in planes parallel to the $\mathbf{r}_1, \mathbf{r}_2$ plane with the center on $\alpha_3 \mathbf{r}_3$

  $$\mathbf{x}(t) = \alpha_1 \mathbf{r}_1 \exp(\sqrt{-I_2} t) + \alpha_2 \mathbf{r}_2 \exp(-\sqrt{-I_2} t) + \alpha_3 \mathbf{r}_3, \qquad (A.40)$$

  so that these flows are called *planar hyperbolic* (see sec. A.2 with $\rho^2 < 1$).

Marginally Weak Flow

If $I_3 = I_2 = 0$ (which is equivalent to $\lambda_1 = \lambda_2 = \lambda_3 = 0$) the flow is classified as *marginally weak* and eq. (A.22) is solved by

$$\mathbf{x}(t) = \beta[\mathbf{r}' + \mathbf{r}''(\alpha_1 + a_1 t) + \mathbf{r}'''(\alpha_2 + 2(a_2 + b\alpha_1 t) + a_1 b t^2)]. \qquad (A.41)$$

Thus, material points in marginally weak flows seperate linearly or quadratically in time and the velocity gradient tensor $\mathbf{A}$ is nilpotent (i.e. there is a $n \in \mathbb{N}$

for which $\mathbf{A}^n = 0$). With $n = 2$, marginally weak flows include the important class of *viscometric flows* which fulfill $\mathbf{A}^2 = 0$ and can be described with a local coordinate system in which $\mathbf{A}$ has the form of a *simple shear flow*:

$$\mathbf{A}' = a \begin{pmatrix} 0 & 1 & 0 \\ 0 & 0 & 0 \\ 0 & 0 & 0 \end{pmatrix}. \tag{A.42}$$

As each fluid element is subject to a simple shear flow with a constant shear rate along the streamlines, viscometric flows are used to measure the shear viscosity of a fluid (see sec. 3.3.1) Fig. A.1 shows some common examples of viscometric flows[74]. A more detailed discussion of simple shear flow is following in sec. A.2.

Strictly Weak Flow

If $I_3 = 0, I_2 > 0$ the flow is called *strictly weak* and the fluid trajectoriess are given by

$$\mathbf{x}(t) = \beta(\mathbf{r}' \cos(\sqrt{I_2}(t - t_0)) + \mathbf{r}'' \sin(\sqrt{I_2}(t - t_0))) + \alpha_3 \mathbf{r}_3. \tag{A.43}$$

These curves are ellipses in planes parallel to $\mathbf{r}', \mathbf{r}''$ - plane with centers on $\alpha_3 \mathbf{r}_3$. Thus, the particle distance in strictiy weak flows just varyies sinusoidal in time and material lines get expanded and shrinked periodically. (Note that in Couette Flow, particle distances vary sinusoidal, but material lines get stretched continuosly).

A.2   Planar Flows

A very descriptive explanation for the classification of flows into strong, marginally weak and strictly weak flows can be given for planar flows, where the velocity-component in one direction is zero, e.g. $\mathbf{u}(\mathbf{x}) = (u_x(x, y,), u_y(x, y), 0)$. Following [35], we write $\mathbf{A} = \nabla \mathbf{u}$ in the principal coordinate system of $\mathbf{D}$:

$$\mathbf{A} = \begin{pmatrix} \dot{\epsilon}_1 & -\omega_3 & 0 \\ \omega_3 & \dot{\epsilon}_2 & 0 \\ 0 & 0 & 0 \end{pmatrix} \tag{A.44}$$

Thus, it is sufficient to discuss the flow in 2D with $\mathbf{A} = \begin{pmatrix} \dot{\epsilon} & -\omega \\ \omega & -\dot{\epsilon} \end{pmatrix}$. In planar flows the axis of the rotational component is perpendicular to the plane of deformation. Here, the fluid elements are rotated around an axis parallel to $\mathbf{e}_3$ while the deformation takes place in the $\mathbf{e}_1, \mathbf{e}_2$ - plane. From A.44 we get

$$I_1 \quad = 0 \tag{A.45}$$
$$I_2 \quad = \omega^2 - \dot{\epsilon}^2 \tag{A.46}$$
$$I_3 \quad = 0. \tag{A.47}$$

Hence, we can classify planar flows with a single flow parameter $\rho = \omega/\dot{\epsilon}$ which gives the ratio of the rotational and the deformational component of the flow.
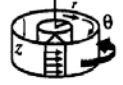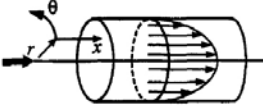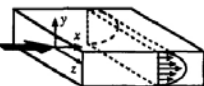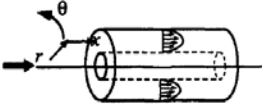
Drag Flows:		Coordinates		
		x_1	x_2	x_3
Sliding plates		x	y	z
Concentric cylinders (Couette flow)		θ	r	z
Cone and plate		ϕ	θ	r
Parallel disks (torsional flow)		θ	z	r
Pressure Flows:				
Capillary (Poiseuille flow)		x	r	θ
Slit flow		x	y	z
Axial annulus flow		x	r	θ

Figure A.1: Various common viscometric flows (picture taken from [74]). In a viscometric flow, each fluid element is subject to a simple shear flow with a constant shear rate along the fluid pathway. The sliding plates, concentric cylinders and cone and plate geometries create homogeneous flow fields.

It is convenient to write $\mathbf{A}$ in a coordinate system that is rotated by $\pi/4$ with respect to the principal coordinate system of $\mathbf{D}$ (see fig. A.2):

$$\mathbf{A} = \begin{pmatrix} 0 & \dot{\epsilon} + \omega \\ \dot{\epsilon} - \omega & 0 \end{pmatrix}. \tag{A.48}$$

(a) coordinate system (b) $\rho = 0$ (c) $\rho^2 < 1$

(d) $\rho^2 = 1$ (e) $\rho^2 > 1$ (f) $\rho^2 = \infty$

Figure A.2: The ratio of the rotational to the deformational component changes the type of flow from strong (b,c) to marginally weak (d) to strictly weak (e,f).

The eigenvalues of A are found as $\lambda_{1,2} = \pm\sqrt{-I_2} = \pm\dot\epsilon\sqrt{1-\rho^2}$, and the differential equation $\dot{\mathbf{x}} = \mathbf{A}\mathbf{x}$ reads:
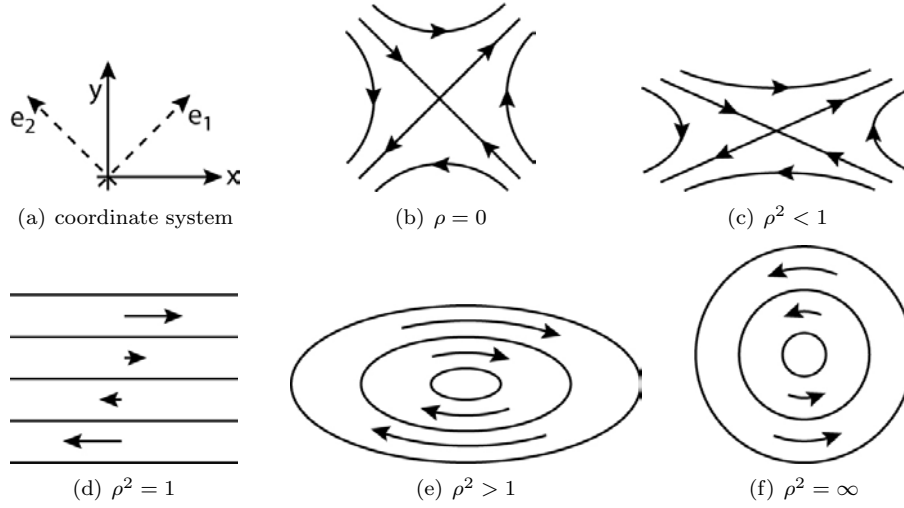
$$\dot{x} = (\dot\epsilon - \omega)y \qquad (A.49)$$
$$\dot{y} = (\dot\epsilon + \omega)x. \qquad (A.50)$$

Depending on whether the rotation rate ω is smaller, larger or equal than the deformation rate $\dot\epsilon$ a planar flow can be strong, strictly weak or marginally weak:

- $\rho^2 < 1$:

  For $|\omega| < |\dot\epsilon|$ we get $I_2 < 0$ and the flow is strong and purely hyperbolic; the fluid trajectories are given by

  $$x(t) \quad = x_0 \cosh(\sqrt{\dot\epsilon^2 - \omega^2}\, t) + y_0 \sqrt{\frac{\dot\epsilon - \omega}{\dot\epsilon + \omega}} \sinh(\sqrt{\dot\epsilon^2 - \omega^2}\, t) \,(A.51)$$

  $$y(t) \quad = y_0 \cosh(\sqrt{\dot\epsilon^2 - \omega^2}\, t) + x_0 \sqrt{\frac{\dot\epsilon + \omega}{\dot\epsilon - \omega}} \sinh(\sqrt{\dot\epsilon^2 - \omega^2}\, t) \,(A.52)$$

  where (x_0, y_0) are the coordinates of a fluid point at time $t = 0$. The trajectories given by eq.(A.51) are hyperbolas with common asymptotes

  $$\frac{x^2}{\chi(1-\rho)} - \frac{y^2}{\chi(1+\rho)} = 1 \qquad (A.53)$$

  and

  $$\chi = \frac{x_0^2}{1-\rho} - \frac{y_0^2}{1+\rho} \qquad (A.54)$$

as a path parameter. The inclination angle of the asymptotes to the x - axis is given by

$$\tan\alpha = \pm\sqrt{\frac{1+\rho}{1-\rho}}. \tag{A.55}$$

Therefore, for a rotation-free planar flow ($\rho = 0$), the asymptotes are perpendicular into the directions of the principal axes of $\mathbf{D}$ and get tilted more and more towards the x (y) - axis with increasing negative (positive) rotation (see fig. A.2)

- $\underline{\rho^2 > 1}$:

  If the rotational rate is larger than the deformation rate, $I_2 > 0$ and the flow is strictly weak. The solutions to eq. (A.49) are

$$x = x_0\cos(\sqrt{\omega^2 - \dot{\epsilon}^2}t) - y_0\sqrt{\frac{\omega - \dot{\epsilon}}{\omega + \dot{\epsilon}}}\sin(\sqrt{\omega^2 - \dot{\epsilon}^2}t) \tag{A.56}$$

$$y = y_0\cos(\sqrt{\omega^2 - \dot{\epsilon}^2}t) - x_0\sqrt{\frac{\omega - \dot{\epsilon}}{\omega + \dot{\epsilon}}}\sin(\sqrt{\omega^2 - \dot{\epsilon}^2}t), \tag{A.57}$$

  where (x_0, y_0) are the coordinates of a point at $t = 0$. These curves are similar ellipses with common center and principal axes along the x and y axes:

$$\frac{x^2}{\chi(1-\rho)} + \frac{y^2}{\chi(1+\rho)} = 1 \tag{A.58}$$

  where

$$\chi = \frac{x_0^2}{1-\rho} + \frac{y_0^2}{1+\rho} \tag{A.59}$$

  is a path parameter.

- $\underline{\rho^2 = 1}$: If the rotational rate is equal to the deformational rate, $I_2 = 0$ and the flow is marginally weak. The homogeneous flow field solution of eq. (A.49) is a simple shearflow with streamlines parallel to the x or y - axis. With $\dot{\epsilon} = \omega = \dot{\gamma}/2$ the fluid pathways are given by

$$x = x_0 \tag{A.60}$$

$$y = y_0 + x_0\dot{\gamma}t, \tag{A.61}$$

for $\dot{\epsilon} = \omega = \dot{\gamma}/2$ we get

$$x = x_0 + y_0\dot{\gamma}t \tag{A.62}$$

$$y = y_0 \tag{A.63}$$

where (x_0, y_0) are the coordinates of a point at $t = 0$. A detailed discussion of simple shearflow is given in the following section.
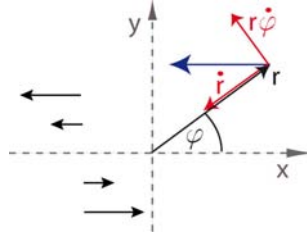
Figure A.3: Velocity field of simple shear flow in cartesian and cylindrical coordinate system.

Unfortunately, it is not possible to classify three-dimensional flows with a single parameter similar to ρ. Even for the case of axisymmetric flows with no flow in the azimuthal direction $\mathbf{u} = (u_r, u_\phi, u_z) = (u_r, 0, u_z)$ the simple flow classification with ρ fails (a more detailed discussion of this case is given in sec. C.8). In 2D, the axis of the rotational component is always fix and perpendicular to the deformation plane, whereas in 3D the rotational axis can be in arbitrary orientation with respect to the principal axes of the deformation $\mathbf{D}$, which brings about the complications in the 3D case.

Simple Shear Flow

Eq. 3.5 shows the decomposition into the rotational and the deformational component. The orthonormal base in which $\mathbf{D}$ is diagonal is found by rotation of the coordinate system by $\pi/4$:

$$\tilde{\mathbf{e}}_1 = \frac{1}{\sqrt{2}} \begin{pmatrix} 1 \\ -1 \\ 0 \end{pmatrix} \tilde{\mathbf{e}}_2 = \frac{1}{\sqrt{2}} \begin{pmatrix} 1 \\ 1 \\ 0 \end{pmatrix}, \tilde{\mathbf{e}}_3 = \begin{pmatrix} 0 \\ 0 \\ 1 \end{pmatrix} \tag{A.64}$$

with

$$\tilde{\mathbf{D}} = \frac{1}{2} \begin{pmatrix} \dot{\gamma} & 0 & 0 \\ 0 & -\dot{\gamma} & 0 \\ 0 & 0 & 0 \end{pmatrix}. \tag{A.65}$$

The composition of simple shear as a mixture of rotation and deformation is directly obvious in the velocity field in a cylindrical coordinate sytem (see fig. A.3), where from

$$\mathbf{v} = \begin{pmatrix} \dot{x} \\ \dot{y} \\ \dot{z} \end{pmatrix} = \begin{pmatrix} -\dot{\gamma}y \\ 0 \\ 0 \end{pmatrix} = \begin{pmatrix} -\dot{\gamma}r\sin\phi \\ 0 \\ 0 \end{pmatrix} \tag{A.66}$$

it follows that

$$\mathbf{v} = \begin{pmatrix} \dot{r} \\ \dot{\phi} \\ \dot{z} \end{pmatrix} = \begin{pmatrix} -\dot{\gamma}r\sin\phi\cos\phi \\ \dot{\gamma}\sin^2\phi \\ 0 \end{pmatrix} = \begin{pmatrix} \text{ext./compression} \\ \text{rotation} \\ 0 \end{pmatrix} \tag{A.67}$$

Comparison with eq. 5.29 yields that the radial component of the shear flow is equivalent to the radial component of a planar extensional flow with extension

rate $\epsilon = \dot{\gamma}/2$ and coordinate axes tilted by $\pi/4$. The difference in rotational component between the shear and this extensional flow is $\dot{\phi} = \dot{\gamma}/2$ confirming that simple shear flow is a mixture of a purely rotational flow and a planar extensional flow with equal rates $\omega = \dot{\epsilon} = \dot{\gamma}/2$.

Extensional Flow

For the flow classification introduced in A.1 we evaluate

$$I_1 = 0, \quad I_2 = -\frac{1}{4}(3 + b^2)\dot{\epsilon}^2, \quad I_3 = -\frac{1}{4}(1 - b^2)\dot{\epsilon}^3 \tag{A.68}$$

$$p = \frac{(1 + \frac{1}{3}b^2)^3}{(1 - b^2)}. \tag{A.69}$$

for $0 \le b \le 1$, which yields that rotation free flows are always strong flows:

$$b = 0 \qquad \rightarrow I_3 \ne 0 \wedge p = 1, \textit{hyperbolic radial flow} \tag{A.70}$$

$$0 < b < 1 \quad \rightarrow I_3 \ne 0 \wedge p > 1, \textit{hyperbolic parabolic flow} \tag{A.71}$$

$$b = 1 \qquad \rightarrow I_3 = 0 \wedge I_2 < 0, \textit{planar hyperbolic flow}, \text{ see sec. A.2 with } \rho^2 < 1. \tag{A.72}$$

Hyperbolic radial flow is of cylindrical symmetry and has no velocity component in the azimuthal direction. The streamlines of uniaxial extensional flow in the r, z - plane are given by

$$r(z) = \sqrt{\frac{a}{z}}. \tag{A.73}$$

Fig. 3.3 shows a cylindrical filament in uniaxial extensional flow with the corresponding hyperbolic radial streamlines. Its flow field, velocity gradient and the fluid trajectories in cylindrical coordinates are given by

$$\mathbf{u}(\mathbf{x}) = \begin{pmatrix} u_r \\ u_\phi \\ u_z \end{pmatrix} = \begin{pmatrix} -\frac{1}{2}\dot{\epsilon}r \\ 0 \\ \dot{\epsilon}z \end{pmatrix} \tag{A.74}$$

$$\mathbf{A} = \begin{pmatrix} -\frac{1}{2}\dot{\epsilon} & 0 & 0 \\ 0 & -\frac{1}{2}\dot{\epsilon} & 0 \\ 0 & 0 & \dot{\epsilon} \end{pmatrix}. \tag{A.75}$$

$$\mathbf{x}(t) = \begin{pmatrix} r(t) \\ \phi(t) \\ z(t) \end{pmatrix} = \begin{pmatrix} r_0 \exp(-\frac{1}{2}\dot{\epsilon}t) \\ \phi_0 \\ z_0 \exp(\dot{\epsilon}t) \end{pmatrix}. \tag{A.76}$$

where $\mathbf{x}(0) = (r_0, \phi_0, z_0)$ are the coordinates of the fluid element at $t = 0$. Biaxial extensional flow is equivalent to uniaxial extensional flow with reversed flow-direction.

A.3   Laminar Flow in Channels with Constant Cross Section

Channels with Circular Cross Section

The steady-state flow profile for a power-law fluid with $\eta(\dot{\gamma}) = A\dot{\gamma}^{n-1}$ flowing down a straight, rigid tube with Radius R, length L and no-slip condition $\mathbf{u} = 0$ at $r = R$ is given by [10]:

$$u_z(r) = \left(\frac{\Delta pR}{2AL}\right)^{1/n} \frac{R}{(1/n)+1}\left[1 - \left(\frac{r}{R}\right)^{(1/n)+1}\right], \quad u_r = 0, \, u_\phi = 0, \quad \text{(A.77)}$$

where Δp is the pressure drop along the channel and the tube axis is parallel to the z-direction. The corresponding flow rate Q is yielded by integration over the tube cross sectional area [10], and the wall shearrate $\dot{\gamma}_w$ can be determined with the Weissenberg-Rabinowitsch equation [74]:

$$Q = \frac{\pi n R^3}{3n+1}\left[\frac{\Delta pR}{2AL}\right]^{1/n}, \quad \dot{\gamma}_w = \frac{Q}{R^3}\frac{3n+1}{\pi n} \qquad \text{(A.78)}$$

With eq. (A.78) the viscosity $\eta(\dot{\gamma})$ can be calculated from pressure drop Δp and flowrate Q:

$$\eta(\dot{\gamma}_w) = A\dot{\gamma}_w^{n-1} = \frac{n\pi}{3n+1}\frac{\Delta pR^4}{2QL}. \qquad \text{(A.79)}$$

For a Newtonian fluid with $n = 1$ and $A = \eta$, eq. (A.78) reduces to the Hagen-Poiseuille equation $Q = \frac{\pi R^4 \Delta p}{8\eta L}$. The corresponding parabolic flow profile and the Newtonian wall shearrate $\dot{\gamma}_w$ are given by:

$$u_z(r) = \frac{\Delta pR^2}{4\eta L}\left[1 - \left(\frac{r}{R}\right)^2\right] \quad \dot{\gamma}_w = \frac{4Q}{\pi R^3} \qquad \text{(A.80)}$$

Channels with Rectangular Cross Section

For a channel with a rectangular cross section of width w and height h there is an analytical solution for flowprofile and flowrate only for a Newtonian fluid [12]:

$$u_z(x,y) = \frac{4h^2\Delta p}{\pi^3\eta L}\sum_{n,\text{odd}}^{\infty}\frac{1}{n^3}\left[1 - \frac{\cosh(n\pi\frac{x}{h})}{\cosh(n\pi\frac{w}{2h})}\right]\sin\left(n\pi\frac{y}{h}\right) \qquad \text{(A.81)}$$

and

$$Q = \frac{h^3w\Delta p}{12\eta L}\left[1 - \sum_{n,\text{odd}}^{\infty}\frac{1}{n^5}\frac{192}{\pi^5}\frac{h}{w}\tanh\left(n\pi\frac{w}{2h}\right)\right]$$

$$\approx \frac{h^3w\Delta p}{12\eta L}\left[1 - 0.630\frac{h}{w}\right], \quad \text{for} \quad h < w \qquad \text{(A.82)}$$

where the channel spans a width $-0.5w < x < 0.5w$ and a height $0 < y < h$. The approximation in eq. (A.82) is exactly valid in the limit of flat, wide channels ($\frac{h}{w} \to 0$), but is only 13 % off in the worst case $h = w$[12]. The wall shearrate is not constant in a rectangular duct, but an apparent shearrate $\dot{\gamma}_a$ averaged on the perimeter can be given for Newtonian fluid flow[101]:

$$\dot{\gamma}_a = \frac{6Q}{wh^2} \left(1 + \frac{h}{w}\right) f^\star \left(\frac{h}{w}\right) \tag{A.83}$$

where $f^\star(x)$ is a numerically calculated function taking values from $f^\star(0) = 1$ to $f^\star(1) = 0.5928$.

A solution for the flow of a power-law fluid in a duct with arbitrary constant cross section can be given with the help of a numerically determined shape factor [69]:

$$Q = \frac{\lambda(n)\tilde{h}^{3+(1/n)} \left(-\frac{\mathrm{d}p}{\mathrm{d}z}\right)^{1/n}}{A^{1/n}} \tag{A.84}$$

where $\tilde{h}$ is the characteristic width of the duct defined by $\tilde{h}^2 = D$ (D being the cross sectional area of the duct) and $\lambda(n)$ is the shape factor defined as $\lambda(n) \equiv \int_D \int \tilde{u} \mathrm{d}\tilde{x} \mathrm{d}\tilde{y}$ with $\tilde{x}, \tilde{y}, \tilde{u}$ as the dimensionless coordinates x, y and the dimensionless velocity in the channel direction u. The shape factor λ depends on the power-law index n of the fluid and on the geometry of the duct. For some special geometries, λ is tabulated in [69], a method to calculate λ for rectangular ducts is given in [90] and in [76]. An expression for the corresponding averaged wall shearrate is given in [101]:

$$\dot{\gamma}_w = \frac{4Q}{wh^2} \left(1 + \frac{h}{w}\right) \left(b^\star(h/w) + \frac{1}{n}a^\star(h/w)\right), \tag{A.85}$$

where $a^\star(x)$ ranges from $a^\star(0) = 0.5$ to $a^\star(1) = 0.2121$ and $b^\star(x)$ from $b^\star(0) = 1$ to $b^\star(1) = 0.6771$. The functions $a^\star, b^\star, f^\star$ are tabulated in [101]. By combination of eqs. (A.84) and (A.85) we can determine the viscosity as

$$\eta(\dot{\gamma}_w) = \frac{p_c h^4}{QL} \left(\frac{w}{h}\right)^{\frac{3+n}{2}} \lambda^n(n) \left[4\left(1 + \frac{h}{w}\right)\left(b^\star(h/w) + \frac{1}{n}a^\star(h/w)\right)\right]^{n-1}. \tag{A.86}$$

Channels with rectangular cross section and aspect ratio $h/w \to 0$

The flow of a power-law fluid between two parallel plates at $y = -h/2$ and $y = h/2$ in the z-direction with a channel length L can be solved analytically to give the solution for the special case of very flat rectangular channel with ($h/w \to 0$) known as *Hele-Shaw flow* [12]: There, the flow profile is given by

$$u_z(y) = \frac{1}{1 + 1/n} \left[\frac{\Delta p}{AL}\right]^{1/n} \left[\left(\frac{h}{2}\right)^{1+1/n} - y^{1+1/n}\right], \quad \text{for} \quad 0 < y < \frac{h}{2}, \tag{A.87}$$

and the flowrate is

$$Q = \frac{wh^2}{2(2 + 1/n)} \left[\frac{h\Delta p}{2AL} \right]^{1/n}.$$

(A.88)

The wall shear rate can be calculated as [101]:

$$\dot{\gamma}_w = \frac{2n + 1}{3n} \left(\frac{6Q}{wh^2} \right) = \frac{2n + 1}{3n} \dot{\gamma}_a$$

(A.89)

where $\dot{\gamma}_a = \frac{6Q}{wh^2}$ is the apparent Newtonian wall shearrate for a Hele-Shaw cell flow.

B. POLYMER DYNAMICS

B.1 Rotational Diffusion of Flexible Chains (Rouse Model)

MSD of a Rigid Rod

For $t \rightarrow \infty$, $\phi(t)$ and $\phi(0)$ are totally uncorrelated. This suggests that the orientational vectors $\mathbf{u}(t)$ and $\mathbf{u}(0)$ are perpendicular to each other

$$\langle \mathbf{u}(t) \cdot \mathbf{u}(0) \rangle_{\lim_{t \to \infty}} = 0 \tag{B.1}$$

and the average angle between them is $\langle \alpha(t) \rangle = \langle \Delta \phi(t) \rangle = \langle (\phi(t) - \phi(0)) \rangle = \pi/2$. This follows also from the probability calculation:

In a random orientation between 2 vectors, the probability density for the angle α between them is given by

$$p(\alpha) = \frac{\sin \alpha}{2} \tag{B.2}$$

The average angle between them is thus given as

$$\langle \alpha \rangle = \int_0^\pi \alpha p(\alpha) \mathrm{d}\alpha = \frac{1}{2} \int_0^\pi \alpha \sin \alpha \mathrm{d}\alpha = \frac{1}{2} \left[\sin \alpha - \alpha \cos \alpha \right]_0^\pi = \frac{\pi}{2} \tag{B.3}$$

In the same way, the mean squared angle between two uncorrelated vectors is calculated as

$$\langle \alpha^2 \rangle = \int_0^\pi \alpha^2 p(\alpha) = \frac{1}{2} \int_0^\pi \alpha^2 \sin \alpha \mathrm{d}\alpha$$

$$= \frac{1}{2} \left[2\alpha \sin \alpha - (\alpha^2 - 2) \cos \alpha \right]_0^\pi = \frac{\pi^2 - 4}{2} \tag{B.4}$$

For long times, the angle of a diffusing rod is uncorrelated to its original orientation, so that the angular mean-squared-displacement of the rod saturates at $\frac{\pi^2-4}{2}$. For short times, the mean-square displacement is approximated by a 2D random walk giving $MSD(t) \approx 4D_{\mathrm{rod}} t$. Unfortunately, the author didn't find an analytical expression describing the time evolution of the angular mean-square displacement of the rigid rod in the standard literature.

Therefore, we will discuss the orientational diffusion in terms of the difference of the orientation vectors $(\mathbf{u}(t) - \mathbf{u}(0))$ instead of the angle $(\phi(t) - \phi(0))$. For small angular differences, both are equivalent. The mean-square-displacement $MSD(t)$ of the orientational vector can be calculated in the usual way:

$$MSD(t) = \langle (\mathbf{u}(t) - \mathbf{u}(0))^2 \rangle = 2(1 - \langle \mathbf{u}(t)\mathbf{u}(0) \rangle). \tag{B.5}$$

With the known exponential decay of the correlation function [27]

$$\langle \mathbf{u}(t)\mathbf{u}(0) \rangle = \exp(-t/\tau) = \exp(-2Dt) \tag{B.6}$$

the orientational MSD of the diffusing rod is given as

$$MSD(t) = \langle (\mathbf{u}(t) - \mathbf{u}(0))^2 \rangle = 2 \left(1 - \exp(-2D_{\mathrm{rod}}t) \right). \tag{B.7}$$

As the timescale of the saturation must be the same for the angular diffusion and the difference in orientational vector diffusion, we could approximate the mean-squared angle between the rod at time t and the rod at time 0 as

$$MSD_{\mathrm{ang}} = \alpha^2(t) \approx \frac{\pi^2 - 4}{2} \left(1 - \exp \frac{8D_{\mathrm{rod}}t}{\pi^2 - 4} \right) \tag{B.8}$$

but we tried to use the difference of orientational vectors MSD for the following calculations.

Rouse Modes

We discuss a chain of N beads. The motion of the the chain is desribed by the independent motion of the $(N-1)$ Rouse modes of the chain. The normal coordinates of the Rouse model are defined as [108]

$$\mathbf{q}_i(t) = \frac{1}{N} \sum_{n=1}^{N} \cos \left(\frac{in\pi}{N} \right) \mathbf{r}_n(t) \tag{B.9}$$

where i is the modenumber and $\mathbf{r}_n(t)$ is the position vector of the n-th bead of the chain. Reversely, the position of the n-th bead is given by the normal mode vectors $\mathbf{q}_i(t)$ as:

$$\mathbf{r}_n(t) = 2 \sum_{i=1}^{N-1} \cos \left(\frac{in\pi}{N} \right) \mathbf{q}_i(t) + \mathbf{q}_0(t) + (-1)^n \mathbf{q}_N(t) \tag{B.10}$$

Thus, the displacement contributed by the i-th mode for the i-th bead is given as

$$\mathbf{r}_{i,n}(t) = 2 \cos \left(\frac{in\pi}{N} \right) \mathbf{q}_i(t) \quad \text{for } i = 1, \dots N-1 \tag{B.11}$$

Calculation of end-to-end vector length

From the definition of the Rouse modes we see immediately, that only modes with odd i contribute to changes of the end-to-end vector of the chain: Even modes displace the first and last bead of the chain by a length $2q_i$ into the direction of $\mathbf{q}_i$ and change neither the length nor the direction of the end-to-end vector $\mathbf{R}_{ee} = \mathbf{r}_N - \mathbf{r}_1$. Odd modes shift the first bead by $2q_i$ into the direction of $\mathbf{q}_i$ and the n-th bead by $2q_i$ into the opposite direction. Thus, length and direction of $\mathbf{R}_{ee}$ are only changed by the odd Rouse modes.

We can now subsequently construct the end-to-end vector length by adding up the odd Rouse modes. Each higher Rouse mode vector $\mathbf{q}_i$ is uncorrelated with the end-to-end vector constructed by the other rouse modes $\mathbf{R}_{ee}^{i=1,..i-2}$. The relative angle δ between $\mathbf{q}_i$ and $\mathbf{R}_{ee}^{i=1,..i-2}$ can vary between 0 and π. The average angle (as expected for uncorrelated vectors) is $<\delta> = \pi/2$. Therefore the length $\mathbf{R}_{ee}^{i=1}$ is calculated as

$$\mathbf{R}_{ee}^{i=1,..i} = \sqrt{\left(\mathbf{R}_{ee}^{i=1,..i-2}\right)^2 + 4^2\mathbf{q}_i^2} \tag{B.12}$$

giving

$$\mathbf{R}_{ee}^2 = \sum_{i=1}^{N} 16\mathbf{q}_i^2. \tag{B.13}$$

With [108]

$$<q_i^2> = \frac{Nb^2}{2\pi^2 i^2} \tag{B.14}$$

where b is the bead seperation, we get:

$$\mathbf{R}_{ee}^2 = \sum_{i=1}^{N} 16\frac{Nb^2}{2\pi^2 i^2} = 16\frac{Nb^2}{2\pi^2} \sum_{i=1}^{N} i^{-2} = \frac{Nb^2}{2\pi^2}\frac{\pi^2}{8} = Nb^2. \tag{B.15}$$

Consider a random walk of n steps of length a: The n-th step is uncorrelated to the path of the $n-1$ steps before. Thus, the expected average angle between n-th step and end-to-end vector of the $n-1$ steps is $\pi/2$, which gives an overall path length for n steps

$$\mathbf{R}_{ee}^2(n) = (n-1)b^2 + a^2 = nb^2 \tag{B.16}$$

giving the same result.

Rotational Diffusion Coefficient of the Rouse Modes

The rotational diffusion coefficient of each mode is given as

$$D_i = \frac{k_B T}{\gamma_i} \tag{B.17}$$

where γ_i is the friction coefficient of each Rouse mode vector given by $\mathbf{r}_{i,n}$ from eq B.11. With the friction coefficient ζ_b for each bead we can calculate γ_i as

$$\gamma_i = \sum_{n=1}^{N} \zeta_b \mathbf{r}_{i,n}^2 \tag{B.18}$$

giving

$$\gamma_i = \zeta_b \sum_{n=1}^{N} \left(2\cos\left(\frac{in\pi}{N}\right)\mathbf{q}_i(t)\right)^2 = 4\zeta_b q_i^2 \sum_{n=1}^{N} \cos^2\left(\frac{in\pi}{N}\right) \tag{B.19}$$

For $N \gg 1$ we can approximate this as

$$
\begin{aligned}
\gamma_i &= 4\zeta_b q_i^2 \frac{N}{\pi} \int_0^\pi \cos^2(i\phi)\mathrm{d}\phi \\
&= 4\zeta_b q_i^2 \frac{N}{\pi} \left[\frac{\phi}{2} + \frac{1}{i\pi} \sin(2i\phi) \right]_0^\pi \\
&= 2\zeta_b N q_i^2
\end{aligned}
\tag{B.20}
$$

With

$$
\langle q_i^2 \rangle = \frac{3k_B T}{k_i}
\tag{B.21}
$$

where

$$
k_i = \frac{6\pi^2 k_B T}{N b^2}
\tag{B.22}
$$

is the spring force constant of the i-th mode [108] we get

$$
\langle q_i^2 \rangle = \frac{N b^2}{2\pi^2 i^2}
\tag{B.23}
$$

and thus

$$
\gamma_i = \frac{\zeta_b N^2 b^2}{\pi^2 i^2}
\tag{B.24}
$$

which gives

$$
D_i = \frac{\pi^2 k_B T}{\zeta_b N^2 b^2} i^2
\tag{B.25}
$$

Comparing this with the Rouse time

$$
\tau_i = \frac{\zeta_b N^2 b^2}{3\pi^2 k_B T} \frac{1}{i^2}
\tag{B.26}
$$

gives

$$
D_i = \frac{1}{3\tau_i}
\tag{B.27}
$$

which is in accordance with Winkler et al [41].

MSD-contribution of the Rouse modes

As a first approximation to calculate the oriental MSD by the diffusing Rouse modes, we assume that the length of the modevectors q_i is constant and given by their mean value $q_i = \sqrt{\langle \mathbf{q}_i^2 \rangle}$. This will of course not give the exact results, because we neglect fluctuations in the angle caused by fluctuations in q_i. On the other hand, we suppose that the main contribution to angular changes originates from the reorientation of the $\mathbf{q}_i$ vectors rather than from fluctuations in q_i.

The rotational diffusion of the first Rouse mode reorients the entire molecule. Thus, the rotational diffusion of the first Rouse mode directly contributes to the

mean-square displacement of the end-to-end vector orientation. We thus get a mean-squared displacement contribution of the first Rouse mode of

$$MSD_1(t) = 2\left(1 - \exp(-2D_1 t)\right). \tag{B.28}$$

The contribution of the higher odd modes ($i > 1$) can now be calculated as follows: We denote α_i as the orientational angle between the i-th mode vector $\mathbf{q}_i$ and the cumulative end to end vector of the lower modes $R_{ee,1,..,i-2}$. A change $(\mathbf{u}_i(t) - \mathbf{u}_i(0))$ in the orientation of the modevector $\mathbf{q}_i$ causes a change in the orientation of $R_{ee,1,..,i-2}$ of

$$\tan(\Delta\phi)_i(t) \approx \frac{4 q_i(t)}{R_{ee,1,..,i-2}(t)} \sin\alpha_i (\mathbf{u}_i(t) - \mathbf{u}_i(0)) \tag{B.29}$$

on short timescales, where $\sin\alpha_i \approx \sin\alpha_i(t) = \sin\alpha_i(0)$. As $\tan(\Delta\phi)_i(t) \ll 1$ is fulfilled, eq. B.29 directly gives the contribution of the i-th mode to the displacement of the orientation vector. For the contribution to the mean-square-displacement of the orientation of R_{ee} we need to calculate

$$\langle \sin^2\alpha_i (\mathbf{u}_i(t) - \mathbf{u}_i(0))^2 \rangle \tag{B.30}$$

As the random change in orientation is independent of the actual orientation, we get

$$\langle \sin^2\alpha_i (\mathbf{u}_i(t) - \mathbf{u}_i(0))^2 \rangle = \langle \sin^2\alpha_i \rangle \langle (\mathbf{u}_i(t) - \mathbf{u}_i(0))^2 \rangle \tag{B.31}$$

Calculating the first term with the probability density $p(\alpha) = \sin(\alpha)/2$ yields

$$\langle \sin^2\alpha_i \rangle = \frac{1}{2} \int_0^\pi \sin^3\alpha_i \mathrm{d}\alpha = \frac{2}{3}. \tag{B.32}$$

The second term is given by the usual orientational diffusion

$$\langle (\mathbf{u}_i(t) - \mathbf{u}_i(0))^2 \rangle = 2(1 - \exp(2D_i t)) \tag{B.33}$$

The contribution of mode i to the mean-square-displacement of the Rouse chain is thus given as

$$\begin{aligned}
MSD_i(t) &= \frac{2}{3} \frac{q_i^2}{\sum_{k=1}^{i-2} q_i^2} 2(1 - \exp(2D_i t)) \\
&\approx \frac{4}{3} \frac{q_i^2}{q_1^2} (1 - \exp(2D_i t)) \\
&= \frac{4}{3} \frac{1}{i^2} (1 - \exp(2D_i t)) \\
&= \frac{4}{3} \frac{D_1}{D_i} (1 - \exp(2D_i t)) \tag{B.34}
\end{aligned}$$

This gives an overall orientational mean-square-displacement of the Rouse chain of

$$MSD(t) = 2 \sum_{i,\text{odd}}^N a_i \frac{D_1}{D_i} (1 - \exp(-2D_i t)) \tag{B.35}$$

where $a_1 = 1$ and $a_i = \frac{2}{3}$ for $i > 1$. We might suspect that all $a_i = 1$ for the calculation including the fluctuations of q_i. On the other hand, keeping 2/3 in the higher modes makes the solution equivalent to the suggestion for the angular diffusion of slightly bending rods given in the next paragraph. However, the first mode will dominate, so this question is of secondary importance.

Comparison with MSD of stiff chains

The solution for the angular MSD of stiff filaments in 2D with hydrodynamic bending modes in the case that $R_{ee} \approx L_c$ is (see eq. B.54)

$$MSD(t) = 2D_{\text{rod}} \left(t + \frac{2}{3} \sum_{n>1,\text{even}}^{\infty} \tau_{\text{Howard},n}(1 - \exp(-t/\tau_{\text{Howard},n})) \right), \quad \text{(B.36)}$$

with $\tau_{\text{Howard},n}$ from eq. B.41. Herein, we didn't take into account the saturation of the rotational diffusion of the rod, because for filaments confined to a plane in 2D, the angular MSD does not saturate. Defining $\tau_{\text{Winkler},n}$ as the τ_n which is defined in *Winkler et. al* [41], we see that $\tau_{\text{Winkler},n+1} = 2/3\tau_{\text{Howard},n}$ in the stiff limit. While *Winkler et. al* use $D_n = 1/(3\tau_n)$, we used $D_n = 1/(2\tau_n)$. Therefore by changing $n \to n+1$ and using D_n instead of τ_n we can rewrite eq. B.36 for comparison with the Rouse mode solution as:

$$MSD(t) = 2D_{\text{rod}}t + \sum_{n>1,\text{odd}}^{\infty} 2D_{\text{rod}}\tau_{\text{Winkler},n}(1 - \exp(-2D_n t))$$

$$= 2D_{\text{rod}}t + \sum_{n>1,\text{odd}}^{\infty} \frac{2}{3} \frac{D_1}{D_n}(1 - \exp(-2D_n t)) \quad \text{(B.37)}$$

Expanding this to the 3D case and incorporating the saturation for the stiff rod diffusion suggests

$$MSD(t) = 2 \sum_{i,\text{odd}}^{\infty} \frac{D_1}{D_i} a_i \left(1 - \exp(-2D_i t)\right) \quad \text{(B.38)}$$

where $a_1 = 1$ and $a_i = \frac{2}{3}$ for $i > 1$, which is the same solution as obtained for the MSD of the Rouse modes, only with D_n given by the Winkler times in the stiff limit instead of the Rouse times. This suggests, that the orientational MSD is approximated over the entire range of rigidity by eq. B.38 using the rotational diffusion constants $D_i = 1/(3\tau_i)$ given by the Winkler times $\tau_{\text{Winkler},n}$.

B.2   Rotational Diffusion of Semiflexible Filament

Hydrodynamic bending modes (2D calculation)

The hydrodynamic bending modes with n even contribute to angular fluctuations of the end-to-end vector. The even modes are given by Howard [47]:

$$y_n(x,t) = A_n(t) \cdot \left[\cosh \alpha_n \sin \left(\frac{2\alpha_n}{L}(x - L/2) \right) + \cos \alpha_n \sinh \left(\frac{2\alpha_n}{L}(x - L/2) \right) \right] \tag{B.39}$$

where

$$\alpha_n = (n + \frac{1}{2})\frac{\pi}{2} \tag{B.40}$$

and

$$\tau_n = \frac{\gamma_{\perp,L}}{k_B T L_p} \left(\frac{L}{2\alpha_n} \right)^4 . \tag{B.41}$$

The relaxation of a bending mode is given by $A_n(t) = A_0 \exp(-t/\tau_n)$.
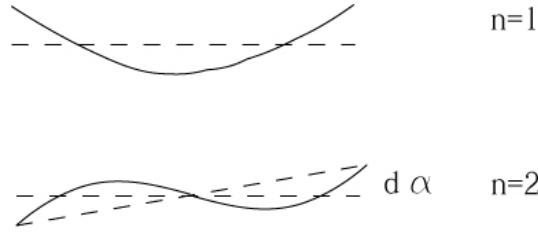
Figure B.1: The first two hydrodynamic modes of the semiflexible filament. Changes in amplitude of the even modes are accompanied by a change in the end-to-end vector angle α_{ee}.

Calculation of bending energy of an even mode n

Differentiation of eq. (B.39) two times with respect to x yields the curvature of the mode as

$$y_n(x,t)'' = A_n(t) \left(\frac{2\alpha_n}{L} \right)^2 \cdot \left[-\cosh \alpha_n \sin \left(\frac{2\alpha_n}{L}(x - L/2) \right) + \cos \alpha_n \sinh \left(\frac{2\alpha_n}{L}(x - L/2) \right) \right] \tag{B.42}$$

The bending energy of the mode is given by

$$
\begin{aligned}
U_{\text{bend}} &= k_B T L_p \int_0^L \frac{1}{R^2} \mathrm{d}s \\
&= k_B T L_p \int_0^L (y'')^2 \mathrm{d}s \\
&= k_B T L_p A_n^2 \left(\frac{2\alpha_n}{L} \right)^4 \frac{L}{8} \left[3\frac{\sinh(2\alpha_n)}{\alpha_n} + 4\cosh^2 \alpha_n - 2 \right]
\end{aligned}
\tag{B.43}
$$

Setting $U_{\text{bend}} = \frac{1}{2}k_B T$ yields the thermal amplitude of the mode A_n^{th}:

$$A_n^{th} = \frac{L}{2}\sqrt{\frac{L}{L_p}}\frac{1}{\alpha_n^2}\frac{1}{\sqrt{3\frac{\sinh(2\alpha_n)}{\alpha_n} + 4\cosh^2\alpha_n - 2}} \tag{B.44}$$

which gives for $\alpha_n \gg 1$:

$$A_n^{th} \approx \frac{L}{2}\sqrt{\frac{L}{L_p}}\frac{1}{\alpha_n^2}\frac{1}{\cosh\alpha_n}, \quad n \quad \text{even} \tag{B.45}$$

The thermal amplitude is connected to the fluctuation angle ϕ_n by

$$\tan\phi_n = \frac{y_n(0) - y_n(L)}{L} = (-1)^{n/2+1}\frac{1}{2}\sqrt{2}A_n^{th}(\cosh\alpha_n + \sinh\alpha_n) \tag{B.46}$$

so that A_n^{th} corresponds to a fluctuation angle of the mode of

$$\tan\phi_n^{th} \approx \phi_n^{th} = \frac{1}{2}\sqrt{2}\sqrt{\frac{L}{L_p}}\frac{1}{\alpha_n^2} \tag{B.47}$$

For the 2nd mode ($n = 2$) this yields $\phi_n^{th} = 4.6 \cdot 10^{-2}\sqrt{\frac{L}{L_p}}$.

Angular Diffusion of End-to-End Vector

The fluctuation angle ϕ_n of each mode diffuses in the potential of the bending energy. For small angles, the bending energy potential is a harmonic potential for the bending mode angle ϕ_n: $U_{\text{bend}} \sim (A_n^{th})^2 \sim \phi_n^2$. Thus, the mean-square displacement for the bending mode angle is given by

$$MSD_n(t) = 2\tau_n D_{\text{free},n}\left(1 - \exp(-t/\tau_n)\right) \tag{B.48}$$

where $D_{\text{free},n}$ is the diffusion coefficient that the angular fluctuation of the n-th mode would have without the bending energy potential. The author unfortunately did not find an analytical proof for eq. B.48, but the result is strongly suggested by a simulation of the diffusion in the potential which has been performed. $D_{\text{free},n}$ can be calculated as follows: Consider the energy dissipated by a bending mode fluctuation from $\phi_n = 0$ to ϕ_0 with a constant velocity $\dot{\phi}$. Setting this energy equal to $1/2k_B T$, we can calculate the diffusion constant

$D_{\text{free},n}$ for the thermally driven change in angle ϕ_0:

$$
\begin{aligned}
U_{\text{bend}} = \frac{1}{2}k_B T &= \int_0^L \gamma_{\perp,L}(\sigma(x))^2 A_0 \dot{A}\mathrm{d}x \\
&= \frac{1}{4}\frac{L^2}{(\sigma(0))^2}\gamma_{\perp,L}\phi_0\dot{\phi}\int_0^L (\sigma(x))^2\mathrm{d}x \\
&= \frac{1}{8}\frac{L^2}{(\sigma(0))^2}\gamma_{\perp,L}\frac{\mathrm{d}\phi_0^2}{\mathrm{d}t}\int_0^L (\sigma(x))^2\mathrm{d}x \\
&= \frac{1}{8}\frac{L^2}{(\sigma(0))^2}\gamma_{\perp,L}2D_{\text{free},n}\int_0^L (\sigma(x))^2\mathrm{d}x
\end{aligned}
$$

(B.49)

where $\sigma(x)$ is defined by $y_n(x,t) = A_n(t)\sigma(x)$, which gives

$$
D_{\text{free},n} = \frac{2k_B T}{\gamma_{\perp,L}}\frac{(\sigma(0))^2}{L^2}\frac{1}{\int_0^L (\sigma(x))^2\mathrm{d}x}.
$$

(B.50)

Performing the integration yields:

$$
D_{\text{free},n} = \frac{2k_B T}{\gamma_{\perp,L}L^3}\frac{(\cosh\alpha_n + \sinh\alpha_n)^2}{\cosh^2\alpha_n + \frac{1}{2\alpha_n}\cosh\alpha_n(\cosh\alpha_n - \sinh\alpha_n) - \frac{1}{2}}.
$$

(B.51)

For $\alpha_n \gg 1$ we get

$$
D_{\text{free},n} = \frac{8k_B T}{\gamma_{\perp,L}L^3} = \frac{2}{3}D_{\text{rot}}
$$

(B.52)

For times much larger than the relaxation time of the mode we get a mean square displacement due to the bending mode of

$$
MSD_{n,\infty} = 2D_{\text{free},n}\tau_n = \frac{L}{L_p}\frac{1}{\alpha_n^4} = 2(\phi_n^{th})^2.
$$

(B.53)

If the above derivation of $D_{\text{free},n}$ does not sound convincing to the reader, $D_{\text{free},n}$ can be alternatively derived from eq. B.48 by setting $MSD_{n,\infty} = 2(\phi_n^{th})^2$.

Together with the rotational diffusion of the 0-th mode (rod-rotation), the mean-square displacement of the end-to-end-angle of a semiflexible filament in 2-D is given by

$$
MSD(t) = 2D_{\text{rod}}\left(t + \frac{2}{3}\sum_{n>1,\text{even}}^{\infty}\tau_n(1 - \exp{(-t/\tau_n)})\right)
$$

(B.54)

For long times $t \gg \tau_2$ we get

$$
MSD(t \gg \tau_2) = 2D_{\text{rod}}\left(t + \frac{2}{3}\sum_{n>1,\text{even}}^{\infty}\tau_n\right) \approx 2D_{\text{rod}}t
$$

(B.55)

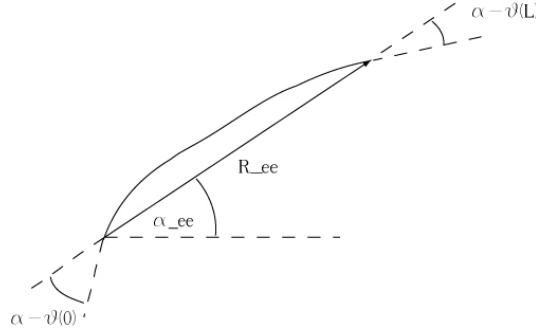and the bending mode fluctuations are negligible.

Figure B.2: Lateral diffusion along the contour is accompanied by a change in the end-to-end vector angle α_{ee} due to the anisotropy of the friction coefficient.

Coupling of translational diffusion to rotational diffusion

Consider a curved filament which is translated in the direction of the end-to-end vector R_{ee}. As the friction coefficient for movement perpendicular to the local filament orientation is twice the friction coefficient parallel to the filament $\zeta_{\perp,L} = 2\zeta_{\parallel,L}$, the translational motion is accompanied by a net torque rotating the filament (unless the filament is pointsymmetric and the net torque vanishes). Thus, the translational and rotational diffusive motions of the filament are coupled.

To estimate the contribution of the translational diffusion to the rotational diffusion we consider relatively stiff filaments, where the local orientational angle $\theta(s)$ is always close to the angle of the end-to-end vector α_{ee} $\theta(s) - \alpha_{ee} \ll 1$. Looking at short times, where the orientational difference of the filament ends is nearly constant $\theta(L_c) - \theta(0) \approx const.$, we split the translational diffusion into a diffusional motion along the end-to-end vector of the filament and perpendicular to R_{ee}. To estimate an upper limit for the coupling influence, we assume that diffusion into the direction of R_{ee} is restricted to motion along the contour of the filament (i.e. $\zeta_{\perp,L} \gg \zeta_{\parallel,L}$). Thus, diffusion of a distance Δs along the contour is coupled to a change in angle $\Delta \alpha$ of

$$\tan(\Delta\alpha) = \frac{\Delta s(\sin(\theta(L_c) - \alpha_{ee}) - \sin(\theta(0) - \alpha_{ee}))}{L + \cos(\theta(L_c) - \alpha_{ee}) - \cos(\theta(0) - \alpha_{ee})} \tag{B.56}$$

With $\cos(\theta(L_c) - \alpha_{ee}) \approx \cos(\theta(0) - \alpha_{ee})$ we get

$$\tan(\Delta\alpha) = \frac{\Delta s}{L}(\sin(\theta(L_c) - \alpha_{ee}) - \sin(\theta(0) - \alpha_{ee})) =$$

$$= 2\frac{\Delta s}{L}\cos\left(\frac{\theta(L_c) + \theta(0) - 2\alpha_{ee}}{2}\right)\sin\left(\frac{\theta(L_c) - \theta(0)}{2}\right)$$

$$\approx 2\frac{\Delta s}{L}\sin\left(\frac{\theta(L_c) - \theta(0)}{2}\right) \approx \frac{\Delta s}{L}\sin\left(\theta(L_c) - \theta(0)\right)$$

$$= \frac{\Delta s}{L}\sqrt{1 - \cos^2\left(\theta(L_c) - \theta(0)\right)} \tag{B.57}$$

The mean angular difference between the filament ends is given by the persistence length L_p:

$$\langle\cos(\theta(L_c) - \theta(0))\rangle = \exp(-L/(2L_p)) \tag{B.58}$$

so that for small diffusing angles $\Delta\alpha$ we can calculate for $L_c/L_p \ll 1$:

$$\langle\Delta\alpha\rangle = \langle\tan(\Delta\alpha)\rangle = \frac{\Delta s}{L}\sqrt{1 - \langle\cos\left(\theta(L_c) - \theta(0)\right)\rangle^2}$$

$$= \frac{\Delta s}{L}\sqrt{1 - \exp(-L_c/L_p)} \approx \frac{\Delta s}{\sqrt{L_c L_p}}. \tag{B.59}$$

The diffusion along the contour is given by the diffusion coefficient $D_\parallel$ of the rod:

$$\left\langle(\Delta s)^2\right\rangle = 2D_\parallel t \tag{B.60}$$

so that the upper limit for the coupled extra angular diffusion is given as:

$$MSD_{\alpha,\text{trans}}(t) = \left\langle(\Delta\alpha)^2\right\rangle = \frac{2D_\parallel t}{L_c L_p}$$

$$= 2\frac{1}{6}\frac{L_c}{L_p}D_{\text{rod}}t \tag{B.61}$$

where D_{rod} is the rotational diffusion coefficient of the rod with length L_c. We suppose that this effect is only significant on short and intermediate timescales. For times longer than the rotational relaxation time we suppose a translational diffusion with an diffusion coefficient $D_{long,x} = D_{long,y} = 0.5(D_\parallel + D_\perp)$ for the rod in 2D and a decoupling of rotational and translational diffusion for the semiflexible filament. We do not know how much the "diffusion along the contour"-approach sugested above overestimates the coupling effect, but the above consideration should give an upper limmit estimate for the effect.

<div align="center">

Correction for $R_{ee} < L_c$-effect

</div>

The fluctuating semiflexible filament has a shorter mean end-to-end distance than the stiff rod: $\langle R_{ee}\rangle < L_c$. Assuming an evenly distributed mass along the end-to-end vector of the semiflexible filament, this reduces the rotational friction by a factor of $(R_{ee}/L_c)^2$, so that the modified rotational diffusion constant of

the semiflexible filament becomes $D_{\text{rot}} = D_{\text{rod}}(L_c/R_{ee})^2$. The mean end-to-end distance can be calculated as (adapted from [47] for 2D):

$$\langle R_{ee}^2 \rangle = 4L_p^2 \left(2\exp\left(-\frac{L_c}{2L_p}\right) - 2 + \frac{L_c}{L_p} \right) \qquad (\text{B.62})$$

For $L_c/L_p \ll 1$ this is approximated by $\langle R_{ee}^2 \rangle \approx L_c^2(1 - \frac{1}{6}\frac{L_c}{L_p})$, so that the rotational diffusion constant can be expressed as $D_{\text{rot}} = D_{\text{rod}}(1 + \frac{1}{6}\frac{L_c}{L_p})$.

Altogether we get an angular rotational diffusion of semi-flexible filaments of

$$MSD(t) = 2D_{\text{rod}}(1 + \frac{1}{6}\frac{L_c}{L_p}) \left((1 + \frac{1}{6}\frac{L_c}{L_p})t + \frac{2}{3} \sum_{n>1,\text{even}}^{\infty} \tau_n(1 - \exp\left(-t/\tau_n\right)) \right).$$
$$(\text{B.63})$$

B.3 Rotational Diffusion Coefficient D_r for Stiff, Semiflexible and Flexible Polymers

As there is no analytical expression available in the literature, the angular rotational diffusion constant for the rotation of the end-to-end vector of a flexible polymer in equilibrium is calculated. To this end the average gyration tensor of a flexible polymer is determined in the average center of mass coordinate system, where we put the direction of the axes such, that the average gyration tensor is diagonal:

$$\langle \mathbf{S} \rangle = \begin{pmatrix} S_\parallel & 0 & 0 \\ 0 & S_\perp & 0 \\ 0 & 0 & S_\perp \end{pmatrix} \qquad (\text{B.64})$$

The direction of the parallel axis is given by the direction of the end-to-end vector $\mathbf{R}_{\text{ee}}$, the other axes are perpendicular to $\mathbf{R}_{\text{ee}}$. Due to symmetry reasons, the components of the gyration tensor perpendicular to $\mathbf{R}_{\text{ee}}$ are equal.

We can consider the conformation of the flexible polymer as a random walk of $N = L_c/b$ steps, where $b = 2L_p$, respectively (in a discrete description) as an ideal chain with $N + 1$ beads with a bead-to-bead distance b. The average end to end vector length is thus $R_{\text{ee}} = \sqrt{N}b$. To determine the average position of the n-th bead with respect to the end-to-end vector we can consider the chain to do a RW with n-steps from bead 1 to bead n and $N - n$ steps from bead n to bead N. As the two RWs are uncorrelated, they are on average perpendicular to each other. Hence, with respect to the end-to-end vector, the average positions of the other beads are located on a sphere with radius $R = R_{\text{ee}}/2$ around the midpoint of $\mathbf{R}_{\text{ee}}/2$ (on average, each bead must lie on a circle of Thales with diameter R_{ee}).

We now want to calculate the contribution of each bead n to the gyration tensor element $S_\parallel$. To this purpose we denote the angle ϕ_n as the angle between $\mathbf{r}_N - \mathbf{r}_n$ and $\mathbf{R}_{\text{ee}}/2$. Then, for $n = 1...N$, ϕ_n runs from 0 to $\pi/2$. We can now calculate the average angle ϕ_n by using the condition, that the length of the random walk from the first bead is given as $\sqrt{n}b$, so that

$$\sin \phi_n = \frac{\sqrt{n}b}{R_{ee}} = \frac{n}{N} \tag{B.65}$$

We can thus write

$$n = \frac{R_{ee}}{b^2} \sin^2 \phi = N \sin^2 \phi \tag{B.66}$$

so that

$$\frac{\mathrm{d}n}{\mathrm{d}\phi} = 2N \sin \phi \cos \phi = N \sin(2\phi) \tag{B.67}$$

Separation of the variables yields

$$\int_0^{\phi_n} \sin(2\phi')\mathrm{d}\phi' = \int_0^n \frac{1}{N}\mathrm{d}n'$$

$$\left[-\frac{1}{2}\cos(2\phi') \right]_0^{\phi_n} = \left[\frac{n'}{N} \right]_0^n$$

$$\frac{1}{2}(1 - \cos(2\phi_n)) = \frac{n}{N} \tag{B.68}$$

so that

$$\cos(2\phi_n) = 1 - 2\frac{n}{N}. \tag{B.69}$$

The average position of bead n lies on a circle of radius $r_n = \frac{1}{2}R_{ee}\sin\alpha$ around the end to end vector. Although the positions on the circle average out to a position on the axis (so that the average c.o.m. lies in the middle between the chain ends), we cannot directly determine the gyration tensor elements $S_\perp$ from r_n, because picking a position on the circle implies shifting the c.o.m away from $\mathbf{R}_{ee}$. However, due to symmetry reasons the center of mass of the polymer will lie somewhere on the symmetry plane between the polymer ends. Thus, picking a particular position of the n-th bead on the circle with r_n shifts the c.o.m. only perpendicular to $\mathbf{R}_{ee}$ leaving $S_\parallel$ unchanged. Hence we can calculate the average contribution of the n-th bead to $S_\parallel$ as

$$S_{\parallel,n} = \left(\frac{1}{2}R_{ee}\cos(2\phi_n) \right)^2 = \frac{1}{4}Nb^2 \left(1 - 2\frac{n}{N} \right)^2 \tag{B.70}$$

Hence, we can determine $S_\parallel$ as

$$S_\parallel = \sum_{n=1}^N \frac{1}{4}Nb^2 \left(1 - 2\frac{n}{N} \right)^2$$

$$= \frac{1}{4}Nb^2 \int_0^1 (1 - 2x)^2 \mathrm{d}x$$

$$= \frac{1}{4}Nb^2(1 - 2 + \frac{4}{3}) = \frac{1}{12}Nb^2 \tag{B.71}$$

To determine $S_\perp$ we consider the gyration tensor of the flexible polymer with random end-to-end vector orientation. Symmetry implies $\langle r_g^2 \rangle = 3\bar{S}$ for the

diagonal elements of the gyration tensor of the randomly oriented flexible polymer. As the trace of the gyration tensor in diagonal form must be the same in the random orientation case and in the coordinate system parallel to $\mathbf{R}_{ee}$ case, we have

$$3\bar{S} = S_{\parallel} + 2S_{\perp} = 3S_{\perp} + S_p = \langle r_g^2 \rangle \tag{B.72}$$

where we split the parallel tensor component $S_{\parallel}$ into the perpendicular part $S_{\perp}$ and the excess part S_p:

$$S_{\parallel} = S_{\perp} + S_p = \frac{1}{12}\langle R_{ee}^2 \rangle \tag{B.73}$$

From eq. B.72 and B.73 we can determine $S_{\perp}$ and S_p and get:

$$S_{\perp} = \frac{1}{2}\langle r_g^2 \rangle - \frac{1}{24}\langle R_{ee}^2 \rangle \tag{B.74}$$

Thus, for a rotation of the flexible polymer perpendicular to the end-to-end vector, we can calculate the friction coefficient assuming an isotropic friction coefficient per unit length c_L

$$\gamma_{\perp} = c_L L_c (S_{\parallel} + S_{\perp}) = c_L L_c \left(\frac{1}{24}\langle R_{ee}^2 \rangle + \frac{1}{2}\langle r_g^2 \rangle \right) = \frac{c_L L_c}{12} \frac{1}{2} \left(\langle R_{ee}^2 \rangle + 12\langle r_g^2 \rangle \right) \tag{B.75}$$

whereas a rotation around the end-to-end vector yields a friction coefficient of

$$\gamma_{\parallel} = 2 c_L L_c S_{\perp} = c_L L_c \left(\langle r_g^2 \rangle - \frac{1}{12}\langle R_{ee}^2 \rangle \right). \tag{B.76}$$

With $c_L = c_{\perp}$ and $\langle r_g^2 \rangle = 1/6 R_{ee}^2$ this yields for the flexible polymer a rotational diffusion constant of

$$D_r = \frac{k_B T}{\gamma_{\perp}} = \frac{2}{3} \frac{12 k_B T}{c_{\perp} L_c R_{ee}^2} = \frac{2}{3} D_{\text{rod}} \frac{L_c^2}{R_{ee}^2} \tag{B.77}$$

Note that in the limit of stiff polymers $\langle r_g^2 \rangle = L_c^2/12$ and $\langle R_{ee}^2 \rangle = L_c^2$, which gives the correct results

$$\gamma_{\perp} = \frac{c_{\perp} L_c^3}{12} \tag{B.78}$$

and

$$\gamma_{\parallel} = 0, \tag{B.79}$$

of the stiff rod. This implies that the above expressions should be a useful approximation for the entire range of rigidities. Introducing an effective polymer extension

$$\langle R^2 \rangle \equiv \frac{1}{2} \left(\langle R_{ee}^2 \rangle + 12\langle r_g^2 \rangle \right) \tag{B.80}$$

we can express the diffusion constant D_r for rotation perpendicular to the end-to-end vector as

$$D_r = \frac{k_B T}{\gamma} = \frac{12 k_B T}{c_{\perp} L_c R^2} = D_{\text{rod}} \frac{L_c^2}{R^2}. \tag{B.81}$$

B.4 Calculation of Diffusive Time τ_{diff}

[1]

A mean first passage time τ_{diff} can be calculated analytically using standard methods starting out from the Langevin equation corresponding to eq 4.35,

$$
\begin{aligned}
\dot{\phi} &= \dot{\gamma}\sin^2\phi + \sqrt{2D_{\text{rot}}}\,\eta, \\
\langle\eta(t)\rangle &= 0, \\
\langle\eta(t)\eta(t')\rangle &= \delta(t-t')
\end{aligned}
\tag{B.82}
$$

We note in passing that the Langevin equation could be solved numerically via Brownian dynamics, $\phi(t+\Delta t) = \phi(t) + \dot{\gamma}\sin^2(\phi(t))\Delta t + \sqrt{2D_{\text{rot}}\Delta t}\,\text{WN}$, where WN is a Gaussian distributed random number with variance unity, and Δt a time step.

Solving the mean first passage time problem

To calculate the mean first passage time we notice that $\phi \leq \phi_c \ll 1$ characterizes the diffusive regime (cf. Section 4.2.3). It is convenient to introduce a potential $U(\phi) = -\dot{\gamma}\phi^3/3$ so that the deterministic term $\dot{\gamma}\sin^2\phi \approx \dot{\gamma}\phi^2 = -U'(\phi)$ can be regarded as the corresponding force. We thus consider an angle ϕ sitting in potential $U(\phi)$, leaving the valley at barrier located at $\phi = \phi_c$ (adsorbing boundary), and assuming a reflecting boundary at $-\phi_c$ (assuming positive rate $\dot{\gamma}$). The mean first passage time for the angle to reach ϕ_c, when starting from $\phi = \phi_0 = 0$ at $t = 0$, and with a reflecting boundary at $-\phi_c$, is [46]

$$
\tau_{\text{diff}} = \frac{1}{D_{\text{rot}}}\int_{\phi_0}^{\phi_c} d\phi\,\frac{1}{\psi(\phi)}\int_{-\phi_c}^{\phi}\psi(\phi')\,d\phi'
\tag{B.83}
$$

with

$$
\begin{aligned}
\psi(\phi) &= \exp\left(\frac{1}{D_{\text{rot}}}\int^{\phi}\dot{\gamma}\phi'^2 d\phi'\right) = \exp(M_\phi), \\
M_\phi &\equiv \frac{\dot{\gamma}\phi^3}{3D_{\text{rot}}}
\end{aligned}
\tag{B.84}
$$

The double integral in eq B.83 thus becomes

$$
\tau_{\text{diff}} = \frac{1}{D_{\text{rot}}}\int_0^{\phi_c} d\phi \int_{-\phi_c}^{\phi} d\phi'\,\exp(M_1\phi'^3 - M_1\phi^3)
\tag{B.85}
$$

and evaluates, with the help of Mathematica$^{\text{TM}}$, as follows

$$
\tau_{\text{diff}} = \frac{B(M_{\phi_c})}{2D_{\text{rot}}M_1^{2/3}},
\tag{B.86}
$$

$$
B(x) \equiv x^{2/3}\,_pF_q^*(x) + \frac{\pi(\xi_0 - 2\xi(x))}{\sqrt{3}\Gamma(-4/3)} + \frac{2\xi^2(x)}{9}
\tag{B.87}
$$

---

[1] This section was written in cooperation with Martin Kroeger, ETH Zuerich
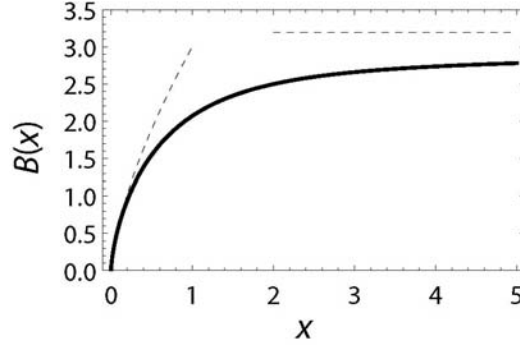
Figure B.3: $B(x)$ given in eq B.87. It is basically a constant for $x \gg 1$ and well approximated by $B(x) = 3\,x^{2/3}$ for $x \ll 1$, cf. eqs B.90.

thus involving both an incomplete Gamma and the hypergeometric function $_pF_q$, defined as [2],

$$\xi(y) \ \equiv \ \Gamma\left(\frac{1}{3}, y\right) = \int_y^\infty t^{-2/3} e^{-t}\, dt, \qquad , \tag{B.88}$$

$$_pF_q^*(x) \ \equiv \ {_pF_q}\left(\{\frac{2}{3}, 1\}, \{\frac{4}{3}, \frac{5}{3}\}, -x\right)$$

$$\equiv \ \sum_{k=0}^\infty \frac{(2/3)_k (1)_k}{(4/3)_k (5/3)_k} \frac{(-x)^k}{k!} \tag{B.89}$$

with $\xi_0 \equiv \xi(0) = 2.67894$ and the Pochhammer symbol $(a)_n \equiv \Gamma(a+n)/\Gamma(a)$. The function $B(x)$ is shown in Fig. B.3, it exhibits the asymptotic features

$$\lim_{x \to \infty} B(x) \ = \ \frac{3\pi^2}{\Gamma^2(-4/3)} \approx \pi,$$

$$\lim_{x \to 0} B(x) \ = \ 3\,x^{2/3} + o(x^{4/3}). \tag{B.90a}$$

Diffusion time τ_{diff}

We are in the position to evaluate τ_{diff} upon inserting the appropriate limiting case of eq B.90 into eq B.86. To this end we make use of eq 4.39 and then notice that M_{ϕ_c} defined in eq B.84 is actually a constant and small compared to unity,

$$M_{\phi_c} = \frac{\dot{\gamma}\phi_c^3}{3D_{\text{rot}}} = \frac{1}{3} \ll 1 \tag{B.91}$$

so that $B(M_{\phi_c}) = B(1/3) \approx 3^{1/3}$ according to eq B.90. Exact numerical evaluation yields $B(1/3) = 1.25762 \approx 5/4$. With $M_1 = \dot{\gamma}/3D_{\text{rot}}$ already defined in

eq B.84 we insert into eq B.86 to arrive at $\tau_{\text{diff}} \approx (5/4)\phi_c^2/D_{\text{rot}}$. Redoing the whole analysis with $\phi_0 = -\phi_c$ at $t = 0$, we obtain a slightly different prefactor, namely 5/3 instead of 5/4, but the calculation is less compact, and thus only illustrated above, for $\phi_0 = 0$. We finally obtain

$$\tau_{\text{diff}} \approx \frac{5}{3}\frac{\phi_c^2}{D_{\text{rot}}} = \frac{5}{3D_{\text{rot}}^{1/3}\dot{\gamma}^{2/3}} \tag{B.92}$$

B.5 Orientational Distribution Function of Brownian Rods in Shear Flow

[2] The Fokker-Planck equation for the orientational probability distribution function $p(\phi, t)$, that is, the stochastic differential equation corresponding to the Langevin equation 4.41 of a tumbling (including telescopic) Brownian rod with diameter–to–length ratio $\kappa = d/L_c \ll 1$, reads

$$\frac{\partial p(\phi)}{\partial t} = \frac{\partial(\dot{\phi}(\phi)p(\phi))}{\partial \phi} + D_{\text{rod}}\frac{\partial^2 p(\phi)}{\partial \phi^2} \tag{B.93}$$

with the deterministic contribution $\dot{\phi}(\phi) = \dot{\gamma}(\sin^2\phi + \kappa^2\cos^2\phi)$ as already mentioned in Section 4.2.3 ($\kappa = 0$ for an infinitely thin rod). The stationary orientational distribution function thus obeys

$$\frac{dp_{\text{stat}}(\phi)}{d\phi} + \frac{\dot{\phi}(\phi)p_{\text{stat}}(\phi)}{D_{\text{rod}}} = C \tag{B.94}$$

Solving this eq with the variation of the constant results in

$$p_{\text{stat}}(\phi) = \frac{C}{\psi(\phi)}\int_{\phi_0}^{\phi}\psi(\phi')\,d\phi', \tag{B.95}$$

with $\psi(\phi) \equiv \exp[a\phi + b\sin(2\phi)]$ and coefficients $a = \dot{\gamma}(\kappa^2 + 1)/2D_{\text{rod}}$ and $b = \dot{\gamma}(\kappa^2 - 1)/4D_{\text{rod}}$. The prefactor C is determined by the normalization condition $\int_0^{2\pi}p(\phi)d\phi = 1$. If we neglect, as before, the thickness of the filament ($\kappa \to 0$) one has $a = \dot{\gamma}/2D_{\text{rod}} = -2b$ and $\psi(\phi)$ in eq B.95 simplifies to

$$\psi(\phi) = \exp\left[a\left(\phi - \frac{\sin(2\phi)}{2}\right)\right]. \tag{B.96}$$

The orientational distribution function $p_{\text{stat}}(\phi)$ can be numerically calculated upon inserting $\psi(\phi)$ from eq B.96 into eq B.95. The cumulative probability density function is then obtained via $p_{\text{cumultative}}(\phi) = \int_0^{2\pi}p_{\text{stat}}(\phi')d\phi'$. We notice that $\psi(\phi)$ for $\phi \ll 1$ reduces to the expression $\psi(\phi) = \exp(M_\phi)$ used to calculate the mean first passage time in Section B.4. According to [58] we can identify ϕ_c in a good approximation with the center–position of the peak occurring around zero, in agreement with eq 4.39.

---

[2] This section was written by Martin Kroeger, ETH Zuerich.

B.6 Forcebalance Description for Tumbling Dynamics of Semiflexible Filaments in Shear Flow

We sit in the c.o.m. frame of the filament. The filament has a contour of length L_c, which fulfills $L_c \leq L_p$, and the filament conformation is given by $\mathbf{R}^{\text{com}}(\sigma) = (x^{\text{com}}(\sigma), y^{\text{com}}(\sigma))$, $\sigma \in [0; L_c]$. The y-coordinate of the center of mass y_S is given by

$$\int_0^{L_c} (y^{\text{com}}(\sigma) - y_S)\mathrm{d}\sigma = 0. \tag{B.97}$$

A filament in the stiff and semiflexible regime free of loops with a monotonic y-coordinate function $y(\sigma)$ can then be divided in an upper an lower part $[0; \sigma_S], [\sigma_S; L_c]$ where the y-coordinate of the dividing point σ_S is given by y_S:

$$\int_0^{\sigma_S} (y^{\text{com}}(\sigma) - y_S)\mathrm{d}\sigma = -\int_{\sigma_S}^{L_c} (y^{\text{com}}(\sigma) - y_S)\mathrm{d}\sigma \tag{B.98}$$

The relative velocity

$$\mathbf{v}_{\text{rel}}(\sigma) = \mathbf{v}_{\text{fluid}} - \dot{\mathbf{R}}^{\text{com}}(\sigma) = (\dot{\gamma}(y(\sigma) - y_S) - v_x(\sigma), v_y(\sigma)) \tag{B.99}$$

determines the local friction force acting on the filament, which is approximated with a friction coefficient per unit length c_L, resp. $c_\perp, c_\parallel$:

$$\mathrm{d}\mathbf{F}^{\text{frict}}(\sigma) = \mathbf{f}^{\text{frict}}(\sigma)\mathrm{d}\sigma = c_L \mathbf{v}_{\text{rel}}(\sigma)\mathrm{d}\sigma \tag{B.100}$$

respectively

$$\mathrm{d}\mathbf{F}^{\text{frict}}(\sigma) = \mathbf{f}^{\text{frict}}(\sigma)\mathrm{d}\sigma = (c_\parallel \mathbf{v}_{\text{rel},\parallel}(\sigma) + c_\perp \mathbf{v}_{\text{rel},\perp}(\sigma))\mathrm{d}\sigma, \tag{B.101}$$

where the relative velocity is divided into its components $\mathbf{v}_{\text{rel}} = \mathbf{v}_{\text{rel},\parallel} + \mathbf{v}_{\text{rel},\perp}$ parallel and perpendicular to the filament. The filament ends are free and have to satisfy the boundary conditions of the beam equation with a zero curvature $\kappa(\sigma) = \partial\alpha/\partial\sigma$ on both ends of the filament $\kappa(0) = 0, \kappa(L_c) = 0$, where α denotes the local angle between the filament and the flow-direction. At the point with the maximum curvature (bending point σ_b), the first derivative of the curvature $\frac{\partial\kappa}{\partial\sigma} = \frac{\partial^2\alpha}{\partial\sigma^2}(\sigma_b) = 0$. This is the boundary condition of a fixed beam, so for the bending in a conformation at one single point in time we can treat the rear part $[0; \sigma_b]$ and the front part $[\sigma_b; L_c]$ of the filament as if they were fixed in a wall with an orientation angle $\alpha(\sigma_b)$. Then, the bending moment of the filament $M(\sigma)$ which determines the local curvature radius $r^{-1}(\sigma) = M(\sigma)/(k_B T L_p)$ in the filament is given by

$$M_{\text{rear}}(\sigma) = \int_0^\sigma \mathbf{f}^{\text{frict}}(\sigma) \times (\mathbf{R}(\sigma) - \mathbf{R}(\sigma'))\mathrm{d}\sigma' \tag{B.102}$$

for $0 < \sigma < \sigma_b$, and

$$M_{\text{front}}(\sigma) = \int_{L_c}^\sigma \mathbf{f}^{\text{frict}}(\sigma) \times (\mathbf{R}(\sigma) - \mathbf{R}(\sigma'))\mathrm{d}\sigma' \tag{B.103}$$

for $\sigma_b < \sigma < L_c$, where the continuity condition

$$M_{\text{rear}}(\sigma_b) = M_{\text{front}}(\sigma_b) \tag{B.104}$$

has to be fulfilled.

Static Description

In a static conformation of the filament with $\dot{\mathbf{R}}(\sigma) = 0$, the friction force is given by $f_x^{\text{friction}}(\sigma) = c_L \dot{\gamma}(y(\sigma) - y_S)$, $f_y^{\text{friction}}(\sigma) = 0$. To keep the bending point $\mathbf{R}(\sigma_b)$ stationary in the c.o.m.-frame, the total force acting on the rear part of the filament must be balanced with the force on the front part of the filament:

$$\int_0^{\sigma_b} \mathbf{f}^{\text{frict}} \mathrm{d}\sigma = -\int_{\sigma_b}^{L_c} \mathbf{f}^{\text{frict}} \mathrm{d}\sigma \tag{B.105}$$

$$\int_0^{\sigma_b} c_L \dot{\gamma}(y(\sigma') - y_S) \mathrm{d}\sigma' = -\int_{\sigma_b}^{L_c} c_L \dot{\gamma}(y(\sigma') - y_S) \mathrm{d}\sigma', \tag{B.106}$$

which leads to the conclusion, that the dividing point is equal to the bending point $\sigma_b = \sigma_S$. Inserting this into the bending moment equation eq. (B.104) in the static conformation yields

$$\int_{L_c}^{\sigma_S} c_L \dot{\gamma}(y_S - y(\sigma'))^2 \mathrm{d}\sigma' = -\int_0^{\sigma_S} c_L \dot{\gamma}(y_S - y(\sigma'))^2 \mathrm{d}\sigma'. \tag{B.107}$$

whereas the force balance is given by

$$\int_0^{\sigma_S} c_L \dot{\gamma}(y_S - y(\sigma')) \mathrm{d}\sigma' = -\int_{\sigma_S}^{L_c} c_L \dot{\gamma}(y_S - y(\sigma')) \mathrm{d}\sigma' \tag{B.108}$$

Both equations can only be fulfilled simultaneously in the trivial case of a completely straight, flow aligned filament $y(\sigma) = y_S \quad \forall \quad \sigma \in [0; L_c]$. Therefore, the completely aligned case is the only stationary point for the system, in any other conformation the force and bending moment balance can only be satisfied with a conformational change $\dot{\mathbf{R}}(\sigma) \neq 0$. Hence, thermal fluctuations away from the aligned state can induce a tumbling cycle. This leads to the conclusion:

To describe the conformational cycle during the tumbling and the dynamics (estimation of τ_T) with a force-balancing approach, the dynamics $\dot{\mathbf{R}}$ have to be taken into account.

Note that the bending moment balance is based on the assumption that there is a point with a maximum curvature σ_b. If the filament is completely straight, but not flow aligned, the flow will induce a rotation with $\dot{\phi} = \dot{\gamma} \sin^2 \phi$ as for a rod. We can now perform a stability analysis for the rod-like conformation:

- For $\pi/2 < \phi < \pi$ the filament will be stretched along the length, so that fluctuations are suppressed and get damped out. Thus, the stretched conformation with $\pi/2 < \phi < \pi$ leads to a nearly rodlike rotation. Near π the rotation gets very slow and the filament appears to be in a metastable quasistatic state (waiting time).

- For $0 < \phi < \pi/2$ the filament gets compressed by the shear flow. The local frictional force in the tangential direction is given by eq. 4.33 in cylindrical coordinates as

$$\mathrm{d}\mathbf{f}^{\mathrm{frict}} r \mathrm{d}r = -c_{\|}\dot{\gamma}\sin\phi\cos\phi r \mathrm{d}r. \tag{B.109}$$

The compressive force $F_{\mathrm{comp}}(x)$ at the position $\sigma = L_c/2(1+x)$, where we introduced $x = 2\sigma/L_c - 1$ with $x \in [-1;1]$ is then calculated as

$$
\begin{aligned}
F_{\mathrm{comp}}(x) \quad &= \int_{xL_c/2}^{L_c/2} \mathrm{d}\mathbf{F}_r^{\mathrm{frict}} = \tfrac{1}{2}c_{\|}\dot{\gamma}\sin\phi\cos\phi[L_c^2/4 - x^2 L_c^2/4] \\
&= \tfrac{1}{16}c_{\|}L_c^2\dot{\gamma}\sin(2\phi)(1-x^2). \tag{B.110}
\end{aligned}
$$

where we used $r = xL_c/2$.

When during the rotation the compressional force $F(x)$ gets bigger than the critical buckling force $F_c = \pi^2 \frac{EI}{l^2}$ [47] exerted by the outer parts onto the middle part of the filament with length $l = xL_c$, the filament will buckle and end up in a strongly bent conformation. Thus, the filament is expected to buckle, if

$$\frac{1}{16}c_{\|}L_c^2\dot{\gamma}\sin(2\phi)(1-x^2) > \pi^2\frac{k_B T L_p}{x^2 L_c^2} \tag{B.111}$$

The maximum of the compressive force on the left occurs at $\phi = \pi/4$. Thus we get

$$L_c^4 > 16\pi^2\frac{k_B T L_p}{c_{\|}\dot{\gamma}}\frac{1}{x^2(1-x^2)} \tag{B.112}$$

The maximum of $1/[x^2(1-x^2)]$ is located at $x = \sqrt{1/2}$. Therefore, the minimum buckling length L_{buckle} is determined by

$$L_b^4 = 64\pi^2\frac{k_B T L_p}{c_{\|}\dot{\gamma}}. \tag{B.113}$$

By introducing the U-turn radius R_{U} of the semiflexible filament (see eq: 4.60) we can express L_{buckle} as:

$$L_b = 2\pi^{3/4} R_{\mathrm{U}} \tag{B.114}$$

If the compression force during the advective phase never excesses the buckling force we can describe the filament as a rodlike filament in first order approximation. Thus eq. (B.114) marks the division between the rodlike ($L_c < L_b$) and the semiflexible regime ($L_c > L_b$). For filaments with $L_c > L_b$ we can estimate the angle α_{buckle} at which the frictional forces overcome the buckling force: With $x = \sqrt{1/2}$ it follows from eq. B.111 for the buckling condition

$$\sin(2\phi) > 64\pi^2\frac{k_B T L_p}{c_{\|}\dot{\gamma}L_c^4} = 16\pi^3\left(\frac{R_{\mathrm{U}}}{L_c}\right)^4 = \left(\frac{L_b}{L_c}\right)^4. \tag{B.115}$$

If $R_{\mathrm{U}} \ll L_c$, we can conclude that $2\phi \ll 1$ to calculate a buckling angle of

$$\alpha_{\mathrm{buckle}} = \frac{1}{2}\left(\frac{L_b}{L_c}\right)^4. \tag{B.116}$$

Dynamic Description

We now try to estimate the filaments conformation in a dynamic description, taking $\dot{\mathbf{R}}$ into account, but still neglecting inertial forces $\ddot{\mathbf{R}} \approx 0$, overdamped case. To this end, we describe the filament conformation during the tumbling motion in a simple two-state-model:

- For end-to-end angles ϕ near flow alignment $\phi < \alpha_{\text{buckle}}, \phi > \pi - \alpha_{\text{buckle}}$, both the filament conformation and dynamics are rod-like.

- For end-to-end angles $\alpha_{\text{buckle}} < \phi < \pi - \alpha_{\text{buckle}}$, the filament is strongly bent and its conformation is approximated by a stadium model. The filament is assumed to perform a U-turn run on a stadium with radius R_{U} and straight parts of length $L_c - \pi R_{\text{U}}$. The center of the right stadium half-circle is located in the origin of the coordinate system x^*, y^* of the U-turn frame. The conformation of the filament is given by a U-turn coordinate s, which is given by the arc length of the filaments leading end on the stadium track, measured with respect to the start of right U-turn at $(x^*, y^*) = (0, -R_{\text{U}}$. The dynamics $\dot{\mathbf{R}}$ in the U-turn model are incorporated by the track velocity $v(s)$, with which the filament runs on the stadiums U-turn track.

We will firstly restrict the calculations in the U-turn description to the conformational interval $s \in [\pi R_{\text{U}}; L_c]$, which corresponds to an end-to-end angle interval of $[\phi_{\min}; \pi - \phi_{\min}]$. Furthermore we introduce the coordinate χ as

$$s = \frac{L_c}{2}[(1 + \frac{\pi R_{\text{U}}}{L_c}) + \chi(1 - \frac{\pi R_{\text{U}}}{L_c})], \tag{B.117}$$

so that $s \in [\pi R_{\text{U}}; L_c]$ corresponds to $\chi \in [-1; 1]$. We will switch between s and χ according to convenience, an overview over the different coordinates is given in fig. 4.3.

Calculation of relative velocity between filament and fluid

To calculate the drag forces in the c.o.m. frame correctly, we need to calculate the relative velocity between the filament and the fluid. To this purpose, we first calculate how the c.o.m moves in the stadium frame. The x-coordinate of the com in the stadium frame $x_S^\star$ is given by:

$$x_S^\star(\chi) = \frac{1}{L_c} \int_{s-L_c}^{L_c} x^\star(\sigma) \mathrm{d}\sigma =$$

$$= \frac{1}{L_c} \left[\int_{s-L_c}^0 \sigma \mathrm{d}\sigma + \int_0^{\pi R_{\text{U}}} R_{\text{U}} \sin\left(\frac{\sigma}{R_{\text{U}}}\right) \mathrm{d}\sigma + \int_{\pi R_{\text{U}}}^s -(\sigma - \pi R_{\text{U}}) \mathrm{d}\sigma \right]$$

$$= \ldots = 2\frac{R_{\text{U}}^2}{L_c} - \frac{1}{4}L_c \left(1 - \frac{\pi R_{\text{U}}}{L_c}\right)^2 (1 + \chi^2) \tag{B.118}$$

where $x \star (\sigma)$ is the x-coordinate in the stadium frame. Analogously we get the y-coordinate of the com in the stadium frame $y_S^\star$:

$$y_S^\star(\chi) = R_U \chi \left(1 - \frac{\pi R_U}{L_c} \right) \tag{B.119}$$

This yields in a stadium frame velocity

$$\mathbf{v}_{\text{frame}}^\star = \begin{pmatrix} \dot{x}_S^\star(\chi) \\ \dot{y}_S^\star(\chi) \end{pmatrix} = \begin{pmatrix} \frac{\mathrm{d}x_S^\star(\chi)}{\mathrm{d}\chi} \frac{\mathrm{d}\chi}{\mathrm{d}s} \frac{\mathrm{d}s}{\mathrm{d}t} \\ \frac{\mathrm{d}y_S^\star(\chi)}{\mathrm{d}\chi} \frac{\mathrm{d}\chi}{\mathrm{d}s} \frac{\mathrm{d}s}{\mathrm{d}t} \end{pmatrix}. \tag{B.120}$$

With the stadium track velocity $v = \mathrm{d}s/\mathrm{d}t$ and

$$\frac{\mathrm{d}\chi}{\mathrm{d}s} = \frac{2}{L_c \left(1 - \frac{\pi R_U}{L_c} \right)} \tag{B.121}$$

we get

$$\mathbf{v}_{\text{frame}}^\star(\chi) = v \begin{pmatrix} -\chi \left(1 - \frac{\pi R_U}{L_c} \right) \\ \frac{2R_U}{L_c} \end{pmatrix}. \tag{B.122}$$

The local filament velocity in the stadium frame is given by

$$\mathbf{v}_{\text{fil}}^\star = v \begin{pmatrix} \cos\alpha \\ \sin\alpha \end{pmatrix}, \tag{B.123}$$

where α is the local angle between the filament and the flow direction. Thus, the filament velocity in the c.o.m. system is given by

$$\mathbf{v}_S^{\text{fil}} = \mathbf{v}_{\text{fil}}^\star - \mathbf{v}_{\text{frame}}^\star = v \begin{pmatrix} \cos\alpha + \chi \left(1 - \frac{\pi R_U}{L_c} \right) \\ \sin\alpha - 2\frac{R_U}{L_c} \end{pmatrix}, \tag{B.124}$$

The fluid velocity at the position of the filament in the com-frame is given as

$$\mathbf{v}_S^{\text{fl}} = \begin{pmatrix} -\dot{\gamma}(y^\star(\chi,\alpha) - y_S^\star(\chi,\alpha)) \\ 0 \end{pmatrix} = \dot{\gamma} R_U \begin{pmatrix} \cos\alpha + \chi \left(1 - \frac{\pi R_U}{L_c} \right) \\ 0 \end{pmatrix} \tag{B.125}$$

The relative velocity between fluid and filament (which gives rise to the friction forces acting on the filament) is thus given as

$$\mathbf{v}_S^{\text{rel}} = \mathbf{v}_S^{\text{fl}} - \mathbf{v}_S^{\text{fil}} = \begin{pmatrix} (\dot{\gamma} R_U - v) \left(\cos\alpha + \chi \left(1 - \frac{\pi R_U}{L_c} \right) \right) \\ -v \left(\sin\alpha - 2\frac{R_U}{L_c} \right) \end{pmatrix}, \tag{B.126}$$

where v is the still unknown track velocity in the stadium frame. To determine the track velocity v we calculate the tangential component of the relative velocity:

$$\begin{aligned} v_S^{\text{rel,tang}}(\chi,\alpha) &= \mathbf{v}_S^{\text{rel}} \cdot (\cos\alpha, \sin\alpha) \tag{B.127} \\ &= (\dot{\gamma} R_U - v) \left(\cos\alpha + \chi \left(1 - \frac{\pi R_U}{L_c} \right) \right) \cos\alpha - v \left(\sin\alpha - 2\frac{R_U}{L_c} \right) \sin\alpha \end{aligned}$$

The filament is not accelerated along the track when the integral over the tangential component of the relative velocity vanishes:

$$\int_{s-L_c}^{s} v_S^{\text{rel,tang}}(\chi, \alpha)\mathrm{d}\sigma = 0 \tag{B.128}$$

$$\int_{s-L_c}^{0} v_S^{\text{rel,tang}}(\chi, \alpha=0)\mathrm{d}\sigma + \int_{0}^{\pi R_U} v_S^{\text{rel,tang}}(\chi, \alpha=\frac{\sigma}{R_U})\mathrm{d}\sigma + \int_{\pi R_U}^{s} v_S^{\text{rel,tang}}(\chi, \alpha=\pi)\mathrm{d}\sigma = 0$$

With

$$v_S^{\text{rel,tang}}(\chi, \alpha = 0) = (\dot{\gamma}R_U - v)\left(1 + \chi\left(1 - \frac{\pi R_U}{L_c}\right)\right)$$

$$v_S^{\text{rel,tang}}(\chi, \alpha = \pi) = (\dot{\gamma}R_U - v)\left(1 - \chi\left(1 - \frac{\pi R_U}{L_c}\right)\right)$$

$$v_S^{\text{rel,tang}}(\chi, \alpha = \frac{\sigma}{R_U}) = \dot{\gamma}R_U \cos^2\frac{\sigma}{R_U} + \dot{\gamma}R_U\chi\left(1 - \frac{\pi R_U}{L_c}\right)\cos\frac{\sigma}{R_U} - v + 2v\frac{R_U}{L_c}\sin\frac{\sigma}{R_U} \tag{B.129}$$

the above integrals can be evaluated resulting in a track velocity of:

$$v = \dot{\gamma}R_U \frac{1 - \frac{\pi}{2}\frac{R_U}{L_c} - \chi^2\left(1 - \left(\frac{\pi R_U}{L_c}\right)^2\right)}{1 - 4\left(\frac{R_U}{L_C}\right)^2 - \chi^2\left(1 - \left(\frac{\pi R_U}{L_c}\right)^2\right)} \tag{B.130}$$

Inserting this into the relative velocity yields

$$\mathbf{v}_S^{\text{rel}} = \begin{pmatrix} \frac{\pi}{2}\dot{\gamma}\frac{R_U^2}{L_c}\frac{\left(1 - \frac{8}{\pi}\frac{R_U}{L_c}\right)\left(\cos\alpha + \chi\left(1 - \frac{\pi R_U}{L_c}\right)\right)}{1 - 4\left(\frac{R_U}{L_c}\right)^2 - \chi^2\left(1 - \left(\frac{\pi R_U}{L_c}\right)^2\right)} \\[2ex] -\dot{\gamma}R_U\left(\sin\alpha - 2\frac{R_U}{L_c}\right)\frac{1 - \frac{\pi}{2}\frac{R_U}{L_c} - \chi^2\left(1 - \left(\frac{\pi R_U}{L_c}\right)^2\right)}{1 - 4\left(\frac{R_U}{L_C}\right)^2 - \chi^2\left(1 - \left(\frac{\pi R_U}{L_c}\right)^2\right)} \end{pmatrix} \tag{B.131}$$

Estimation of U-turn radius R_U from frictional drag forces

To estimate the U-turn radius R_U we first neglect the forces arising from drag along the stadium arc $(0 < \sigma < \pi R_U)$ and just consider the forces $F_{\text{up}}, F_{\text{low}}$ arising from drag on the straight ends of the stadium-"U" (this will be a good approximation for long filaments as long as $1 - |\chi| \gg \frac{\pi R_U}{L_c}$). Then, we will calculate the maximum curvature κ_{max} in the arc arising from these bending forces, which acts as an estimate for the inverse of the stadium radius $R_U \approx \kappa_{\text{max}}^{-1}$. The "upper" straight end has a length

$$L_{\text{up}} = s - \pi R_U = \frac{L_c}{2}\left(1 - \frac{\pi R_U}{L_c}\right)(1 + \chi), \tag{B.132}$$

the lower ends length is given by

$$L_{\text{low}} = -s + L_c = \frac{L_c}{2}\left(1 - \frac{\pi R_{\text{U}}}{L_c}\right)(1-\chi). \tag{B.133}$$

The forces with which the upper and the lower end are pulling / pushing on the arc at $\sigma = \pi R_{\text{U}}, \sigma = 0$ are thus given by

$$F_{\text{up}} = c_{\parallel}L_{\text{up}}\mathbf{v}_S^{\text{rel},\chi}(\alpha = \pi)$$

$$= -\frac{\pi}{4}c_{\parallel}\dot{\gamma}R_{\text{U}}^2\left(1 - \frac{\pi R_{\text{U}}}{L_c}\right)(1+\chi)\frac{\left(1-\frac{8}{\pi}\frac{R_{\text{U}}}{L_c}\right)\left(1-\chi\left(1-\frac{\pi R_{\text{U}}}{L_c}\right)\right)}{1-4\left(\frac{R_{\text{U}}}{L_c}\right)^2-\chi^2\left(1-\left(\frac{\pi R_{\text{U}}}{L_c}\right)^2\right)} \tag{B.134}$$

$$F_{\text{low}} = c_{\parallel}L_{\text{low}}\mathbf{v}_S^{\text{rel},\chi}(\alpha = 0)$$

$$= \frac{\pi}{4}c_{\parallel}\dot{\gamma}R_{\text{U}}^2\left(1 - \frac{\pi R_{\text{U}}}{L_c}\right)(1-\chi)\frac{\left(1 - \frac{8}{\pi}\frac{R_{\text{U}}}{L_c}\right)\left(1 + \chi\left(1 - \frac{\pi R_{\text{U}}}{L_c}\right)\right)}{1 - 4\left(\frac{R_{\text{U}}}{L_c}\right)^2 - \chi^2\left(1 - \left(\frac{\pi R_{\text{U}}}{L_c}\right)^2\right)}$$

$$\tag{B.135}$$

With these forces, the y-coordinate of the "bending point" with the maximum curvature in the stadium frame $y_b^{\star}$ can be calculated:

$$F_{\text{up}}(R_{\text{U}} - y_b^{\star}) = -F_{\text{low}}(-R_{\text{U}} - y_b^{\star}) \tag{B.136}$$

which yields

$$y_b = \frac{\chi\pi\frac{R_{\text{U}}^2}{L_c}}{1 - \chi^2\left(1 - \frac{\pi R_{\text{U}}}{L_c}\right)}. \tag{B.137}$$

This gives the bending point coordinate $\sigma_b = R_{\text{U}}\alpha_b = R_{\text{U}}\arccos(-y_b^{\star}/R_{\text{U}})$. With the bending point known, the bending moment M_b at the bending point can be calculated as the product of the force F_{up} and the lever $(R_{\text{U}} - y_b^{\star})$:

$$M_b = F_{\text{up}}(R_{\text{U}} - y_b^{\star})$$

$$= F_{\text{up}}R_{\text{U}}\frac{1 - \chi^2\left(1 - \frac{\pi R_{\text{U}}}{L_c}\right) - \chi\frac{\pi R_{\text{U}}}{L_c}}{1 - \chi^2\left(1 - \frac{\pi R_{\text{U}}}{L_c}\right)}$$

$$= -\frac{\pi}{4}c_{\parallel}\dot{\gamma}R_{\text{U}}^3\left(1 - \frac{\pi R_{\text{U}}}{L_c}\right)(1+\chi)\frac{\left(1 - \frac{8}{\pi}\frac{R_{\text{U}}}{L_c}\right)\left(1 - \chi\left(1 - \frac{\pi R_{\text{U}}}{L_c}\right)\right)}{1 - 4\left(\frac{R_{\text{U}}}{L_c}\right)^2 - \chi^2\left(1 - \left(\frac{\pi R_{\text{U}}}{L_c}\right)^2\right)} \cdot \frac{1 - \chi^2\left(1 - \frac{\pi R_{\text{U}}}{L_c}\right) - \chi\frac{\pi R_{\text{U}}}{L_c}}{1 - \chi^2\left(1 - \frac{\pi R_{\text{U}}}{L_c}\right)}$$

$$= -\frac{\pi}{4}c_{\parallel}\dot{\gamma}R_{\text{U}}^3\frac{\left(1 - \frac{8}{\pi}\frac{R_{\text{U}}}{L_c}\right)\left(1 - \chi^2\left(1 - \frac{\pi R_{\text{U}}}{L_c}\right)^2\right)}{1 - 4\left(\frac{R_{\text{U}}}{L_c}\right)^2 - \chi^2\left(1 - \left(\frac{\pi R_{\text{U}}}{L_c}\right)^2\right)} \cdot \frac{(1-\chi^2)\left(1 - \frac{\pi R_{\text{U}}}{L_c}\right)}{1 - \chi^2\left(1 - \frac{\pi R_{\text{U}}}{L_c}\right)}$$

$$\tag{B.138}$$

The relation between the bending moment and the Radius R_U is given by the beam equation 4.55

$$\frac{1}{R_U} = -\frac{M_b}{EI} = -\frac{M_b}{k_B T L_p} \tag{B.139}$$

In the limit of long filaments ($\pi R_U / L_c \ll 1$) we get $M_b = -\frac{\pi}{4} c_\parallel \dot\gamma R_U^3$ and thus

$$R_U = \left(\frac{4}{\pi} \frac{k_B T L_p}{c_\parallel \dot\gamma}\right)^{\frac{1}{4}}. \tag{B.140}$$

Thus, the stadium radius is approximately constant for $\chi \in [-1; 1]$ for long filaments, which supports the assumption of a constant R_U without considering terms of $dR_U/d\chi$ in the above calculations.

Determination of angular velocity $\dot\phi$ of the end-to-end vector

With $R_U(\chi) \approx$ const. we can now estimate the angular velocity $\dot\phi(\phi)$ of the filaments end-to-end vector $\mathbf{R}_{ee}$ in dependence of the angle ϕ between the filaments end-to-end vector and the flow direction. In the stadium conformation with $\chi \in [-1; 1]$, the x-component of the end-to-end vector is given by

$$R_{ee,x} = 2R_U \frac{\cos\phi}{\sin\phi} \tag{B.141}$$

The angular velocity $\dot\phi$ can be obtained by differentiating $R_{ee,x}$ with respect to the time:

$$\dot{R}_{ee,x} = \frac{dR_{ee,x}}{d\phi}\dot\phi = -\frac{2R_U}{\sin^2\phi}\dot\phi \tag{B.142}$$

The stadium track velocity is related to the x-component of the end-to-end vector as

$$v = -\frac{1}{2}\dot{R}_{ee,x} \tag{B.143}$$

so that the angular velocity $\dot\phi$ is obtained as

$$\dot\phi(\phi) = \frac{v}{R_U}\sin^2\phi \tag{B.144}$$

Taking the limit of long filaments, the U-turn track velocity is given by $v = \dot\gamma R_U$, which results in

$$\dot\phi(\phi) = \dot\gamma \sin^2\phi \tag{B.145}$$

which should be a good first-order approximation for angles corresponding to $\chi \in [-1; 1]$. At $\chi = \pm 1$, the end-to-end vector is given by

$$\mathbf{R}_{ee} = \begin{pmatrix} \pm(L_c - \pi R_U) \\ 2R_U \end{pmatrix}, \tag{B.146}$$

which gives the interval of angles $[\phi_{\min}; \phi_{\max}]$ for the stadium conformation as

$$\phi_{\min} = \arctan\frac{2R_U/L_c}{1 - \frac{\pi R_U}{L_c}}, \quad \phi_{\max} = \pi - \phi_{\min}, \tag{B.147}$$

which is in a first order approximation for long filaments:

$$\phi_{\min} \approx 2\frac{R_{\mathrm{U}}}{L_c}, \quad \phi_{\max} = \pi - \phi_{\min} \tag{B.148}$$

By comparing with the buckling angle from eq. B.116 we get that $\phi_{\min} > \phi_{\mathrm{buckle}}$ if

$$L_c > 2\pi R_{\mathrm{U}} \approx L_b. \tag{B.149}$$

Thus, in the range where the U-turn description can be used, the minimum U-turn angle is bigger than the buckling angle. On the other hand, a comparison between the buckling angle and the critical angle ϕ_c seperating the advective and diffusive phases of the tumbling Brownian rod shows, that for

$$\mathrm{Wi} = \frac{\dot{\gamma}}{2D_{\mathrm{rod}}} < (4\pi)^3 \frac{\sqrt{2}}{3^{3/2}} \left(\frac{L_p}{L_c}\right)^{3/2} \approx 540 \left(\frac{L_p}{L_c}\right)^{3/2} \tag{B.150}$$

the critical angle ϕ_c is smaller than the buckling angle. This is the range, where we can approximate the rotational diffusion coefficient of the filament by D_{rod}, as long as $L_p/L_c \leq 1$, because the filament is not bent by the shear force in the diffusive phase. In this regime, we hence have $\phi_c < \alpha_{\mathrm{buckle}} < \phi_{\min}$.

With $\phi_c < \alpha_{\mathrm{buckle}}$, the conformation of the semiflexible filament can be approximated by the stiff rod conformation in the angular intervals $[0; \alpha_{\mathrm{buckle}}]$ and $[\pi - \alpha_{\mathrm{buckle}}; \pi]$. Consequently, the dynamics of the filament are expected to be equivalent to the Brownian rod dynamics in these intervals. As $\phi_{\min} > \phi_c$, the interval $\phi_{\min}, \phi_{\max}$ is dominated by advection, and we have shown that the dynamics of the strongly bent filament is also equivalent to the stiff rod dynamics. In first order, the dynamics of the strongly bent filament on the U-turn track and of the unbent filament are equivalent. This suggests, that also in the remaining small intervals $[\alpha_{\mathrm{buckle}}; \phi_{\min}]$ and $[\phi_{\max}; \pi - \alpha_{\mathrm{buckle}}]$ the dynamics should be well approximated by the stiff rod dynamics. Thus, the entire angular dynamics of the semiflexible filament is approximately equivalent to the tumbling dynamics of the Brownian rod, if $\mathrm{Wi} < 540 \left(\frac{L_p}{L_c}\right)^{3/2}$.

If $\mathrm{Wi} > 540 \left(\frac{L_p}{L_c}\right)^{3/2}$ it follows that $\alpha_{\mathrm{buckle}} < \phi_c < \phi_{\min}$. Then, the filament gets buckled by the shear flow already in the diffusive phase. Thus, we cannot approximate the rotational diffusion of the end-to-end vector by using D_{rod} anymore. Instead D_r has to be corrected and we can treat semiflexible filaments in very strong flow equivalently to flexible polymers. The same applies to semiflexible polymers with $L_c > L_p$.

Telescopic Rod Model

Within $[\phi_{\min}; \phi_{\max}]$ the U-turn description also predicts the length of the end-to-end vector R_{ee}. With setting $\phi(t = 0) = \pi/2$, the end-to-end vector length can be calculated from the distance in x-direction between the filament ends,

$$R_{\mathrm{ee},x}(t) = 2vt = 2\dot{\gamma}R_{\mathrm{U}}t \tag{B.151}$$

with $R_{\text{ee},y} = 2R_{\text{U}}$ as

$$R_{\text{ee}}(t) = 2R_{\text{U}}\sqrt{1 + (\dot{\gamma}t)^2}. \qquad (B.152)$$

C. DIFFERENTIAL VISCOMETER

C.1 Rheology of (Semi)-Dilute Polymer Soluions

Steady-State Shear Viscosity of Polymer Solutions

Polymer solutions of polyacrylamid (PAA) polymers with a molecular weight of about 5-6 MDa were prepared in aqueous solution in various concentrations to investigate the shear-thinning and the concentration dependence of the shear viscosity. The shear viscosity of the polymer solutions was measured with a rotational rheometer in cone-plate geometry over a range of shear rates from $\dot{\gamma} = 10^{-2} - 10^4 \text{s}^{-1}$ for polymer concentrations from $c = 10^{-2} - 2$ % (w/w) PAA in deionized water. Fig. C.1a shows a set of viscosity measurements for concentrations ranging from $c = 10^{-1} - 2$ % (w/w). For concentrations $c > 2$ % (w/w) PAA gelation occured. The zero-shear viscosity η_0 was determined
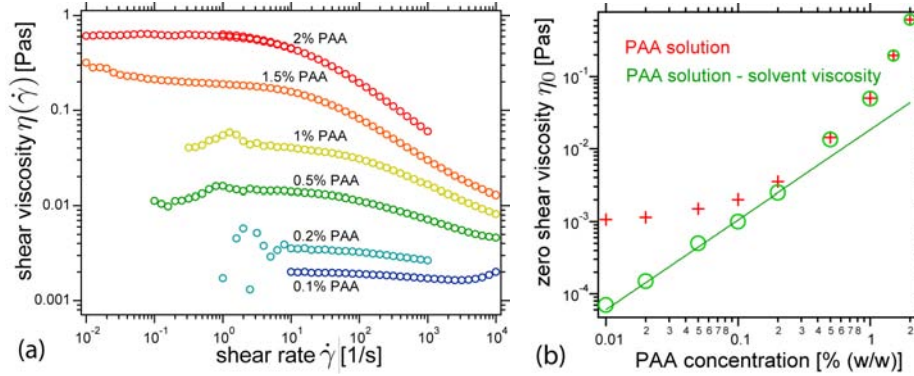

Figure C.1: (a) Rate dependence of the shear viscosity $\eta(\dot{\gamma})$ for PAA (5-6 MDa) aqueous solutions in various concentrations measured with a cone-plate rheometer. (b) Zero-shear viscosities of PAA-solutions extracted by fitting Carreau-Yasuda model to $\eta(\dot{\gamma})$-curves in dependence of the concentration (+). By subtraction of the solvent viscosity of $1\,\text{mPAS}$ the polymer contribution $\eta_{\text{polym}}(c)$ to the zero-shear viscosity was determined ($\circ$). The green line shows a linear fit to the polymer contribution at low concnetrations. The overlap concentration $c^\star$ marks the onset of the nonlinear regime of $\eta_{\text{polym}}(c)$.

by fitting a Carreau-Yasuda model to the viscosity curves (see eq. 3.34), its concentration dependence is shown in fig. C.1b by the red crosses. Subtract-

ing the solvent viscosity $\eta(water) = 1 \cdot 10^{-3}$ Pas from the zero shear viscosity η_0 yields the polymer contribution $\eta_{\text{polym}}(c)$ to the shear viscosity (green circles). For small polymer concentrations $c < 0.5\%$ PAA the polymer viscosity rises linearly with the concentration indicating a dilute polymer solution. The onset of the more rapid rise in the viscosity marks the overlap concentration $c^\star$ of the polymer solution and is identified as $c^\star \approx 0.4\,\%\,(\text{w/w})$ PAA from fig. C.1b. A PAA polymer with a molecular mass of $u \approx 5.5\,\text{MDa}$ consists of approximately $n = 77 \cdot 10^3$ monomers, which corresponds to a contour length of $L_c \approx n \cdot l \cdot 0.82 = 20\,\mu\text{m}$, where a monomer length of $l = 2 \cdot 154$ pm and a tetrahedral bonding angle of $109°$ has been assumed [65]. From the overlap concentration $c^\star = 0.4\%\,(\text{w/w})$ we can calculate a radius of gyration of $R_g \approx 82$ nm for the polymers. With $R_g^2 = N_K b_K^2/6$ and $N_K b_K = L_c$ this corresponds to a number of Kuhn segments of about $N_K = 1 \cdot 10^4$ and a Kuhn length of $b_K \approx 2$ nm.

Extensional Viscosity of PAA solutions determined by CaBER

For comparison with the results in the differential extensional rheometer, measurements in a capillary breakup extensional rheometer were performed. The results for a 0.1% and a 0.2% (w/w) PAA solution of 5-6 MDa in a glycerol/water mixture of 80% (w/w) glycerol and the result for the worm-like-micellar solution are shown in fig. C.2. Hereby, literature values for the surface tension σ for an 80% glycerol solution were used as estimates for the surface tension of the dilute polymer solutions. The value used for the surface tension of the WLM-solution is just a rough estimate, and Λ_{WLM} is only shown to demonstrate the 2 orders of magnitude difference for Λ in comparison to the dilute polymer solutions.
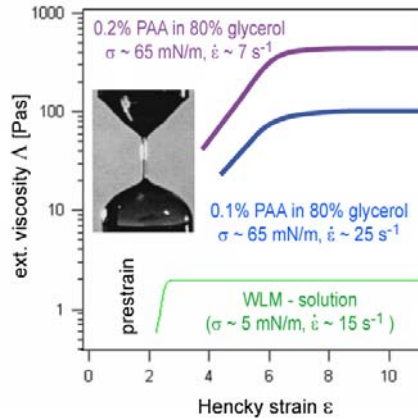

Figure C.2: Results of CaBER measurements for dilute polymer solutions and worm-like-micellar solution. A prestrain occurs during the seperation of the cylinders. Data from the filament width is evaluated to get Λ once the cylinders have reached their final seperation distance. Inset: Picture of CaBER measurement taken from [5]

C.2 Numerical Evaluation of Differential Shear Viscometer Data

For strongly shear thinning fluids the power-law description of the shear viscosity may be a poor approximation if the interval of the shearrates $[\dot{\gamma}_r; \dot{\gamma}_a]$ spans the region where the local powerlaw index changes a lot. If the flowrate ratio is measured for an interval of flowrates $[Q_{\min}; Q_{\max}]$ with N measured flowrates Q_i, an improved evaluation of the measurement data X_i can be done numerically. The principle of the method, which has been developed in cooperation with Christian Cyron[1] is illustrated in fig. C.3. The flowrate ratio X is given by eq. 5.5 as:

$$X = \frac{\eta(\dot{\gamma}_r)}{\eta(\dot{\gamma}_a)} \cdot \frac{L_r}{L_a} \tag{C.1}$$

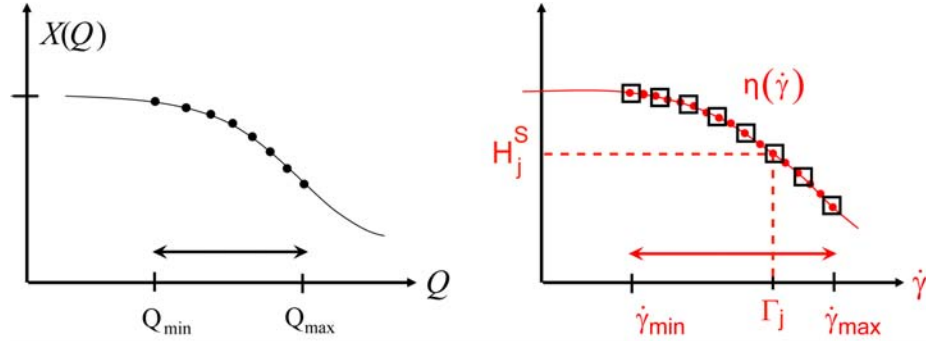Thus, N measurement values $X_i(Q_i)$ correspond to $2N$ unknown values of the

Figure C.3: Schematics of the numerical evaluation method: The N measurement values of X on $[Q_{\min}, Q_{\max}]$ ($\bullet$, left) correspond to $2N$ unknown viscosity values at $2N$ shearrates on $[\dot{\gamma}_{\min}; \dot{\gamma}_{\max}]$ ($\bullet$, right). The $2N$ viscosity values are approximated by interpolation between N viscosity values ($\square$), for which a linear equation system containing the N measured values for X can be solved.

shear viscosity $\eta(\dot{\gamma}_{a,i}), \eta(\dot{\gamma}_{r,i})$, where the $2N$ corresponding shearrates are given by Q_i via eqs. 5.6, 3.20. As the roughness of the viscosity functions η and Λ is limited by $n \geq 0$, the function $\eta(\dot{\gamma})$ can be approximated by interpolation between a sufficient number of basic values. To this purpose, N interpolation points Γ_j are distributed over the interval $[\dot{\gamma}_{\min}, \dot{\gamma}_{\max}]$

$$\Gamma_j = \dot{\gamma}_{\min} \cdot \left(\frac{\dot{\gamma}_{\max}}{\dot{\gamma}_{\min}} \right)^{j/(N-1)} \tag{C.2}$$

where the according interpolation values are set:

$$H_j^S \equiv \eta(\Gamma_j) \tag{C.3}$$

---

[1] TUM, Department for Numerical Mechanics, Chair of Prof. W.A. Wall

The $2N$ unknown values $\eta(\dot{\gamma}_{a,i}), \eta(\dot{\gamma}_{r,i})$ can thus be expressed by the N unknown interpolation values H_j^S using the interpolation hat function

$$F_h(x) = \begin{cases} 0 & \text{for} \quad x < -1 \\ x + 1 & \text{for} \quad -1 \le x \le 0 \\ 1 - x & \text{for} \quad 0 < x \le 1 \\ 0 & \text{for} \quad x > 1 \end{cases} \tag{C.4}$$

as

$$\eta(\dot{\gamma}_{k,i}) = \sum_j N_{k,ij}^S(\dot{\gamma}_{k,i}) H_j^S, \quad \text{with} \quad N_{k,ij}^S(\dot{\gamma}_{k,i}) = F_h(x_{k,ij}^S(\dot{\gamma}_{k,i})) \tag{C.5}$$

where $k = a, r$ and

$$x_{k,ij}^S(\dot{\gamma}_{k,i}) = (N - 1)\frac{\log \dot{\gamma}_{k,i} - \log \dot{\gamma}_{\min}}{\log \dot{\gamma}_{\max} - \log \dot{\gamma}_{\min}} - j + 1 \tag{C.6}$$

Using eq. (C.5) we can rewrite eq. (C.1) as:

$$(X_i L_a \sum_j N_{a,ij}^S H_j^S - L_r \sum_j N_{r,ij}^S H_j^S) = 0. \tag{C.7}$$

This is a linear, homogeneous equation system with N equations, which can be written with the vector $\mathbf{H} = (H_1^S, ..., H_N^S)^T$ as:

$$\mathbf{M}^S \cdot \mathbf{H} = 0, \tag{C.8}$$

where

$$M_{i,j}^S = X_i L_a G_S N_{a,ij}^S - L_r G_S N_{r,ij}^S, \quad i, j = 1, ..., N \tag{C.9}$$

Eq. C.8 does not define a unique solution for the viscosity, and any multiple $\mathbf{H}' = a\mathbf{H}$ of a solution $\mathbf{H}$ is a solution too. To obtain absolute values of the viscosity, one value of $\eta(\dot{\gamma})$ on the interval has to be known. However, the local powerlaw exponents which can be obtained by differentiating the numerical solution given by $\mathbf{H}$ are uniquely defined.

C.3 Pressure Drop in Hyperbolical Constrictions

Pressure Drop in Semihyperbolic Cylindrical Constriction

Adapting Cogswells model for power-law fluids fulfilling eqs. (3.32) in a conical constriction[21, 33] we will calculate P_S^{ent} and P_E^{ent} for the semi-hyperbolic constrictions used in this work.

Shear Flow Contribution P_S^{ent}

For the shear contribution to the pressure drop, we determine P_S^{ent} for a small segment of length $\mathrm{d}z$ of a circular channel constriction with a local radius $R(z)$ first and then integrate along z over the entire constriction. For $\mathrm{d}P_S^{ent}$ it is

assumed that the flow profile $\mathbf{u}(r, z)$ at the position z with the channel radius $R(z)$ can be approximated locally by the flow profile of fully developed flow in a straight tube of radius R [33]. Then, $\mathrm{d}P_S^{ent}$ can be calculated by solving eq. (A.78) for ΔP and setting $\Delta p \to \mathrm{d}P_S^{ent}$ and $L \to \mathrm{d}z$:

$$\mathrm{d}P_S^{ent} = \frac{2A}{R^{3n+1}} \left(\frac{3n+1}{n\pi} \right)^n Q^n \mathrm{d}z \tag{C.10}$$

With

$$R(z) = \sqrt{\frac{a}{\pi z}} \tag{C.11}$$

and thus $\mathrm{d}z = -2a/(\pi R^3)\mathrm{d}R$ we can calculate the contribution of the shear resistance to the pressure drop as

$$
\begin{aligned}
P_S^{ent} &= -\frac{4AaQ^n}{\pi} \left(\frac{3n+1}{n\pi} \right)^n \int_{R_{\text{out}}}^{R_{\text{in}}} \frac{\mathrm{d}R}{R^{3n+4}} \\
&= \frac{4}{(3n+3)\pi} \left(\frac{3n+1}{n\pi} \right)^n \frac{AaQ^n}{R_{\text{in}}^{3n+3}} \left[1 - \left(\frac{R_{\text{in}}}{R_{\text{out}}} \right)^{3n+3} \right]
\end{aligned}
\tag{C.12}
$$

where R_{out} and R_{in} are the outer and inner radius of the hyperbolic die. From eq. (C.12) it becomes clear, that the shear resistance is mainly determined by the resistance of the die at the smallest diameter and the dominating shearrate will be the wall shearrate $\dot{\gamma}_{in}$ at $R = R_{\text{in}}$ which is obtained for a power-law fluid by the Rabinowitsch relation (eq. A.78) as $\dot{\gamma}_{in} = \frac{Q}{R_{\text{in}}^3} \frac{3n+1}{\pi n}$. Thus we can relate P_S^{ent} to the viscosity $\eta(\dot{\gamma}_{in})$ at the dominating wall shear rate $\dot{\gamma}_{in}$ as:

$$P_S^{ent} = \eta(\dot{\gamma}_{in}) \frac{4}{n\pi^2} \frac{3n+1}{3n+3} \frac{aQ}{R_{\text{in}}^6} \left[1 - \left(\frac{R_{\text{in}}}{R_{\text{out}}} \right)^{3n+3} \right]. \tag{C.13}$$

Extensional Flow Contribution P_E^{ent}

The extensional contribution to the pressure drop $\mathrm{d}P_E^{ent}$ is calculated by approximating the flow field as an uniaxial extensional flow $\mathbf{u}(r, z) \approx (-\frac{1}{2}\dot{\epsilon}(z)x, -\frac{1}{2}\dot{\epsilon}(z)y, \dot{\epsilon}(z)z)$. The local average extension rate $\bar{\dot{\epsilon}}(z)$ is approximated by differentiating the flow velocity averaged over the cross section of the channel $\bar{u}_z(z) = Q/(\pi R^2)$ with respect to the flow direction, which yields a constant extension rate along the die in the semihyperbolic constriction with $R(z) = \sqrt{\frac{a}{\pi z}}$:

$$\bar{\dot{\epsilon}}(z) = \frac{\partial \bar{u}}{\partial z} = \frac{\partial}{\partial z} \frac{Q}{\pi R^2} = \frac{\partial}{\partial z} \frac{Qz}{a} = \frac{Q}{a}. \tag{C.14}$$

The differential contribution $\mathrm{d}P_E^{ent}$ of the extensional energy dissipation to the pressure drop in a short segment is given by[33]:

$$\mathrm{d}P_E^{ent} = \sigma \mathrm{d}\epsilon = \Lambda(\bar{\dot{\epsilon}}) \bar{\dot{\epsilon}} \mathrm{d}\epsilon = B \bar{\dot{\epsilon}}^k \mathrm{d}\epsilon \tag{C.15}$$

where ϵ is the extensional Hencky strain. Volume conservation requires that a cylindrical fluid slice at the entrance of the die with radius R_{out} and length $\mathrm{d}z$ gets stretched to a length $\lambda \mathrm{d}z = (R_{\text{out}}/R_{\text{in}})^2 \mathrm{d}z$ at the orifice of the die, so that the total Hencky strain of the die is $\epsilon = 2\ln(R_{\text{out}}/R_{\text{in}})$. As the extension rate $\bar{\dot{\epsilon}}$ is constant along the constriction, the total pressure drop P_E^{ent} is yielded by integration of eq. (C.15) as

$$P_E^{ent} = \Lambda(\bar{\dot{\epsilon}})\bar{\dot{\epsilon}}\epsilon = 2\Lambda(\bar{\dot{\epsilon}})\frac{Q}{a}\ln(R_{\text{out}}/R_{\text{in}}). \tag{C.16}$$

For a power-law fluid the solution reads:

$$P_E^{ent} = 2B\left(\frac{Q}{a}\right)^k \ln(R_{\text{out}}/R_{\text{in}}). \tag{C.17}$$

For a Newtonian fluid in a semi-hyperbolic cylindrical die ($n = k = 1, A = B/3 = \eta$), the ratio of the extensional hydrodynamic resistance R_E and the shear resistance R_S for a flow Q in the converging die is:

$$\frac{R_E^{ent}}{R_S^{ent}} = \frac{P_E^{ent}}{P_S^{ent}} = \frac{9\pi^2}{4}\frac{R_{\text{in}}^6}{a^2}\ln(R_{\text{out}}/R_{\text{in}}) \tag{C.18}$$

where $(R_{\text{in}}/R_{\text{out}})^6 \ll 1$ was used. If the constriction entrance becomes too steep, the fluid streamlines will not follow the semi-hyperbolic geometry of the wall. Therefore, we choose an upper limit for the absolute value of the slope of $R(z)$ for the geometries used in the differential viscometers as $|\mathrm{d}R(z)/\mathrm{d}z|_{R_{\text{out}}} \leq 2$. With $R_{\text{out}} = 4R_{\text{in}}$ this condition corresponds to $\frac{R_{\text{in}}^3}{a} \leq \frac{1}{4^2\pi}$, so that for Newtonian fluids the extensional resistance of the constriction can be neglected:

$$\frac{R_E^{ent}}{R_S^{ent}}(R_{\text{out}} = 4R_{\text{in}}) = \frac{9}{2^9}\ln 2 \approx 0.012 \tag{C.19}$$

Pressure Drop in Hyperbolical Rectangular Constriction

Shear Flow Contribution P_S^{ent}

Analogously to the semi-hyperbolical die we can calculate the shear contribution of the pressure drop across the die P_S^{ent} by calculating the shear resistance of a thin rectangular channel segment with width w and length $\mathrm{d}x$ and integrating from the wide end w_{out} to the thin end w_{in}.

The pressure drop for a small straight channel segment of length $\mathrm{d}x$ for a Newtonian fluid is given by eq. (A.82) as:

$$\mathrm{d}P_S = \frac{12\eta Q}{h^3 w}\frac{\mathrm{d}z}{1 - 0.630\frac{h}{w}} \tag{C.20}$$

With $\mathrm{d}z = -a/(hw^2)\mathrm{d}w$ we can integrate and evaluate the pressure drop across the narrowing die:

$$
\begin{aligned}
P_S^{ent} &= \int_{w_{\text{out}}}^{w_{\text{in}}} dP_S^{ent} = -\int_{w_{\text{out}}}^{w_{\text{in}}} \frac{12\eta aQ}{h^4} \frac{dw}{w^2(w - 0.63h)} \\
&= -\frac{12\eta aQ}{0.63h^5} \left[\frac{1}{w} + \frac{1}{0.63h} \ln(1 - 0.63h/w) \right]_{w_{\text{out}}}^{w_{\text{in}}} \\
&= \frac{6\eta aQ}{h^4 w^2} \left[1 + \frac{2}{3}(0.63\frac{h}{w}) + \frac{1}{2}(0.63\frac{h}{w})^2 + \frac{2}{5}(0.63\frac{h}{w})^3 + ... \right]_{w_{\text{out}}}^{w_{\text{in}}} \\
&\overset{w_{\text{out}} \gg w_{\text{in}}}{\approx} \frac{6\eta aQ}{h^4 w_{\text{in}}^2} \left[1 + \frac{2}{3}(0.63\frac{h}{w_{\text{in}}}) + \frac{1}{2}(0.63\frac{h}{w_{\text{in}}})^2 + \frac{2}{5}(0.63\frac{h}{w_{\text{in}}})^3 + ... \right]
\end{aligned}
$$

$$(C.21)$$

For a power-law fluid, we use eq. (A.84) and get:

$$
dP_S^{ent} = -\frac{AQ^n dz}{(\lambda(n))^n \tilde{h}^{3n+1}} = \frac{AaQ^n dw}{(\lambda(n))^n (hw)^{\frac{3}{2}(n+1)} w} \tag{C.22}
$$

As the shape factor $\lambda(n)$ depends on the aspect ratio of the rectangular channel, which changes along the convergence, a direct integration of eq. (C.22) is not possible and P_S^{ent} has to be determined numerically, yielding a shape factor $f'_{hyp}(n)$ depending on the power-law index n of the fluid and the geometric measures $w_{\text{in}}, w_{\text{out}}, h$ of the constriction:

$$
P_S^{ent} = AaQ^n \int_{w_{\text{out}}}^{w_{\text{in}}} \frac{dw}{(\lambda(n))^n (hw)^{3(n+1)/2} w} = \frac{AaQ^n}{\tilde{h}_{\text{in}}^{3(n+1)} f'_{hyp}(n)} \tag{C.23}
$$

where $\tilde{h}_{\text{in}} = \sqrt{D_{\text{in}}} = \sqrt{hw_{\text{in}}}$ is the average diameter at the tight end of the die. Using eq. (3.20) for the shearrate $\dot{\gamma}_{in}$ at $w = w_{\text{in}}$ and $\eta(\dot{\gamma}_{in}) = A\dot{\gamma}_{in}^{n-1}$ we can rewrite eq. (C.23) as

$$
P_S^{ent} = \eta(\dot{\gamma}_{in}) \frac{aQ}{F_{\dot{\gamma}_{in}}(n)^{n-1} f'_{hyp}(n) D_{\text{in}}^3} = \eta(\dot{\gamma}_{in}) \frac{aQ}{D_{\text{in}}^3 f_{hyp}(n)} \tag{C.24}
$$

where $f_{hyp}(n)$ is defined as $f_{hyp}(n) \equiv F_{\dot{\gamma}_{in}}(n)^{n-1} f'_{hyp}(n)$.

Extensional Flow Contribution P_E^{ent}

The total extensional strain for a die narowing from w_{out} to w_{in} is given by $\epsilon = \ln(w_{\text{out}}/w_{\text{in}})$ and integration of $dP_E^{ent} = \sigma d\epsilon = \Lambda_p(\bar{\dot{\epsilon}})\dot{\epsilon} d\epsilon$ yields the extensional pressure drop for a power-law fluid as

$$
P_E^{ent} = \Lambda_p(\bar{\dot{\epsilon}})\bar{\dot{\epsilon}}\epsilon = \Lambda_p(\bar{\dot{\epsilon}}) \frac{Q}{a} \ln \frac{w_{\text{out}}}{w_{\text{in}}} = B \left(\frac{Q}{a} \right)^k \ln \frac{w_{\text{out}}}{w_{\text{in}}} \tag{C.25}
$$

and is thus analogous to the cylindrical case described by eq. (C.17). For a Newtonian fluid with $n = k = 1$ and $B = 4A = 4\eta$ the ratio of the extensional

and shear resistance in the die is given by

$$\frac{P_E^{ent}}{P_S^{ent}} = \frac{2h^4 w_{\text{in}}^2 \ln \frac{w_{\text{out}}}{w_{\text{in}}}}{3a^2 \left[1 + \frac{2}{3}(0.63\frac{h}{w_{\text{in}}}) + \frac{1}{2}(0.63\frac{h}{w_{\text{in}}})^2 + ...\right]} \tag{C.26}$$

With the same constraint for the steepness of the die at the beginning of the constriction as in the cylindrical case $\left(\left|\frac{\mathrm{d}w(z)}{\mathrm{d}z}\right|_{w_{\text{out}}} < 2\right)$ it follows for a $w_{\text{out}}/w_{\text{in}} = 10 : 1$ constriction

$$\frac{P_E^{ent}}{P_S^{ent}} < 6 \cdot 10^{-2} \frac{h^2}{w_{\text{in}}^2}, \tag{C.27}$$

so that for a Newtonian fluid the contribution of the extensional viscosity can be neglected. The total shear resistance of a narrowing and expanding constriction composed of two identical dies in series is given by twice the shear resistance of a single die: $R_S = R_S^{ent} + R_S^{ex} = 2R_S^{ent}$. In the rectangular hyperbolic geometry, the fluid in the expanding die undergoes a planar extension with the same extension rate and total extensional strain as in the narrowing die, only the direction of extension is now perpendicular to the channel axis instead of parallel. Thus, in a first approximation the pressure contribution from the expanding die can be estimated to be approximately equal to the pressure drop in the narrowing die ($R_E = R_E^{ent} + R_E^{ex} \approx 2R_E^{ent}$), although due to mixed flow and flow history effects the pressure drop in the expanding die is expected to be smaller (see discussion in section 5.4.6).

Pressure Drop in Hyperbolical Dies of Arbitrary Cross Section

Generalizing the above approach, the extensional viscosity can be determined from any constriction with a cross sectional area D that varies from D_{out} to D_{in} along the flow direction as $D(z) = \frac{a}{z}$. This generates an average extension rate $\bar{\dot{\epsilon}} = \frac{Q}{a}$ that is constant along the narrowing die. The shear resistance of a power-law fluid flowing through the constriction can be expressed as (comp. eq. (C.13,C.24))

$$R_S^{ent} = \frac{P_S^{ent}}{Q} = \eta(\dot{\gamma}_{in}) \frac{a}{D_{\text{in}}^3 f_{hyp}(n)}, \tag{C.28}$$

where the shape factor $f_{hyp}(n)$ depends on the geometry of the cross section and the power-law index n. The extensional resistance for flow through the narrowing die is given by (comp. eq. (C.16, C.25))

$$R_E^{ent} = \frac{P_E^{ent}}{Q} = \frac{\Lambda(\bar{\dot{\epsilon}})}{a} \ln \frac{D_{\text{out}}}{D_{\text{in}}}. \tag{C.29}$$

C.4   Calculation of Flowrate Ratio X in Differential Extensional Viscometer

The total shear resistance of the straight connecting channel sections R_{Sc} in the reference or analyzer channel is given by eq. (3.22) , the shear resistance of the constrictions is determined by eq. (C.28) . Thus, the total shear resistances of analyzer and reference channel are given as:

$$R_{Sa} = R_{Sc,a} + N_a R_{S,a}^{hyp} = \frac{\eta(\dot{\gamma}_{w,a}) L_a}{D_{\text{out}}^2 F^\star(n)} + \frac{2\eta(\dot{\gamma}_{in,a}) N_a a_a}{D_{\text{in}}^3 f_{hyp}(n)} \tag{C.30}$$

$$R_{Sr} = R_{Sc,r} + N_r R_{S,r}^{hyp} = \frac{\eta(\dot{\gamma}_{w,r}) L_r}{D_{\text{out}}^2 F^\star(n)} + \frac{2\eta(\dot{\gamma}_{in,r}) N_r a_r}{D_{\text{in}}^3 f_{hyp}(n)}$$

$$= \frac{\eta(\dot{\gamma}_{w,r}) L_a}{D_{\text{out}}^2 F^\star(n)} \frac{L_r}{L_a} + \frac{2\eta(\dot{\gamma}_{in,r}) N_a a_a}{D_{\text{in}}^3 f_{hyp}(n)} \frac{L_r}{L_a}$$

where $\dot{\gamma}_{w,a}, \dot{\gamma}_{w,r}$ are obtained from eq. (3.20) and $\dot{\gamma}_{in,a}, \dot{\gamma}_{in,r}$ from eq. (5.17) as

$$\dot{\gamma}_{w,a} = \frac{Q_a}{\tilde{h}_{\text{out}}^3} \cdot F_{\dot{\gamma}}(n) \qquad\qquad \dot{\gamma}_{w,r} = \frac{Q_r}{\tilde{h}_{\text{out}}^3} \cdot F_{\dot{\gamma}}(n)$$

$$\dot{\gamma}_{in,a} = \frac{Q_a}{\tilde{h}_{\text{in}}^3} \cdot F_{\dot{\gamma}}^{hyp}(n) \qquad\qquad \dot{\gamma}_{in,r} = \frac{Q_r}{\tilde{h}_{\text{in}}^3} \cdot F_{\dot{\gamma}}^{hyp}(n) \tag{C.31}$$

Using the local power-law description of eq. (3.33) and defining the local shear-rate

$$\dot{\gamma}_0 \equiv \sqrt{\dot{\gamma}_{in,a} \dot{\gamma}_{in,r}} = \frac{\sqrt{Q_a Q_r}}{\tilde{h}_{\text{in}}^3} F_{\dot{\gamma}}^{hyp}(n) \tag{C.32}$$

we get

$$R_{Sa} = \sqrt{\frac{Q_a}{Q_r}}^{n-1} \sqrt{\frac{L_a}{L_r}} \cdot R_{S0}, \qquad R_{Sr} = \sqrt{\frac{Q_r}{Q_a}}^{n-1} \sqrt{\frac{L_r}{L_a}} \cdot R_{S0} \tag{C.33}$$

where R_{S0} is defined as

$$R_{S0} \equiv \sqrt{R_{Sa} R_{Sr}} = \frac{\eta_0 \sqrt{L_a L_r}}{D_{\text{in}}^2} \left[\left(\frac{F_{\dot{\gamma}}(n)}{F_{\dot{\gamma}}^{hyp}(n)} \right)^{n-1} \sqrt{\frac{D_{\text{in}}}{D_{\text{out}}}}^{-3n+1} \frac{1}{F^\star(n)} + \frac{2 N_a a_a}{f_{hyp}(n) D_{\text{in}} L_a} \right] \tag{C.34}$$

and R_{S0} depends on the power-law index n and the chosen geometry.

The extensional resistance in analyzer and reference channel can be determined with eqs. (C.29, 5.18) as

$$R_{Ea} = \Lambda(\bar{\dot{\epsilon}}_a) \frac{N_a b}{a_a} \ln \frac{D_{\text{out}}}{D_{\text{in}}}$$

$$R_{Er} = \Lambda(\bar{\dot{\epsilon}}_r) \frac{N_r b}{a_r} \ln \frac{D_{\text{out}}}{D_{\text{in}}} \tag{C.35}$$

The extension rates $\bar{\dot{\epsilon}}_a, \bar{\dot{\epsilon}}_r$ are obtained from eq. (5.17). Defining an average extension rate

$$\bar{\dot{\epsilon}}_0 \equiv \sqrt{\bar{\dot{\epsilon}}_a \bar{\dot{\epsilon}}_r} = \sqrt{\frac{Q_a Q_r}{a_a a_r}} F_{\dot{\epsilon}} \tag{C.36}$$

and using eq. (3.33), we can rewrite eq. (C.35) as

$$R_{Ea} = \Lambda_0 \sqrt{\frac{Q_a}{Q_r} \frac{a_r}{a_a}}^{k-1} \frac{N_a b}{a_a} \ln \frac{D_{\text{out}}}{D_{\text{in}}} = \sqrt{\frac{Q_a}{Q_r}}^{k-1} \sqrt{\frac{a_r}{a_a}}^{k+1} \sqrt{\frac{L_a}{L_r}} R_{E0}$$

$$R_{Er} = \Lambda_0 \sqrt{\frac{Q_r}{Q_a} \frac{a_a}{a_r}}^{k-1} \frac{N_r b}{a_r} \ln \frac{D_{\text{out}}}{D_{\text{in}}} = \sqrt{\frac{Q_r}{Q_a}}^{k-1} \sqrt{\frac{a_a}{a_r}}^{k+1} \sqrt{\frac{L_r}{L_a}} R_{E0} \tag{C.37}$$

where R_{E0} is defined as

$$R_{E0} = \sqrt{R_{Ea} R_{Er}} = \Lambda_0 \frac{N_a b}{a_r} \sqrt{\frac{L_r}{L_a}} \ln \frac{D_{\text{out}}}{D_{\text{in}}} \tag{C.38}$$

Thus, the total resistances of the analyzer and reference channel are

$$R_a = R_{Sa} + R_{Ea} \quad = \sqrt{\frac{Q_a}{Q_r}}^{n-1} \sqrt{\frac{L_a}{L_r}} \cdot R_{S0} + \sqrt{\frac{Q_a}{Q_r}}^{k-1} \sqrt{\frac{a_r}{a_a}}^{k+1} \sqrt{\frac{L_a}{L_r}} R_{E0}$$

$$R_r = R_{Sr} + R_{Er} \quad = \sqrt{\frac{Q_r}{Q_a}}^{n-1} \sqrt{\frac{L_r}{L_a}} \cdot R_{S0} + \sqrt{\frac{Q_r}{Q_a}}^{k-1} \sqrt{\frac{a_a}{a_r}}^{k+1} \sqrt{\frac{L_r}{L_a}} R_{E0}. \tag{C.39}$$

Calculating the ratio of the hydrodynamic resistances R_r/R_a and using $X = Q_a/Q_r$ yields an equation defining the resulting flowrate ratio X:

$$X = \frac{L_r}{L_a} \frac{\sqrt{X}^{1-n} + \sqrt{X}^{1-k} \sqrt{\frac{a_a}{a_r}}^{k+1} \frac{R_{E0}}{R_{S0}}}{\sqrt{X}^{n-1} + \sqrt{X}^{k-1} \sqrt{\frac{a_r}{a_a}}^{k+1} \frac{R_{E0}}{R_{S0}}} \tag{C.40}$$

C.5 Determination of Extensional Viscosity from Flowrate Measurements $X(Q)$

Based on eq. C.40 different methods to extract the power-law exponent of the extensional viscosity k and the ratio of extensional and shear resistance R_{E0}/R_{S0} have been derived and tested in the evaluation of the experimental data. For simplicity, the evaluation methods will be discussed for the case of a known viscosity exponent n and a known shear viscosity $\eta(\dot{\gamma})$ In this case, $\Lambda(\dot{\epsilon})$ can be directly calculated once R_{E0}/R_{S0} is determined from the measured $X(Q)$ values.

Semi-Analytical Determination of Extensional Viscosity

For a semi-analytical solution with known n eq. (C.40) is solved for R_{E0}/R_{S0}:

$$\frac{R_{E0}}{R_{S0}} = \frac{\frac{L_r}{L_a}\sqrt{X}^{-n} - \sqrt{X}^n}{\sqrt{X}^k\sqrt{\frac{a_r}{a_a}}^{k+1} - \frac{L_r}{L_a}\sqrt{X}^{-k}\sqrt{\frac{a_a}{a_r}}^{k+1}} \qquad (C.41)$$

With assuming a local power-law description of $\Lambda(\dot{\epsilon})$ and $\eta(\dot{\gamma})$ we can calculate $\frac{R_{E0}}{R_{S0}}$ for two different measurement points $X_1(Q_1), X_2(Q_2)$ and get:

$$\frac{R_{E0}(Q_2)}{R_{S0}(Q_2)} = \frac{R_{E0}(Q_1)}{R_{S0}(Q_1)} \cdot \left(\sqrt{\frac{X_2}{X_1}} \frac{(X_1 + 1)}{(X_2 + 1)} \frac{Q_2}{Q_1} \right)^{k-n} \qquad (C.42)$$

Replacing $\frac{R_{E0}(Q_1)}{R_{S0}(Q_1)}, \frac{R_{E0}(Q_2)}{R_{S0}(Q_2)}$ with eq. (C.41) for $X_1(Q_1), X_2(Q_2)$, k can be numerically determined from eq. (C.42), yielding $\frac{R_{E0}(Q_1)}{R_{S0}(Q_1)}$ with the determined k afterwards.

Alternatively, two viscometers with different geometry constants $(a_r, a_a)_X$, $(a_r, a_a)_Y$ can be used in series yielding $X(Q)$ and $Y(Q)$.

As the powerlaw assumption is only valid locally, the accuracy of this method can be improved by forming the limit $Q_2 \to Q_1$ and using the first derivative $\mathrm{d}X/\mathrm{d}Q$ and $X(Q)$ instead of the two values X_1, X_2 to determine k and $\frac{R_{E0(Q_1)}}{R_{S0(Q_1)}}$ and thus $\Lambda(\dot{\epsilon})$.

C.6   Smoothing Function for Flowrate Measurement Data $X(Q)$

As eq. (C.40) is only valid in the power-law regime, it is mandatory for an evaluation of the measurement points $X_i(Q_i)$ that the shear and extension rates involved in R_{E0i}, R_{S0i} for the different flowrates Q_i fall within an interval in which the local power-law description is fairly accurate. Then, the same n, k are valid for at least $2X_i(Q_i)$ values which can be simultaneously evaluated to eliminate the two unknowns $k, R_{E0}/R_{ES0}$. With the viscosity curves $\eta(\dot{\gamma}), \Lambda(\dot{\epsilon})$ of a complex fluid to be analyzed being a priori unknown, the validity of the power-law approach on the rate intervals $[\dot{\gamma}_{min,i-1}, \dot{\gamma}_{max,i}], [\dot{\epsilon}_{min,i-1}, \dot{\epsilon}_{max,i}]$ resulting from the chosen measurement interval $[Q_{i-1}, Q_i]$ is unclear.

Thus, the smaller the measurement interval $[Q_{i-1}, Q_i]$ can be chosen, the more accurate the power-law assumption will be. Contrary, the difference $X_i - X_{i-1}$ between adjacent measurement points gets small for a small interval $[Q_{i-1}, Q_i]$, so that the uncertainty due to the experimental error ΔX rises with a decreasing measurement interval. This problem can be adressed by fitting a smoothing function to the measured values $X_i(Q_i)$:

As the slope of the viscosity curves $\eta(\dot{\gamma}), \Lambda(\dot{\epsilon})$ is subject to physical limitations, the slope of the $X(Q)$ curves is also limited. Generally, the power-law index of the shear viscosity n is positive and the shear stress σ increases with the

shearrate. However, in special fluids (e.g. wormlike micellar solutions) a power-law index $n \approx 0$ can occur [23]. In this case, the fluid in a viscometric flow geometry splits into subdomains with different shearrates (*shear banding*) leading to a plateau in the apparent shear stress function $\sigma(\dot{\gamma})$, so that the apparent power-law index n stays positive and approaches zero at the utmost. Analogous considerations suggest $k \geq 0$. Thus, the shear stress and the extensional stress rise monotonically with the flow rate, so that the pressure drop $p(Q)$ across K_a and K_r has to increase with rising Q: $Q_2 > Q_1 \rightarrow p_2 \geq p_1$. Consequently, $Q_{r,2} \geq Q_{r,1}$ and $Q_{a,2} \geq Q_{a,1}$. With $Q_a = 1/(X+1)Q, Q_r = X/(X+1)Q$ this leads to the inequations

$$\frac{X_1}{X_1\left(\frac{Q_2}{Q_1}-1\right)+\frac{Q_2}{Q_1}} \leq X_2 \leq X_1\frac{Q_2}{Q_1}+\left(\frac{Q_2}{Q_1}-1\right) \tag{C.43}$$

which gives a lower and upper limit for the slope of $X(Q)$:

$$-\frac{X(X+1)}{Q} \leq \frac{\mathrm{d}X}{\mathrm{d}Q} \leq \frac{X+1}{Q}. \tag{C.44}$$

Therefore, the measurement points $X_i(Q)$ can be fitted with a smoothing function $\tilde{X}(Q)$ that fulfills eq (C.44) without losing any information, and $\tilde{X}(Q)$ can be used to evaluate eq. (C.40).

C.7   Numerical Evaluation of Differential Extensional Viscometer Data

Due to the threshold-type behaviour of the extensional viscosity especially of dilute polymer solutions the power-law description of the extensional viscosity may be a poor approximation in the vicinity of the onset of the rise in $\Lambda(\dot{\epsilon})$. To circumvent this problem, a similar numerical method to evaluate $X(Q)$ as introduced above for the differential shear viscometer has been developed[2], which does not require a powerlaw description of the viscosity functions $\eta(\dot{\gamma}), \Lambda(\dot{\epsilon})$.

Starting from equation (C.30), the total shear resistance in the reference and analyzer channel is given as a function of the shear viscosity η by:

$$R_{Sa}(\eta(\dot{\gamma}_a)) = \frac{2\eta(\dot{\gamma}_{in,a})N_a a_a}{D_{\mathrm{in}}^3 f_{hyp}(n)} = \eta(\dot{\gamma}_a)\sqrt{\frac{L_a}{L_r}}G_S \tag{C.45}$$

$$R_{Sr}(\eta(\dot{\gamma}_r)) = \frac{2\eta(\dot{\gamma}_{in,r})N_a a_a}{D_{\mathrm{in}}^3 f_{hyp}(n)}\frac{L_r}{L_a} = \eta(\dot{\gamma}_r)\sqrt{\frac{L_r}{L_a}}G_S$$

where we set $\dot{\gamma}_{in,a} \equiv \dot{\gamma}_a$, $\dot{\gamma}_{in,r} \equiv \dot{\gamma}_r$, introduced the geometry factor

$$G_S = \frac{2N_a a_a}{D_{\mathrm{in}}^3 f_{hyp}(n)}\sqrt{\frac{L_r}{L_a}}, \quad [G_S] = \mathrm{m}^{-3} \tag{C.46}$$

---

[2] development has been assisted by Christian Cyron, TUM, Institute for Computational Mechanics

and assumed for simplicity, that the shear resistance in the straight connecting channels is negligible:

$$\frac{L_{a,r}}{D_{\text{out}}^2 F^\star(n)} \ll \frac{2 N_{a,r} a_{a,r}}{D_{\text{in}}^3 f_{hyp}(n)}. \tag{C.47}$$

(A non-negligible contribution of the connecting channels can be accounted for analogously.) The dependence of the extensional flow resistance of the channels on the extensional viscosity Λ is given by eq. (C.37) as

$$R_{Ea}(\Lambda(\dot{\epsilon}_a)) = \Lambda(\dot{\epsilon}_a)\sqrt{\frac{L_a}{L_r}}\frac{a_r}{a_a}G_E$$

$$R_{Er}(\Lambda(\dot{\epsilon}_r)) = \Lambda(\dot{\epsilon}_r)\sqrt{\frac{L_r}{L_a}}\frac{a_a}{a_r}G_E \tag{C.48}$$

where we ommitted the bar $\bar{\dot{\epsilon}} \equiv \dot{\epsilon}$ for simplicity and introduced a geometry factor for the extensional resistance

$$G_E = \sqrt{\frac{N_a N_r}{a_a a_r}}b \ln \frac{D_{\text{in}}}{D_{\text{out}}}, \quad [G_E] = \text{m}^{-3}. \tag{C.49}$$

Then, each measurement point $X_i(Q_i)$ corresponds to four unknown viscosity values
$\eta(\dot{\gamma}_{a,i}), \eta(\dot{\gamma}_{r,i}), \Lambda(\dot{\epsilon}_{a,i}), \Lambda(\dot{\epsilon}_{r,i})$:

$$X_i(Q_i) = \frac{R_{Sr}(\eta(\dot{\gamma}_{r,i})) + R_{Er}(\Lambda(\dot{\epsilon}_{r,i}))}{R_{Sa}(\eta(\dot{\gamma}_{a,i})) + R_{Ea}(\Lambda(\dot{\epsilon}_{a,i}))} = \frac{L_r}{L_a} \cdot \frac{\eta(\dot{\gamma}_{r,i})G_S + \Lambda(\dot{\epsilon}_{r,i})\frac{a_a}{a_r}G_E}{\eta(\dot{\gamma}_{a,i})G_S + \Lambda(\dot{\epsilon}_{a,i})\frac{a_r}{a_a}G_E} \tag{C.50}$$

where the shear- and flowrates are given by Q_i via eq. (C.31). The main principle of the numerical method is illustrated in fig. 5.19: The function $X(Q)$ is determined by taking N measurement points $X_1(Q_1)...X_N(Q_N)$ on an interval of flowrates $[Q_1, Q_n]$. These measurement points correspond to $2N$ unknown values of the shear viscosity function $\eta(\dot{\gamma})$ and $2N$ unknown values of the extensional viscosity function $\Lambda(\dot{\epsilon})$ which lie on the intervals $[\dot{\gamma}_{\min}, \dot{\gamma}_{\max}]$ and $[\dot{\epsilon}_{\min}, \dot{\epsilon}_{\max}]$.

As the roughness of the viscosity functions η and Λ is limited by $n, k \geq 0$ (see sec. 5.4.2), the functions $\eta(\dot{\gamma}), \Lambda(\dot{\epsilon})$ can be approximated by interpolation between a sufficient number of basic values. To this purpose, $N/2$ interpolation points Γ_j, E_j are distributed among the two intervals $[\dot{\gamma}_{\min}, \dot{\gamma}_{\max}]$ and $[\dot{\epsilon}_{\min}, \dot{\epsilon}_{\max}]$,

$$\Gamma_j = \dot{\gamma}_{\min} \cdot \left(\frac{\dot{\gamma}_{\max}}{\dot{\gamma}_{\min}}\right)^{j/(N/2-1)}$$

$$\mathrm{E}_j = \dot{\epsilon}_{\min} \cdot \left(\frac{\dot{\epsilon}_{\max}}{\dot{\epsilon}_{\min}}\right)^{j/(N/2-1)} \qquad j = 0, ..., N/2 - 1 \tag{C.51}$$

where the according interpolation values are set:

$$H_j^S \equiv \eta(\Gamma_j)$$
$$H_j^E \equiv \Lambda(\mathrm{E}_j) \tag{C.52}$$

The $4N$ unknown values $\eta(\dot\gamma_{a,i}), \eta(\dot\gamma_{r,i}), \Lambda(\dot\epsilon_{a,i}), \Lambda(\dot\epsilon_{r,i})$ can thus be expressed by the N unknown interpolation values H_j^S, H_j^E using the interpolation hat function from eq. C.4 as:

$$\eta(\dot\gamma_{k,i}) = \sum_j N_{k,ij}^S(\dot\gamma_{k,i}) H_j^S, \qquad \text{with} \quad N_{k,ij}^S(\dot\gamma_{k,i}) = F_h(x_{k,ij}^S(\dot\gamma_{k,i}))$$

$$\Lambda(\dot\epsilon_{k,i}) = \sum_j N_{ki,j}^E(\dot\epsilon_{k,i}) H_j^S, \qquad \text{with} \quad N_{k,ij}^E(\dot\epsilon_{k,i}) = F_h(x_{k,ij}^E(\dot\epsilon_{k,i})), \tag{C.53}$$

where $k = a, r$ and

$$x_{k,ij}^S(\dot\gamma_{k,i}) = (N/2 - 1)\frac{\log \dot\gamma_{k,i} - \log \dot\gamma_{\min}}{\log \dot\gamma_{\max} - \log \dot\gamma_{\min}} - j + 1$$

$$x_{k,ij}^E(\dot\epsilon_{k,i}) = (N/2 - 1)\frac{\log \dot\epsilon_{k,i} - \log \dot\epsilon_{\min}}{\log \dot\epsilon_{\max} - \log \dot\epsilon_{\min}} - j + 1. \tag{C.54}$$

Using eq. (C.53) we can rewrite eq. (C.50) as:

$$\left(X_i L_a \sum_j N_{a,ij}^S H_j^S - L_r \sum_j N_{r,ij}^S H_j^S\right)G_S + \left(X_i L_a \frac{a_r}{a_a} \sum_j N_{a,ij}^E H_j^E - L_r \frac{a_a}{a_r} \sum_j N_{r,ij}^E H_j^E\right)G_E = 0. \tag{C.55}$$

This is a linear, homogeneous equation system with N equations, which we can write with the vector $\mathbf{H} = (H_1^S, ..., H_{N/2}^S, H_1^E, ..., H_{N/2}^E)^T$ as:

$$\mathbf{M} \cdot \mathbf{H} = 0, \quad \mathbf{M} = (\mathbf{M}^S \mathbf{M}^E) \tag{C.56}$$

where

$$M_{i,j}^S = X_i L_a G_S N_{a,ij}^S - L_r G_S N_{r,ij}^S, \qquad i = 1, ..., N \quad j = 1, ..., N/2$$

$$M_{i,j}^E = X_i L_a \frac{a_r}{a_a} G_E N_{a,ij}^E - L_r \frac{a_a}{a_r} G_E N_{r,ij}^E, \qquad i = 1, ..., N \quad j = 1, ..., N/2. \tag{C.57}$$

Note that if there is a non-trivial solution $\mathbf{H}$ to eq. (C.56), then any multiple of $\mathbf{H}$ is also a solution. This reflects the fact that the differential measurement values $X_i(Q_i)$ only depend on the ratio of $\Lambda(\dot\epsilon)/\eta(\dot\gamma)$ and not on the absolute values of Λ, η. Thus, to solve for absolute values of the extensional viscosity, more information is needed. This information could be provided by additionally measuring the pressure drop along reference or analyzer channel or by putting a known value of the shear viscosity curve $\eta(\dot\gamma_1)$ (e.g. from a shear rheometer measurement) into eq. (C.56).

However, even if $\eta(\dot\gamma)$ is known and all the values $(H_1^S, ..., H_{N/2}^S)$ are put into eq. (C.56), there may be multiple solutions for $(H_1^E, ..., H_{N/2}^E)$. This problem will be illustrated for the simple case of Newtonian shear viscosity ($n = 1$) and measures to overcome it will be adressed in the following section.

Differential Extensional Viscometer in Constant Shear-Viscosity Regime
(n = 1)

For some complex fluids, the shear viscosity is nearly constant ($n \approx 1$), while the extensional viscosity can be highly non-Newtonian if the extension rate passes a threshold rate $\dot{\epsilon} > \dot{\epsilon}_t$. A typical example for such fluids are dilute polymer solutions with very long polymers of high molecular weight. If $n = 1$, we can set $G_S\eta(\dot{\gamma}) \equiv R_S = const.$, so that eq. (C.50) simplifies to

$$X_i(Q_i) = \frac{L_r}{L_a} \cdot \frac{R_S + \Lambda(\dot{\epsilon}_{r,i})\frac{a_a}{a_r}G_E}{R_S + \Lambda(\dot{\epsilon}_{a,i})\frac{a_r}{a_a}G_E}. \tag{C.58}$$

This can be rewritten as a linear equation system for $\mathbf{H}^E = (H_1^E, ..., H_N^E)^T$:

$$\mathbf{M} \cdot \mathbf{H}^E = \mathbf{R}^S \tag{C.59}$$

with

$$M_{i,j} = X_i L_a \frac{a_r}{a_a} G_E N_{a,ij}^E - L_r \frac{a_a}{a_r} G_E N_{r,ij}^E \quad i,j = 1, ..., N \tag{C.60}$$

and

$$\mathbf{R} = (R_1, ..., R_N)^T, \quad R_i = (L_r - X_i L_a)R_S, \tag{C.61}$$

where $N_{r,ij}^E$ is defined as in eq. (C.53), only this time N interpolation values H_j^E are distributed on $[\dot{\epsilon}_{\min}, \dot{\epsilon}_{\max}]$:

$$E_j = \dot{\epsilon}_{\min} \cdot \left(\frac{\dot{\epsilon}_{\max}}{\dot{\epsilon}_{\min}}\right)^{j/(N-1)} \quad j = 0, ..., N-1. \tag{C.62}$$

Then, by setting a known value for the shear viscosity $R_S = G_s\eta$, the N measurement values X_i give a linear equation system eq. (C.59) with N equations to determine the N interpolation values H_j^E of the extensional viscosity.

However, $\mathbf{H}$ is not uniquely defined by eq. (C.59). The ratio of the extensional flowrates in reference and analyzer channel is given by

$$\dot{\epsilon}_{a,i} = \frac{a_r}{a_a}\frac{Q_{a,i}}{Q_{r,i}}\dot{\epsilon}_{r,i} = X_i\frac{a_r}{a_a}\dot{\epsilon}_{r,i} \tag{C.63}$$

Thus, if $\Lambda(\dot{\epsilon})$ is a solution to eq. (C.58), then $\Lambda^\star(\dot{\epsilon})$ with

$$\Lambda^\star(\dot{\epsilon}) = \Lambda(\dot{\epsilon}) + c\dot{\epsilon}^p, \text{with} \quad p = -\frac{\ln\frac{L_a}{L_r} + \ln\frac{a_r}{a_a}}{\ln X_i + \ln\frac{a_r}{a_a}} - 1 \tag{C.64}$$

is also a possible solution, which can be seen by putting $H_j^{E\star}$ into eq. (C.58). This problem can be solved in different ways:

- The measurement interval $[Q_{\min}, Q_{\max}]$ includes the low flowrate regime where the extensional viscosity is Newtonian. Then, the extensional viscosity can be obtained from the numerical solution $\Lambda_{\text{num}}(\dot{\epsilon})$ by substracting $c\dot{\epsilon}^p$, where p is determined from the measured $X(Q)$-curve and c is

chosen by setting the extensional viscosity $\Lambda(\dot{\epsilon})$ to the Newtonian value in the Newtonian regime where $X(Q) \approx L_r/L_a$. For the determination of $\dot{\epsilon}^p$, the exponent $p(X(Q))$ is taken as the exponent at the average extension rate $\dot{\epsilon}_0 = \sqrt{\dot{\epsilon}_a \dot{\epsilon}_r}$ associated with Q and $\dot{\epsilon}^p$ is obtained by numerical integration.

- Alternatively H_j^E can be determined by measuring two geometries with different numbers of constrictions $(N_a/N_r)_X \neq (N_a/N_r)_Y$ yielding $X_i(Q_i)$ and $Y_i(Q_i)$. Then, $[\dot{\epsilon}_{\min}, \dot{\epsilon}_{\max}]$ is determined from both measurements, and N interpolation values H_j^E are set on the interval. The two measurements $X_i(Q_i), Y_i(Q_i)$ provide a set of $2N$ linear equations for the N unknown values H_j^E, so that the equation system is overdetermined and can be numerically solved with a least square method. Because of the different geometries of the measurement sets, the multiple solution $c\dot{\epsilon}^p$ has a different exponent p for $X(Q)$ and $Y(Q)$, so that only the actual extensional viscosity $\Lambda(\dot{\epsilon})$ fulfills the $2N$ equations simultaneously and is obtained in the numerical solution.

  Like in the semi-analytical solution, the measurement on two different geometries is a useful test for the postulated additivity of the shear and extensional resistance. If the two equation sets for different geometries $X_i(Q_i), Y_i(Q_i)$ cannot be fulfilled with a common extensional viscosity function $\Lambda(\dot{\epsilon})$, the underlying additivity assumption obviously does not hold for the tested fluid.

Differential Extensional Viscometer in non-Newtonian Shear Viscosity Regime
$(n \neq 1)$

If the shear viscosity is in the non-Newtonian regime, and $\eta(\dot{\gamma})$ can be measured seperately, the extensional viscosity can be determined numerically by solving the linear equation system

$$\mathbf{M} \cdot \mathbf{H} = \mathbf{R}_S \qquad (C.65)$$

where $\mathbf{M} = \mathbf{M}^E$ is defined by eq. (C.57) with $i, j = 1...N$, $\mathbf{H} = (H_1^S, ..., H_N^S)$ is set analogous to eq. (C.52) and

$$\mathbf{R} = (R_1, ..., R_N)^T, \quad R_i = (L_r \eta(\dot{\gamma_{r,i}}) - X_i L_a \eta(\dot{\gamma_{a,i}})) G_S, \qquad (C.66)$$

are the shear viscosity resistance values set by the known shear viscosity.

C.8 Flow Classification of Cylindrical Semi-Hyperbolic Constrictions

To analyze the flow in the cylindrical constrictions we will generally discuss flow fields with cylindrical symmetry without velocity in the azimuthal direction:

$$\mathbf{u}(r, \phi, z) = \begin{pmatrix} u_r \\ u_\phi \\ u_z \end{pmatrix} = \begin{pmatrix} u_r(r, z) \\ 0 \\ u_z(r, z) \end{pmatrix}. \qquad (C.67)$$

The velocity gradient of the flow is given by [10]

$$\mathbf{A} = \begin{pmatrix} \frac{\partial u_r}{\partial r} & 0 & \frac{\partial u_r}{\partial z} \\ 0 & \frac{u_r}{r} & 0 \\ \frac{\partial u_z}{\partial r} & 0 & \frac{\partial u_z}{\partial z} \end{pmatrix} = \underbrace{\begin{pmatrix} \dot{\epsilon}_{rr} & 0 & \dot{\epsilon}_{rz} \\ 0 & -(\dot{\epsilon}_{rr} + \dot{\epsilon}_{zz}) & 0 \\ \dot{\epsilon}_{rz} & 0 & \dot{\epsilon}_{zz} \end{pmatrix}}_{\mathbf{D}} + \underbrace{\begin{pmatrix} 0 & 0 & \omega \\ 0 & 0 & 0 \\ -\omega & 0 & 0 \end{pmatrix}}_{\mathbf{S}}$$

(C.68)

where $\dot{\epsilon}_{rr} = \frac{\partial u_r}{\partial r}$, $\dot{\epsilon}_{rz} = \frac{1}{2}(\frac{\partial u_r}{\partial z} + \frac{\partial u_z}{\partial r})$, $\dot{\epsilon}_{zz} = \frac{\partial u_z}{\partial z}$ and $\omega = \frac{1}{2}(\frac{\partial u_r}{\partial z} - \frac{\partial u_z}{\partial r})$. It is obvious from $\mathbf{S}$ that the axis of the rotational flow component flow is always perpendicular to the r, z - plane and the rotational rate is given by ω. The eigenvalues of $\mathbf{A}$ are obtained as

$$\lambda_1 = \frac{u_r}{r} \tag{C.69}$$

$$\lambda_{2,3} = \frac{\dot{\epsilon}_{rr} + \dot{\epsilon}_{zz}}{2} \pm \frac{1}{2}\sqrt{(\dot{\epsilon}_{rr} - \dot{\epsilon}_{zz})^2 - 4(\omega^2 - \dot{\epsilon}_{rz}^2)} \tag{C.70}$$

$$\tag{C.71}$$

The classification given in sec. A.1 depends on the values of the components of the velocity gradient tensor $\mathbf{A}$:

- If the radial velocity $u_r = 0$, the streamlines are parallel to the z-axis and

$$I_3 = 0 \tag{C.72}$$

$$I_2 = \omega^2 + \dot{\epsilon}_{rr}\dot{\epsilon}_{zz} - \dot{\epsilon}_{rz}^2 \tag{C.73}$$

  In a homogeneous flow field $\frac{\partial u_r}{\partial r} = \frac{\partial u_r}{\partial z} = 0$, so that $\dot{\epsilon}_{rr} = 0$ and $\dot{\epsilon}_{rz} = -\omega$. Thus, $I_2 = 0$, all the streamlines are parallel in the z-direction and the flow is viscometric. In inhomogeneous flows, the flowtype then depends on the value of I_2. For $\omega^2 < \dot{\epsilon}_{rr}\dot{\epsilon}_{zz} - \dot{\epsilon}_{rz}^2$ (i.e. $I_2 < 0$) the flow is locallly strong and purely hyperbolic, for $\omega^2 = \dot{\epsilon}_{rr}\dot{\epsilon}_{zz} - \dot{\epsilon}_{rz}^2$ (i.e. $I_2 = 0$) the flow is locally marginally weak and for $\omega^2 > \dot{\epsilon}_{rr}\dot{\epsilon}_{zz} - \dot{\epsilon}_{rz}^2$ (i.e. $I_2 > 0$) the flow is locally strictly weak.

- If the radial velocity $u_r \neq 0$ and $\omega^2 = \dot{\epsilon}_{rz}^2 - \dot{\epsilon}_{rr}\dot{\epsilon}_{zz}$, then $I_3 = 0$ and $I_2 = -(\frac{u_r}{r})^2 < 0$. Consequently, the flow is strong and purely hyperbolic.

- If $u_r \neq 0$ and $\omega^2 \neq \dot{\epsilon}_{rz}^2 - \dot{\epsilon}_{rr}\dot{\epsilon}_{zz}$ the flow is strong. The type of strong flow is determined by the parameter $p = ((\dot{\epsilon}_{rr} - \dot{\epsilon}_{zz})^2 + 4\dot{\epsilon}_{rz}^2)/4\omega^2$. For $p > 1$ the flow is hyperbolic-parabolic, for $p = 1$ the flow is hyperbolic logarithmic and for $p < 1$ the flow is elliptic spiral.

As already mentioned in sec. A.1 it is not possible to distinguish between the several flow types with a single flow parameter although the axis of the rotational component is fixed. The principal axes of the coordinate system in which $\mathbf{D}$ is diagonal are given by

$$E_1 = \begin{pmatrix} 0 \\ 1 \\ 0 \end{pmatrix}, E_2 = \begin{pmatrix} 1 \\ 0 \\ \frac{\dot{\epsilon}_{rr} - \dot{\epsilon}_{zz}}{2\dot{\epsilon}_{rz}} + \sqrt{(\frac{\dot{\epsilon}_{rr} - \dot{\epsilon}_{zz}}{2\dot{\epsilon}_{rz}})^2 + 1} \end{pmatrix}, E_3 = \begin{pmatrix} 1 \\ 0 \\ \frac{\dot{\epsilon}_{rr} - \dot{\epsilon}_{zz}}{2\dot{\epsilon}_{rz}} - \sqrt{(\frac{\dot{\epsilon}_{rr} - \dot{\epsilon}_{zz}}{2\dot{\epsilon}_{rz}})^2 + 1} \end{pmatrix}$$

(C.74)

D. FLUID-STRUCTURE-INTERACTIONS

D.1 Apparent Phase Velocity $v_{ph}(\omega_n)$ of Pressure Propagation

To calculate the phase velocity of the pressure propagation we evaluate the phase difference $\Delta\Phi_{0-x_i}^{n,p}$ of the Fourier component of the pressure $p_n(\omega_n)$ between the channel entrance $x = 0$ and position $x = x_i$. From there we can determine the apparent phase velocity $v_{ph}(\omega_n)$ with which a point with a given phase of p_n travels along the channel[105]:

$$v_{ph}(x_i, \omega_n) = -\omega/k = -\omega_n / \left(\frac{\mathrm{d}(\Delta\Phi_{0-x_i}^{n,p})}{\mathrm{d}x_i} \right) \tag{D.1}$$

To enable a comparison with the experimental data, we define an average phase velocity $\bar{v}_{ph}(\omega_n)$ for the propagation from the channel entrance $x = 0$ to $x = x_i$ by replacing $\mathrm{d}(\Delta\Phi_{0-x_i}^{n,p})/\mathrm{d}x_i$ with the phase difference and the traveled distance $\Delta x = x_i$: $\bar{v}_{ph}(\omega_n, x_i) = -x_i\omega_n/\Delta\Phi_{0-x_i}^{n,p}$. The ratio of the pressure at position x with respect to the channel entrance is given for each Fourier component as:

$$\frac{p_n(x_i, t)}{p_n(0, t)} = \frac{\sinh[\lambda_n(l - x)]}{\sinh[\lambda_n l]} \tag{D.2}$$

In the low frequency limit $\omega \ll \omega_{\mathrm{cutoff}}$ the viscous dissipation of the PDMS channel wall is negligible ($\delta \approx 0$). Together with negligible inertia $L_x \approx 0$ we get $\lambda_n = \sqrt{i\omega_n R_x C_x}$, so that we can write λ_n in the form of $\lambda_n = a + ia$ (imaginary and real parts are of equal absolute value). We can now calculate the real and imaginary parts $\mathrm{Re}(\lambda_n)$ and $\mathrm{Im}(\lambda_n)$ of $\frac{p_n(x_i,t)}{p_n(0,t)}$ from eq. D.2. The phase difference $\Delta\Phi$ between $p_n(x_i, t)$ and $p_n(0, t)$ can then be calculated from

$$\tan\Delta\Phi_{0-x_i}^{n,p} = \frac{\mathrm{Im}(\lambda_n)}{\mathrm{Re}(\lambda_n)}, \tag{D.3}$$

which yields

$$\Delta\Phi_{0-x_i}^{n,p} = \arctan\left[\frac{\tanh(al)\tan(a(l-x_i)) - \tan(al)\tanh(a(l-x_i))}{\tanh(al)\tanh(a(l-x_i)) - \tan(al)\tan(a(l-x_i))}\right] \tag{D.4}$$

For $\omega \to 0$ we have $al \ll 1$ and $a(l - x_i) \ll 1$. Taylor expansion of eq. D.4 yields:

$$\Delta\Phi_{0-x_i}^{n,p} \approx \arctan\left[\frac{1}{3}a^2(x_i^2 - 2lx_i)\right] \approx -\frac{1}{6}\omega_n R_x C_x(2lx_i - x_i^2) \tag{D.5}$$

The phase velocity is then calculated as

$$v_{ph}(x_i) = \frac{\omega_n}{\partial \Delta \Phi_{0-x_i}^{n,p}/\partial x_i} = \frac{\omega}{\frac{1}{3}\omega R_x C_x (l - x_i)} \tag{D.6}$$

In the low frequency limit $\omega \ll \omega_{\text{cutoff}}$ we thus obtain a phase velocity of

$$v_{ph}(x_i) = \frac{3D_p}{l - x_i}. \tag{D.7}$$

Eq. D.1 yields an average phase velocity $\bar{v}_{ph}(\omega_n)(0 \to x_i)$

$$\bar{v}_{ph}(x_i) = \frac{\omega x_i}{\Delta \Phi_{0-x_i}^{n,p}} = \frac{6D_p}{2l - x_i} \tag{D.8}$$

which are independent of the frequency but dependent on the x-position along the channel. Thus, the time for a pulse to cross the entire channel is given as $\tau(0 \to l) = \frac{l}{\bar{v}_{ph}(l)} = \frac{l^2}{6 \cdot D_p}$.

For high frequencies $\omega \gg \omega_{\text{cutoff}}$ with $\delta \sim 0$ and amplitudes where inertia is still negligible $L_x \approx 0$ we get

$$\lambda_n = \sqrt{\frac{\omega_n C_x R_x}{1 + \tan^2 \delta_n}(\tan \delta_n + i)} \equiv K'\sqrt{\tan \delta_n + i} \tag{D.9}$$

with $\lambda_n \gg 1$. Away from the channel end $x \neq l$ the arguments of sinh and cosh in eq. 6.6 are big and we can approximate

$$\begin{aligned} p_n(x,t) &\approx \Pi_{0n} \exp(-\lambda_n x + i\omega_n t) \\ Q_n(x,t) &\approx \Pi_{0n} \frac{\lambda_n}{R_x + i\omega_n L_x} \exp(-\lambda_n x + i\omega_n t). \end{aligned} \tag{D.10}$$

For negligible inertia, the phase difference $\Delta\theta$ between the pressure and the flowrate is thus given by the ratio of imaginary and real parts of λ_n. From $\lambda = K'\sqrt{\tan \delta_n + i}$ it follows

$$\tan(2\Delta\theta) = \frac{1}{\tan \delta_n} \tag{D.11}$$

which can be written as

$$\tan(\Delta\theta) = \frac{1 - \sin \delta_n}{\cos \delta_n} = \cot\frac{\delta_n + \pi/2}{2} = \tan(-\pi/4 - \delta_n/2), \tag{D.12}$$

The phase difference between p and Q for x away from $x = l$ is thus given as

$$\Delta\theta = -(\pi/4 + \delta_n/2). \tag{D.13}$$

The phase difference $\Delta \Phi_{0-x_i}^{n,p}$ between the pressure at $x = 0$ and $x = x_i$ is directly given by the imaginary part of λ_n:

$$\Delta \Phi_{0-x_i}^{n,p} = x_i \text{Im}(\lambda_n) \tag{D.14}$$

The calculation of the imaginary part of λ_n yields

$$\Delta\Phi_{0-x_i}^{n,p} = x_i\sqrt{\frac{1}{2}\omega_n C_x R_x \cos\delta_n(1 - \sin\delta_n)} \tag{D.15}$$

which gives a phase velocity of

$$v_{ph}(\omega_n) = \overline{v}_{ph}(\omega_n) = \frac{\omega_n}{\partial\Delta\Phi_{0-x}^{n,p}/\partial x} = \sqrt{\frac{2\omega_n D_p}{\cos\delta_n(1 - \sin\delta_n)}} \tag{D.16}$$

which is independent of x_i and thus equal to the averaged phase velocity. For a purely elastic channel we get a phase difference of $\pi/4$ between p and Q and a phase velocity of $v_{ph} = \sqrt{2\omega_n D_p}$.

BIBLIOGRAPHY

[1] A. R. Abate and D. A. Weitz. Single-layer membrane valves for elastomeric microfluidic devices. *Applied Physics Letters*, 92, 2008.

[2] M. Abramowitz and I. A. Stegun. *Handbook of mathematical functions.* National Bureau of Standards, U.S. governement, 1964.

[3] J. Alastruey, K. H. Parker, J. Peiro, and S. J. Sherwin. Lumped parameter outflow models for 1-d blood flow simulations: Effect on pulse waves and parameter estimation. *Communications in Computational Physics*, 4(2):317–336, 2007.

[4] R. Y. Amenzadeh. Analytical solution of the problem of wave flow of a viscoelastic fluid in an elastic tube taking into account the effect of narrowing. *Doklady Physics*, 53(1):39–42, 2008.

[5] S. L. Anna and G. H. McKinley. Elasto-capillary thinning and breakup of model elastic liquids. *Journal of Rheology*, 45:115–138, 2001.

[6] P. E. Arratia, J. P. Gollub, and D. J. Durian. Polymeric filament thinning and breakup in microchannels. *Physical Review E*, 77:036309, 2008.

[7] J. Y. Baek, J. Y. Park, J. I. Ju, T. S. Lee, and S. H. Lee. A pneumatically controllable flexible and polymeric microfluidic valve fabricated via in situ development. *J. Micromech. Microeng.*, 15:10151020, 2005.

[8] D. G. Baird, T. W. Chan, C. McGrady, and S. M. Mazahir. Evaluation of the use of a semi-hyperbolic die for measuring elongational viscosity of polymer melts. *Applied Rheology*, 20, 2009.

[9] J-F Berret, J. Appell, and G. Porte. Linear rheology of entangled wormlike micelles. *Langmuir*, 9:2851–2854, 1993.

[10] R. B. Bird, R. C. Armstrong, and O. Hassager. *Dynamics of Polymeric Liquids.* Wiley-Interscience, 1987.

[11] P. O. Brunn. Objective flow classification parameters and their use in general steady flows. *Rheologica Acta*, 46:171–181, 2006.

[12] Henrik Bruus. *Theoretical Microfluidics.* Oxford University Press, 2007.

[13] C. G. Caro, K. H. Parker, and D. J. Doorly. Essentials of blood flow. *Perfusion*, 10:131–134, 1995.

[14] L. Casanellas and J. Ortin. Laminar oscillatory flow of Maxwell and Oldroyd-B fluids: Theoretical analysis. *Journal of non-Newtonian Fluid Mechanics*, 166:1315–1326, 2011.

[15] A. Celani, A. Puliafito, and K. Turitsyn. Polymers in linear shear flow: A numerical study. *EPL (Europhys. Lett.)*, 70(4):464, 2005.

[16] Y.-L. Chen, M. D. Graham, J. J. de Pablo, K. Jo, and D. C. Schwartz. Dna molecules in microfluidic oscillatory flow. *Macromolecules*, 38:6680–6687, 2005.

[17] S. Cheng and S.-Q. Wang. Is shear banding a metastable property of well-entangled polymer solutions? *Journal of Rheology*, 56:1413–1428, 2012.

[18] M. Chertkov, I. Kolokolov, V. Lebedev, and K. Turitsyn. Polymer statistics in a random flow with mean shear. *J. Fluid Mech.*, 531:251, 2005.

[19] S. Choi and J.-K. Park. Microfluidic rheometer for characterization of protein unfolding and aggregation in microflows. *Small*, 10, 2010.

[20] A. J. Chorin and J. E. Marsden. *A Mathematical Introduction to Fluid Mechanics*. Springer, 3rd edition, 1990.

[21] F. N. Cogswell. Converging flow and stretching flow - compilation. *Journal of Non-Newtonian Fluid Mechanics*, 4:23–38, 1978.

[22] R. H. Colby, D. C. Boris, W. E. Krause, and S. Dou. Shear thinning of unentangled flexible polymer liquids. *Rheol. Acta*, 46:569–575, 2007.

[23] M. Cromer, P. L. Cook, and G. H. McKinley. Pressure-driven flow of wormlike micellar solutions in rectilinear microchannels. *Journal of Non-Newtonian Fluid Mechanics*, 166:180–193, 2011.

[24] I. S. Dalal, N. Hoda, and R. G. Larson. Multiple regimes of deformation in shearing flow of isolated polymers. *J. Rheology*, 56:305–332, 2012.

[25] P. G. DeGennes. Reptation of a polymer chain in presence of fixed obstacles. *Journal of Chemical Physics*, 55:572–579, 1971.

[26] J. K. G. Dhont and W. J. Briels. Rod-like brownian particles in shear flow. In *Soft Matter*, pages 147–216. Wiley-VCH Verlag GmbH & Co. KGaA, 2007.

[27] M. Doi and S. F. Edwards. *The Theory of Polymer Dynamics*. Oxford University Press, 1986.

[28] L. Q. Evertz, E. M. Rassi, J. R. M. Kennedy, S. L. Codd, and J. D. Seymour. Oscillatory flow phenomena in simple and complex fluids. *Applied Magnetic Resonance*, 42:211–225, 2012.

[29] M. A. Fardin, T. Divoux, M. A. Guedeau-Boudeville, I. Bouchet-Maulien, J. Browaeys, G. H. McKinley, S. Manneville, and S. Lerouge. Shear-banding in surfactant wormlike micelles: elastic instabilities and wall slip. *Soft Matter*, 8:2535–2553, 2012.

[30] L. Formaggia, D. Lamponi, and A. Quarteroni. One-dimensional models for blood flow in arteries. *Journal of Engineering Mathematics*, 47:251–276, 2003.

[31] S. Gerashchenko and V. Steinberg. Statistics of a single polymer molecule in shear flow. *Phys. Rev. Lett.*, 96:038304, 2006.

[32] T. Gervais, J. El-Ali, A. Günther, and K. F. Jensen. Flow-induced deformation of shallow microfluidic channels. *Lab Chip*, 6:500–507, 2006.

[33] A. G. Gibson. *Converging Dies, in "Rheological Measurement" by A. A. Collier amd D. W. Clegg*. Elsevier Applied Science, London, 2nd edition, 1988.

[34] H. Giesekus. Strömungen mit konstantem Geschwindigkeitsgradienten und die Bewegung von darin suspendierten Teilchen: Teil 1. *Rheologica Acta*, 2(2):101–112, 1962.

[35] H. Giesekus. Strömungen mit konstantem Geschwindigkeitsgradienten und die Bewegung von darin suspendierten Teilchen: Teil 2. *Rheologica Acta*, 2(2):112–122, 1962.

[36] J. Glaser, D. Chakraborty, K. Kroy, I. Lauter, M. Degawa, N. Kirchgessner, B. Hoffmann, R. Merkel, and M. Giesen. Tube width fluctuations in F-actin solutions. *Phys. Rev. Lett.*, 105, 2010.

[37] J. S. Go and S. Shoji. A disposable, dead volume-free and leak-free in-plane PDMS microvalve. *Sensors and Actuators A*, 114:438444, 2004.

[38] N. J. Graf and M. J. Bowser. A soft-polymer piezoelectric bimorph cantilever-actuated peristaltic micropump. *Lab Chip*, 8:16641670, 2008.

[39] W. Gu, X. Zhu, N. Futai, B. S. Cho, and S. Takayama. Computerized microfluidic cell culture using elastomeric channels and braille displays. *PNAS*, 101(45):1586115866, 2004.

[40] B. S. Hardy, K. Uechi, J. Zhen, and H. P. Kavehpour. The deformation of flexible PDMS microchannels under a pressure driven flow. *Lab Chip*, 7:935–938, 2009.

[41] L. Harnau, R. G. Winkler, and P. Reineker. Dynamic structure factor of semiflexible macromolecules in dilute solution. *J. Chem. Phys.*, 104(16):6355–6368, 1996.

[42] E. F. Hasselbrink, T. J. Shepodd, and J. E. Rehm. High-pressure microfluidic control in lab-on-a-chip devices using mobile polymer monoliths. *Anal. Chem.*, 74:4913–4918, 2002.

[43] S. J. Haward, V. Sharma, and J. A. Odell. Extensional opto-rheometry with biofluids and ultra-dilute polymer solutions. *Soft Matter*, 7:9908–9921, 2011.

[44] H. Hinsch and E. Frey. Conformations of entangled semiflexible polymers: Entropic trapping and transient non-equilibrium distributions. *ChemPhysChem*, 10:2891–2899, 2009.

[45] H. Hinsch, J. Wilhelm, and E. Frey. Quantitative tube model for semiflexible polymer solutions. *European Physical Journal E*, 24:35–46, 2007.

[46] J. Honerkamp. *Stochastic dynamical systems: Concepts, numerical methods, data analysis*. Wiley–VCH, 1994.

[47] Jonathon Howard. *Mechanics of Motor Proteins and the Cytoskeleton*. Palgrave Macmillan, 2005.

[48] J. S. Hur, E. S. G. Shaqfeh, and R. G. Larson. Brownian dynamics simulations of single DNA molecules in shear flow. *J. Rheol.*, 44(4):713–742, 2000.

[49] K. Hyun, S. H. Kim, K. H. Ahn, and S. J. Lee. Large amplitude oscillatory shear as a way to classify the complex fluids. *Journal of non-Newtonian Fluid Mechanics*, 107:51–65, 2002.

[50] G. B. Jeffery. The motion of ellipsoidal particles immersed in a viscous fluid. *Proc. R. Soc. Lond. A*, 102(715):161–179, November 1922.

[51] K. Jo, Y.-L. Chen, J. J. de Pablo, and D. C. Schwartz. Elongation and migration of single dna molecules in microchannels using oscillatory shear flows. *Lab on a Chip*, 9, 2009.

[52] A. Karnis, H. L. Goldsmith, and S. G. Mason. Axial migration of particles in Poiseuille flow. *Nature*, 200:159–160, 1963.

[53] A. W. Khir, A. O'Brien, J. S. R. Gibbs, and K. H. Parker. Determination of wave speed and wave separation in the arteries. *Journal of Biomechanics*, 34:11451155, 2001.

[54] A. W. Khir and K. H. Parker. Measurements of wave speed and reflected waves in elastic tubes and bifurcations. *Journal of Biomechanics*, 35:775783, 2002.

[55] J. Y. Kim, J. Y. Baek, K. H. Lee, Y. D. Park, K. Sun, T. S. Lee, and S. H. Lee. Photopolymerized check valve and its integration into a pneumatic pumping system for biocompatible sample delivery. *Lab Chip*, 6:1091–1094, 2006.

[56] Y. T. Kim, B. Kuczenski, P. R. LeDuc, and W. C. Messner. Modulation of fluidic resistance and capacitance for long-term, high-speed feedback control of a microfluidic interface. *Lab Chip*, 9:26032609, 2009.

[57] U. A. Klessinger, B. K. Wunderlich, and A. R. Bausch. Transient flow behaviour of complex fluids in microfluidic channels. *submitted to Microfluidics and Nanofluidics*, 2012.

[58] H. Kobayashi and R. Yamamoto. Tumbling motion of a single chain in shear flow: a crossover from Brownian to non-Brownian behavior. *Phys. Rev. E*, 81:041807, 2010.

[59] G. P. Krishnan and D. T. Leighton. Inertial lift on a moving sphere in contact with a plane wall in a shear flow. *Physics of Fluids*, 7:2538–2545, 1995.

[60] M. Kröger and M. Hütter. Symbolic computation of the phoretic acceleration of convex particles suspended in a non-uniform gas. *Comput. Phys. Commun.*, 175:650–664, 2006.

[61] M. Kröger and M. Hütter. Unifying kinetic approach to phoretic forces and torques for moving and rotating convex particles. *J. Chem. Phys.*, 125:044105, 2006.

[62] Martin Kröger. *Models for polymeric and anisotropic liquids.* Springer, Berlin, 2005.

[63] S. M. Langelier, D. S. Chang, R. I. Zeitoun, and M. A. Burns. Acoustically driven programmable liquid motion using resonance cavities. *PNAS*, 106(31):1261712622, 2009.

[64] R. G. Larson. Arrested tumbling in shearing flows of liquid crystal polymers. *Macromolecules*, 23:3938–3992, 1990.

[65] R. G. Larson. *The Structure and Rheology of Complex Fluids.* John Wiley & Sons, 1994.

[66] S. Lee, W. Jeonga, and D. J. Beebe. Microfluidic valve with cored glass microneedle for microinjection. *Lab Chip*, 3:164167, 2003.

[67] N. L. Leon, D. T. Chiu, C. J. Wargo, H. Wu, I. S. Choi, J. R. Anderson, and G. M. Whitesides. Design and fabrication of integrated passive valves and pumps for flexible polymer 3-dimensional microfluidic systems. *Biomedical Microdevices*, 4:117–121, 2002.

[68] D. C. Leslie, C. J. Easley, E. Seker, J. M. Karlinsey, M. Utz, M. R. Begley, and J. P. Landers. Frequency-specific flow control in microfluidic circuits with passive elastomeric features. *Nature Physics*, 5:231–235, 2009.

[69] T. Liu. Fully developed flow of power-law fluids in ducts. *Ind. Eng. Chem. Fundam.*, 22:183–186, 1983.

[70] J. Loverich, I. Kanno, and H. Kotera. Concepts for a new class of all-polymer micropumps. *Lab Chip*, 6:1147–1154, 2007.

[71] J. Loverich, I. Kanno, and H. Kotera. Single-step replicable microfluidic check valve for rectifying and sensing low reynolds number flow. *Microfluid. Nanofluid.*, 3:427435, 2007.

[72] J. L. Lumley. Drag reduction by additives. *Annual Review of Fluid Mechanics*, 1:367–&, 1969.

[73] J. M. Tarbell M. Klanchar and D. M. Wang. In vitro study of the influence of radial wall motion on wall shear stress in an elastic tube model of the aorta. *Circulation Research*, 66:1624–1635, 1990.

[74] C. W. Macosco. *Rhelogy. Principles, Measurements and Applications.* John Wiley & Sons, 1994.

[75] J. C. McDonald and G. M. Whitesides. Poly(dimethylsiloxane) as a material for fabricating microfluidic devices. *Accounts of Chemical Research*, 35:491–499, 2002.

[76] S. Middleman. Flow of power law fluids in rectangular ducts. *Trans. Soc. Rheol.*, 9, 1965.

[77] A. Montesi, D. C. Morse, and M. Pascali. Brownian dynamics algorithm for bead-rod semiflexible chain with anisotropic friction. *J. Chem. Phys*, 122:084903, 2005.

[78] T. Munk, O. Hallatschek, C. H. Wiggins, and E. Frey. Dynamics of semiflexible polymers in a flow field. *Phys. Rev. E*, 74(4 Pt 1):041911, Oct 2006.

[79] P. Nghe, E. Terriac, M. Schneider, Z. Z. Li, M. Cloitre, B. Abecasis, and P. Tabeling. Microfluidics and complex fluids. *Lab Chip*, 11:788–794, 2011.

[80] W. W. Nichols and M. F. O'Rourke. *McDonald's Blood Flow in Arteries: Theoretical, Experimental.* Oxford University Press, 5 edition, 2005.

[81] C. J. S. Petrie. Extensional viscosity: A critical discussion. *Journal of Non-Newtonian Fluid Mechanics*, 137:15–23, 2006.

[82] C. J. Pipe and G. H. McKinley. Microfluidic rheometry. *Mechanics Research Communications*, 36:110–120, 2009.

[83] X. G. Qi, D. M. Scott, and D. I. Wilson. Modelling laminar pulsed flow in rectangular microchannels. *Chemical Engineering Science*, 63:2682–2689, 2008.

[84] S. Rammensee. *Assembly of Engineered Spider Silk in Microfluidic Devices and Free Surface Flow.* Ph.D. Thesis, Technische Universität München, 2009.

[85] A. R. Rao. Oscillatory flow in an elastic tube of variable cross-section. *Acta Mechanica*, 46:155–165, 1983.

[86] M. Reiner. The Deborah number. *Physics today*, 17:62–64, 1964.

[87] M. Romanska, H. Hinsch, N. Kirchgessner, M. Giesen, M. Degawa, B. Hoffmann, E. Frey, and R. Merkel. Direct observation of the tube model in F-actin solutions: Tube dimensions and curvatures. *EPL*, 86, 2009.

[88] M. Rubinstein and R. H. Colby. *Polymer Physics.* Oxford University Press, New York, 2003.

[89] N. B. Sanches, M. L. Dias, and E. B. A. V. Pacheco. Comparative techniques for molecular weight evaluation of poly (ethylene terephthalate) (PET). *Polymer Testing*, 24:688–693, 2005.

[90] R. S. Schechter. On the steady flow of a non-Newtonian fluid in cylinder ducts. *AIChE Journal*, 7:445–448, 1961.

[91] J. Schilling, E. Sackmann, and A. R. Bausch. Digital imaging processing for biophysical applications. *Rev Sci Instrum*, 75:28222827, 2004.

[92] K. M. Schmoller, C. Semmrich, and A. R. Bausch. Slow down of actin depolymerization by cross-linking molecules. *J. Struct. Biol.*, 173(2):350–357, 2011.

[93] C. M. Schroeder, H. P. Babcock, E. S. G. Shaqfeh, S. Chu, and S. Chu. Observation of polymer conformation hysteresis in extensional flow. *Science*, 301:1515–1519, 2003.

[94] N. Sedaghatizadeh, G. Atefi, A. A. Fardad, A. Barari, S. Soleimani, and S. Khani. Analysis of blood flow through a viscoelastic artery using the Cosserat continuum with the large-amplitude oscillatory shear deformation model. *Journal of the mechanical behaviour of biomedical materials*, 4:1123–1131, 2011.

[95] C. Sendner and R. Netz. Shear-induced repulsion of a semiflexible polymer from wall. *EPL*, 81:54006, 2008.

[96] C. Sendner and R. Netz. Single flexible and semiflexible polymers at high shear: non-monotonic and non-universal stretching response. *European Physical Journal*, 30:75–81, 2009.

[97] V. Sharma, A. Jaishankar, Y.-C. Wang, and G. H. McKinley. Rheology of globular proteins: apparent yield stress, high shear rate viscosity and interfacial viscoelasticity of bovine serum albuminum solutions. *Soft Matter*, 7:5150–5160, 2011.

[98] S. J. Sherwin, V. Franke, J. Peiro, and K. Parker. One-dimensional modelling of a vascular network in space-time variables. *Journal of Engineering Mathematics*, 47(3-4):217–250, 2003.

[99] D. E. Smith, H. P. Babcock, and S. Chu. Single-polymer dynamics in steady shear flow. *Science*, 283(5408):1724–1727, Mar 1999.

[100] D. E. Smith and S. Chu. Response of flexible polymers to a sudden elongational flow. *Science*, 281:1335–1340, 1998.

[101] Y. Son. Determination of shear viscosity and shear rate from pressure drop and flow rate relationship in a rectangular channel. *Polymer*, 48:632–637, 2006.

[102] T. M. Squires and S. R. Quake. Microfluidics: Fluid physics at the nanoliter scale. *Review of Modern Physics*, 77:977–1026, 2005.

[103] R. Tanner and R. R. Huilgol. On a classification scheme for flow fields. *Rheologica Acta*, 14:959–962, 1975.

[104] M. G. Taylor. An approach to an analysis of the arterial pulse wave 1. oscillations in an attenuating line. *Physics in Medicine and Biology*, 1:258–269, 1957.

[105] M. G. Taylor. An approach to an analysis of the arterial pulse wave 2. fluid oscillations in an elastic pipe. *Physics in Medicine and Biology*, 1:321–329, 1957.

[106] R. E. Teixeira, H. P. Babcock, E. S. G. Shaqfeh, and S. Chu. Shear thinning and tumbling dynamics of single polymers in the flow-gradient plane. *Macromolecules*, 38:581, 2005.

[107] R. E. Teixeira, A. K. Dambal, D. H. Richter, E. S. G. Shaqfeh, and S. Chu. The individualistic dynamics of entangled DNA in solution. *Macromolecules*, 40(7):2461–2476, 2007.

[108] I. Teraoka. *Polymer Solutions: An Introduction to Physical Properties*. John Wiley & Sons, 2002.

[109] A. S. Tijsseling. Water hammer with fluid-structure interaction in thickwalled pipes. *Computers & Structures*, 85:844–851, 2007.

[110] B. A. Toms. Some observations on the flow of linear polymer solutions through straight tubes at large Reynolds numbers. *Proc. 1st Int. Congress on Rheology*, 2:135–141, 1948.

[111] M. A. Unger, H.-P. Chou, T. Thorsen, A. Scherer, and S. R. Quake. Monolithic microfabricated valves and pumps by multilayer soft lithography. *Science*, 288(5463):113–116, 2000.

[112] E. Wada. Effect of rate of shear on viscosity of a dilute linear polymer and of tobacco mosaic virus in solution. *Journal of Polymer Science*, 14:305–307, 1954.

[113] B. Wang, J. Guan, S. M. Anthony, S. C. Bae, K. S. Schweizer, and S. Granick. Confining potential when a biopolymer filament reptates. *Phys. Rev. Lett.*, 104, 2010.

[114] D. M. Wang and J. M. Tarbell. Nonlinear analysis of oscillatory flow, with a nonzero mean, in an elastic tube (artery). *Journal of Biomechanical Engineering*, 117:127–135, 1995.

[115] R. G. Winkler. Semiflexible polymers in shear flow. *Phys. Rev. Lett.*, 97(12):128301, Sep 2006.

[116] R. G. Winkler. Conformational and rheological properties of semiflexible polymers in shear flow. *J. Chem. Phys.*, 133(16):164905, Oct 2010.

[117] J. R. Womersley. Oscillatory flow in arteries: the constrained elastic tube as a model of arterial flow and pulse transmission. *Physics in Medicine and Biology*, 2:178–187, 1957.

[118] S. Yamamoto and T. Matsuoka. Viscosity of dilute suspensions of rodlike particles: A numerical simulation method. *J.Chem.Phys*, 100:3317–3324, 1994.

[119] B. Yang and Q. Lin. A planar compliance-based self-adaptive microfluid-variable resistor. *Journal of Microelectromechanical Systems*, 16(2):411–419, 2007.

E. LIST OF PUBLICATIONS

- M. Harasim, B. Wunderlich, O. Peleg, M. Kröger, and A. Bausch, *Direct observation of the dynamics of semiflexible polymers in shear flow*, submitted (2012).

- U.A. Klessinger, B.K. Wunderlich, and A.R. Bausch, *Transient flow behavior of complex fluids in microfluidic channels*, submitted (2012).

- B.K. Wunderlich, and A.R. Bausch, *Differential capillary viscometer for measurement of non-Newtonian fluids* to be submitted (2012).

- B.K. Wunderlich, U.A. Klessinger, and A.R. Bausch, *Diffusive spreading of time-dependent pressures in elastic microfluidic devices*, Lab on a Chip, Volume: **10**, Issue: 8 (2010), 3317–3324.

- P.A. Neff, A. Serr, B.K. Wunderlich, and A.R. Bausch, *Label-free electrical determination of trypsin activity by a silicon-on-insulator based thin film resistor*, ChemPhysChem, Volume: **8**, Issue: 14 (2007), 2133–2137

- B.K. Wunderlich, P.A. Neff, and A.R. Bausch, *Mechanism and sensitivity of the intrinsic charge detection of biomolecular interactions by field effect devices*, Applied Physics Letters, Volume: **91**, Issue: 8 (2007), id. 083904.

- P.A. Neff, B.K. Wunderlich, R. von Klitzing, and A.R. Bausch, *Formation and dielectric properties of polyelectrolyte multilayers studied by a silicon-on-insulator based thin film resistor*, Langmuir, Volume: **23**, Issue: 7 (2007), 4048–4052

- P.A. Neff, B.K. Wunderlich, S.Q. Lud, and A.R. Bausch, *Silicon-on-insulator based thin film resistors for quantitative biosensing applications*, Physica Status Solidi A - Applications and Materials Science, Volume: **203**, Issue: 14 (2006), 3417–3423

DANKSAGUNG